

University of Southern Queensland



**Role of Silanised Halloysite Nanotubes on the
Morphological and Materials Characteristics of Thermoset
Composites**

A thesis submitted by

Mushtaq Taleb Ali Albdiry

B.Sc. Eng., M.Sc. Eng.

Supervised by

Dr Harry S. Ku

Dr Belal F. Yousif

For the award of
Doctor of Philosophy

2014

Abstract

The effects of nano-reinforcements on the material characteristics of thermoset nanocomposites in relation to their different morphological structures are not yet well understood. This study investigates the effects of untreated halloysite (HNT) and vinyltrimethoxysilane (VTMS)-treated halloysite nanotubes (s-HNT) on the morphological and materials characteristics of highly crosslinked unsaturated polyester (UPE) nanocomposites. The grafting of the VTMS coupling agent on the halloysite surface was performed using the sol-gel process. Nanocomposites based on different weight percentages (1 wt % to 9 wt %) of HNT or s-HNT were prepared via high shear disperser, followed by the ultrasonication technique.

The morphological structures and dispersion of halloysite particles in the UPE matrix were examined using transmission electron microscopy (TEM), and wide-angle and small-angle x-ray scattering (WAXS and SAXS). Fourier Transform Infrared (FT-IR) spectroscopy was used to determine the molecular structures and indicate the vibrational states of the chemical bonds obtained after curing. Thermogravimetric analysis (TGA) was applied to detect the thermal stability, and differential scanning calorimetry (DSC) spectra were applied to measure the glass transition temperature (T_g) in heating mode. The viscoelastic properties—the storage modulus (E'), loss modulus (E'') and $\tan(\delta)$ —were measured using dynamic mechanical analysis (DMA).

Mechanical properties viz. tensile strength, Young's modulus, elongation at break, flexural strength and modulus of the developed materials were determined. The elastic modulus was predicted using different mathematical models—the Halpin-Tsai, Smallwood-Einstein, Kerner, and Guth and Gold models—in order to further understand the correlation between the mechanical properties and the morphology.

The tribological performance of neat UPE and different nanocomposite systems was also explored. Wear resistance was evaluated using block-on-ring (BOR) configuration against a stainless steel counterpart under dry sliding conditions with

different operating parameters. The topography analysis of worn surfaces was examined using scanning electron microscopy (SEM) analysis to determine the wear mechanisms occurring in such materials.

The micromechanism of plastic deformation of neat UPE and its nanocomposite systems was characterised under impact loading conditions. The impact strength and total energy were performed with a falling-weight impact tester at different temperatures (-20 °C, +20 °C and +60 °C). The morphologies of tensile-fractured surfaces and impacted-fractured surfaces of unfilled UPE and UPE filled with HNT and s-HNT nanocomposites were identified to delineate their fracture modes.

The fracture toughness measurements represented by the critical stress intensity factor (K_{Ic}) and critical strain energy release rate (G_{Ic}) were calculated based on linear elastic fracture mechanics (LEFM) and two different geometries tested under two different loading conditions: a single-edge notch (SEN) specimen under three-point bending (SEN-3PB) and a compact tension (CT) specimen under tension. The crack initiation and propagation phenomenon were simulated using a traction-separation cohesive element method via ABAQUS finite element (FE) software. The SEM observations were used to identify the roles of HNT and s-HNT particles in toughening mechanisms and initiating plastic deformation in the nanocomposites.

The results showed that the surface of s-HNT was rougher than the untreated HNT particles due to the presence of multiple interfacial bonding sites on the silanised surface, which induced better adhesion and load transfer among the interface regions. A more well-dispersed structure with less skewed-like aggregates was observed in the UPE/s-HNT over the UPE/HNT composites. The incorporation of HNT or s-HNT particles into the UPE nanocomposites changed their crystalline structure, indicating a high degree of nanotube orientation.

The FT-IR spectra of the s-HNT powder exhibited that the Si-O-Si absorption band occurred in the region of 701 to 1,085 cm^{-1} wavenumbers. No significant change in the thermal stability of the nanocomposites was observed with the use of silane-treated nanoparticles. The effect of HNT or s-HNT on the T_g values was relatively insignificant, while they slightly reduced with increasing halloysite concentrations.

This was likely because coupling of halloysite to the polymer through adsorption and hydrogen bonding led to strengthening the interface and reducing the T_g values.

All material properties—such as tensile and flexural strength, impact strength and fracture toughness—except wear resistance, exhibited a steady-state increasing trend with the incorporation of up to 5 wt% HNT or s-HNT into the UPE resin. The 3% HNT/UPE or 3% s-HNT/UPE nanocomposites were found to obtain the highest values of these properties supported with uniformly dispersed particles. It was also proven that the computational results of damage zone and unstable crack propagation validated by the cohesive element method were convergent with the experimental data.

Compared to the HNT, the addition of the same content of s-HNT particles indicated slightly higher strength and toughness owing to the well-dispersed silanised particles and the enhanced interfacial adhesion thereof on initiating/participating in plastic deformation in the nanocomposites. Further increase of halloysite, irrespective of whether they were untreated or silane-treated, showed gradual decreases in most material properties associated with the presence of large clusters in the UPE nanocomposites.

The SEM observations of the fracture surfaces showed brittle fast fracture for neat UPE and coarser surfaces with different energy dissipation mechanisms for the nanocomposites. With the introduction of untreated halloysite, zone shielding and shear yielding mechanisms with the presence of full particle debonding—which activates void expansion and matrix shear deformation—were observed and suggested to be responsible for the toughness improvement in the the UPE/HNT nanocomposites. In addition, other major mechanisms—massive shear banding, crack deflection and local plastic deformation—occurred around the crack initiation zone, while river line patterns, a tail-like structure and the formation of microcracks mechanisms were observed in the UPE/s-HNT nanocomposites.

Certification of Dissertation

I certify that the thoughts, experimental work, numerical outcomes and conclusions reported in this dissertation ‘**Role of Silanised Halloysite Nanotubes on the Morphological and Materials Characteristics of Thermoset Composites**’ are entirely my own efforts, except where otherwise acknowledged. To the best of my knowledge, I also certify that the work presented in this thesis is original, except where due references are made.

.....

Signature of candidature

/ / 2014

Mushtaq Taleb Albdiry

Date

ENDORSEMENT

.....

/ / 2014

Date

Signature of supervisor

.....

/ / 2014

Signature of co-supervisor

Date

Acknowledgments

From the bottom of my heart, I would like to express my special thanks to my father and mother for their prayers and invocations to me. My thanks go to all my brothers, sisters and relatives for their support and help. My gratitude and thanks also go to my wife and beautiful children for their understanding, patience and continuous encouragement during these years, without whom this work would be impossible.

I would like to express my gratitude and appreciation to Dr Harry Ku, my principal supervisor, for his guidance, encouragement and suggestions throughout the course of my research at the University of Southern Queensland (USQ). My special thanks go to Dr Belal Yousif, my co-supervisor and dear friend, for his kindness, useful discussions and helpful criticisms that improved my thought process and the quality of my work.

I would also like to acknowledge the contributions of various members of the Faculty of Health, Engineering and Science (HES) and Centre of Excellence in Engineering Fibre Composites (CEEFC) for all the help they gave me during the work—particularly, Dr Francisco Cardona, Wayne Crowell and Mohan Trada. Many thanks are also extended to people working at the Plastic and Rubber Technical Education Centre (PARTEC) for their friendly help and valuable advice: Roger Cater (Manager), Mark Halford (Composites Consultant) and Corrie Gower (Plastic Fabrication Lecturer).

I would also like to thank the Academic Program Support Officer, Mrs Juanita Ryan, for her assistance to me with a big smile and ‘hello’. My thanks go to all colleagues and friends who helped and supported me by encouraging and stimulating me.

Financial support from the Australian Government and the USQ in the forms of an Australian Postgraduate Award (APA) and HES Scholarship are sincerely acknowledged as having made it possible for me to undertake my PhD program at the USQ.

Associated Publications

Journal Papers

Albdiry, MT & Yousif, BF 2014, ‘Role of silanized halloysite nanotubes on structural, mechanical properties and fracture toughness of thermoset nanocomposites’ *Materials and Design* vol. 57, pp. 279-288.

Albdiry, MT, Ku, H & Yousif, BF 2013, ‘Impact fracture behavior of silane-treated halloysite nanotubes-reinforced unsaturated polyester’, *Engineering Failure Analysis*, vol. 35, pp. 718-725.

Albdiry, MT & Yousif, BF 2013, ‘Morphological structures and tribological performance of unsaturated polyester based untreated/silane-treated halloysite nanotubes’, *Materials and Design*, vol. 48, pp. 68–76.

Albdiry, MT, Yousif, BF, Ku, H & Lau, KT 2013, ‘A critical review on the manufacturing processes in relation to the properties of nanoclay/polymer composites’, *Journal of Composite Materials*, vol. 47, no. 9, pp. 1093–1115

Albdiry, MT & Yousif, BF, under review, ‘Failure analysis and toughening mechanisms of silanized halloysite nanotubes filled unsaturated polyester nanocomposite under Mode I fracture toughness and bending testing’, *Engineering Fracture Mechanics*.

Albdiry, MT, Ku, H & Yousif, BF, In preparation, ‘Experimental and numerical evaluation of crack growth in halloysite nanotubes toughened unsaturated polyester nanocomposites using cohesive zone method’.

Conference Proceedings

Albdiry, MT, Yousif, BF & Ku, H, ‘Fracture toughness and toughening mechanisms of unsaturated polyester-based clay nanocomposites’, *Proceeding of 13th international conference on fracture (ICF13)*, 16–21 June 2013, Beijing, China.

Albdiry, MT, Yousif, BF & Ku, H, ‘Fracture toughness evaluation of halloysite nanotubes filled unsaturated polyester using J-integral technique’, *Proceedings of fifth international conference on engineering failure analysis (ICEFA-V)*, 1–4 July 2012, The Hague, The Netherlands.

Contents

Abstract	i
Certification of Dissertation	iv
Acknowledgments	v
Associated Publications	vi
Contents	viii
List of Figures	xi
List of Tables	xviii
List of Abbreviations	xix
Chapter 1: Introduction	1
1.1 General	1
1.2 HNT.....	1
1.3 UPE	3
1.4 Characterisation of Polymer Nanocomposites	4
1.5 Objectives of the Thesis	6
1.6 Scope of the Thesis	7
1.7 Outline of the Thesis	8
Chapter 2: Literature Review	11
2.1 Polymer-based Nanocomposites	11
2.2 Structure-property Relationship	11
2.2.1 Effect of Chemical Treatment on Morphology and Properties	13
2.2.2 Glass Transition Temperature (T_g).....	20
2.2.3 Thermal, Thermodynamic and Mechanical Properties	21
2.2.4 UPE-based Nanocomposites	22
2.3 Tribological Behaviour	25
2.4 Impact Strength	27
2.5 Fracture Toughness of Polymer Nanocomposites.....	29
2.6 Toughening Mechanisms in Polymer Nanocomposites	31
2.7 FEM Models for Prediction Crack Propagation.....	34
2.8 Summary	36
Chapter 3: Materials and Experimental Procedure	38
3.1 Description of Materials Used.....	38
3.2 Silane Chemical Treatment of Halloysite Nanotubes	39
3.3 Nanocomposite Preparation	40
3.4 Characterisation of Nanocomposites.....	42
3.4.1 Morphological Characterisation	42
3.4.2 FT-IR.....	43
3.4.3 Thermal Property Analysis.....	44
3.4.4 Glass Transition Temperature (T_g).....	45
3.4.5 Viscoelastic Properties	46
3.4.6 Mechanical Characteristics	47

3.4.7 Impact Fracture Toughness	50
3.4.8 Wear Characterisation	51
3.4.9 Fracture Toughness Measurement	53
Chapter 4: Role of Silanised Halloysite on Morphological Characteristics	60
4.1 Role of Silane Treatment on Structure of Halloysite	60
4.1.1 Introduction	60
4.1.2 Structure of Halloysite Before and After Silanisation	60
4.2 Characterisation of Nanocomposite Morphology	63
4.2.1 TEM	63
4.2.2 XRD	69
4.2.3 SEM and EDS Analysis	73
4.3 FT-IR Spectra	75
4.4 Summary	80
Chapter 5: Role of Silanised Halloysite on Thermo, Thermodynamic and Mechanical Properties	82
5.1 Results and Discussion	83
5.1.1 TGA	83
5.1.2 Thermodynamic Properties	85
5.1.2.1 Glass Transition Temperature	85
5.1.2.2 DMA	87
5.1.3 Mechanical Tests	90
5.1.4 Morphology of Tensile-fractured Surface	96
5.1.5 Mathematical Models for Modulus Predictions	99
5.2 Summary of the Results	102
Chapter 6: Role of Silanised Halloysite on Tribological Characteristics and Impact Fracture Behaviour	104
6.1 Role of Silanised Halloysite on Tribological Performance	104
6.1.1 Introduction	104
6.1.2 Results and Discussion	106
6.1.2.1 Weight Loss	106
6.1.2.2 The CoF (μ)	109
6.1.2.3 The Specific Wear Rate (W_s)	113
6.1.3 Summary of the Results	121
6.2 Role of Silanised Halloysite on Impact Fracture Behaviour	122
6.2.1 Background	122
6.2.2 Results and Discussion	124
6.2.2.1 Impact Testing	124
6.2.2.2 Impact-fracture Morphology	128
6.2.3 Summary	132
Chapter 7: Role of Silanised Halloysite on Failure and Toughening Mechanisms of Thermoset Nanocomposites	133
7.1 Background	133
7.2 Cohesive Element Model	135
7.3 Computational Simulations	136
7.3.1 FE Model	136
7.3.2 Initiation and Evolution of Damage	136
7.3.3 The Geometry of Model, Mesh Module and Boundary Conditions	138
7.4 Results and Discussion	139

7.4.1 Fracture Toughness Test	139
7.4.2 Cohesive Model Versus Experimental Results	146
7.4.3 Toughening Mechanisms	149
7.5 Summary	169
Chapter 8: Conclusion and Future Works	172
8.1 Conclusion.....	172
8.1.1 Morphological Characteristics	172
8.1.2 Thermo, Thermodynamic and Mechanical Properties	173
8.1.3 Tribological Behaviour	174
8.1.4 Impact Toughness	174
8.1.5 Failure Analysis and Toughening Mechanisms	175
8.2 Future Works.....	176
References	178
Appendix A: Preliminary Study	193

List of Figures

Figure 1.1: (a) Scanning Electron Microscope Image of HNTs and (b) Transmission Electron Microscopy (TEM) Micrograph of HNT	2
Figure 1.2: Schematic Illustration of the Scope of the Current Research	8
Figure 2.1: Schematic Diagram for Dispersion State of Polymer Nanocomposites ..	12
Figure 2.2: Mechanism of Silane Deposition on an Active Substrate	15
Figure 2.3: Crystalline Structures of HNTs	16
Figure 2.4: Modification of a Nanoparticle with 3-methacryloxypropyl Trimethoxysilane.....	16
Figure 2.5: X-ray Diffraction (XRD) Patterns of As-received and Modified HNTs	17
Figure 2.6: XRD Patterns for Natural Halloysite (H0) and Acid-treated Halloysite at Different Treatment Durations (H1-H21).....	18
Figure 2.7: TEM Micrographs of: (a) EPDM/10% HNT and (b) EPDM/10% s-HNT Nanocomposites	19
Figure 2.8: TEM Micrographs of: (a) Untreated Organoclay/PP and (b) Silanised Organoclay/PP Nanocomposites	19
Figure 2.9: SEM Micrographs of the Worn Tracks for Pure Epoxy and Different Nanocomposites Systems.....	27
Figure 2.10: SEM Micrographs of Fracture Surface from Epoxy Filled with 17.4% Silica Nanocomposites: (a) Matrix Ligament Bridging and (b) Circled Debonded Particles	31
Figure 2.11: SEM Micrographs of the Fracture Surfaces of: (a) Epoxy/1 wt% Organoclay/PES, (b) Characteristic Tail Structure in the Fracture Surface of Epoxy/1 wt% Organoclay/PES, (c) Characteristic Tail Structure on the Rough Fracture Surface of the Epoxy/3 wt% Organoclay/PES and (d) Various Fracture Positions Inside One Agglomerate on the Fracture Surface of the Epoxy/1 wt% Organoclay/PES Hybrid Nanocomposites	33
Figure 2.12: SEM Images of Fracture Surfaces of Epoxy Filled with Nanoclay Nanocomposite at: (a) Low Magnification and (b) High Magnification ..	34

Figure 2.13: VCCT for a 2-D Eight-noded Element.....	35
Figure 2.14: (a) Schematic of DCZM and (b) Definition of DCZM Element and its Node Numbering	36
Figure 3.1: Magnetic Stirrer Used in the Preparation of Silane Treatment.....	40
Figure 3.2: Sonicator Probe Used for the Sonication Process.....	41
Figure 3.3: Samples of: (a) Dog-bone Tensile Test and SEN and (b) CT	42
Figure 3.4: FT-IR Spectrophotometer Used in the Study	44
Figure 3.5: TGA-Q500 Used for Thermal Property Analysis.....	45
Figure 3.6: Differential Scanning Calorimeter (DSC-Q200) Used in the Study	46
Figure 3.7: DMA-Q800 Used to Measure the Viscoelastic Properties	47
Figure 3.8: Instron Alliance RT/10 MTS: (a) Universal Machine and (b) Laser Extensometer.....	48
Figure 3.9: Flexural Strength Testing Using MTS Universal Machine	49
Figure 3.10: Instron Dynatup 9250 HV Machine Used for Impact Test.....	50
Figure 3.11: (a) Tribometer Machine Used for Wear Testing and (b) Wear Testing Block	52
Figure 3.12: Specimen Configuration Used for Fracture Toughness Measurements for: (a) SENB Sample and (b) CT Geometry.....	55
Figure 3.13: (a) Bending Rig and (b) SEN Bend Geometry Used in this Study.....	56
Figure 3.14: (a) Tension Test and (b) Clevis Design Used for CT	59
Figure 4.1: Schematic Presentation of the Crystalline Structure of Halloysite.....	61
Figure 4.2: Schematic Presentation of Organosilane Treatment on Halloysite Surface.....	62
Figure 4.3: Schematic Presentation of the Interface Interaction between HNT Particle and UPE Polymer	63
Figure 4.4: TEM Micrographs of Untreated Halloysite Nanotubes (Loose Powders).....	64
Figure 4.5: TEM Micrographs of s-HNT (Loose Powders).....	64
Figure 4.6: TEM Images at Low Magnification of: (a, b) Cured UPE/HNT and (A, B) UPE/s-HNT Nanocomposites	65
Figure 4.7: TEM Micrographs of: (a–e) UPE-based Different Pristine HNT Nanocomposites and (A–E) UPE-based Different s-HNT Nanocomposites	68

Figure 4.8: Comparison of X-ray Scattering Scans for Neat UPE, Untreated HNT and Silane-treated HNT Loose Tubes	69
Figure 4.9: X-ray Scattering Scans for Neat UPE and Different UPE/HNT Nanocomposites	70
Figure 4.10: X-ray Scattering Scans of Different UPE/Silane-treated HNT Nanocomposites	71
Figure 4.11: Comparison of X-ray Scattering Scans of Neat UPE, UPE/3 wt% HNT and UPE/3 wt% s-HNT Nanocomposites	72
Figure 4.12: SEM Images Showing the Difference between: (a) UPE/3 Wt% Untreated HNT Surface and (b) UPE/3 Wt% S-HNT Nanocomposites Surface	73
Figure 4.13: SEM Image of UPE/5% HNT Nanocomposites Showing: (a) Large Halloysite Clusters and (b) the EDX Elemental Analysis Data for Different Spots in the Nanocomposites.....	74
Figure 4.14: (a) SEM Image of UPE/5 wt% s-HNT Nanocomposite and (b) its EDX Elemental Analysis	75
Figure 4.15: FT-IR Spectra of: (a) Neat UPE, HNT and s-HNT Powders and (b) Different UPE/Untreated HNT Nanocomposites.....	76
Figure 4.16: Comparison of FT-IR Spectres between Different UPE/HNT and UPE/s-HNT Nanocomposites	79
Figure 5.1: (a) TGA of Neat UPE, UPE/3% HNT and UPE/3% s-HNT Nanocomposites and (b) Close-up Image Showing 5% Weight Loss	84
Figure 5.2: DSC Thermograms of Neat UPE and its Untreated HNT Composites ...	85
Figure 5.3: DSC Thermograms of Neat UPE and its Silanised HNT Composites	86
Figure 5.4: Variation of Dynamic Mechanical Properties of Neat UPE and its Untreated HNT Nanocomposites as Functions of Temperature: (a) Storage Modulus, (b) Loss Modulus and (c) Tan δ	89
Figure 5.5: Representative Stress–strain Curves for Neat UPE and: (A) Different HNT and (B) S-HNT Nanocomposites	91
Figure 5.6: Tensile Properties of Neat UPE and UPE-based Different HNT and s-HNT Nanocomposites	93
Figure 5.7: Flexural Properties of Neat UPE and UPE-based: (a) Different HNT and (b) s-HNT Nanocomposites	94
Figure 5.8: SEM Images of the Fractured Surfaces of Neat UPE and UPE-based Different HNT and s-HNT Nanocomposites	98

Figure 5.9: Comparison of Experimental and Mathematical Results of Young's Modulus for UPE-based Different HNT and s-HNT Nanocomposites...	101
Figure 6.1: Variation of Weight Loss as a Function of HNT Contents with Various Sliding Times: (a) UPE/HNT and (b) UPE/s-HNT Nanocomposites	107
Figure 6.2: Hardness Results of Neat UPE and its HNT and s-HNT Nanocomposites	109
Figure 6.3: The CoF of UPE/HNT and UPE/s-HNT Nanocomposites.....	110
Figure 6.4: Friction Coefficient of Neat UPE and its Nanocomposites as a Function of Sliding Distance	111
Figure 6.5: Roughness Profile of the Counterface After Testing Different Nanocomposite Samples	112
Figure 6.6: Specific Wear Rate of Neat UPE and UPE/HNT Nanocomposites Tested at Sliding Distance of 11.5 Km, Normal Load of 20 N and Sliding Speed of 2.8 m/s	113
Figure 6.7: Specific Wear Rate of Neat UPE and UPE/s-HNT Nanocomposites Tested at Sliding Distance of 11.5 Km, Normal Load of 20 N and Sliding Speed of 2.8 m/s	114
Figure 6.8: Specific Wear Rate of Neat UPE and its Nanocomposites Under Wearing Conditions of Sliding Distance: 11.5 Km, Load: 20 N and Sliding Speed: 2.8 m/s.....	115
Figure 6.9: Typical Curves of Contact Temperatures as Functions of Sliding Time for Neat UPE and its Nanocomposites	116
Figure 6.10: SEM Micrographs of the Worn Surfaces for: (a) UPE/1% HNT, (b) UPE/3% HNT, (c) UPE/5% HNT and (d) UPE/7% HNT Nanocomposites	117
Figure 6.11: SEM Micrographs of the Worn Surfaces for: (a) UPE/1% s-HNT, (b) UPE/3% s-HNT, (c) and (d) UPE/5% s-HNT Nanocomposites	118
Figure 6.12: SEM Micrographs of the Worn Surfaces for: (a) UPE/3% HNT, (b) UPE/5% HNT, (c) UPE/7% HNT, (d) UPE/3% s-HNT, (e) UPE/5% s-HNT and (f) UPE/7% s-HNT at a Sliding Speed of 2.8 m/s and Applied Load of 20 N.....	119
Figure 6.13: Schematic Represents a Dry Interfacial Wear Mechanism	120

Figure 6.14: Comparison of the Impact Strength for Neat UPE and its Nanocomposites as a Function of Untreated Halloysite (HNT) and Temperature	124
Figure 6.15: Variation of the Total Energy for Neat UPE and its Nanocomposites as a Function of Untreated Halloysite (HNT) and Temperature.....	125
Figure 6.16: Impact Strength of Neat UPE and its Nanocomposites as a Function of s-HNT Content and Temperature	126
Figure 6.17: Variation of the Total Energy for Neat UPE and its Nanocomposites as a Function of S-HNT Loading and Temperature.....	127
Figure 6.18: TEM Micrographs of UPE Filled with: (a) 3 wt% HNT Nanocomposite and (b) UPE with 3 wt% s-HNT Nanocomposite.....	128
Figure 6.19: SEM Micrographs of Fractured Surfaces for: (a) Neat UPE, (b) UPE/3 wt% HNT and (c) UPE/3 wt% s-HNT Nanocomposites Impacted at Room Temperature.....	129
Figure 6.20: Variations of the Impact Strengths for Neat UPE and its Nanocomposites as a Function of Different Halloysite (HNT and s-HNT) Contents and Testing Temperatures (-20°C, +20°C and +60°C) .	131
Figure 6.21: Variations of Total Energies for Neat UPE and its Nanocomposites as a Function of Different Halloysite (HNT and s-HNT) Contents and Testing Temperatures (-20°C, +20°C and +60°C).....	131
Figure 7.1: Schematic of Fracture Process by the Cohesive Zone Model	135
Figure 7.2: (a) Typical Linear Traction-separation Law and (b) Linear Damage Evolution.....	137
Figure 7.3: (a) Partitioning the CT Geometry Using Datum Plane and (b) Master and Slave Surfaces	138
Figure 7.4: (a) Applied Load and Boundary Conditions and (b) FE Mesh of the Part Used in the Analysis	139
Figure 7.5: Load-displacement Curves of CT Samples for: (a) Neat UPE and Different UPE/HNT Nanocomposites and (b) Neat UPE and Different UPE/s-HNT Nanocomposites Fractured Under Tensile Loads	141
Figure 7.6: Load-displacement Curves of SENB Samples for: (a) Neat UPE and Different UPE/HNT Nanocomposites and (b) Neat UPE and Different UPE/s-HNT Nanocomposites Fractured Under 3PB Technique	143

Figure 7.7: Propagation of the Crack of CT Sample for 3% HNT Nanocomposite: (a) Specimen Before Crack Initiation, (b) Crack Path, (c) Final Failure of the Sample and (d) Comparison of the Real and Final Failure Situation, Demonstrating the COD.....	148
Figure 7.8: Stress-strain Curves for Neat UPE and 3% HNT-UPE Nanocomposite Obtained Theoretically and Experimentally	149
Figure 7.9: SEM Images of Different Fractured Surfaces for Unfilled Brittle UPE Matrix Fractured Under Different Loads and Specimen Geometries	151
Figure 7.9 (Continued): Fracture Surface of Unfilled UPE Matrix Fractured Under Tension Load and CT Geometry	152
Figure 7.10: Fractography of Mode I Fracture Toughness Using CT Geometry for 5% HNT/UPE Nanocomposite Showing the Process Zone	153
Figure 7.11: Fracture Surface for UPE/3% HNT Nanocomposite Showing the Microvoids that Occurred due to the Particle-polymer Interface Debonding	154
Figure 7.12: Fracture Surface of: (a) 1% HNT/UPE Nanocomposite, (b) 3% HNT/UPE and (c) 5% HNT/UPE Tested with the SENB Geometry Under Bending, Showing Shear Yielding Mechanism	156
Figure 7.13: SEM Images Illustrating the Fracture Surface of: (a) 3% HNT/UPE Nanocomposite and (b) 5% HNT/UPE After Debonding.....	157
Figure 7.14: SEM Images Illustrating the Fracture Surface of: (a) 1% S- HNT/UPE Nanocomposite and (b) 3% S-HNT/UPE Nanocomposite After Debonding.....	158
Figure 7.15: Fracture Surfaces from SENB Geometries of: (a) 3% s-HNT/UPE and (b) 5% s-HNT/UPE Nanocomposite, Showing Matrix Shear Band Mechanism	160
Figure 7.16: Fracture Surfaces from SENB Geometry of 7% s-HNT/UPE Nanocomposite Showing the Massive Shear Yielding Mechanism.....	161
Figure 7.17: SEM Images of Fracture Surfaces near Crack Tip of: (a) 5% s- HNT/UPE and (b) 7% s-HNT/UPE Nanocomposites, Showing Crack Bridging Mechanism	163
Figure 7.18: SEM Micrographs of the Fracture Surfaces Near Crack Tip After SEN-3PB Testing of 3% S-HNT/UPE Nanocomposite, Showing the	

Crack Initiation Zone at Different Magnifications with a Local Deformation Process	164
Figure 7.19: Scanning Electron Micrographs of Fracture Surface for 5% S- HNT/UPE Nanocomposite After SEN-3PB Testing, Showing Crack Initiation Zone at Different Magnifications with River Liners.....	165
Figure 7.20: SEM Micrographs Illustrating the Fracture Surface of UPE Reinforced with: (a) 3 wt% s-HNT and (b) 5 wt% s-HNT Nanocomposites, Demonstrating the Tail-like Structures	166
Figure 7.21: Fracture Surface Morphology After SEN-3PB Test of 5% S- HNT/UPE Nanocomposite.....	167
Figure 7.22: Fracture Surface Morphology After SEN-3PB Test of 5% S- HNT/UPE Nanocomposite, Showing Macrocracks.....	168
Figure 7.23: SEM Micrographs of the Fracture Surface for: (a) 7% s-HNT/UPE and (b) 9% s-HNT/UPE Nanocomposites	169

List of Tables

Table 2.1: Comparison of Mechanical and Fractural Characteristics for UPE Filled with Different Nanoparticles.....	24
Table 2.2: Summary of Flexural, Modulus and Impact Strength for Different Polymers-based HNTs.....	24
Table 3.1: Description of Materials Used in this Study	38
Table 4.1: Assignment of FT-IR Absorption Bands of UPE/HNT and UPE/s-HNT Nanocomposites	77
Table 5.1: Values of T_g and Viscosity of Neat UPE and UPE/HNT	86
Table 5.2: Comparison of Viscoelastic Results (DMA) between UPE/HNT and UPE/s-HNT Nanocomposites	89
Table 5.3: Summary of Mechanical Properties for Different Polymers-based HNTs	96
Table 7.1: Fracture Properties of Neat UPE and UPE/HNT Nanocomposites	144

List of Abbreviations

3-D	three-dimensional
3PB	three-point bending
BOR	block-on-ring
CNT	carbon nanotube
COD	crack opening displacement
CoF	coefficient of friction
CT	compact tension
DBTT	ductile-brittle transition temperature
DCZM	discrete cohesive zone model
DMA	dynamic mechanical analysis
DSC	differential scanning calorimetry
EDS	energy-dispersive spectroscopy
EDX	energy-dispersive x-ray
EPDM	ethylene propylene diene monomer
FE	finite element
FT-IR	Fourier Transform Infrared
HNT	halloysite nanotube
LEFM	linear elastic fracture mechanics
MEKP	Methyl Ethyl Ketone Peroxide
MMT	montmorillonite
MPS	γ -methacryloxypropyl trimethoxysilane
MWCNT	multi-wall carbon nanotube
NS	nanosilica
PES	polyethersulphone
PNC	polymer matrix-based nanocomposite
PP	polypropylene
PPA	phenylphosphonic acid
PS	polystyrene
SAXS	small-angle x-ray scattering
SEM	scanning electron microscopy

SEN	single-edge notch
SEN-3PB	single-edge notch under three-point bending
SENB	single edge notch bending
s-HNT	silanised halloysite nanotube
SS	stainless steel
TEM	transmission electron microscopy
TGA	thermogravimetric analysis
UPE	unsaturated polyester
US	United States
VCCT	virtual crack closure technique
VTES	vinyltriethoxysilane
VTMS	vinyltrimethoxysilane
XFEM	extended finite element method
XRD	x-ray diffraction
WAXS	wide-angle x-ray scattering

Chapter 1: Introduction

1.1 General

In the area of nanotechnology, polymer matrix-based nanocomposites (PNCs) have attracted a remarkable amount of attention in recent literature. This is because PNCs have at least one of their dimensions less than 100 nm, showing good mechanical and thermal properties with the addition of a small amount of nanofillers, compared to neat polymers or conventional polymer-based microcomposites (Krishnamoorti & Vaia 2002; Friedrich, Fakirov & Zhang 2005; Bhattacharya, Kamal & Guptaet 2008). These good properties are thought to be owing to the small dimension sizes of the particles, which is normally associated with smaller sizes of flaws and higher surface-to-volume ratios, as well as a large area of interface between the reinforcements and polymer matrix. These characteristics all induce better stress transfer from the polymer to the nanoparticles (Bhattacharya, Kamal & Guptaet 2008; Young & Lovell 2011).

In the literature, three different types of nanosized particles have commonly been used as fillers in the field of polymers-based nanocomposites: spherical particles (such as nano- Al_2O_3 , nano- TiO_2 and nanosilica [SiO_2]), platelet-like shape particles (such as montmorillonite ([MMT]) and nanotubes (such as carbon nanotubes [CNT] and halloysite nanotubes [HNT]) (Paul & Robeson 2008). In principle, polymer nanocomposites can be experimentally synthesised via one of four strategies: solution intercalation, *in situ* intercalative polymerisation, melt intercalation and *in situ* direct mixing (Koo 2006; Wang, Hoa & Wood-Adams 2006; Pavlidou & Papaspyrides 2008).

1.2 HNT

Among the many nanofillers mentioned above, naturally occurring HNTs, which are produced by the long weathering of aluminosilicate rocks, have continuously gained considerable attention from both industrial and academic researchers in currently

developed polymer nanocomposites. This is because of the good features of HNTs, such as large aspect ratio and ease of processing (Ye et al. 2011). HNTs also combine the nanotube geometry that is similar to multi-wall carbon nanotubes (MWCNTs) with kaolinite chemistry, while being much cheaper and more readily obtainable than MWCNTs. The HNT has an empirical chemical formula $(Al_2Si_2O_5(OH)_4-nH_2O)$ where n equals two for hydrated, or zero for dehydrated, halloysites (Ismail & Shaari 2010). The lengths of halloysite nanotubes typically range from 0.5 to 3.0 μm , their external diameters range from 30 to 100 nm, and their internal diameters range from 15 to 30 nm, as illustrated in Figure 1.1.

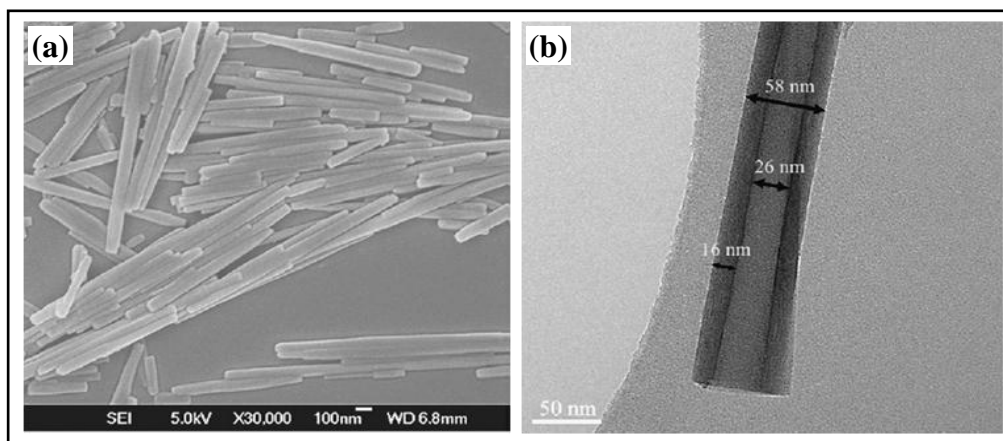


Figure 1.1: (a) Scanning Electron Microscope Image of HNTs and (b) Transmission Electron Microscopy (TEM) Micrograph of HNT

Source: Ye et al. (2007)

In contrast to the structure of montmorillonite (MMT), which consists of platelets with an inner alumina octahedral layer sandwiched by two silicate tetrahedral layers in a 1:2 ratio, the hollow-tubular structure of HNT consists of one alumina octahedron sheet and one silica tetrahedron sheet in a 1:1 stoichiometric ratio. Even though the halloysite tube has a multi-wall structure with a few hydroxyl groups—that is, low density of hydroxyl located on its outer wall that may help reduce particle–particle interaction and impart uniform dispersion—various chemical treatments have been implemented on the surface of halloysite to obtain better interfacial bonding between the particles and the polymer, and better alignment of the particles (Deng, Zhang & Ye 2009; Guo et al. 2009). One of these treatments is reactive treatment, which assumes that the coupling agent reacts and forms covalent

bonds with both components—fillers and polymer matrix. Silane coupling agents are successfully used for fillers that have reactive -OH groups on their surfaces, such as glass beads, glass fibres and clay or halloysite (Moczo & Pukanszky 2008). During silane treatment, hydrolysis and condensation reactions occur on bifunctional silane molecules, leading to the generation of siloxane (-Si-O-Si-), which creates a bridge bond between the hydroxyl (-OH) group on the silanised particle surface and the polymer matrix. The silanol groups change the hydrophilic nature of these surfaces to a hydrophobic nature (Mittal 2009).

Many different thermosets and thermoplastics, as well as elastomer rubbery materials have been broadly used as polymeric matrices in the production of PNCs. In comparison, thermosets plastic materials—such as epoxy, vinyl ester and unsaturated polyester—have not been quantitatively researched to understand the property changes in relation to the morphological structures of the nanocomposites. Only a few studies have examined this, which is probably because thermosets are rigid materials and network polymers, in which chain motion is greatly restricted by a high degree of crosslinking. Hence, thermosetting unsaturated polyester (UPE) resin was chosen for this investigation in order to examine the basic relationship between the nanoscale structural variables and macroscale properties of thermosetting polymers-based halloysite particulate nanocomposites.

1.3 UPE

UPE resins are one of the most frequently used thermosetting polymers. Crosslinked UPE with a long-chain molecule can be formed by free-radical copolymerisation of a monomer with a prepolymer that has several C=C bonds during the heat or curing process. The typical material of the reactive monomer (solvent) is styrene and the most common material of the unsaturated prepolymer is polyester resin that comprises low molar mass unsaturated polyester dissolved in styrene (Young & Lovell 2011).

Despite the rigid features of UPE resins, their good mechanical properties, good dimensional stability at elevated temperatures, low density and easy processing make

them successful materials for different industrial applications, such as encapsulating materials, tooling and boat components, tanks and building panels, and different automobile applications (Kotsilkova & Pissis 2007). However, their high crosslink density and polymer chain stiffness drastically localise their plastic deformation in front of a crack tip. This highly localised plastic deformation causes little absorption of energy, leading to catastrophic brittle failure (Srivastava & Koratkar 2010). Thus, it was suggested that the introduction of a second phase into single-phase UPE resins could help yielding their crosslink density, reducing brittleness and subsequently improving their strength and toughness. The enhancements in thermoset characteristics with the incorporation of second-phase fillers were postulated to be due either to the confinement effects of interrupting the high crosslink density of thermosets or to the preferential interaction of the crosslinking agent with the particle surface (Paul & Robeson 2008).

1.4 Characterisation of Polymer Nanocomposites

One of the most important issues in today's nanotechnology research is to relate the performance of nanocomposites to their morphological structures. The degree of reinforcement and nanometric scale immobilisation of the polymer chains depend on the interfacial contact between the polymer matrix and the filler. Fully dispersed or exfoliated nanocomposite structures lead to useful nanocomposites and high property enhancements, due to homogeneous dispersion and large interfacial area, as reported by Xanthos (2010). The morphology of the PNCs also relates to the compatibiliser content or reactive coupling agent, if any, and the matrix viscosity (Chabert et al. 2004). Wide and small angle x-ray scattering (WAXS and SAXS) are frequently used to analyse the status of morphological characterisation. Such analyses are relatively simple to complete and are somewhat quantitative, as explained by numerous authors (Nuhiji et al. 2011; Dayma & Satapathy 2012). TEM is a far more direct technique than WAXS and SAXS in visualising nanocomposite morphology. While the use of TEM is often criticised because it reveals the morphology in a very small region, this can be overcome by taking images at various magnifications and from various locations and orientations, until a representative picture of the morphology is established (Paul & Robeson 2008).

In turn, most reinforcement properties (such as mechanical and fractural) and non-reinforcement properties (such as gas barrier or flammability) of PNCs are directly dependent on the state of nanoparticle dispersion in the polymer matrix (Chinellato et al. 2010). Besides, the mechanical properties of the PNCs basically depend on the nanofiller type and their aspect ratios and volume fractions, the nanofiller and polymer moduli, and the interface interaction between the particles and the polymer at a molecular level. Indeed, a good interface does transfer the load or stress between the filler and the matrix (Merhari 2009). Further, the orientation of filler and orientation of polymer crystallites play a key role in the basic premise of composite theories to delineate the reinforcements of filler in the polymer matrix.

The conventional micromechanical models (such as the Halpin-Tsai and Mori-Tanaka models) have been successfully applied to predict the material properties of well-aligned short-fibre composites and to estimate the elastic modulus, thermo-mechanical properties and so forth, in simple closed-form analytical solutions (Weon 2009). In addition, different computational methods have been applied to investigate the fracture behaviour and mechanical characteristics in fully homogenous particulates-filled polymer nanocomposites, such as molecular scale (e.g., molecular dynamics and Monte Carlo), mesoscale and macroscale (e.g., equivalent-continuum and self-similar approaches, and finite element [FE] method) (Zeng, Yu & Lu 2008).

Toughness, as a measure of material resistance to fracture, has long been evaluated using the linear elastic fracture mechanics (LEFM) approach and concepts of stress intensity factor (K_c) and energy release rate (G_c) (Milne, Ritchie & Karihaloo 2003; Janssen, Zuidema & Wanhill 2004). These mechanics were originally developed for brittle or quasi-brittle fracture materials. In terms of large-scale plasticity, the characterisation of fracture behaviour is usually evaluated by elastic-plastic fracture parameters according to post-yield fracture mechanics (such as J-integral, stretch zone width, and crack-tip opening displacement). The enhancement of polymer toughness due to reinforcement with nanoparticles is associated with a change in the primary mechanism of plastic deformation. The tremendous surface area of nanoparticles enables them to interact and constrain the surrounding matrix material molecularly, and limits its ability to undergo plastic deformation. In addition, the

well-dispersed particles align with their high aspect ratios, and good interfacial adhesion can make certain toughening mechanisms effective, such as crack bridging, crack deflection and crack-tip blunting, thereby enhancing toughness. Hence, it was necessary in this study to understand the roles of halloysite particles on the morphological and materials characteristics of thermosetting-based nanocomposites.

1.5 Objectives of the Thesis

This investigation sought to determine the effects of HNT and s-HNT on the material characteristics of UPE-based nanocomposites in relation to their morphological structures. The main objectives of the thesis were as follows:

- Identify the difference in dispersion status between HNT and s-HNT particles of the UPE/HNT and UPE/s-HNT nanocomposites prepared by high shear disperser and ultrasonic process. Identify the chemical composition of halloysite before and after silanisation treatment by conducting elemental analysis of certain nanocomposite systems.
- Characterise the molecular structures of polymers and indicate the vibrational states of chemical bonds obtained after the curing process of nanocomposites, as well as understand the role of s-HNT on the vibrational states of these chemical bonds.
- Experimentally investigate the thermal, viscoelastic, glass transition temperature and mechanical properties of neat UPE and its different nanocomposite systems in order to relate the performance of these systems to their different morphological structures. Examine the morphology of tensile-fractured surfaces of the nanocomposites at a microscopic level. Implement different mathematical models to predict the elastic modulus of different nanocomposites and compare to the experimental results.
- Quantitatively determine the effective role of HNT and s-HNT particles on the tribological behaviour of the UPE nanocomposites. Measure, as wear resistance parameters, the coefficient of friction (CoF) and specific wear rate (w_s) for neat UPE and its different nanocomposites. Examine the morphology of the worn surfaces in order to determine the wear mechanisms taking place in the nanocomposites after introducing the HNT and s-HNT particles.

- Understand the effects of HNT and s-HNT particles on the impact fracture behaviour of the UPE/HNT and UPE/s-HNT nanocomposites. Consider the relationship between the morphological structures and total energy absorption under impact loading in a range of temperatures from -20 to +60 °C.
- Experimentally and theoretically evaluate failure analysis and crack initiation and propagation in neat UPE and its nanocomposites. Measure the fracture toughness in terms of stress intensity factor (K_{Ic}) and strain energy release rate (G_{Ic}) using two different testing geometries and two different loading conditions: single-edge notch (SEN) under three-point bending (SEN-3PB) and compact tension (CT) with tensile load. Simulate the crack initiation and propagation in the nanocomposites using an FE calculation with ABAQUS software and cohesive element method. Identify the toughening mechanisms occurring in the nanocomposites after HNT and s-HNT incorporation to comprehensively grasp the effect of good adhesion silanised halloysite on the UPE matrix in changing the fracture mechanics. Determine the answer to whether these particles have bridged or deflected the crack.

1.6 Scope of the Thesis

This study investigates experimentally and theoretically the roles of HNT and s-HNT on material characteristics in relation to the different morphological structures of UPE/HNT and UPE/s-HNT nanocomposites. A schematic illustration indicating the main concepts of this study is shown in Figure 1.2.

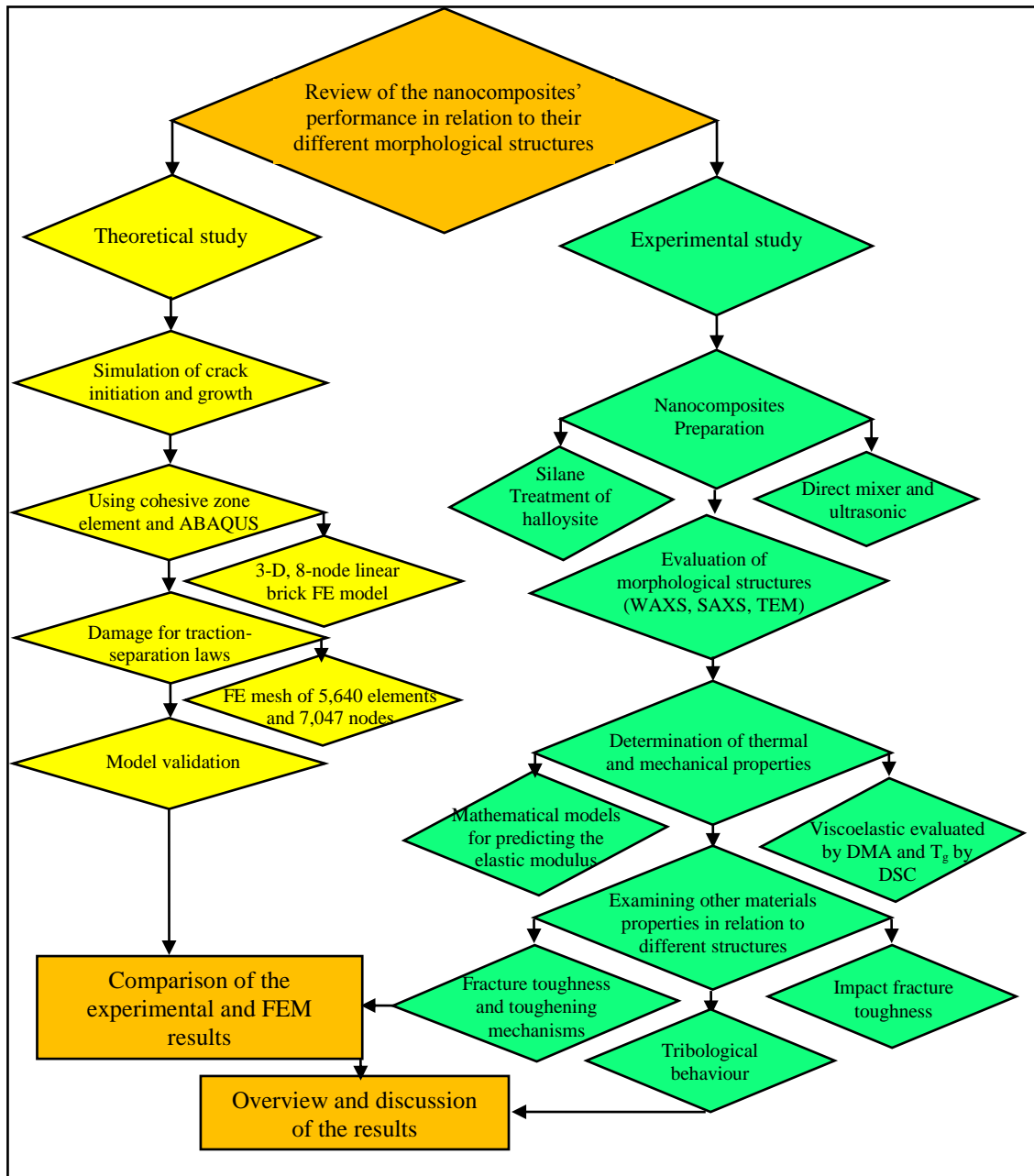


Figure 1.2: Schematic Illustration of the Scope of the Current Research

1.7 Outline of the Thesis

Beyond the short introduction given above, the following points briefly outline the content of the present research, with this thesis divided into eight chapters as follows:

- **Chapter 1** is the introduction; it presents a brief definition of PNCs, as well as a description of HNTs and UPE resin, the characteristics of PNCs and the structure of the thesis.

- **Chapter 2** is a literature review that is classified into different sections in order to provide a clear picture of the relationship between the morphological structures and different material properties of various nanocomposite systems prepared from different nanoparticles and different polymer matrices. It also reviews a number of mathematical models that were used in most literature examples to simulate the crack initiation and propagation.
- **Chapter 3** discusses the materials used for the experimental investigation, and describes the methods and equipment used to prepare the nanocomposites, as well as the characteristics tested in the thesis.
- **Chapter 4** describes the effect of organosilane treatment on halloysite surfaces, and how the silane molecule bridges the silanised halloysite with polymer chains. This chapter also comprehensively describes the morphological structures of different nanocomposite systems. The results of the Fourier Transform Infrared (FT-IR) analysis for neat UPE and its different nanocomposites are also discussed.
- **Chapter 5** concerns with the thermal, viscoelastic and mechanical properties of the nanocomposites. The evaluation of glass transition temperature using differential scanning calorimetry (DSC) spectra is discussed. The prediction of the elastic modulus of different nanocomposites using different mathematical models is also discussed.
- **Chapter 6**, in one part, presents the effects of HNT and s-HNT particles on the tribological behaviour, represented by the CoF and specific wear rate (w_s), as well as the wear mechanisms of the nanocomposites. The other part of Chapter 6 presents the experimental investigation of the impact fracture toughness and total energy in a range of temperatures from - 20 to + 60 °C for the nanocomposites in relation to their different morphological structures.
- **Chapter 7** focuses on the experimental determination of the fracture toughness values of neat UPE and its different nanocomposites. The theoretical evaluation to simulate the crack initiation and propagation based on the cohesive element model and ABAQUS package is discussed. The toughening mechanisms occurring with the addition of HNT and s-HNT into the UPE are quantitatively discussed.

- **Chapter 8** summarises the main findings of the current research and suggests some recommendations for future work.

Chapter 2: Literature Review

2.1 Polymer-based Nanocomposites

Understanding the physical relationships between nanoscale structure and macroscale properties is the cornerstone of producing effective polymer-based nanocomposites with superior mechanical performance. As the work in this thesis deals with thermosetting unsaturated polyester as a polymer matrix for nanocomposites, the literature review given here will focus mostly on polymer matrix nanocomposites in which different thermosets-based nanosized particles were involved—unless no relevant work was found, in which case, thermoplastics are considered instead.

Most of the studies on polymer-based nanocomposites available in the literature report the effects of inserting different types of nanofillers on the characteristics of nanocomposites—that is, the reinforcement properties in relation to the nanocomposite structures. Nanocomposite properties other than reinforcement—such as barrier and membrane properties, flammability resistance, fuel cell application and electro-optical properties—have gained less attention than reinforcement properties; hence, they are not considered in this review. This review chapter broadly discusses the reinforcement aspects of polymer-based nanocomposites because they are the primary area of this thesis's interest.

2.2 Structure-property Relationship

Diverse studies have been undertaken to understand the relationship between the morphological structure and mechanical properties of PNCs. In general, the characteristics of polymer-clay nanocomposites are highly dependent on the dispersion status of particles in the polymer matrix, whether they are immiscible (conventional or microcomposite), intercalated or exfoliated (miscible) nanocomposites (Jancar et al. 2010), as shown in Figure 2.1. An immiscible nanostructure composite is obtained due to the formation of separated phases. In this

structure, chemical attractions between similar molecules are strong in each phase. Intercalates nanocomposites are obtained when a polymer is located between the particle layers. While the layer spacing is increased, there are attractive forces between these layers that make them regularly spaced stacks or tactoids. Exfoliated nanocomposites are obtained when the spacing of particle layers increases to the point that there is no longer sufficient attraction between these layers. The dispersion status of particles in the PNCs (or structure) is mostly related to the characteristics of these particles (such as particle size, size distribution, specific surface area and particle shape). Further, the structure of the PNCs is also determined by segregation, aggregation (particle/particle interaction) and the orientation of anisotropic particles in the polymer matrix (Moczo & Pukanszky 2008).

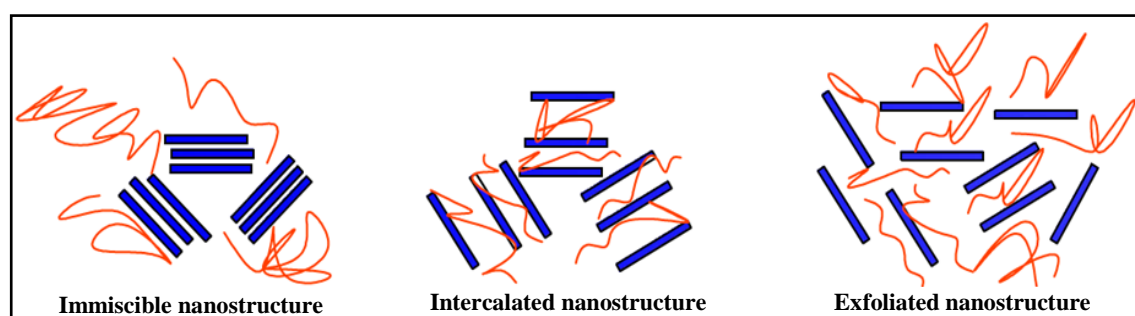


Figure 2.1: Schematic Diagram for Dispersion State of Polymer Nanocomposites

In addition, the mechanical properties viz. yield stress, tensile strength and impact resistance of the PNCs are mainly affected by interfacial interactions. The formation of a stiff interface between the filler and polymer matrix considerably influences the properties of the PNCs. Matrix/filler interactions are in turn affected by the surface-free energy of fillers, which can be changed by surface modification. Surface modifications (such as nonreactive treatment, reactive coupling and functionalised or grafting polymers) tend to perform a perfect wetting (or affinity) between fillers and the polymer segments, and thus obtain maximum performance of the nanocomposites. These aspects will be discussed in detail in the following section.

One of the most important factors that also influences the morphological and material characteristics of the PNCs is component properties. This means that the reinforcing effect of the reinforcement (or filler) increases with decreasing matrix stiffness. Different relative yield stresses have been observed for different

nanocomposites containing the same filler type and same volume fraction, but different polymer matrices (Moczo & Pukanszky 2008). Each polymer used as a matrix in particulate-filled composites has a diverse physical and chemical structure. This phenomenon also aligns with filler/matrix interfacial interactions; thus, a wide variety of interactions can form between them. Polymers can be classified into two types: amorphous (non-crystalline) and crystalline or semi-crystalline. Examples of the former polymers are thermoplastics, with irreversible secondary chemical bonds, softening when heated and firming again when cooled; and rubbery amorphous polymers that experience viscous flow when heated. Thermosets are an example of the latter polymers (semi-crystalline), with covalent bonds, softening when heated and ability to be moulded, but then permanent hardening and inability to be reheated (Sawyer, Grubb & Meyers 2008).

Irrespective of the thermoplastics, different thermosetting polymers—such as resoles and novolaks phenol-formaldehyde resins, epoxy, vinyl ester, UPE resins and so forth—have been used as matrices in polymer matrix-based nanocomposites. Among them, UPE was chosen to develop the experimental research in the current thesis. Further observations on the effect of using various fillers on the characteristics of the UPE matrix will be presented in Section 2.2.4.

2.2.1 Effect of Chemical Treatment on Morphology and Properties

Surface modification of inorganic fillers has attracted a great deal of attention because it produces excellent integration and an improved interface between the fillers and polymer matrix. Pristine MMT clay is often modified with an organic compound, such as alkylammonium salts as surfactants, or reactive treatments, such as a silane coupling agent. These modifications decrease the energy of adhesion between clay layers and polymer chains, enable the occurrence of molecular diffusion and shear, and alleviate its behaviour to be lesser hydrophilic or to be hydrophobic (non-polar molecules) (Park et al. 2009; Yilmaz et al. 2010; Barick & Tripathy 2010; Chinellato et al. 2010). Several studies have been reported on the influence of introducing modified organoclay on the:

- macromolecular structure, crystalline phases and crystallisation of polymers (Anderson & Zukoski 2010; Paci, Filippi & Magagnini 2010; Dayma & Satapathy 2012)
- physical properties (such as equilibrium melting point (T_m), glass transition temperature (T_g) and heat distortion temperature) of polymers (Yuan et al. 2010; Arora, Choudhary & Sharma 2010)
- morphological and rheological properties and viscoelastic behaviour (Gahleitner et al. 2006; Anderson & Zukoski 2010; Behradfar, Shojaei & Nasrin 2010)
- thermal and mechanical properties (Santos et al. 2009; Pettarin et al. 2009; Chacko, Sadiku & Vorster 2010; Valles-Lluch, Ferrer & Pradas 2010).

HNTs have weak secondary hydrogen bonds and van der Waals's forces interactions between the nanotubes that may result in little or no surface charge of the HNTs. Despite this, various surface modifications have been applied on HNT particles to improve the intercalations between halloysite tubes and organic compounds, prevent the coalescence retaining and improved dispersion after shear mixing. The adsorption of organofunctional silanes is usually accompanied by polycondensation. The adsorbed amount of coupling agent, as well as the structure, properties and thus adhesion of the polysiloxane layer, depend very much on the chemical composition of the organofunctional group of silane.

When a silane coupling agent is introduced to filler surfaces in a nanocomposite system, two interfaces can be produced: a filler/silane interface and a silane/polymer interface. At the first interface, the hydroxyl silane groups and filler surfaces can react and form water molecules through the siloxane bonds. Thus, this mechanism can promote interfacial adhesion, as illustrated in Figure 2.2, which shows the mechanism of silane deposition on an active substrate. An active substrate with a reactive (-OH) group is the halloysite particles with a crystalline structure, as shown in Figure 2.3. Figure 2.4 shows this modified with a 3-methacryloxypropyl trimethoxysilane coupling agent. The modified particles behave differently within organic solvents or polymer matrices than do unmodified particles; for example, the

modified particles show comparatively better dispersion in both media (Kango et al. 2013).

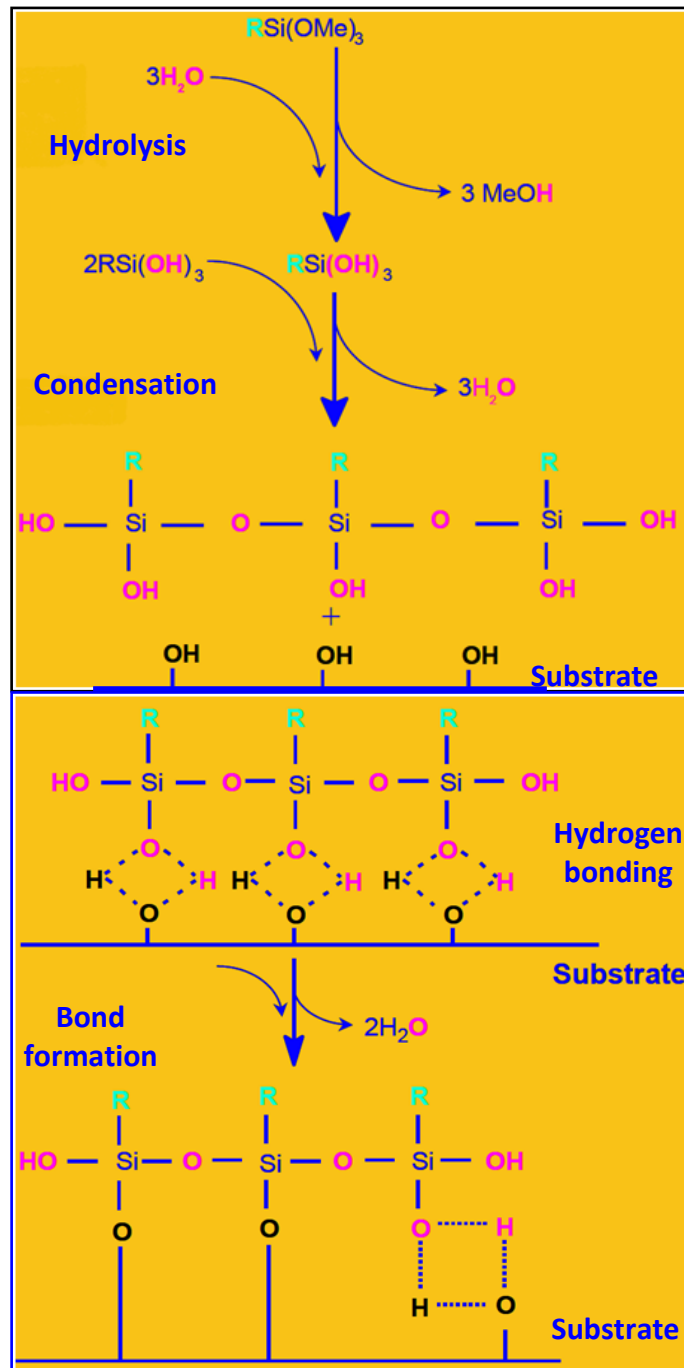


Figure 2.2: Mechanism of Silane Deposition on an Active Substrate

Source: MacMillan (1997)

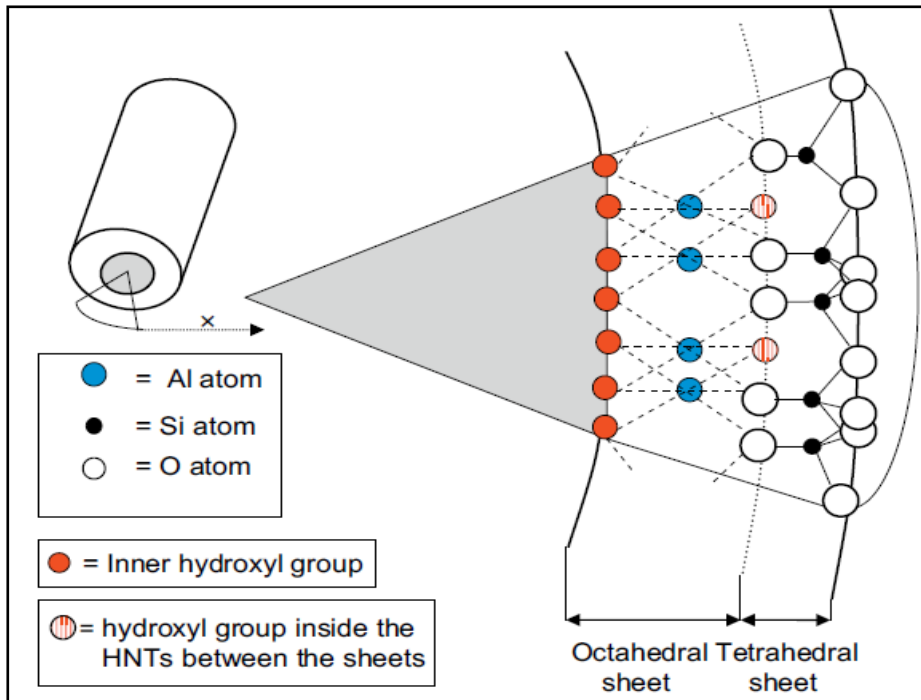


Figure 2.3: Crystalline Structures of HNTs

Source: Pasbakhsh et al. (2009)

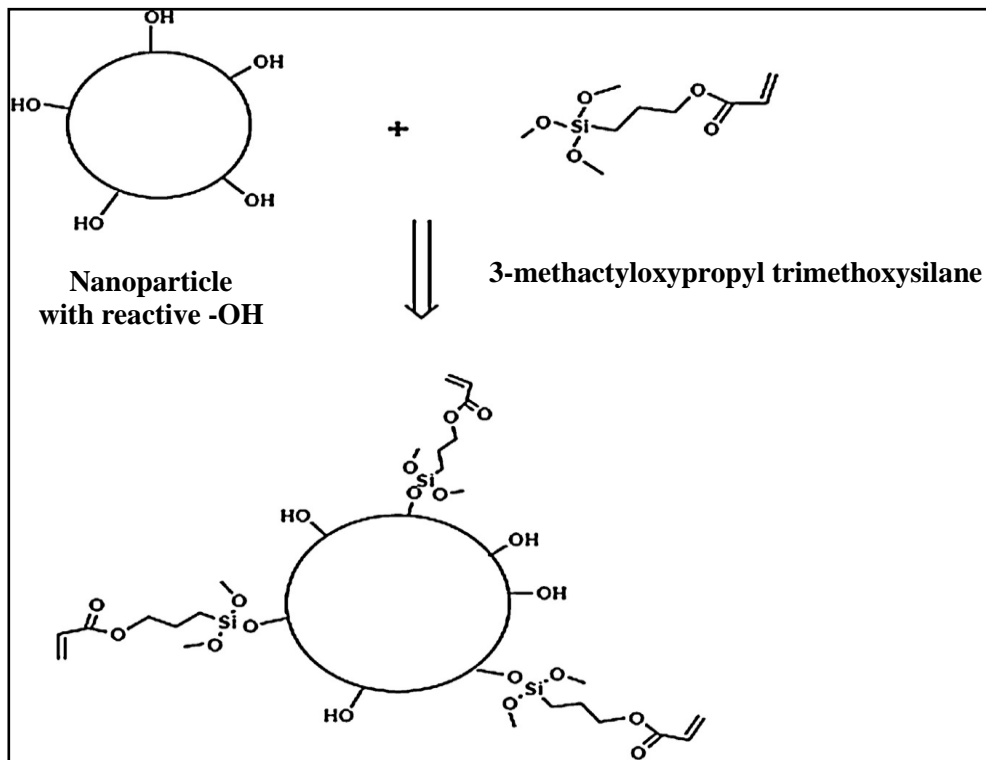
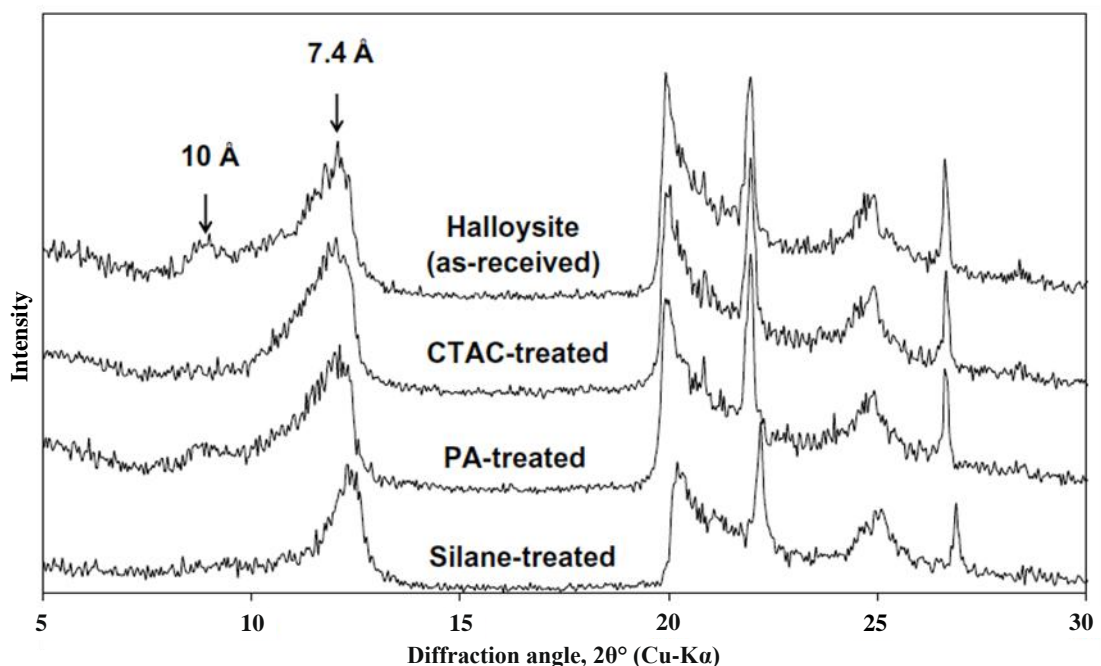


Figure 2.4: Modification of a Nanoparticle with 3-methacryloxypropyl Trimethoxysilane

Source: Kango et al. (2013)

To qualitatively understand the role of using surface treatment on the dispersion status of particles in the polymer matrix, a short review is given here, cited from different literature in which different surface modifications were applied. Deng, Zhang and Ye (2009) treated halloysite surfaces with three different chemical solutions—silane, potassium acetate and cetyl trimethyl ammonium chloride—in order to investigate their effects on the particle dispersion and material properties of epoxy/nanocomposites prepared by mechanical mixing. The basal spacing of the as-received halloysite particles was approximately 7.4 Å, and there was a tiny 10 Å peak, indicating that the halloysite particles used in the study were mostly dehydrated (7.4 Å), with only a small amount of hydrated particles (10 Å). As illustrated in Figure 2.5, the silane treatment moved the intensity peak slightly to the right, corresponding to a small reduction of the basal spacing, which was probably due to further dehydration during the course of the chemical treatment.



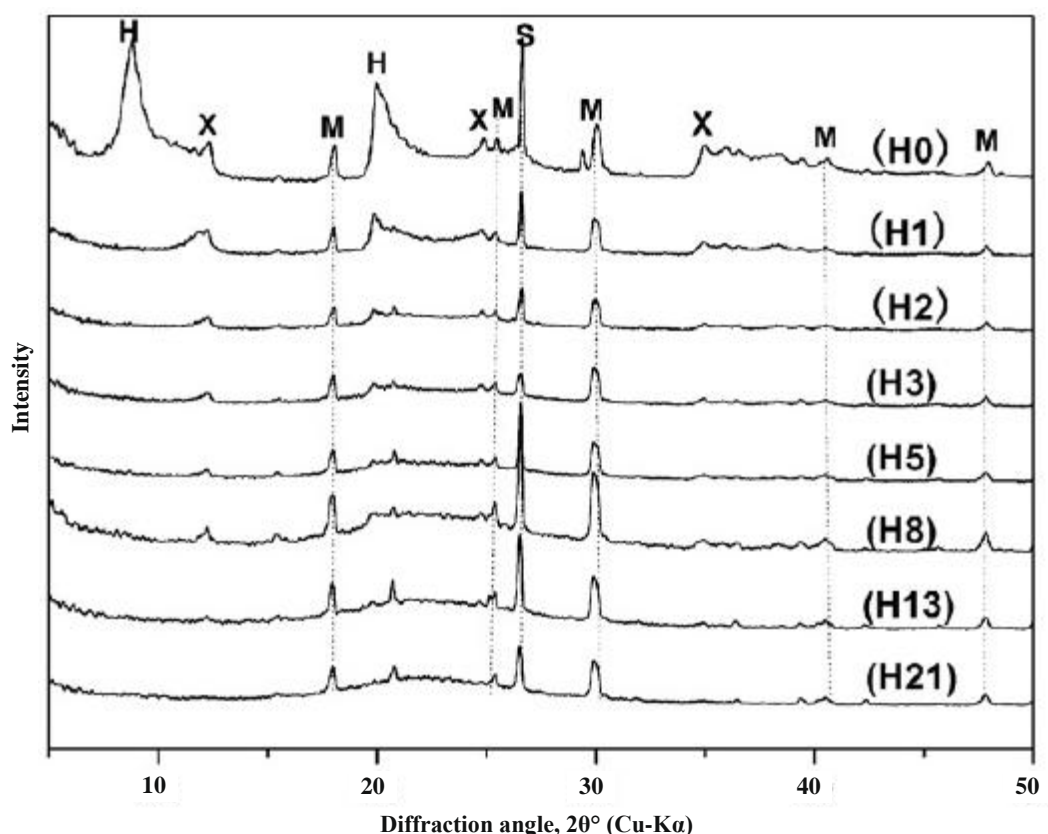
Note: H = Halloysite-(10Å), X = Halloysite-(7Å), M = Alumite and S = Quartz.

Figure 2.5: X-ray Diffraction (XRD) Patterns of As-received and Modified HNTs

Source: Deng, Zhang and Ye (2009)

Later, Zhang et al. (2012a) confirmed that a sharp peak at 2θ of 8.80° with corresponding d_{001} value of 10.04 \AA appeared in the crystal structure of natural

halloysite, as shown in Figure 2.6. Another tiny peak appeared at 2θ of 12.36° ($d_{001} = 7.17 \text{ \AA}$), which was ascribed to halloysite-(7 \AA). In addition, several characteristic peaks of halloysite (7 \AA) appeared at $2\theta = 12.36^\circ$, 18.18° and 25.28° . The characteristic (001) peak disappeared from the crystal structure of treated halloysite with sulfuric acid (H_2SO_4) for one hour (H1 in Figure 2.6). Moreover, increasing the durations of acid treatment on the halloysite surface led to lowering the intensities of the characteristic peaks at $2\theta = 12.36^\circ$, 18.18° and 25.28° .



Note: H = Halloysite-(10 \AA), X = Halloysite-(7 \AA), M = Alumite and S = Quartz.

Figure 2.6: XRD Patterns for Natural Halloysite (H0) and Acid-treated Halloysite at Different Treatment Durations (H1-H21)

Source: Zhang et al. (2012a)

The HNTs were modified with γ -methacryloxypropyl trimethoxysilane (MPS) in order to improve their dispersion in ethylene propylene diene monomer (EPDM) nanocomposite (Pاسبakhsh et al. 2010). TEM micrographs (Figure 2.7) showed that unmodified HNTs had a tendency to form edge-to-edge and face-to-edge contacts, while modification of the HNTs with MPS showed a better dispersion of s-HNT in

the EPDM matrix. Spencer et al. (2011) also revealed that modified organoclay with MPS exhibited a decreased tactoid size and increased density of tactoids per unit area of the 2-D images in polypropylene (PP)-based nanocomposite, compared to large tactoids of untreated organoclay. This indicated a poor degree of exfoliation, as shown in Figure 2.8.

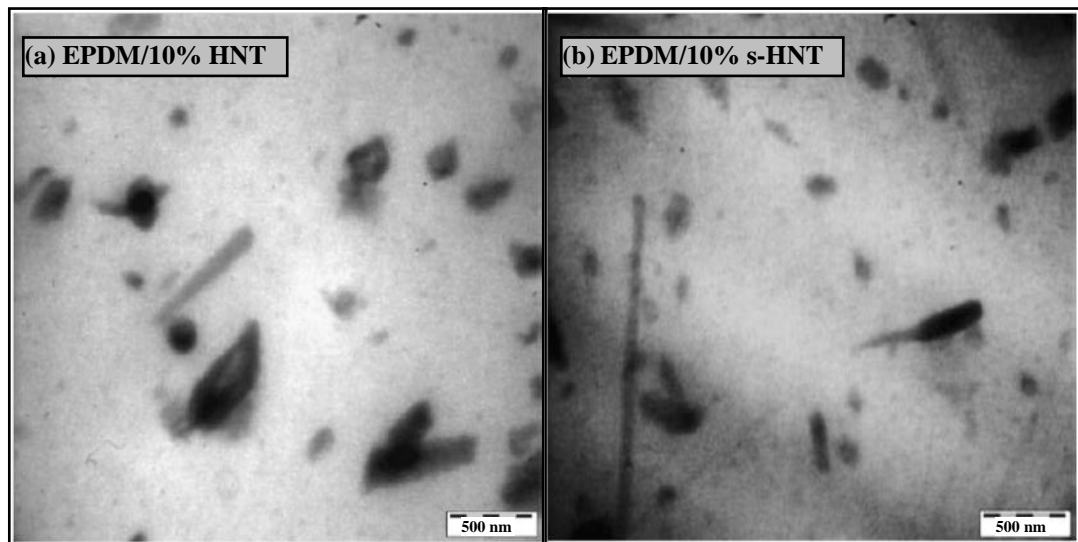


Figure 2.7: TEM Micrographs of: (a) EPDM/10% HNT and (b) EPDM/10% s-HNT Nanocomposites

Source: Pasbakhsh et al. (2010)

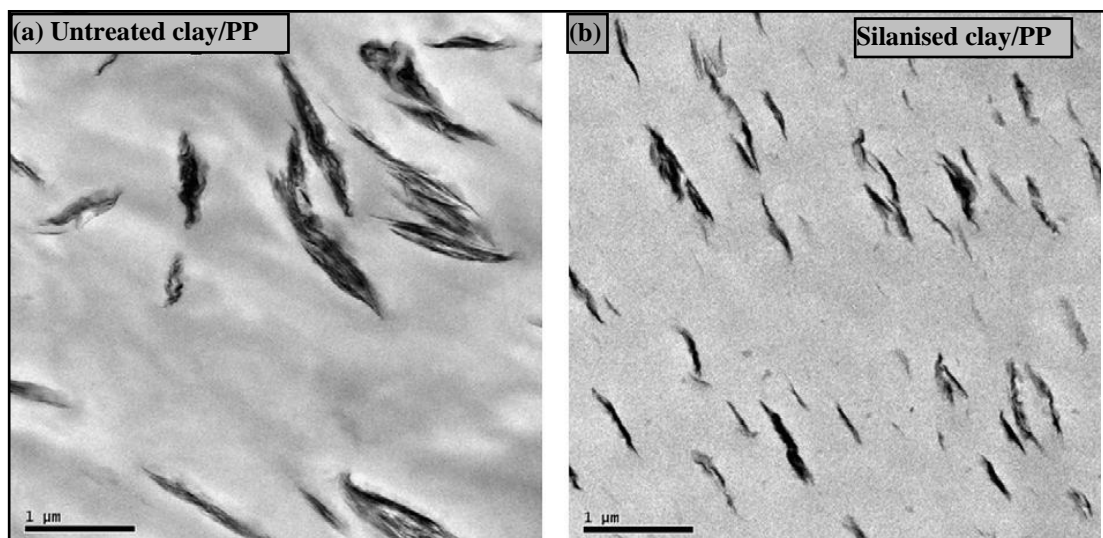


Figure 2.8: TEM Micrographs of: (a) Untreated Organoclay/PP and (b) Silanised Organoclay/PP Nanocomposites

Source: Spencer et al. (2011)

FT-IR spectroscopy was also used to investigate the surfaces of HNT before and after grafting them with aminosilane (Barrientos-Ramirez et al. 2011). The spectrum of unmodified HNT showed Al₂O-H stretching absorption bands at 3,698 and 3,624 cm⁻¹; in-plane Si-O-Si stretching (1,088 and 1,025 cm⁻¹); Al₂O-H deformation (912 cm⁻¹); and bands at 1,030 cm⁻¹ and Si-O symmetric stretching vibration (790 cm⁻¹). The spectra that correspond to the grafting of halloysite with aminosilane showed— together with the absorption bands for unmodified HNT—bands at 3,485 and 3,350 cm⁻¹ (N-H₂ stretching); 2,938 and 2,842 cm⁻¹ (N-H stretching and symmetric C-H₂ stretching); 1,654 (N-H bending); 1,556 (N-H₂ scissoring); 1,466 cm⁻¹ (C-H₂ scissoring); 1,385 cm⁻¹ (C-H₂ wagging); Si-CH scissoring deformation (1,329 cm⁻¹); and 1,195 cm⁻¹ (C-N stretching).

2.2.2 Glass Transition Temperature (T_g)

The effect of using different nanometre-sized fillers on the thermodynamic and physical properties of PNCs is one of the most interesting topics in recent researched nanocomposites. The crystallinity, glass transition temperature (T_g), melting temperature (T_m) and many others are important and sensitive physical properties to determine the structure, phase formation and mobility of polymers. This importance arises because improvement of the mechanical and thermal properties of the PNCs without changing the T_g of the polymer is more desirable, especially for elastic and flexible polymers. Hence, studying the roles of different nanofillers on thermodynamic properties and T_{gs} is necessary to delineate the other relevant PNC properties, since the nano-effects or property improvements over larger scale dimensions is the major property change of interest, while the T_g and crystallinity are the others.

Changing the mobility of polymer chains in the vicinity of the polymer/particle interface and thermodynamic interaction is a good indication of the change in T_g (Yuan et al. 2010). In other words, with an increase of nanoparticle loading, the T_g for polymeric matrices shifts towards lower temperatures, owing to the intercalated morphology of the nanoparticles that restrains the molecular mobility of the polymer molecules, as well as due to the plasticisation of the polymer matrix (John et al. 2010). Further, lower temperatures of glass transitions in the polymers filled with

nanoparticles are also attributed to the immobilisation of polymer chains in the form of shell and/or trapped polymer (Samadi & Kashani 2010) and to the free volume existing at the polymer surface interface due to poor wetting (Pluta, Jeszka & Boiteux 2007). In contrast, others believe that nanoparticles play a key role in increasing the T_g of polymers because they confine the movement of polymer chains, especially in the case of intercalated nanocomposites (Ingram et al. 2008; Maji, Guchhait & Bhowmick 2009).

2.2.3 Thermal, Thermodynamic and Mechanical Properties

The recent emergence of newly developed nanometre-sized fillers (such as nano-SiO₂, nano-Al₂O₃, nano-TiO₂, nanoclay, HNTs and CNTs) has caused the literature on polymer nanocomposites to become one of the most popular areas for current research and development. As aforementioned, to ascertain how to produce a perfect nanocomposite with full stiffness enhancement, one needs to comprehensively verify the status of dispersion, the strength of the filler/polymer interfacial adhesion and the kind of plastic materials used. A large number of investigations covering a broad range of topics have been performed to examine the ‘nano-effect’—that is, decreasing the nanoscale dimensions on the composite property changes in order to optimise the resultant nanocomposite. For instance, Deng, Zhang and Ye (2009) examined the effect of 5 wt% addition of untreated HNT or s-HNT particles on the weight loss (thermal stability) and mechanical properties of epoxy matrix-based nanocomposites. They found that a weight loss of 16% occurred after the temperature exceeded 500°C, representing the removal of the interlayer water. Slight improvements in tensile strength by 4% and 5%, and Young’s modulus by 2% and 4%, were also found with the addition of 5% HNT and s-HNT, respectively.

Later, Uddin and Sun (2010) fabricated hybrid nanocomposite-filled epoxy matrix via three different processes: conventional sonication, sol–gel, and a combination of sonication and sol–gel. This was undertaken in order to investigate the effect of different dispersion status on the mechanical properties. It was revealed that the improvement in dispersion for nanocomposites produced by sonication in the presence of sol-gel was reflected in greatly improved mechanical properties. At various particle loadings (1.5 to 3 wt %), alumina nanocomposites showed 5 to 9 %

improvement in flexural strength and modulus, with 6 to 10% reduction in strain at break. However, a further increase in loading of alumina particles caused particle agglomerations.

The mechanical properties of 5 wt% (0.6 vol. %) silanised clay-filled multilayer lamination of carbon fibre-reinforced epoxy composites were significantly improved by 40%, 24%, 16% and 14% for storage modulus, flexural modulus, tensile modulus and Mode I interlaminar fracture toughness, respectively. The enhanced properties were attributed to the high exfoliation of clay and strongly interfacial interaction between clay and epoxy resin (Phonthammachai et al. 2011). Alamri and Low (2012) investigated the effect of water absorption and different nanofiller types, nanoclay platelets, HNTs and nano-silicon carbide (n-SiC) particles on the mechanical properties of epoxy nanocomposites. They found that the role of nanofillers in the epoxy matrix decreased both water uptake and diffusivity, compared to unfilled epoxy. Among all nanofillers, the presence of halloysite in epoxy nanocomposites exhibited the highest increases in flexural strength and modulus, fracture toughness and impact strength. Flexural strength increased by 16%, modulus by 44% and fracture toughness by 44% with the addition of 1% HNT into dry epoxy (before placing in water)-based nanocomposites. However, the 1% HNT addition did not show any change in the impact strength, while the 3% HNT exhibited the highest impact strength by 14% improvement, compared to the unfilled epoxy. Meanwhile, wet epoxy (after placing in water) had an insignificant effect on the mechanical properties of nanocomposites.

2.2.4 UPE-based Nanocomposites

UPE has grown continuously and been used overwhelmingly as a matrix material in polymer composites, such as fibre-reinforced composites and nanofiller-reinforced composites for different industrial applications (such as marine constructions, offshore applications, water pipes, chemical containers, infrastructure industries, automotives and so forth) due to its good mechanical properties, low cost and low density (Xu & Lee 2004; Pereira et al. 2009). The processing of thermosetting unsaturated polyester involves a radical polymerisation between a prepolymer that

contains unsaturated groups and styrene that acts both as a diluent for the prepolymer and as a crosslinking agent.

UPE resins have been widely used as a matrix for PNCs. For example, Evora and Shukla (2003) filled UPE resin with TiO_2 nanoparticles. The tensile and compression strengths and fracture toughness of the UPE nanocomposites significantly improved due to the reinforcement role of TiO_2 particles. Similarly, Zhang and Singh (2004) and Baskaran, Sarojadevi and Vijayakumar (2011) filled UPE with alumina (Al_2O_3) nanoparticles. Compounding of 5% Al_2O_3 was found to give higher mechanical properties and fracture toughness of the UPE/ Al_2O_3 nanocomposites. Additionally, several studies have been conducted the roles of single- and multi-walled carbon nanotubes, SWCNTs and MWCNTs (Seyhan et al. 2007, 2009; Vera-Agullo et al. 2009) on different characteristics of UPE-based nanocomposites. Further, much work has been conducted to examine the roles of clay particles on UPE-based nanocomposites. To this end, Zhou, Yang and Jia (2007) studied the cure behaviour of UPE-based clay nanocomposites. They found that the addition of clay markedly increased the gel time, increased the activation energy of the nanocomposite systems and hence improved the composite properties.

The roles of vinyltriethoxysilane (VTES) surface-modified nanoclay particles on the morphology and mechanical properties of UPE nanocomposites were examined by Sen (2010) and Lu, Xu and Liu (2011), respectively. Both observed that an exfoliated structure and improved mechanical properties of the UPE-clay nanocomposites were obtained when nanoclay was modified with VTES coupling agent.

In addition to aforementioned reports on UPE matrix-based nanocomposites, Table 2.1 lists several mechanical and fractural properties taken from different experimental literature, in which UPE resin was used as polymer matrix. Table 2.2 compares some characteristics for different nanocomposites containing different HNT particle loadings. However, no particular work has yet been conducted to examine whether the effect of untreated or silane-treated halloysites on structural and material properties particularly influences the strength, tribological behaviour,

fracture toughness and toughening mechanisms of UPE nanocomposites. Thus, the objectives of this investigation considered these characteristics of the composites.

Table 2.1: Comparison of Mechanical and Fractural Characteristics for UPE Filled with Different Nanoparticles

Materials (neat UPE)	Tensile strength (MPa)	Young's modulus (GPa)	Impact strength (KJ/m ²)	Flexural strength (MPa)	K _{IC} (MPa.m ^{1/2})	Comments and reference
UPE/40% bamboo fibre	61 [50]	3.6 [3.5]	-	-	1.2 [0.5] {CT} [#]	Laminating lay-up process (Wong et al. 2010)
UPE/1% alumina	-	-	-	-	1.42 [1] {SENB} [#]	Prepared by direct mixing (Zhang & Singh 2004)
UPE/5 wt% alumina	66.5 [55.5]	-	31.5 [20]	109 [98]	-	Mechanical stirrer (Baskaran, Sarojadevi & Vijayakumar 2011)
UPE/1 wt% TiO ₂	50.5 [48.5]	3.75 [3.6]	-	-	0.85 [0.5] {SENB}	Direct ultrasonification method (Evora & Shukla 2003)
UPE/0.3 MWCNTs	66 [58]	3200 [2420]	-	-	0.66 [0.5] {CT}	3-roll milling (Seyhan et al. 2009)
UPE/3 wt% nanoclay	66 [46]	3.2 [2.7]	5.9 [3.9]	-	-	Made by using homogeniser (Esfahani, Sabet, & Esfandeh 2011)

Note: # refers to fracture geometry testing; SENB = single edge notch bending.

Table 2.2: Summary of Flexural, Modulus and Impact Strength for Different Polymers-based HNTs

Materials [neat polymer]	Flexural strength (MPa)	Flexural modulus (GPa)	Impact strength (KJ/m ²)	Reference
Epoxy/2.3% HNTs	84 [76]	2.9 [2.85]	2.7 [1.5]	Ye et al. (2007)
Polystyrene (PS)/5% HNTs	-	2.95 [2.25]	58 [19]	Lin et al. (2011)
Polyethylene (PP)/4% HNT	40 (41.5) [§] [35]	1.41 (1.45) [§] [1.05]	3.2 (3.6) [*] [2.25]	Prashantha, Lacrampe and Krawczak (2011)

Note: *HNTs were treated with quaternary ammonium salt (QM-HNTs).

2.3 Tribological Behaviour

The addition of a small amount of rigid inorganic nanoparticles into polymers significantly improves many of their mechanical properties, such as stiffness and strength, owing to the availability of large numbers of nanoparticles with huge interfacial areas. However, from the tribological perspective, although the nanoparticles have similar sizes to the segments of surrounding polymer chains—compared to micro- or macro-particles—that may act to reduce material removal, there is no decisive answer regarding whether the nanofillers always improve the wear/scratch (and friction) properties of polymers, especially thermosets. Moreover, material characteristics (such as modulus, hardness and fracture toughness) are not always the sole indicators for comparing the extent of wear rate or scratch penetration depth (Dasari, Yu & Mai 2009). In addition, Wang and Pei (2013) revealed that the role of nanofillers in modifying the friction and wear behaviour of polymer matrices can be either detrimental or positive, based on the component of the nanofillers and traditional tribofillers.

To further understand the role of different nano-additives on the material loss or damage (or tribological behaviour) of polymer matrix-based nanocomposites, a brief review is given here. Jawahar, Gnanamoorthy and Balasubramanian (2006) found that the CoF and wear loss of thermosetting polyester/clay nanocomposites reduced with the presence of organoclay. The decrease in wear loss was attributed to good dispersion of organoclay in the polymer matrix, and to the combined effect of three-body roller bearing action of both nanoclay and nanoclay-reinforced wear debris and the formation of transfer film on the steel counterface. Similarly, Rashmi et al. (2011) found that dry sliding wear resistance enhanced with the addition of 5% organoclay into epoxy nanocomposites, due to the uniformly distributed particles and the improved hardness of the nanocomposites thereof.

Further, Ha and Rhee (2008) reported that the silylation reaction on inorganic nanoparticles improved their compatibility with polymer molecules, hence leading to lower the friction coefficient and specific wear rate in the nanocomposites. Zhang et al. (2012b) found that the effect of monodispersed SiO₂ nanoparticles on the

tribological behaviour of conventional epoxy composites led to a significant reduction in the friction and wear rate with the use of lubricating filler and graphite flakes, due to the formation of a homogeneous transfer film before the counterbody was severely scratched. However, it was also found that the presence of lubricant led to a reduction in the strength of the composites because they led to a weak bond in the material. The function of graphite flakes (lubricating filler) was to decrease the surface energy, while polar materials normally associate with high surface energy and high shear strength that is undesirable to increase the friction coefficient (Dasari, Yu & Mai 2009).

Barus et al. (2009) found that the amount of material abraded increased—that is, that there was lower wear resistance in silica nanocomposites than in pure polymer. They also revealed that a tenacious material (or not a crosslinked one) presents a higher wear resistance in regard to reticulated material. Recently, Zhang et al. (2013) studied the effects of silica nanoparticles on the tribological performances of epoxy nanocomposites by using a ball-on-plate apparatus in dry sliding conditions with a hardened steel ball. It was shown that the wear resistance of the composites could improve only when the content of silica nanoparticles was higher than 10 wt%, where the continuous transfer film on the steel ball could be formed only with relatively high nanoparticle contents. The mechanisms of the worn surfaces (see Figure 2.9) showed micro-sized wear debris detached from epoxy specimen, leaving irregular craters for pure epoxy matrix, while microcracks generated on the worn surfaces—due to the fatigue wear of the adhesive contact—were observed for the epoxy nanocomposites.

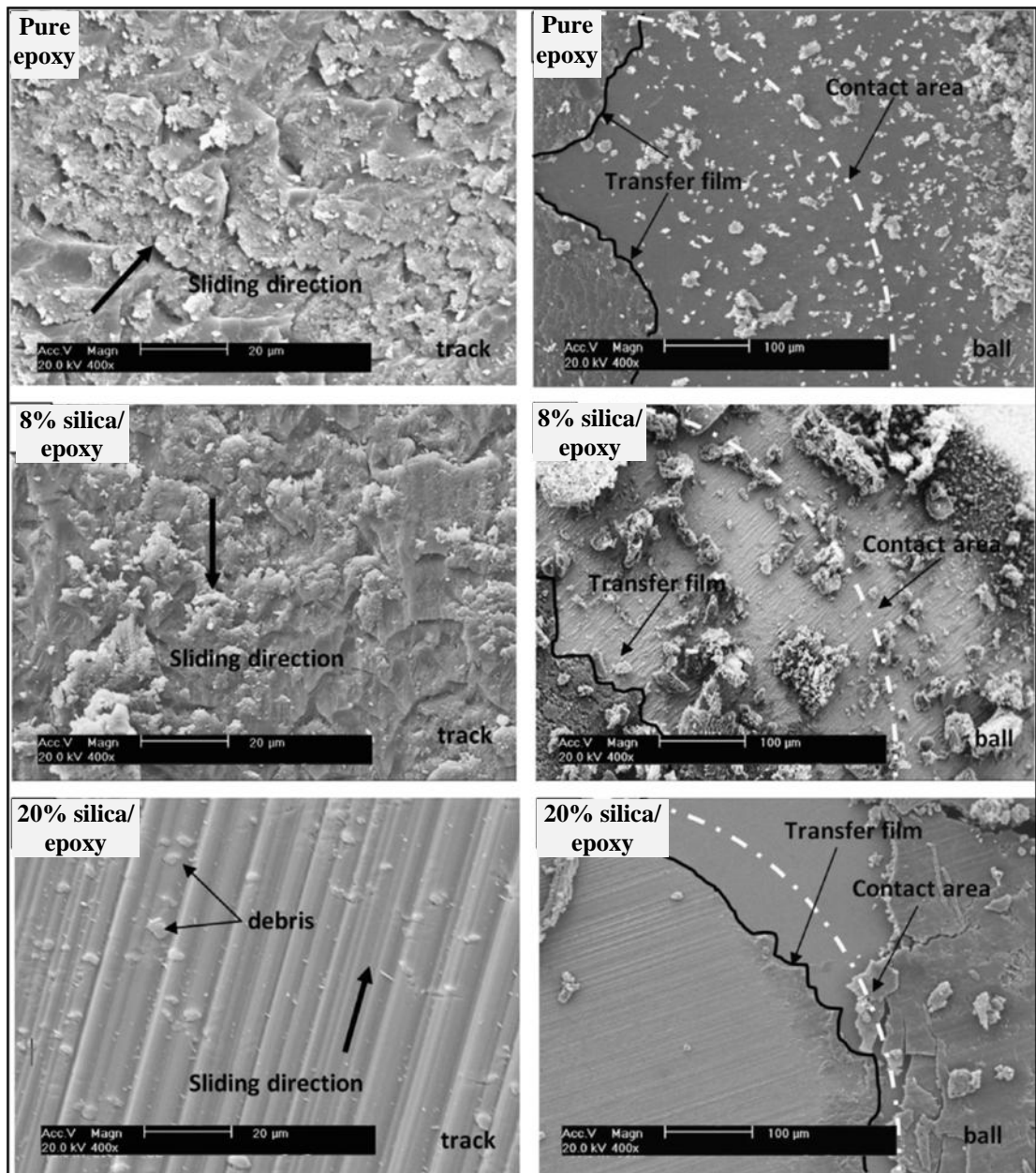


Figure 2.9: SEM Micrographs of the Worn Tracks for Pure Epoxy and Different Nanocomposites Systems

Source: Zhang et al. (2013)

2.4 Impact Strength

An impact test is used to study the toughness of materials. The impact values of materials change with the structure of materials. Impact damage is generally not considered a threat in ductile materials owing to the large amounts of energy that can be absorbed in such materials. However, it is different story with brittle materials that

can only absorb a little energy in elastic deformation and through damage mechanisms, not via plastic deformation (Richardson & Wisheart 1996). The impact energy of a material can also change with thickness of sample and temperature, where it is decreased at lower temperatures (Chen & Evans 2008). Hence, much work has been done on the introduction of a second phase in brittle materials, such as thermosetting polymers-based composites to reduce their brittleness and damage severity and decrease their brittle-ductile transition temperature.

For instance, Ye et al. (2007) and Lin et al. (2011) studied the effect of introducing HNTs on the impact strength of epoxy and polystyrene (PS) nanocomposites, respectively. The first authors revealed that Charpy impact strength improved four times with the content of 2.3 wt% HNTs, due to the formation of damage zones with a large number of microcracks stabilised by nanotube bridging in front of the main crack. The latter authors found that the notched Izod impact strength of the PS/5 wt% HNTs nanocomposite was approximately 300% higher than that of the neat PS matrix, as shown in Table 2.2. However, further increase in the loading of HNTs considerably decreased the impact strength of PS/HNT nanocomposites.

The impact toughness of a nanocomposite containing annealed PP and CaCO_3 nanoparticles was studied by applying a falling-weight impact test (Lin et al. 2008). The results revealed that the plastic deformation zone that formed in the crack-initiation stage was responsible for a high impact toughness in the annealed nanocomposites. Esfahani, Sabet and Esfandeh (2011) assessed the performance of nanoclay filled polyester (UPE) resin under impact loads. The results of Izod impact test indicated that the UPE nanocomposites containing 1.5% nanoclay had the highest value of impact strength, compared to the neat UPE matrix. Nevertheless, in terms of thermosets-based nanocomposites, thus far no study has examined the reinforcement role of nanoparticles on the impact toughness behaviour and micromechanism of fracture under impact and a range of testing temperatures, except Deshmane et al. (2007), who investigated the reinforcement of thermoplastic PP matrix with 4 wt% nanoclay. They found a striking variation in the impact toughness behaviour in the temperature range of -40°C to $+70^\circ\text{C}$ under identical processing conditions, and the impact strength increased due to a strong PP/nanoclay interaction that was responsible for significant change in physical and mechanical properties.

2.5 Fracture Toughness of Polymer Nanocomposites

To analyse the relationship between stresses, cracks and fracture toughness, fracture mechanics seek to determine the response of a cracked material to an applied load. Fracture mechanics was first introduced by Griffith in the 1920s. It was in relation to the flaw size and fracture stresses and was limited only to brittle materials. In the 1950s, Irwin extended this theory to materials with some ductile behaviour through the concept of strain energy release rate. Around the 1960s, the fundamentals of LEFM were established, while the stress intensity factor was used to characterise the crack-tip conditions, depending on the global applied stress and the local stress near the crack tip in linear elastic material. The LEFM works for brittle systems that fail by catastrophic crack growth after reaching a threshold load (stress) value. The related criteria rely either on the stress field ahead of the crack tip (stress intensity factor or fracture toughness, K_c) or the energy release during crack extension (strain energy release rate or fracture energy, G_c).

Fracture toughness is a critical mechanical property that characterises the resistance of a material to crack propagation or fracture. Measurements of fracture toughness and a material's resistance to crack growth in brittle systems—such as thermosetting polymer-based composites—have received considerable attention in current research due to the nature of their giant macromolecule network structure with a high crosslink density and little dissipated energy. To this end, efforts have been devoted to initiate localised energy-absorbing mechanisms in the fracture process zone of such materials in order to reduce plastic resistance and delay reaching brittle strength (Chen et al. 2008; Liang & Pearson 2010; Gubeljak et al. 2011; Kumar, Chitsiriphanit & Sun 2011; Quaresimin, Salviato & Zappalorto 2012; Zamanian et al. 2013).

The fracture properties and toughening mechanisms of epoxy modified with untreated (HNT) and silane-treated halloysite (s-HNT) prepared via direct mixing stirrer were measured by Deng, Zhang and Ye (2009). They found that HNT and s-HNT effectively increased the fracture toughness of epoxy resins without sacrificing other properties, such as strength, modulus and glass transition temperature, due to

their large aspect ratios. The K_{Ic} improved from 0.92 for neat epoxy to 1.26 and 1.27 for epoxy filled with 5 wt% of HNT and s-HNT, respectively. The fracture toughness of the epoxy/nanosilica composites increased with increasing nanosilica content due to the generation of a zone shielding mechanism that involved plastic deformation. No significant change in toughness was noticed with the change of nanosilica particle sizes (Liang & Pearson 2010). Four toughening mechanisms were observed in the epoxy/nanosilica composites: particle debonding, matrix ligament bridging, matrix dilation bands and matrix shear banding.

Ha et al. (2010) conducted the effects of silanised clay and temperature on the fracture behaviours of epoxy/clay nanocomposites. The fracture toughness of silane-treated clay/epoxy nanocomposites increased by 82% from 8.52 J/m² for untreated to 15.55 J/m² for silanised clay, due to good dispersion of clay layers in the epoxy matrix and improvement in interfacial adhesive strength between the clay layers and the epoxy.

Tang et al. (2012a) used phenylphosphonic acid (PPA) to unfold halloysite and investigate the effects of PPA treatment and intercalated halloysites on the fracture properties of halloysite-epoxy nanocomposites. The addition of 10 wt% of unfolded and intercalated halloysites exhibited an improvement of 78% in the K_{Ic} due to the substantial increase in the contact area between the halloysite and the epoxy. The morphology of halloysite in the nanocomposites changed from nanotubes to nanoplatelets as a result of the PPA treatment. Tang et al. (2012b) studied the fracture mechanisms of epoxy-based ternary composites filled with rigid (silica) nanoparticles and soft (phase-separated submicron rubber) particles, and compared the binary composites with single-phase particles. They observed that the synergistic effect of multi-phase particles offered a good balance in stiffness, strength and fracture toughness. The fracture toughness enhanced due to the enlarged plastic deformation that initiated around the crack tip via the combination of rigid and soft particles. They also observed that the debonding of silica particles from the matrix in the ternary composites was less pronounced than that in the binary composites.

The effects of different silica particle sizes (average diameter = 12, 20 and 40 nm) on the fracture toughness of epoxy nanocomposites prepared by mechanical mixing and

ultrasonic instrument were examined by Zamanian et al. (2013). The fracture energy increased to 620 J/m^2 for epoxy modified with 3.17 vol. % of 12 nm diameter nanoparticles, versus 283.2 J/m^2 for the unmodified epoxy matrix.

2.6 Toughening Mechanisms in Polymer Nanocomposites

In addition to the above discussion cited from previous reports, a brief review is given here on the toughening mechanisms occurring in PNCs, with emphasis on thermosetting polymers to understand how they contribute to achieve significant improvements in stiffness, impact energy absorption and fracture toughness. Liang and Pearson (2009) and Dittanet and Pearson (2012) studied the effects of silica particles on toughening mechanisms, and the relationship between the fracture toughness, yield strength and corresponding plastic zone in epoxy-silica nanocomposites, respectively. The fracture toughness and fracture energy definitely improved with the addition of silica particles due to the occurrence of silica particles debonding, matrix void growth and matrix shear banding, as shown in Figure 2.10. The shear banding toughening mechanism was the dominant mechanism, while particle debonding and plastic growth were the minor mechanisms.

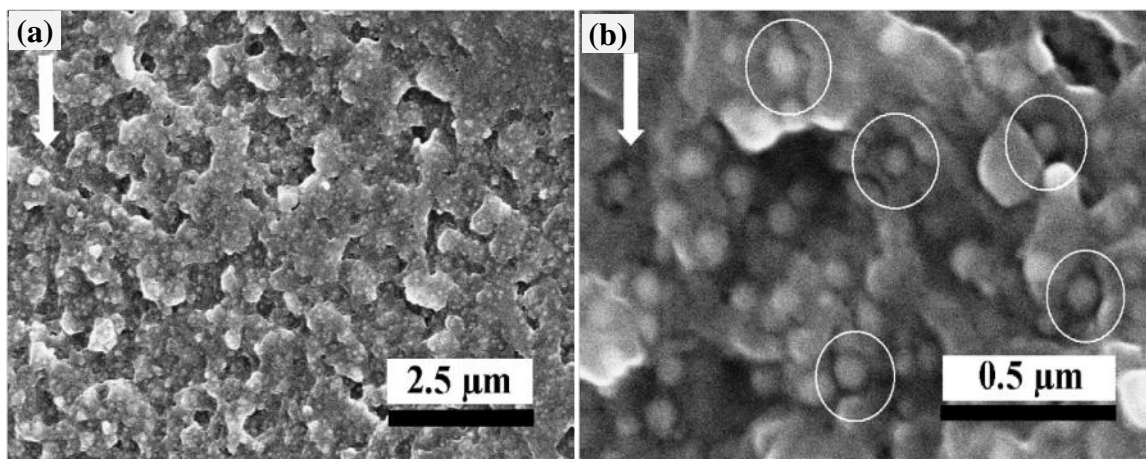


Figure 2.10: SEM Micrographs of Fracture Surface from Epoxy Filled with 17.4% Silica Nanocomposites: (a) Matrix Ligament Bridging and (b) Circled Debonded Particles

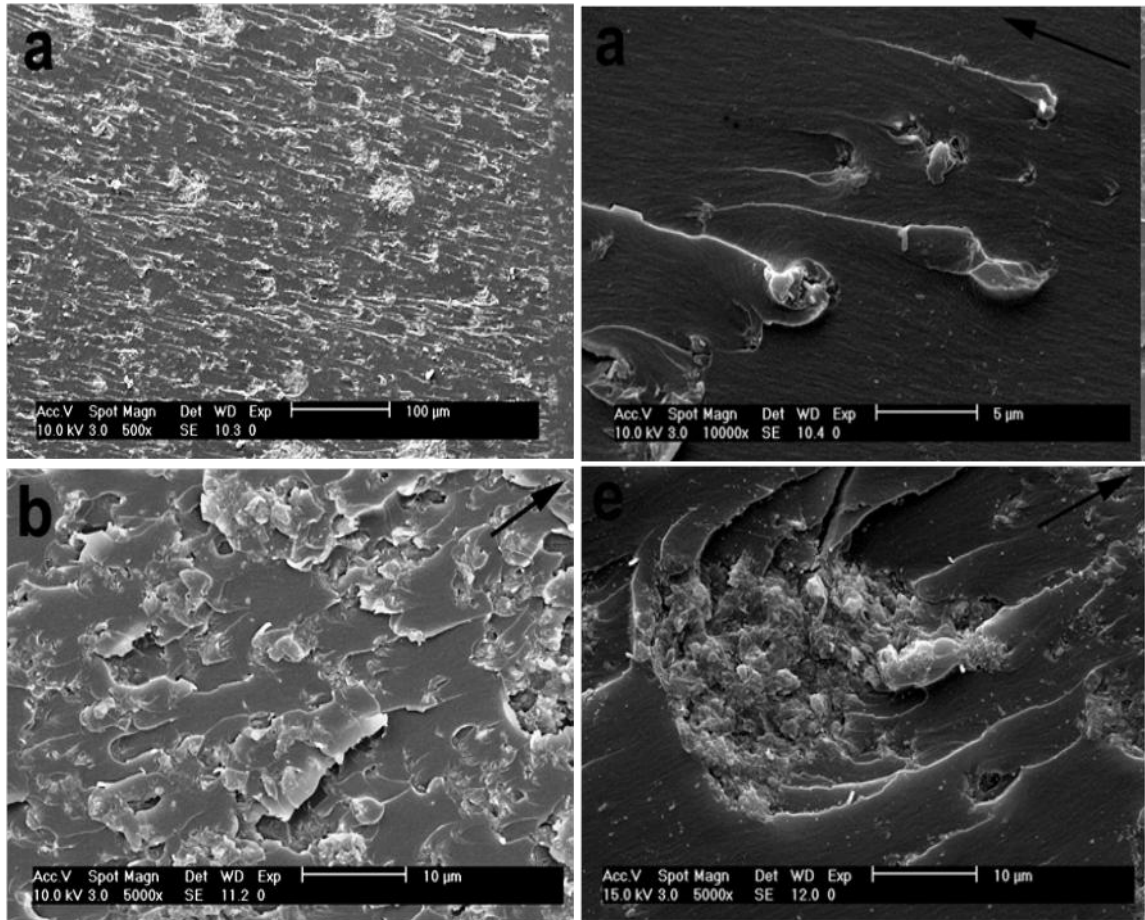
Source: Liang and Pearson (2009)

Hsieh et al. (2010b) examined the fracture properties of four different epoxy polymers containing 10 and 20 wt% of well-dispersed silica nanoparticles. They found that the presence of silica nanoparticles always led to an increase in the toughness of any given epoxy polymer, where the two toughening mechanisms occurring in all nanocomposites were:

1. localised shear bands initiated by the stress concentrations around the periphery of the silica nanoparticles
2. debonding of the silica particles followed by subsequent plastic void growth of the epoxy polymer.

The relationship between the toughening mechanisms and microstructure of epoxy-based hybrid nanocomposites filled with two tougheners—polyethersulphone (PES) and organoclay—was investigated by Wang, Zhang and Ye (2011). They found that the PES improved the ductility of material and made it easier to deform, and the organoclay agglomerates induced different toughening mechanisms—that is, crack front bowing, crack bridging, crack deflection, crack bifurcation and plastic deformation of the matrices—as illustrated in Figure 2.11.

Bashar, Sundararaj and Mertiny (2012) investigated the role of organophilic layered silicate nanoclay and acrylic tri-block-copolymer on toughening mechanisms in epoxy hybrid nanocomposites. Three-phase ternary nanocomposites showed the coexistence of both intercalated nanoclay and nanostructured block-copolymer in epoxy and, as a result, enhanced fracture toughness. The SEM examination of fracture surface morphology showed discrete nanoscopic holes formed by cavitating block-copolymers and intercalated nanoclay in epoxy nanocomposite. The fracture toughness enhancement was thought to be due to void formation followed by matrix yielding, as indicated in Figure 2.12.



Note: The black arrows in the images indicate the direction of crack propagation.

Figure 2.11: SEM Micrographs of the Fracture Surfaces of: (a) Epoxy/1 wt% Organoclay/PES, (b) Characteristic Tail Structure in the Fracture Surface of Epoxy/1 wt% Organoclay/PES, (c) Characteristic Tail Structure on the Rough Fracture Surface of the Epoxy/3 wt% Organoclay/PES and (d) Various Fracture Positions Inside One Agglomerate on the Fracture Surface of the Epoxy/1 wt% Organoclay/PES Hybrid Nanocomposites

Source: Wang, Zhang and Ye (2011)

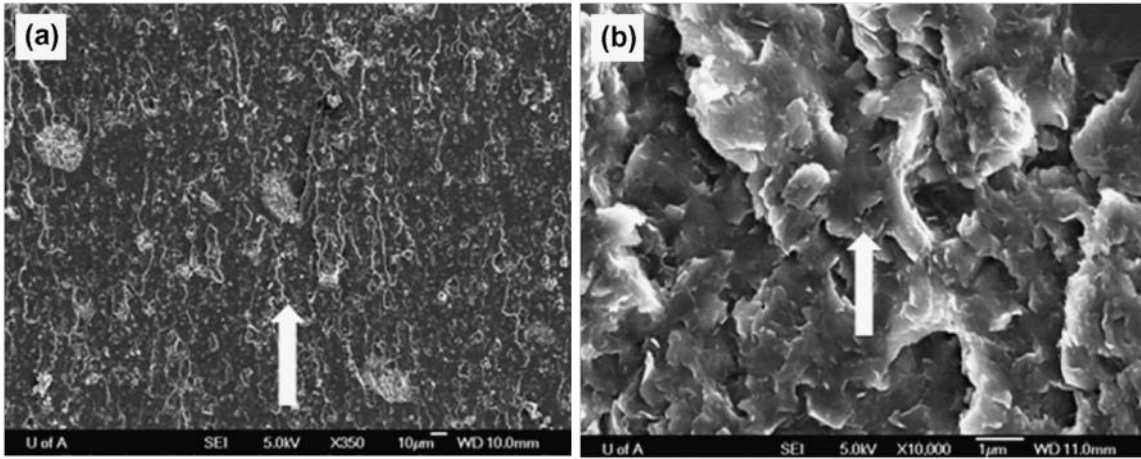


Figure 2.12: SEM Images of Fracture Surfaces of Epoxy Filled with Nanoclay Nanocomposite at: (a) Low Magnification and (b) High Magnification

Source: Bashar, Sundararaj and Mertiny (2012)

2.7 FEM Models for Prediction Crack Propagation

Previous studies have sought to further develop the properties of PNCs depending on a fundamental understanding of the hierarchical structures and behaviours of these composites. Thus, various multiscale modelling and simulation strategies have been undertaken to predict these properties (such as morphology, thermodynamic, processing behaviour, molecular structure and mechanical properties) with seamless coupling among various length and time scales (Zeng, Yu & Lu 2008). Understanding the resistance of a material to crack propagation (or fracture toughness) is one of the most important features in the PNCs that underlie their superior properties and functions. To this extent, some computational methods have been applied to encompass molecular scale, microscale and macroscale.

For example, Lauke (2008) calculated the total crack resistance, R , by the separate contributions of the mechanisms in the process and dissipation zones. Giner et al. (2009) and Silani et al. (2012) used the extended FE method (XFEM) to simulate crack initiation and propagation in epoxy/nanoclay composites under mixed-mode conditions based on linear elastic traction-separation behaviour and phantom nodes. Compared to the experimental results, this method successfully proved its ability to predict the crack initiation and propagation of epoxy/clay composites. Sun, Gibson and Gordaninejad (2011) and Kumar, Chitsiriphanit and Sun (2011) predicted the

growth criteria—including the 3-D Benzeggagh and Kenane criterion, the 3-D Wu and Reuter law (power law) and the Reeder law criterion—were used to investigate the effects of the platelet aspect ratio, clustering and orientation on crack propagation. It was observed that a crack tends to initiate on the side of ‘intrastack phase’—that is, between disks in a cluster, rather than on the effective interface surrounding clusters and single platelets. The crack first grows further in the intrastack phase and slower in the matrix. However, the analysis of crack propagation mechanisms in thermosets-based nanocomposites has not yet been well researched because shear yielding and multiple crazing often takes place at the vicinity of the crack tip. Unstable crack growth in thermosets is further complicated the analysis.

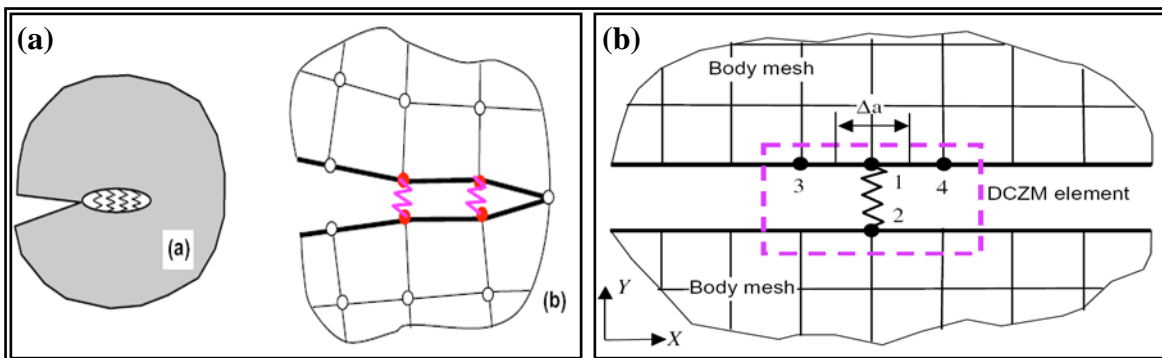


Figure 2.14: (a) Schematic of DCZM and (b) Definition of DCZM Element and its Node Numbering

Source: Xie and Waas (2006)

2.8 Summary

Understanding the relationship between nanoscale structure and macroscale properties and identifying the ‘nano-effect’ of different nanoparticles on the final characteristics of PNCs have become prominent areas in current research and development. To this end, many reports in the literature have been undertaken. However, different recently developed nanocomposite systems must still be researched, particularly in terms of investigating the role of nanoparticles on the structural and material properties of thermosets matrix-based nanocomposites. Thus, the current investigation sought to examine the effects of untreated and silane-treated

halloysite nanotubes on the morphological and materials characteristics—thermo, thermodynamic and mechanical properties, as well as tribological, impact strength and fracture toughness—of unsaturated polyester-based nanocomposites. The crack initiation and propagation in the nanocomposites under Mode I tensile loading was also mathematically investigated.

Chapter 3: Materials and Experimental Procedure

This chapter discusses the materials used for the experimental work, the methods and the equipment used to prepare the materials and fulfil all the characteristics. The materials used and experimental methods are described in the sections as follows: Section 3.1 describes the materials used, Section 3.2 describes the silane chemical treatment of the halloysite nanotubes, Section 3.3 outlines the nanocomposites preparation and Section 3.4 discusses the characterisation of the nanocomposites.

3.1 Description of Materials Used

The materials used for the experimental investigation are listed in Table 3.1.

Table 3.1: Description of Materials Used in this Study

Materials	Supplier designation	Specifications	Supplier
HNTs	Dragonite brand	Chemical formula: (Al ₂ Si ₂ O ₅ (OH) ₄ -2H ₂ O) Specific gravity = 2.26*	Applied Minerals Inc., United States (US)
UPE	AROPOL [®] -1472 PLSE	Viscosity= 350 cp, Styrene = 45%	Nupol, Australia
Methyl ethyl ketone peroxide (MEKP)	Butanox-M50	Catalyst with a peroxide content = 33%	Nupol, Australia
Vinyltrimethoxysilane (VTMS)-98%	Coupling agent	Linear formula: C ₅ H ₁₂ O ₃ Si, Molecular weight: 148.24	Sigma-Aldrich Co., Ltd., US

Note: *The density of halloysite was determined by measuring the sample's volume with a multi-pycnometer (Quanta-chrome instruments).

The Dragonite brand HNTs that were used as the reinforcing nanofiller in this study were provided by Applied Mineral Inc., US. These nanotubes have a length in the range of 0.5 to 3.0 μm , an exterior diameter in the range of 50 to 70 nm, an internal diameter in the range of 15 to 30 nm and a specific gravity of 2.26. They have uniform charges on the exterior surface with a low density of hydroxyl functional groups.

The polymer matrix used in the study was AROPOL®-1472PLSE brand UPE, provided by Nupol, Australia. UPE resin has a low viscosity of 350 cp to permit better compatibility with the nanofiller and a high styrene of 45% to promote polymerisation. There are several reasons why the UPE resin was chosen as a matrix resin within this study, including the common applications of UPE in automotives, expected to be a continuation of this work particularly within theoretical aspects to complete constitutive models, or assessing further necessary properties. Thus, it is advantageous to have such a real resin as a base.

The catalyst used to initiate the crosslinking of the UPE resin was MEKP/Butanox-M50, which contains 33% peroxide content. VTMS-98% solution with a linear formula of C₅H₁₂O₃Si and a molecular weight of 148.23 purchased from Sigma-Aldrich, was used as coupling agent to improve the dispersibility of halloysite in the polymer matrix.

3.2 Silane Chemical Treatment of Halloysite Nanotubes

The sol-gel process was applied to functionalise the pristine as-received HNT surface with VTMS coupling agent in order to improve its affinity with the organic polymer. For this process, the minimum amount of the VTMS was determined according to Equation 3.1 to ensure uniform silane distribution on the inorganic halloysite surface. The typical surface area of HNT is 65 m²/g from Sigma-Aldrich, and specific surface wetting of VTMS is 280 m²/g (MacMillan 1997):

$$\text{Amount of VTMS (g)} = \frac{\text{Amount of HNT (g)} \times \text{surface area of HNT (m}^2 / \text{g)}}{\text{specific surface wetting of VTMS (m}^2 / \text{g)}} \quad (3.1)$$

Fifty grams of HNT and 12 g of VTMS were dissolved under agitation in 500 ml of ethanol absolute to produce s-HNT. One ml of acetic acid and 50 ml of distilled water were then added to the aqueous solution to keep the pH value in the range of 4.5 to 5.5. The solution was mixed for three hours at 50°C on a hotplate with a magnetic stirrer (Figure 3.1).

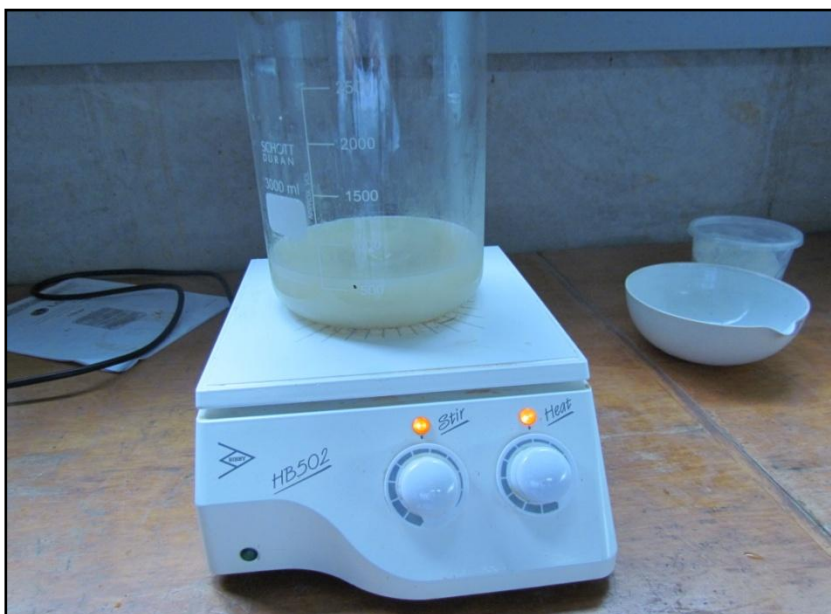


Figure 3.1: Magnetic Stirrer Used in the Preparation of Silane Treatment

On completion of the reaction, the solution was filtered and washed with deionised water until neutral. The final product was dried under a fuming hood overnight and later at 100°C for eight hours to remove any remnant of the solvent. The dried product (slurry) was ground in a porcelain mortar and pestle to primary powders to crush the bulk aggregates, and then sieved using different fine metal sieves to exclude micro- and nanoparticles of the primary filler.

3.3 Nanocomposite Preparation

Nanocomposites based on different weight percentages (1, 3, 5, 7, and 9 wt %) of pristine HNT, s-HNT and the UPE resin were prepared using a combination of direct mechanical stirrer rotated at 2,000 rpm and ultra-sonication (agitation) process at ambient temperature. Note that the halloysite nanotubes were pre-dried in a vacuum furnace at 100°C for two hours to remove any moisture. However, this process did not last long because the pre-dried particles did not release any change in dispersion status compared with that of the un-dried (as-received) particles.

The mixing process of halloysite particles in the liquid UPE resin was completed for 30 minutes at 24°C. During the rotation process, the halloysite particles were slowly

added to avoid particle agglomeration and ensure good dispersion. The produced mixture was later placed under ultrasonic probe at a frequency of 25 KHz (see Figure 3.2) for two hours to agitate the halloysite particles well inside the resin and remove the air bubbles. Interestingly, the ultrasonic probe was operated intermittently to avoid overheating and styrene emission.

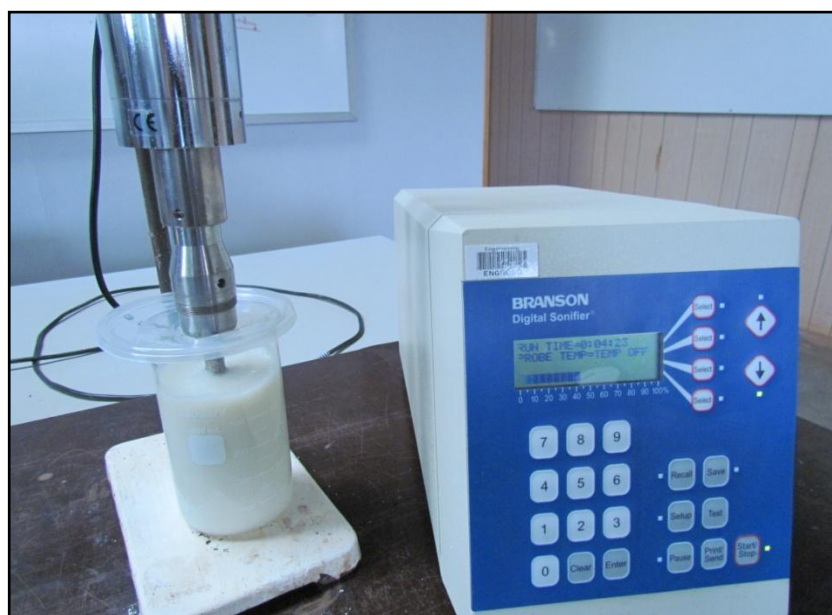


Figure 3.2: Sonicator Probe Used for the Sonication Process

To complete the polymerisation of unsaturated polyester-based nanocomposites, the MEKP catalyst was added to the produced mixture at 1.5% of the UPE weight, as recommended by the manufacturer. It was re-stirred by hand to achieve a homogenised hardener throughout the whole mixture. Based on the designated tests, the processed mixture was then cast into the pre-designed moulds with cavities to match the desired finishing dimensions. Figure 3.3 shows several types of pre-designed moulds used to produce the different testing samples. The samples were cured at room temperature for 24 hours and post-cured at 60°C for two hours in the oven, and later at 90°C for two hours to ensure full polymerisation of the network. The post-curing process was determined from the thermal analysis results of the liquid UPE resin. Samples of the neat UPE were prepared following the same curing process as a baseline for comparing the results. Upon completing the curing process, the specimens were removed from the moulds and finally set up in accordance to the required testing.

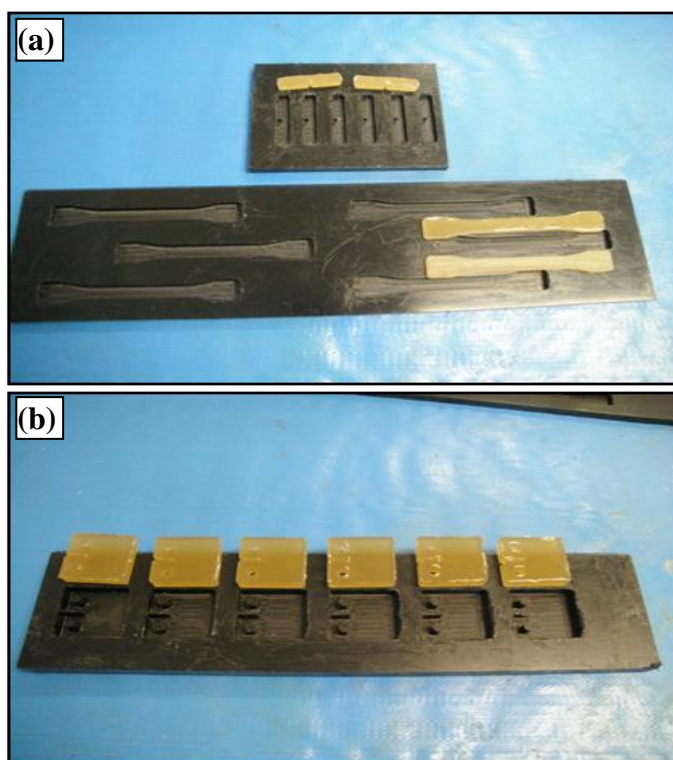


Figure 3.3: Samples of: (a) Dog-bone Tensile Test and SEN and (b) CT

3.4 Characterisation of Nanocomposites

3.4.1 Morphological Characterisation

The morphological structures and distribution of the untreated and silanised halloysites in the developed nanocomposites were examined using a transmission electron microscope (JEOL-1010) with an acceleration voltage of 100 KV. Ultrathin sections (~70 nm in thickness) of the composite were cut with a diamond knife at room temperature and placed on carbon-coated copper grids.

SAXS and WAXS scans were performed using an advance Bruker D-8 x-ray diffractometer and $\text{CuK}\alpha$ radiation generated at 40 KV and 30 mA. The SAXS and WAXS scans were carried out at a scan rate of $1.2^\circ/\text{min}$ over the range of $2\theta = 2^\circ - 40^\circ$ to characterise the crystalline structure and the basal spacing of the halloysite particles.

A scanning electron microscope (Philip XL-30) was used to identify the role of HNT and s-HNT particles on the fracture mechanics and toughening mechanisms occurring in the nanocomposites. All SEM samples—viz. samples of fracture surfaces from tensile testing, fracture surfaces from impact testing, worn surfaces to identify the wear mechanisms, fracture surfaces of CT samples after tensile load, and fracture surfaces of SEN-3PB—were sputter coated with a thin layer of platinum before the examination to improve their electrical conductivity. Energy-dispersive x-ray (EDX) or energy-dispersive spectroscopy (EDS) was used to determine the elemental analysis or chemical characterisation of halloysite particles before and after silanisation.

3.4.2 FT-IR

FT-IR spectroscopy measurements were performed using a Thermo Nicolet NEXUS 670 FT-IR spectrophotometer (see Figure 3.4) to characterise the molecular structures of the nanocomposites and identify the vibrational states of the chemical bonds obtained after curing process. The FT-IR test was also undertaken to determine the role of silanised halloysite on the bending vibration of C-H groups and C-C bonds of the neat UPE resin. The FT-IR samples were prepared by mixing ground parts of cured composites with KBr powder at 1:100 ratios to form transparent pellets.



Figure 3.4: FT-IR Spectrophotometer Used in the Study

3.4.3 Thermal Property Analysis

Thermal degradation of neat UPE and its different nanocomposites were measured using a thermogravimetric analysis (TGA-Q500) (see Figure 3.5) at temperatures from 25°C to 600°C under a 100 cm³/min nitrogen gas flow and a 10°C/min heating rate. The decomposition temperature and weight loss percentage of the materials were recorded directly.



Figure 3.5: TGA-Q500 Used for Thermal Property Analysis

3.4.4 Glass Transition Temperature (T_g)

Figure 3.6 shows the differential scanning calorimeter, DSC-Q200, that was used to measure the glass transition temperature (T_g) and the heat capacity of phase change for neat UPE and its different HNT and s-HNT nanocomposites. The DSC measurement was undertaken at a range of temperatures, from 5°C to 180°C at 10°C/min heating rate under a 100 cm³/min dry nitrogen gas flow. The specific samples for the DSC spectra were cut from different nanocomposite systems, with a weight ranging from 15 to 30 mg, and then packed in aluminium pans. To complete the measurement, these samples were heated to 200°C and held at the temperature for five minutes to reset the thermal history. The melting temperature and heat of fusion were determined from the second heating scan.



Figure 3.6: Differential Scanning Calorimeter (DSC-Q200) Used in the Study

3.4.5 Viscoelastic Properties

The dynamic mechanical analyser (DMA-Q800, TA Instruments) shown in Figure 3.7 was applied to measure the viscoelastic properties of neat UPE and UPE/HNT and UPE/s-HNT nanocomposites. The tensile viscoelastic properties represented by storage modulus (E'), loss modulus (E'') and tan delta ($\tan \delta$) were tested against a range of temperatures (25°C to 180°C) at a heating rate of $3^{\circ}\text{C}/\text{min}$, frequency of 1 Hz and displacement amplitude of $20\ \mu\text{m}$. The DMA samples were prepared from neat UPE and different nanocomposites systems with dimensions of $50 \times 10 \times 4.5\ \text{mm}^3$.

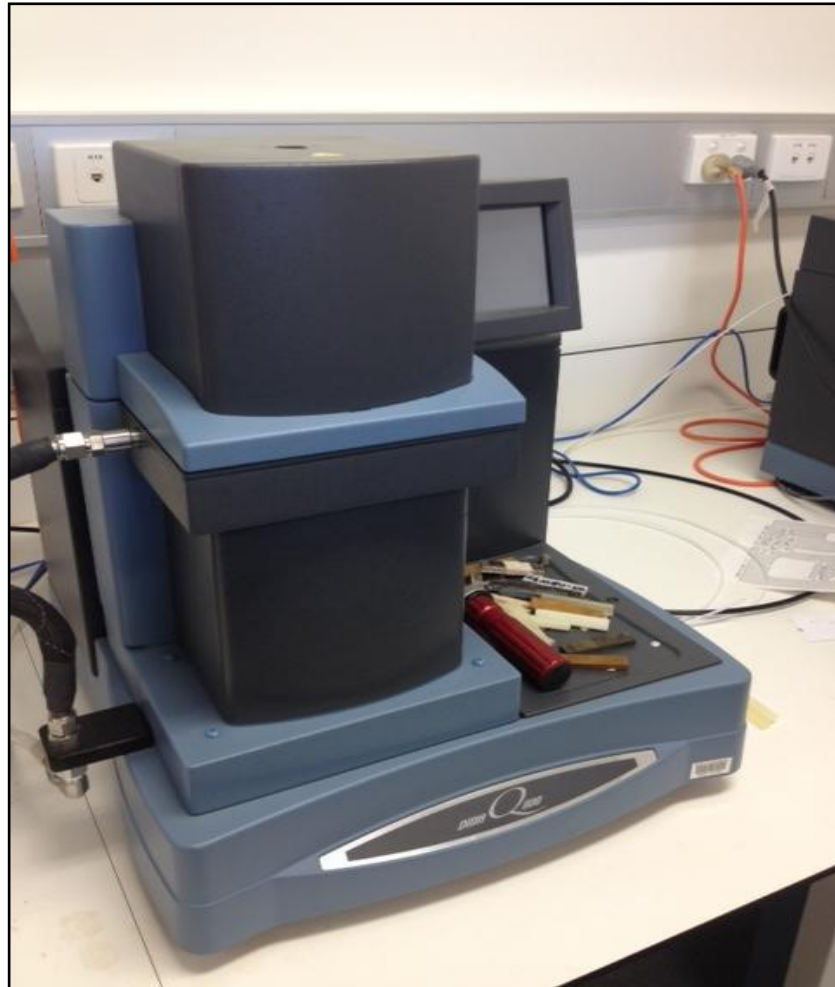


Figure 3.7: DMA-Q800 Used to Measure the Viscoelastic Properties

3.4.6 Mechanical Characteristics

The mechanical properties—including tensile strength, Young’s modulus and elongation at the break—were calculated according to ASTM standard, D-638. An Instron Alliance RT/10 MTS universal machine (Figure 3.8a) connected to a computerised data acquisition system was used to complete all tensile, flexural and fracture tests. Six dog-bone tensile samples, as shown in Figure 3.3a, of neat UPE and each nanocomposite system were tested at room temperature with a crosshead speed of 1 mm/min. The average value was determined as a peak tensile stress.

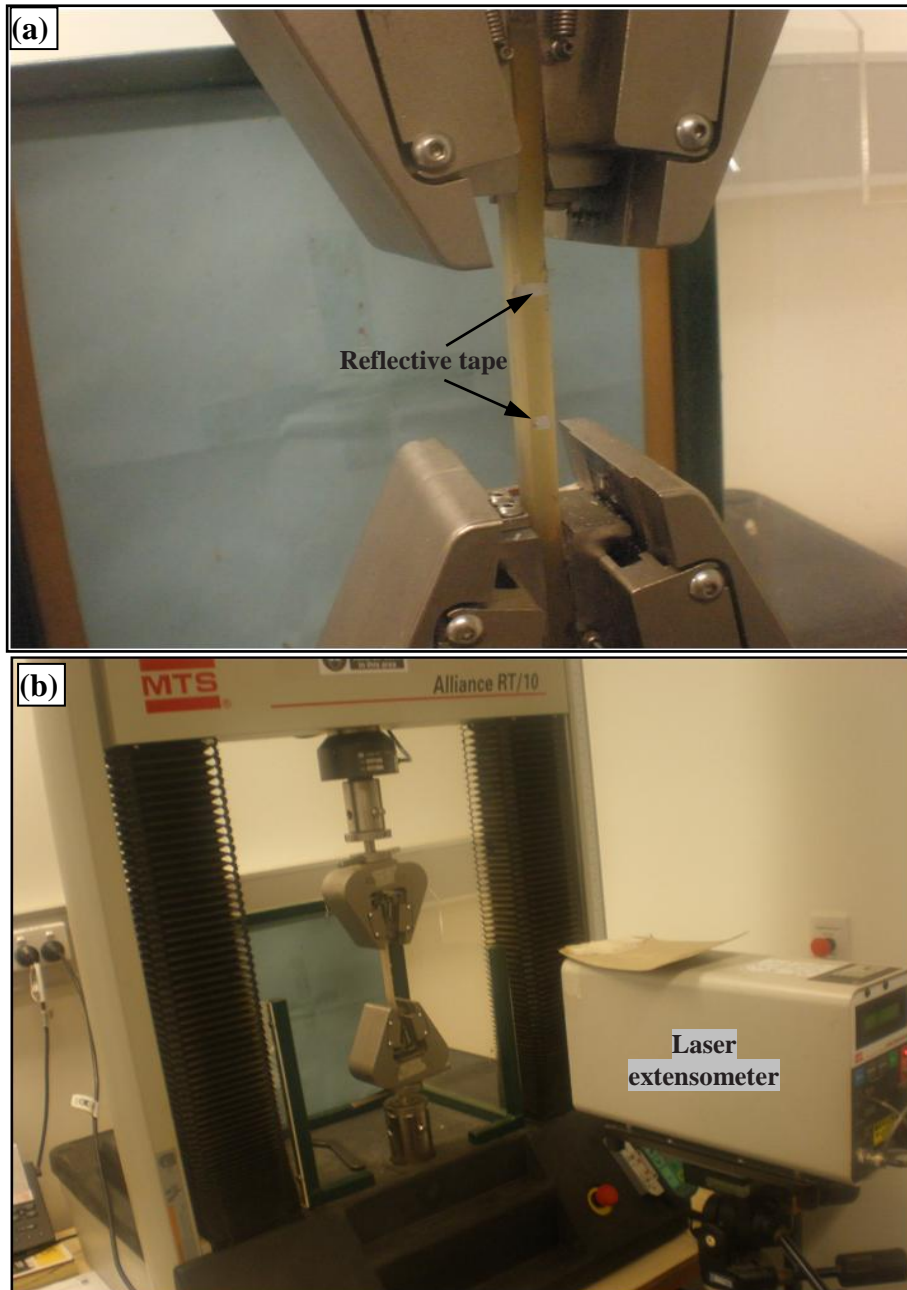


Figure 3.8: Instron Alliance RT/10 MTS: (a) Universal Machine and (b) Laser Extensometer

The values of tensile modulus and strain at the break of the tensile-tested samples were determined directly from the computer that was connected to the MTS machine by a laser extensometer. To enable the laser extensometer to read all strain measurements, a special reflective tape was stuck on all tested samples.

The flexural strengths of neat UPE and its different nanocomposites were measured at room temperature using the same MTS machine (Figure 3.9), applying a 3PB test. Flexural experiments were undertaken at a crosshead rate of 1 mm/min on samples' dimensions of $52 \times 12 \times 6 \text{ mm}^3$ and a 40 mm bending span.



Figure 3.9: Flexural Strength Testing Using MTS Universal Machine

Shore D hardness is normally used to measure material resistance to a permanent deformation under indenter action. This kind of hardness is highly related to structural parameters, since the mechanical properties are structure-dependent. According to ASTM D-2240 standard (ASTM 2010b), the measurements of Shore D hardness were undertaken using LX-D portable tester. Several different positions of nanocomposite blocks, covering different areas along their surfaces, were indented, and the average of five readings was considered.

3.4.7 Impact Fracture Toughness

The impact tests of neat UPE and different UPE/HNT and UPE/s-HNT nanocomposites were conducted at room temperature by using Instron Dynatup 9250 HV machine (Figure 3.10). A hammer weighing 2.84 Kg was dropped from the top of a 0.8 metre height at a 2.9 m/s impact velocity. The impact samples for neat UPE and its different nanocomposites with final dimensions of 6 mm × 25 mm × 150 mm were prepared following the same preparation and curing procedure for all other nanocomposite samples.

The impact test was performed at three different temperatures: -20°C, 20°C and +60°C. The impact strength was inspected for at least three samples of each composite systems and the average was taken. Additional information for the impacted samples—including total impact energy, load-time-energy characteristics and deflection at peak load—were automatically measured and recorded directly from the Dynatup machine.

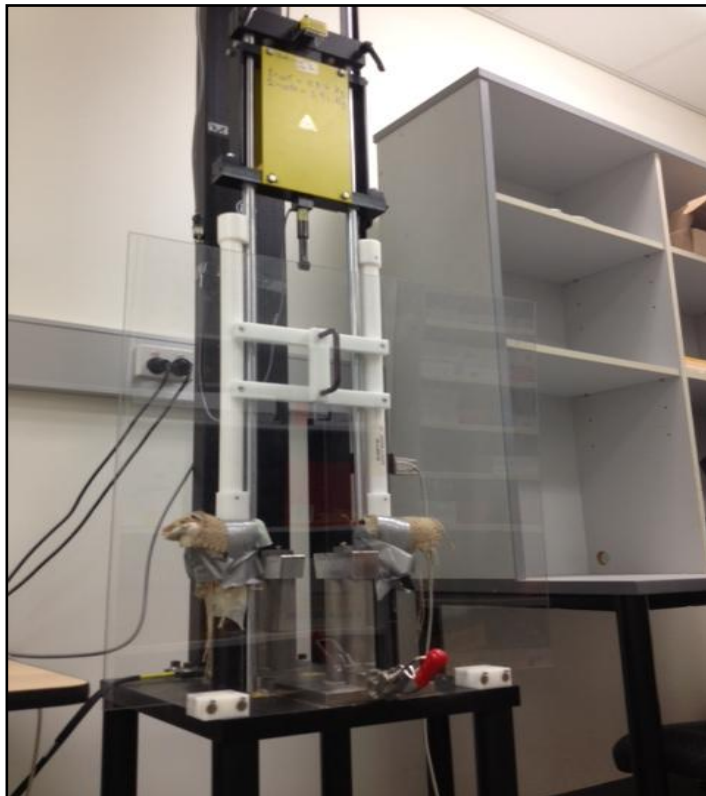


Figure 3.10: Instron Dynatup 9250 HV Machine Used for Impact Test

3.4.8 Wear Characterisation

Tribological parameters represented by CoF and weight loss were conducted at room temperature for neat UPE and its different nanocomposites using the tribometer machine, as shown in Figure 3.11a.

Block-on-ring (BOR) configuration under certain dry sliding conditions—sliding speed = 2.8 m/s, sliding distance = 11.5 Km, and normal applied force (F_N) = 20 N—were used for all wear testing. The ring used material was stainless steel (SS) of 23 cm in diameter and hardness of 900 (HV 10).

Before each wear test, the ring was rubbed with grinding paper and cleaned by methane to maintain a smooth counter surface. To start the wear test, specific samples with dimensions of 10 mm × 20 mm × 50 mm (Figure 3.11b) were prepared from neat UPE and each nanocomposite system as wear testing blocks. These wear blocks were polished well using different diamond grinding wheels to obtain a mirror face. Later, the blocks were weighed by an electronic balance with an accuracy of 0.1 mg as (m1) and loaded against the SS ring.

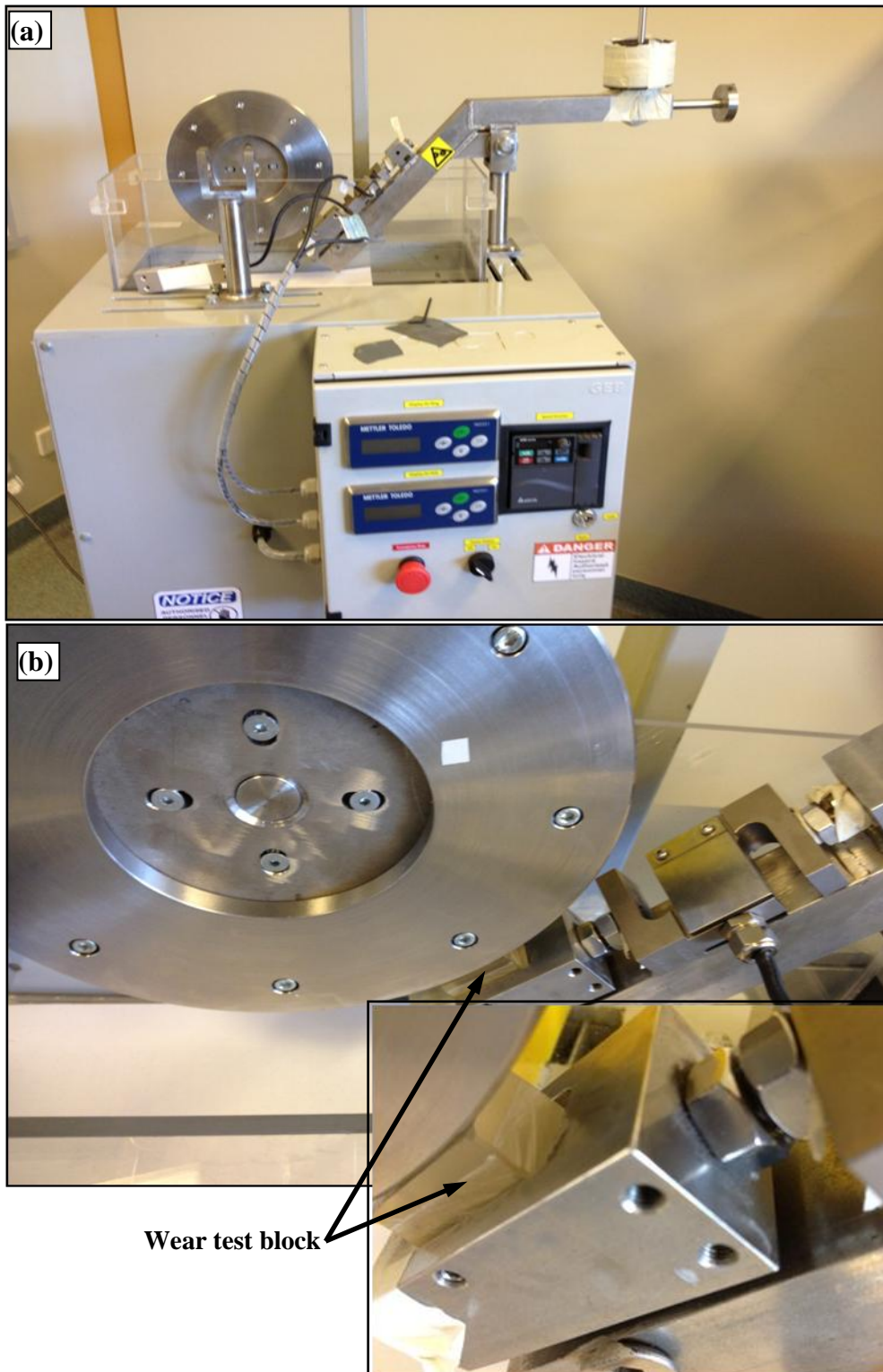


Figure 3.11: (a) Tribometer Machine Used for Wear Testing and (b) Wear Testing Block

During the wear test, the friction force and CoF between the composite wear blocks and the SS ring were recorded after each 0.5 minute. Upon completing each five

minutes of continuous wear test, the worn block was weighed again (m_2) and the wear debris was collected. The surface roughness of the SS counter surface was measured using a Mahr Metrology (MarSurf-PS1) instrument. The temperature generated through the contact point between the wear block and the SS counter surface was also measured using a laser thermometer. The specific wear rate of the wear testing blocks was calculated by applying Equation 3.2 below (ASTM 2010a):

$$w_s = \frac{(m_1 - m_2)}{\rho \cdot v \cdot t \cdot F_N} \quad (3.2)$$

where w_s is the specific wear rate (mm^3/Nm); m_1 and m_2 are the mass of the composite wear samples (g) before and after the wear testing, respectively; ρ is the specimen's density; v is the rotating speed of the counterpart (rpm); t is the time of testing (min); and F_N is the normal force (N).

3.4.9 Fracture Toughness Measurement

Fracture toughness was measured using two common testing geometries: single edge notch bending (SENB) and CT configuration based on LEFM. The SENB geometry is more popular because it requires less material without complicated machining, compared to the CT sample geometry. However, the CT geometry measures more accurate plain-strain fracture toughness because it allows more space for crack propagation.

The SENB and CT configurations used for the fracture toughness measurements are illustrated in Figures 3.12a and b, respectively. For both test geometries, a pre-crack was generated by tapping a fresh razor blade into the notch tip with a drop weight to maintain accurate fracture toughness values. The crack length-to-width ratio (a/w) was limited to 0.5 and a loading rate of 5 mm/min, as recommended by ASTM D 5045 (ASTM 2007).

In the case of the SENB specimen, the support span-to-specimen width ratio (s/w) was maintained at four, loaded in 3PB. The critical stress intensity factor (K_{Ic}) was

calculated for at least five samples, as per the following formulae, and the average was taken:

$$K_Q = \frac{P_Q}{BW^{1/2}} \cdot f\left(\frac{a}{w}\right) \quad (3.3)$$

$$f\left(\frac{a}{w}\right) = 6\left(\frac{a}{w}\right)^{1/2} \times \frac{\left[1.99 - \frac{a}{w}\left(1 - \frac{a}{w}\right)\left(2.15 - 3.93\frac{a}{w} + 2.7\left(\frac{a}{w}\right)^2\right)\right]}{\left(1 + 2\frac{a}{w}\right)\left(1 - \frac{a}{w}\right)^{3/2}} \quad (3.4)$$

where P_Q is the maximum load determined from the load-displacement curve and B is the specimen thickness.

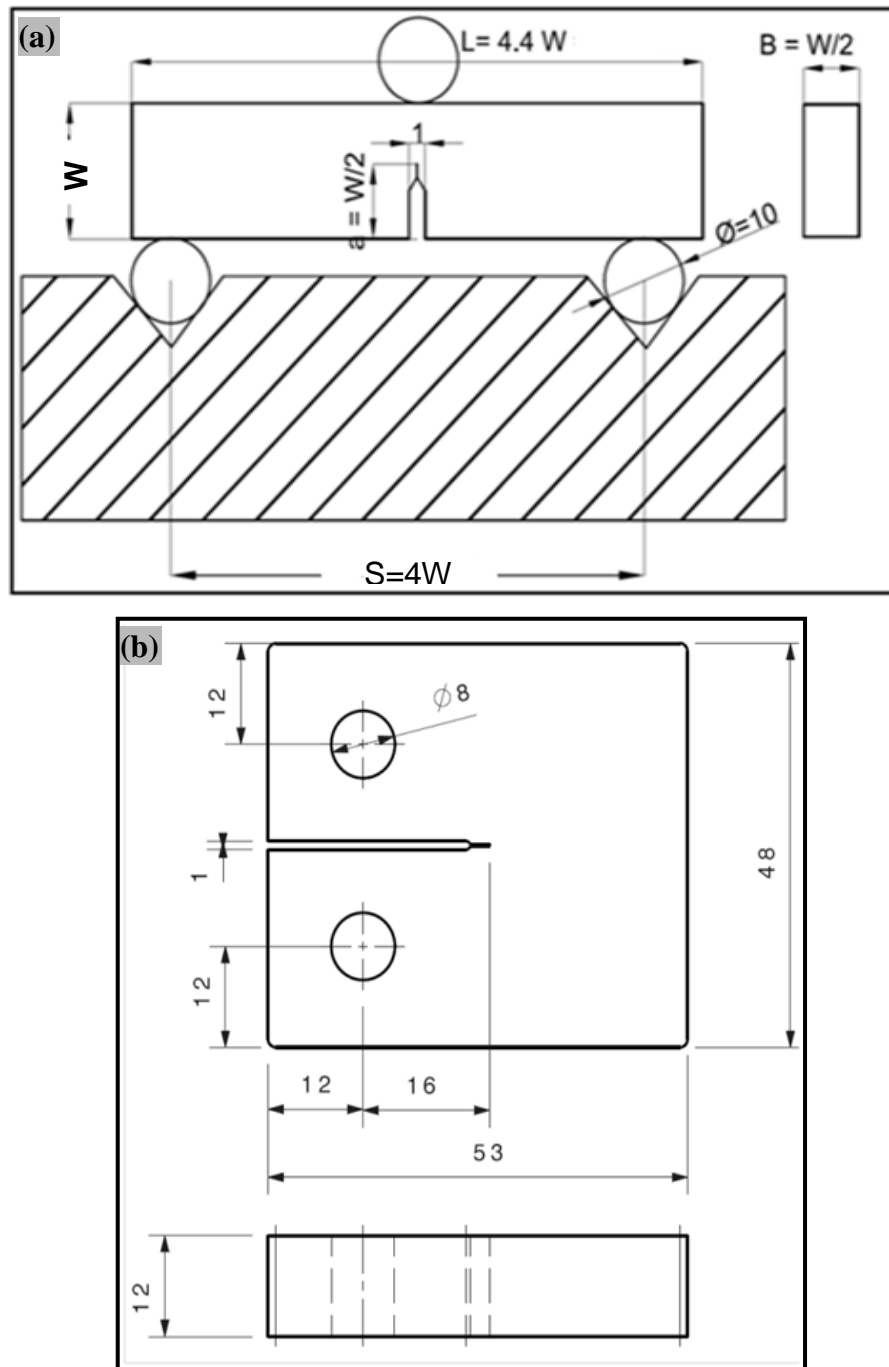


Figure 3.12: Specimen Configuration Used for Fracture Toughness Measurements for: (a) SENB Sample and (b) CT Geometry

In terms of the SEN-3PB specimen, the general principle of the bend-test fixture is illustrated in Figures 3.13a and b, respectively. As shown in Figure 3.13a, the line of action of the applied load passed midway between the support roll centres, the span ($S = 4$, $W = 48$ mm). The bend-test was performed at room temperature by using the MTS machine, and the load versus loading-point displacement curve was obtained.

The load-displacement curves were almost a linear diagram with an abrupt drop of load to zero, as described in detail in Chapter 7.

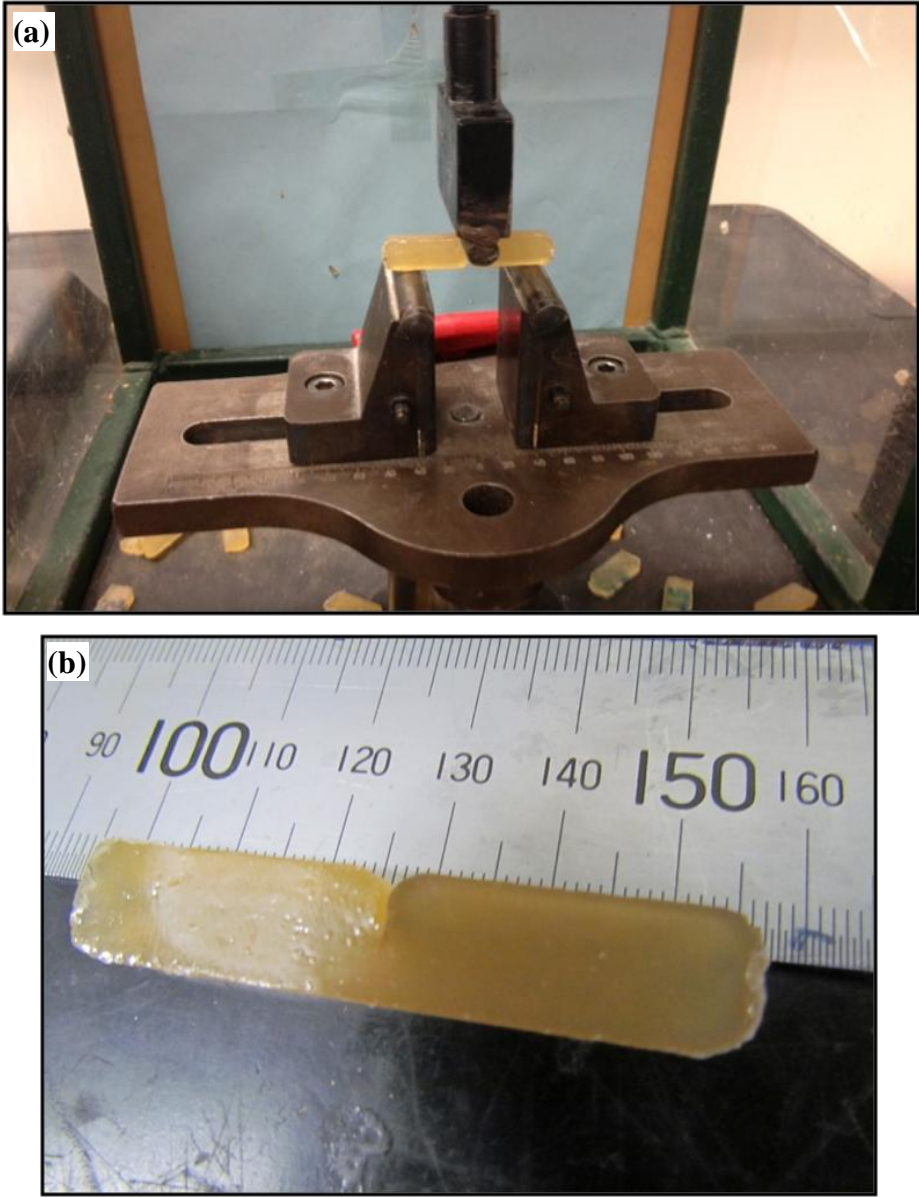


Figure 3.13: (a) Bending Rig and (b) SEN Bend Geometry Used in this Study

The determination of the energy per unit area of crack surface or the critical strain energy release rate (G_{Ic}) of neat UPE and its nanocomposites was determined using the following formula:

$$G_{Ic} = \frac{K_{Ic}^2}{E} \tag{3.5}$$

The above equation was applied as for the SENB geometry and plane stress conditions, where E is the obtained elastic modulus of a material at the same time and temperature conditions as the fracture test. The value of K_{Ic} is the same as that obtained from Equation 3.3. In terms of using CT geometry, the plain-strain fracture toughness test was measured under the opening mode as follows:

$$K_Q = \frac{P}{BW^{1/2}} \cdot f\left(\frac{a}{w}\right) \quad (3.6)$$

$$f\left(\frac{a}{w}\right) = \frac{\left(2 + \frac{a}{w}\right) \left\{ 0.886 + 4.64\left(\frac{a}{w}\right) - 13.32\left(\frac{a}{w}\right)^2 + 14.72\left(\frac{a}{w}\right)^3 - 5.6\left(\frac{a}{w}\right)^4 \right\}}{\left(1 - \frac{a}{w}\right)^{3/2}} \quad (3.7)$$

In order to determine a valid plain-strain fracture toughness, K_{Ic} , in accordance with this test method, the conditional K_Q obtained from Equation 3.6 with the use of P as the maximum load to be checked, with the satisfaction of specimen thickness used, against:

$$B, a, (w - a) > 2.5(K_Q / \sigma_y)^2 \quad (3.8)$$

where K_Q is the conditional or trial fracture toughness and σ_y is the yield strength (MPa).

After checking the conditional result, K_Q , against the size criteria following Equation 3.8, the calculated fracture toughness (K_{Ic}) was valid because the quantity of $2.5(K_Q / \sigma_y)^2$ was less than the values of specimen thickness (B), the crack length (a) and the ligament ($w - a$).

To determine the fracture toughness measurements of neat UPE and its different nanocomposites using CT geometry, the tension-testing clevis and set up of the test

fixture are shown in Figure 3.14. To start the experiment, both ends of the CT specimen (see Figure 3.14b) were held by special clevises and loaded through pins in order to provide rolling contact between the loading pins and the clevis holes. These holes were provided with small flats on the loading surfaces. Afterwards, the CT testing specimen was loaded at rate of 5 mm/min, as specified above.

The measurement of the critical strain energy release rate (G_{Ic}) of the materials was determined as for the CT specimen geometry and plane strain condition as follows:

$$G_{Ic} = \frac{K_{Ic}^2(1-\nu^2)}{E} \quad (3.9)$$

where E is the elastic modulus of material obtained at the same time and temperature conditions as the fracture test. The value of K_{Ic} is obtained from Equation 3.6, and ν is the Poisson's ratio of unsaturated polyester resin ($\nu = 0.38$).

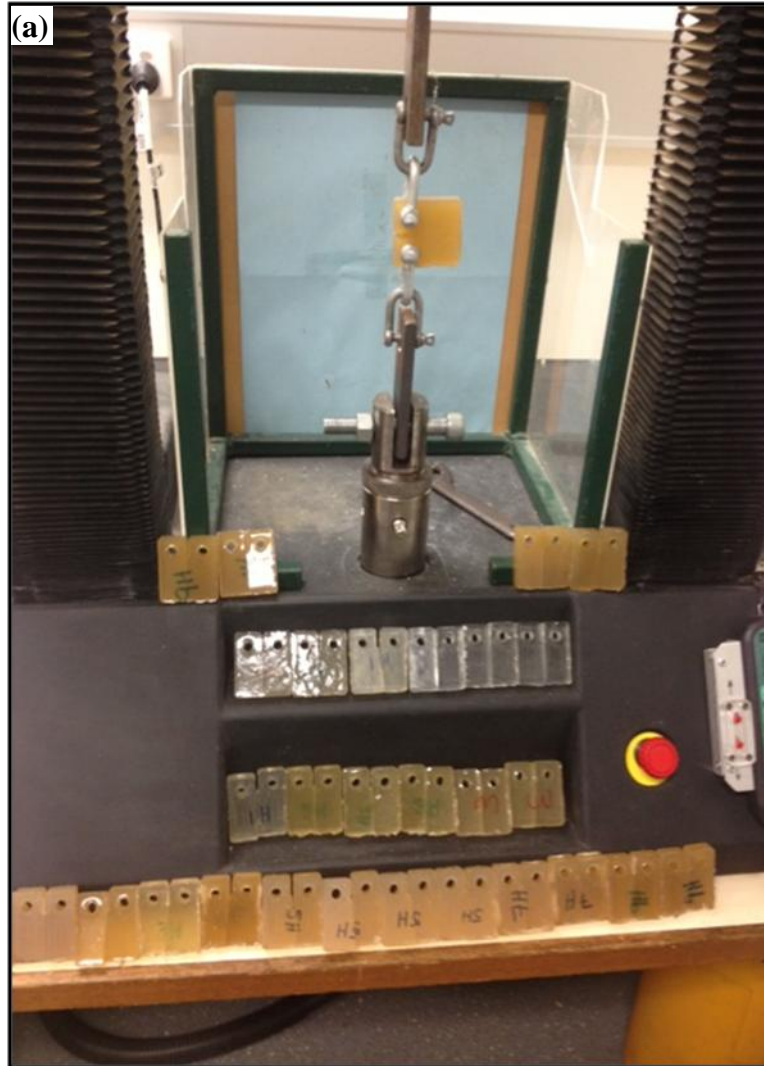


Figure 3.14: (a) Tension Test and (b) Clevis Design Used for CT

Chapter 4: Role of Silanised Halloysite on Morphological Characteristics

4.1 Role of Silane Treatment on Structure of Halloysite

4.1.1 Introduction

During silane treatment, hydrolysis and condensation reactions occur on bifunctional silane molecules $((RO)_3SiCH_2CH_2CH_2-X)$, leading to the generation of siloxane (-Si-O-Si-), which creates a bridge bond between the hydroxyl (OH) group on the silanised surface and the polymer matrix. The silanol groups change the hydrophilic nature of these surfaces to a hydrophobic nature (Mittal 2009). RO in silane molecules refers to a hydrolysable group that can be any one of three reactive groups on the silicon (methoxy, ethoxy or acetoxy), while the active X group is a functional organic group—either amino, methacryloxy or epoxy.

4.1.2 Structure of Halloysite Before and After Silanisation

Figure 4.1 shows the crystal structure of a halloysite nanotube, in which three different views (a-a, a-b and a-c) for the crystalline structure of halloysite are drawn. The tubular shape of halloysite contains two layers: tetrahedral and octahedral. On the outside layer of the tube, the Si atom is negatively charged, while on the inside layer, the Al atom carries a positive charge. In general, a halloysite tube is negatively charged because, at both ends of the tube, the O and OH atoms carry negative charges. The potential replacement of hydrophilic groups on inorganic fillers with hydrophobic groups during the grafting of HNT surfaces with the VTMS agent is crucial to reduce the number of charges on the surface, reduce the hydrophilic nature of the filler and improve the filler-matrix interface.

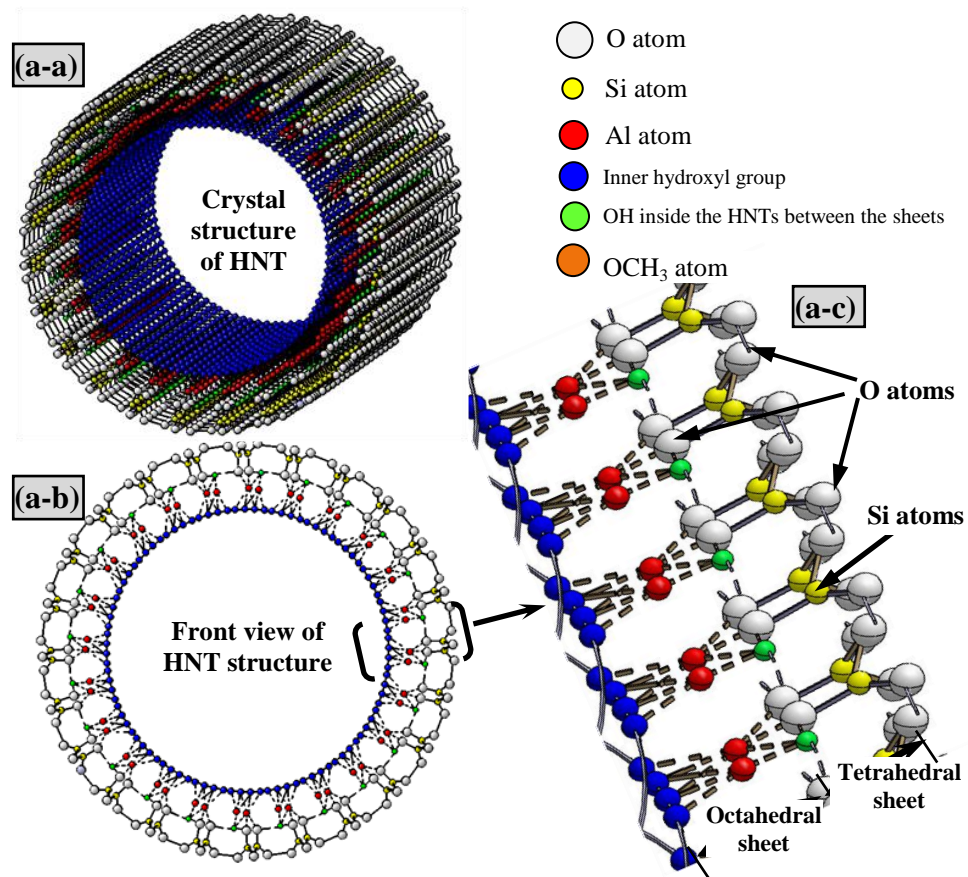


Figure 4.1: Schematic Presentation of the Crystalline Structure of Halloysite

The organosilane treatment on halloysite surface or silanisation mechanism between halloysite and silane molecules is schematically depicted in Figure 4.2, where several reactions occur. A hydrolysis reaction occurs between alkoxy groups on VTMS surface and water to form silanol groups. A condensation reaction occurs, in which the silanol groups react with the hydroxyl (OH⁻) groups on the HNT surface and form covalent siloxane bonds (Zhou et al. 2010). Then, the silanetriol latex (silsesquioxane networks) that is built on the functionalised HNT surface penetrates and bonds that surface with polymer chains through the interface reaction.

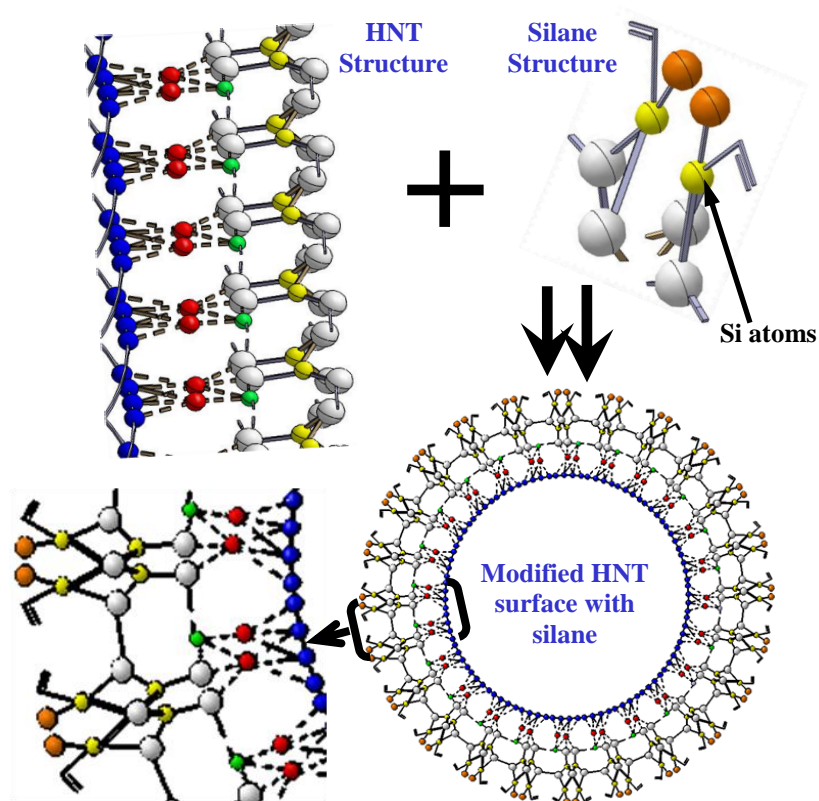


Figure 4.2: Schematic Presentation of Organosilane Treatment on Halloysite Surface

Figure 4.3 shows the interface reaction between the functionalised HNT and crosslinked UPE that can occur through either molecular entanglement, hydrogen bonding, van der Waals's interactions or covalent chemical bonding (MacMillan 1997). The compatibility between the inorganic particles and the organic polymer may be affected by different factors that consequently affect the mechanical properties of the nanocomposites (Plueddemann 1991; Schwartz 1997). These factors result from the choice of the right silane coupling agent or right organic functional group, concentration of coupling agent and matching reactivity or thermodynamic compatibility between silane and the polymer. The mechanism of bonding is also affected by the pH value at the interface (acidity or basicity), the activation energy needed to achieve covalent bond, the treatment time, the pre-treatment method (stirring or sonication) and the reaction temperature.

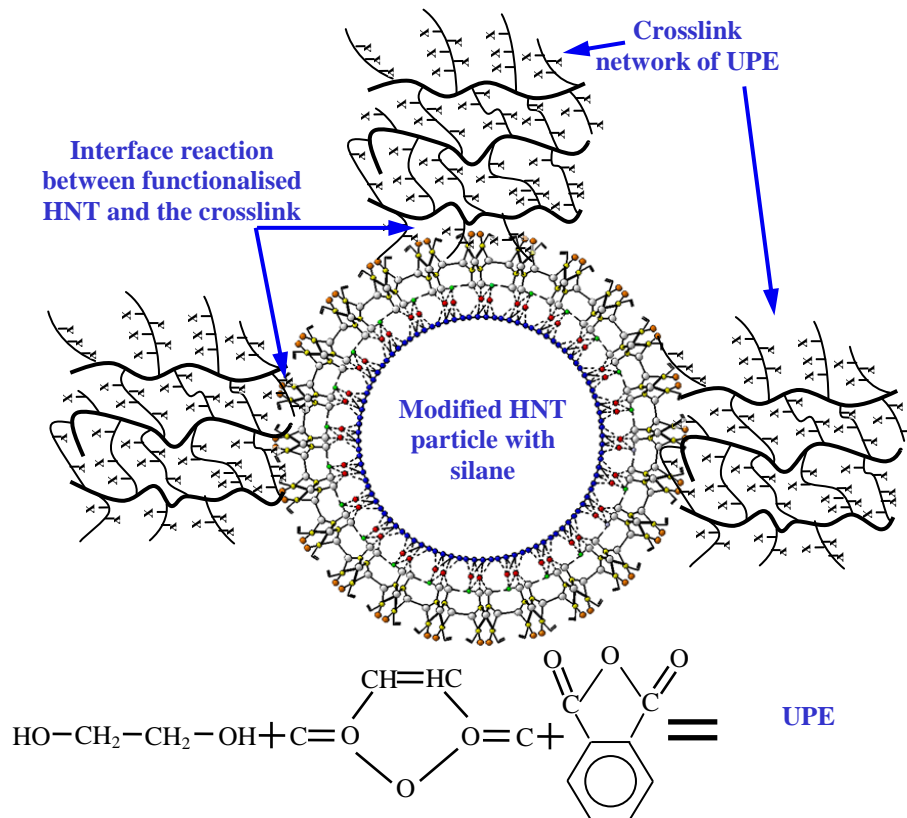


Figure 4.3: Schematic Presentation of the Interface Interaction between HNT Particle and UPE Polymer

4.2 Characterisation of Nanocomposite Morphology

4.2.1 TEM

Typical TEM images of halloysite loose powders are shown in Figure 4.4 (a to d). Despite a low density of hydroxyl groups on the surface of the halloysite, skewed-like agglomerates creating long unidirectional clusters are displayed in the morphology of untreated halloysite (see Figure 4.4a). Curved and random closely packed particles are also observed in the structure (Figure 4.4d). The halloysite tubes, to some extent, seem to have a hollow-tubular geometry that is similar in shape to MWCNTs (Ye et al. 2007). The average length of the tube is around 200 nm (0.2 μm), with an outside diameter (OD) of 40 nm and an inside diameter (ID) less than 25 nm. Hence, the aspect ratio of the tubes (length-to-diameter, L/D) is in the range of five to eight. In contrast, the TEM observations of s-HNT loose powder (Figures 4.5a and b) show that the silanised tubes are individually separated, are well dispersed and have no skewed clusters, as the untreated do.

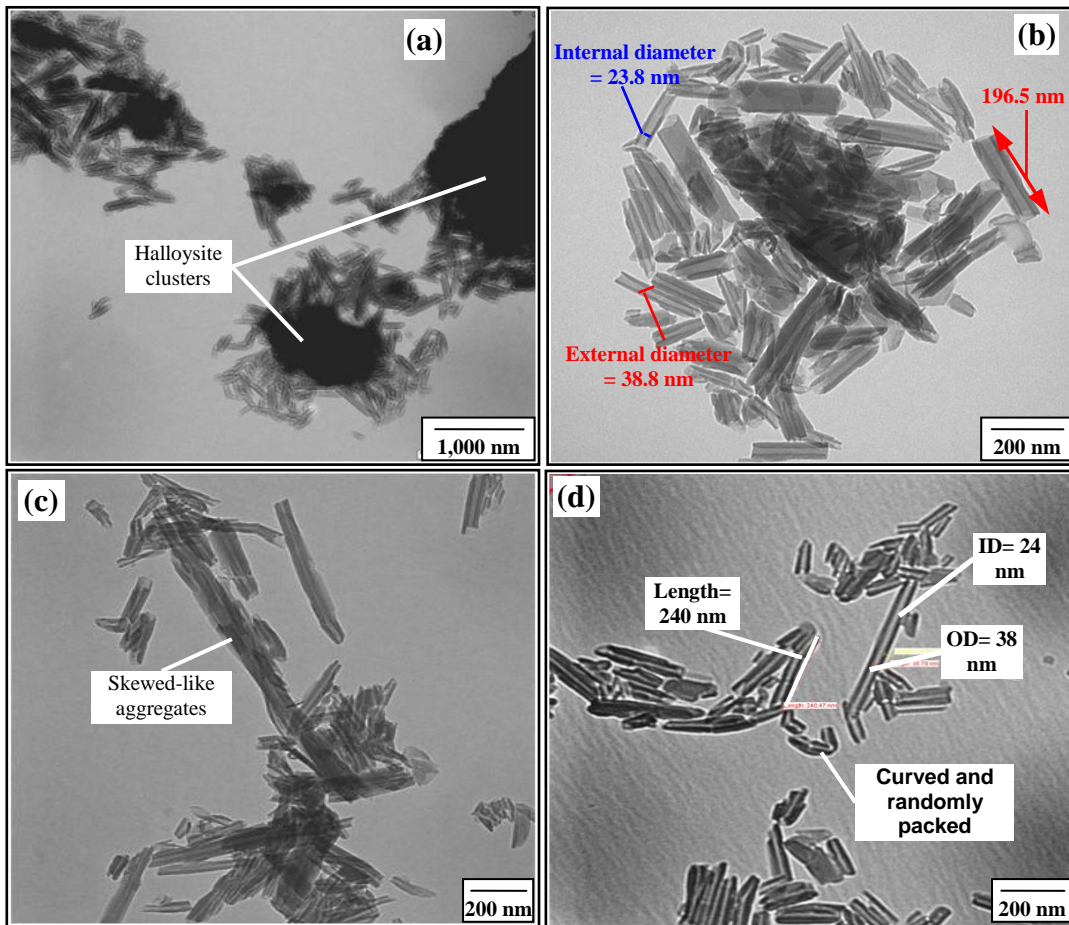


Figure 4.4: TEM Micrographs of Untreated Halloysite Nanotubes (Loose Powders)

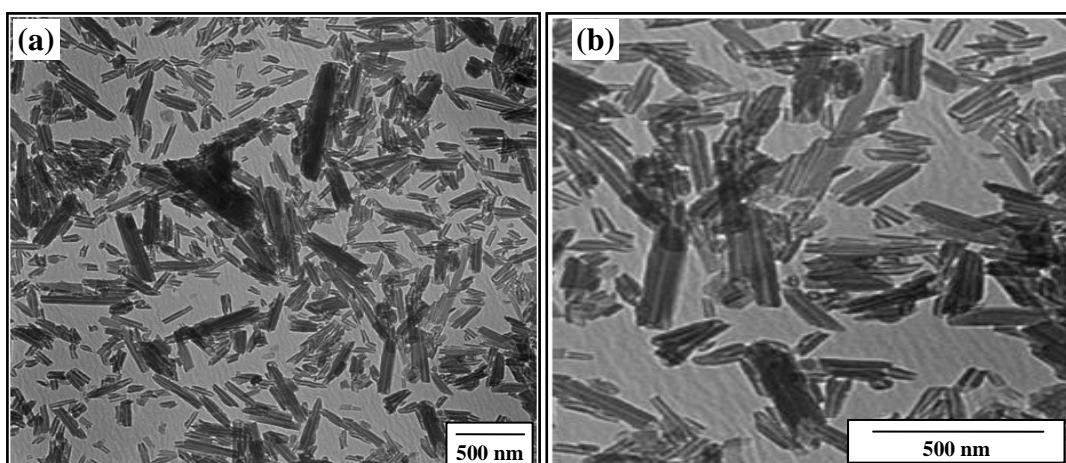


Figure 4.5: TEM Micrographs of s-HNT (Loose Powders)

For a visual and qualitative assessment of the morphology of the UPE nanocomposite, representative TEM micrographs with low magnification of UPE/1% HNT, UPE/3% HNT and UPE/1% s-HNT and UPE/3% s-HNT nanocomposites are shown in Figure 4.6. Large tactoids of HNT formed in the cured UPE nanocomposites can be seen in Figures 4.6a and b, indicating poor HNT dispersion. The s-HNT particles demonstrate a decreased tactoid size with an increased density of materials randomly dispersed per unit area of the image (see Figures 4.6A and B).

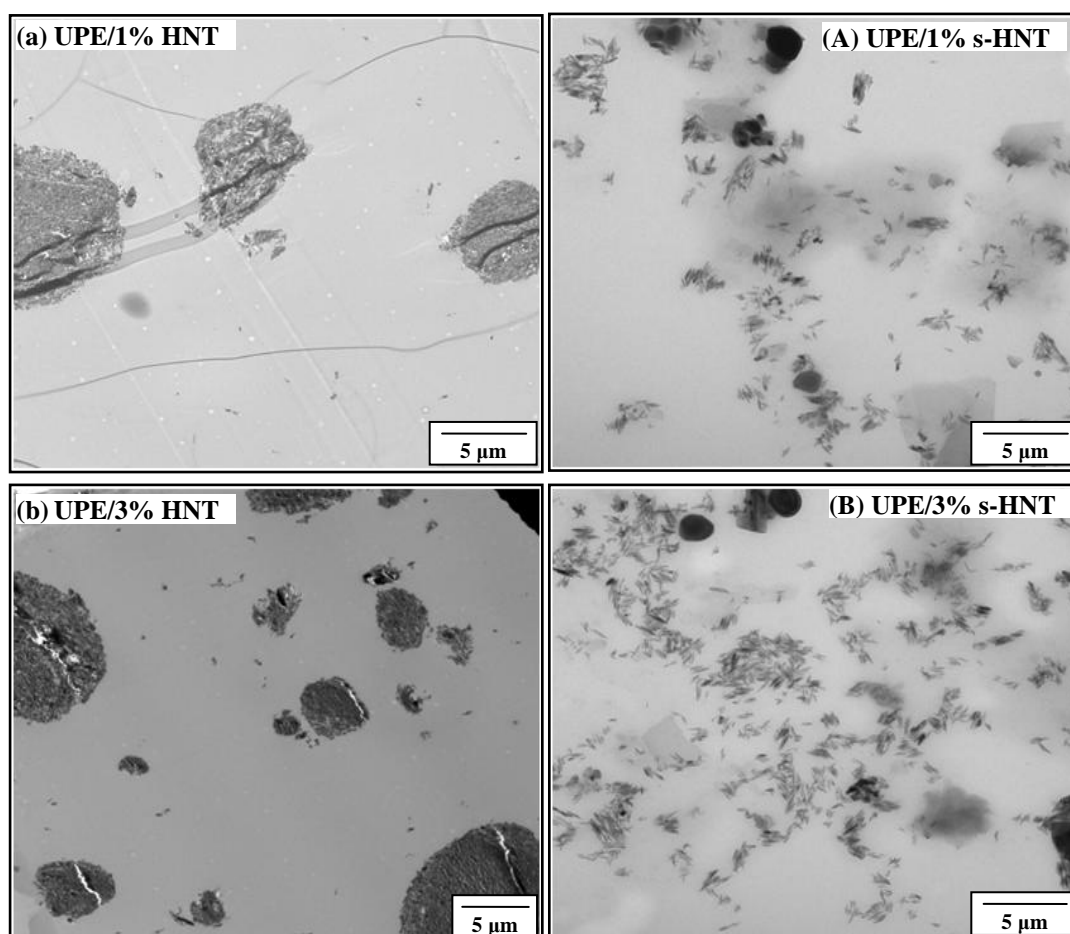
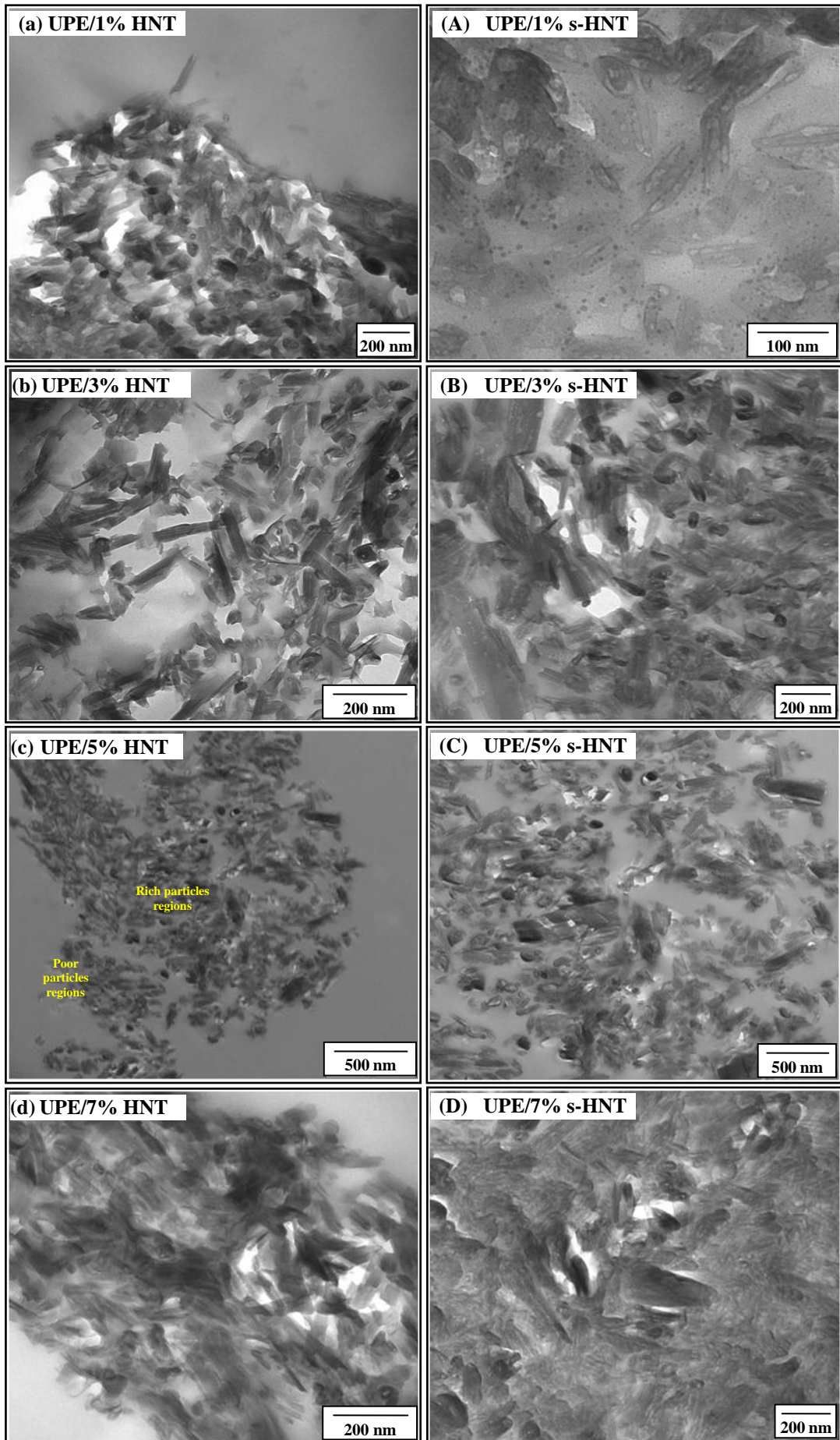


Figure 4.6: TEM Images at Low Magnification of: (a, b) Cured UPE/HNT and (A, B) UPE/s-HNT Nanocomposites

Another observation that can be seen in Figures 4.6A and B is that the lengths of functionalised halloysite nanotubes seem to be shorter (broken) and their aspect ratios are lower than that for their un-functionalised counterparts, due to further preparation processes (Yudin et al. 2008).

The degree of particle dispersion in the polymer matrix was further examined by close observation with TEM of various sections for different UPE nanocomposites, as shown in Figure 4.7. There is uniform distribution of HNT and s-HNT particles over the whole sections of nanocomposites containing low weight fractions of halloysite (see Figures 4.7a, b and 4.7A, B). The structure of cured UPE/HNT nanocomposites is characterised by a variation of rich and poor regions—some regions are crowded with halloysites, while some regions do not have any, and there are more such regions with a further increase of halloysite content in the polymer matrix (see Figures 4.7a to e). This phenomenon is attributed to the curved and random closely packed particles in the structure and to the strong electrostatic force acting between the inorganic particles. The electrostatic force induces strong particle–particle interaction that would not be broken by the high-speed shearing force (mechanical mixing) used in this investigation. The role of grafting HNT with silane on the structural characteristics of the UPE/s-HNT composites is obvious (Figures 4.7 A to E) where particles are intercalated and non-uniformly dispersed, without entanglement through the UPE matrix, regardless of the halloysite content.

At higher incorporation—5 wt%, 7 wt% and 9 wt%—of HNT or s-HNT into the UPE matrix (Figures 4.7 c to e and Figures 4.7 C to E), the particles do not exhibit the same uniformity as at low halloysite contents, where some regions are completely free of nanoparticles, while others have individual sheets of particles separated by UPE molecules that then make an intercalated structure. That may be a result of insufficient mixing because the high shear process is dependent on time and mixing-shear force, while all nanocomposite systems were prepared following an identical mixing time.



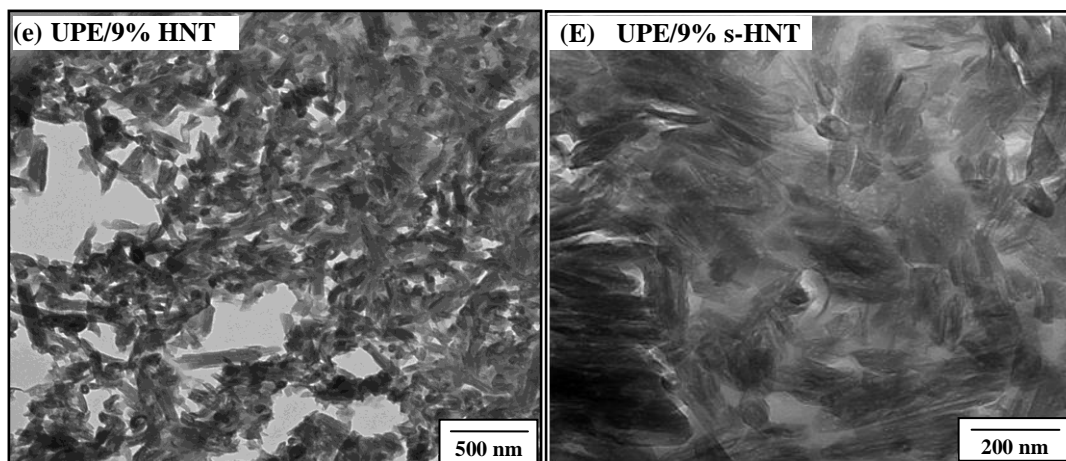


Figure 4.7: TEM Micrographs of: (a–e) UPE-based Different Pristine HNT Nanocomposites and (A–E) UPE-based Different s-HNT Nanocomposites

At higher halloysite contents, the intercalation of the monomer into the space between halloysite particles is shorted and the repulsive interaction potential between the particles is increased. As a result, the aggregation of particles also increases. Nevertheless, it is hard to make a decisive judgement regarding whether the use of high shear mixing is suitable for preparing halloysite nanocomposites, since halloysite neither tends to form aggregates, nor requires a higher shear force due to low hydroxyl on its outside surface. However, it can be assuredly suggested that high shear mixing is effectively applicable for nanocomposites with low filler contents, and is not effective for nanocomposites with high filler contents.

The silanised halloysite induces lower attractive potential among particles and higher repulsive potential between particle/polymer—that is, better particle/polymer interaction. In addition, the viscosity of used UPE resin is relatively low (288 cp) at 23°C, which can assist better particle dispersion due to the improved compatibility between halloysite and the polymer molecules. The compatibility between the particles and polymer chains is one of the most important factors influencing the state of dispersion in the nanocomposites. The nature and interactions of the components and affinity between the particles and polymer are also responsible for determining good particle distribution. The structural classification, state of particles' dispersion and other critical characteristics (such as physical, thermodynamic and mechanical) vary with each processing technique (Bhattacharya, Kamal & Guptaet 2008).

4.2.2 XRD

The morphology of nanocomposites was further investigated by x-ray spectra to characterise the particles' dispersion in the polymer matrix and identify the role of silane treatment on the crystalline structure of the UPE nanocomposites. The patterns of SAXS and WAXS for neat UPE, untreated HNT and silane-treated HNT loose powders were conducted as a function of diffraction angle (2θ), as shown in Figure 4.8.

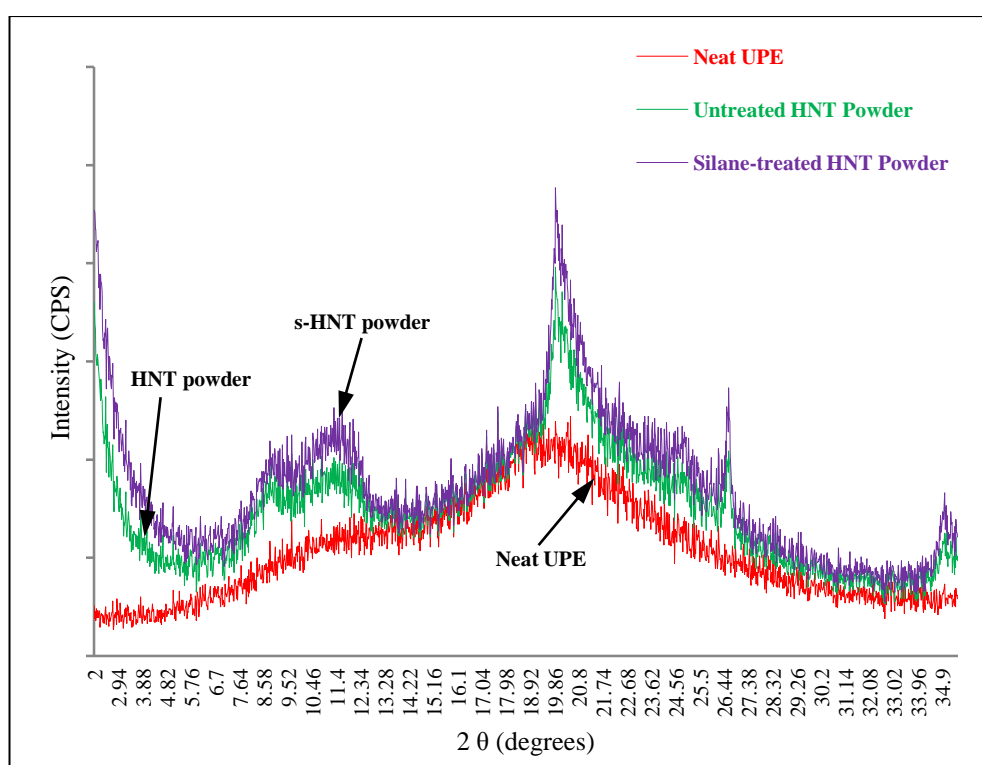


Figure 4.8: Comparison of X-ray Scattering Scans for Neat UPE, Untreated HNT and Silane-treated HNT Loose Tubes

The XRD pattern of neat UPE was considered the baseline diffraction pattern. The basal spacing (001) of HNT and s-HNT loose powders were approximately similar at 7.42 Å, based on a diffraction angle of $2\theta = 11.92^\circ$ and wavelength of Cu $K\alpha$ ($\lambda=1.54$ Å). The WAXS scans of HNT and s-HNT revealed a sharp basal reflection due to the random orientation of halloysite, because of a high alignment of the tactoids in the flow direction, or because a high alignment of the nanotubes within the tactoids.

The XRD spectra of neat UPE and different UPE/as-received untreated HNT nanocomposites are shown in Figure 4.9. Short reflections presented at $2\theta \approx 2.78^\circ$ in the XRD patterns of all UPE/HNT composites corresponded with the interlayer spacing of un-intercalated halloysite ($d_{001} = 14.7\text{\AA}$). These reflections were absent in the XRD patterns of the neat UPE, or HNT and s-HNT loose powders (Figure 4.8).

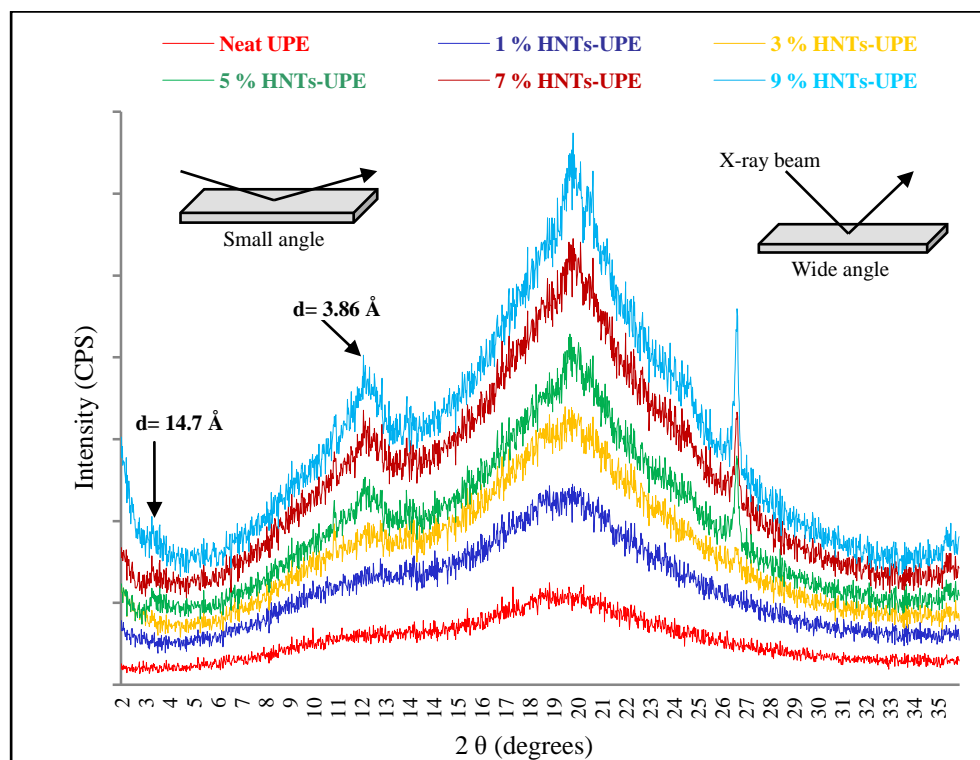


Figure 4.9: X-ray Scattering Scans for Neat UPE and Different UPE/HNT Nanocomposites

In Figure 4.9, the d_{001} peak increases with increasing halloysite content, which may reflect the presence of large halloysite tactoids in the morphology of these nanocomposites. In addition, two characteristic peaks in the x-ray diffraction analysis—one at the diffraction angle, $2\theta = 11.74^\circ$, and the other at the $2\theta = 26.42^\circ$ —appear in the XRD patterns for all UPE nanocomposites and are sharper at a high halloysite content. This also indicates the appearance of isolated halloysite bundle clusters in the UPE matrix. A free-radical copolymerisation between unsaturated polyester and styrene is obviously caused by noticeable volume shrinkage of the final product. This high degree of shrinkage (about seven to 10%) sometimes tends to cause severe surface quality and dimension control problems during manufacturing by generating a curvature (meniscus) in the specimens that

results in large separation between the incident beam and the scattered radiation that would possibly stand behind these sharp reflections in the XRD patterns. The basal spacing observed in the UPE/HNT nanocomposites is inconsistent with recent experimental investigations in which the morphology of halloysite nanocomposites was obtained (Deng, Zhang & Ye 2009; Barrientos-Ramirez et al. 2011).

The incorporation of s-HNT into the neat UPE matrix (Figure 4.10) shows, to a large extent, the same lots of halos (diffraction peaks) in the XRD patterns of all UPE/s-HNT nanocomposites as UPE/HNT nanocomposites, indicating a high degree of nanotube orientation (Garea et al. 2011). Inserting either HNT or s-HNT particles into the UPE matrix changes its crystalline structure, lessens the degree of exfoliation and increases the frequency of peaks with higher loadings of halloysite particles. In such cases, the diffraction peaks could be categorised into sharper peaks that represent poor dispersion of particles, lower peaks that represent intercalated structure, and flat or no peaks that represent an exfoliated structure.

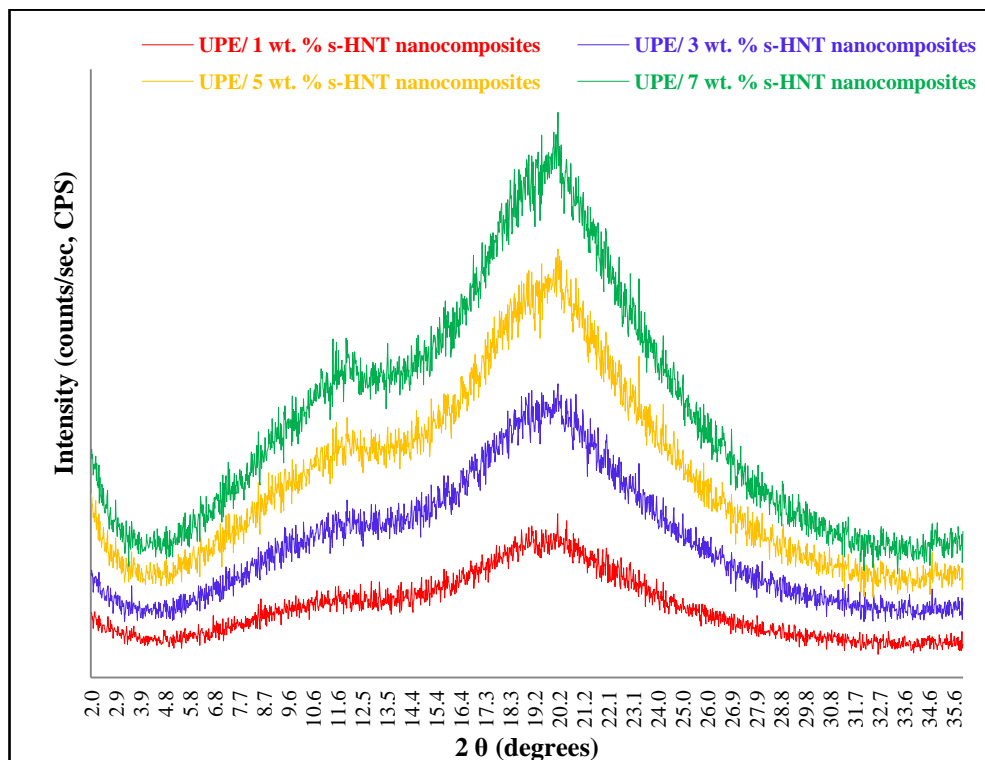


Figure 4.10: X-ray Scattering Scans of Different UPE/Silane-treated HNT Nanocomposites

To better understand the role of HNT or s-HNT on the interlayer spacing of the UPE nanocomposites, the x-ray intensity of UPE/3% HNT and UPE/3% s-HNT nanocomposites versus neat UPE is compared in Figure 4.11.

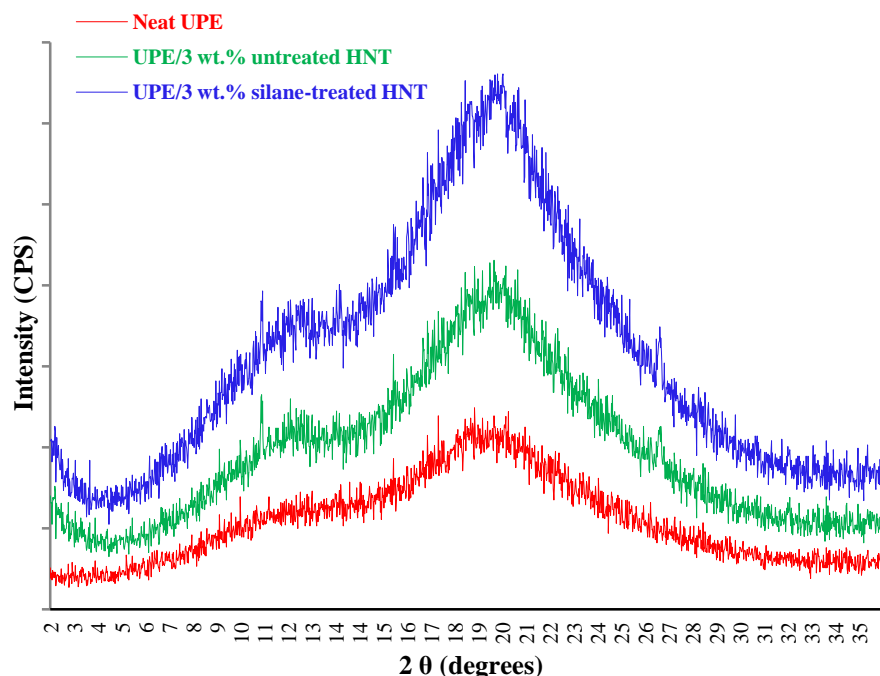


Figure 4.11: Comparison of X-ray Scattering Scans of Neat UPE, UPE/3 wt% HNT and UPE/3 wt% s-HNT Nanocomposites

The diffraction peaks in the intensity of UPE/3% HNT and UPE/3% s-HNT nanocomposites were approximately identical, with each staying in the same position (diffraction angles) and having no significant difference in the interlayer spacing [d_{001}] or [d_{002}] when silane treatment was done. This similarity means that the crystalline structure of HNT particles does not change when they are modified with silane agent, indicating that most of silanol occurs on the edge hydroxyl sites or on the external surface of the particle, rather than on the interlayer surface (Joo et al. 2008; Spencer et al. 2011). A more uniform structure of s-HNT particles (Figures 4.7 A to E) does not necessarily change the XRD patterns of the nanocomposite. It has been similarly found that the crystalline structure does not change and the basal spacing does not increase in halloysite tactoids (Mu, Zhao & Liu 2008) or clay tactoids (Ianchis et al. 2012) after modifying them with 2-bromoisobutyric acid or silylation reaction, respectively. This is attributed to the functional alkoxy silane reacting by the edge covalent bonding only, rather than between the nanofiller layers.

4.2.3 SEM and EDS Analysis

The role of organosilane treatment on the halloysite surface was inspected by a SEM examination. The surface of nonreactive HNT (Figure 4.12a) appears smoother than that which was modified with silane (Figure 4.12b).

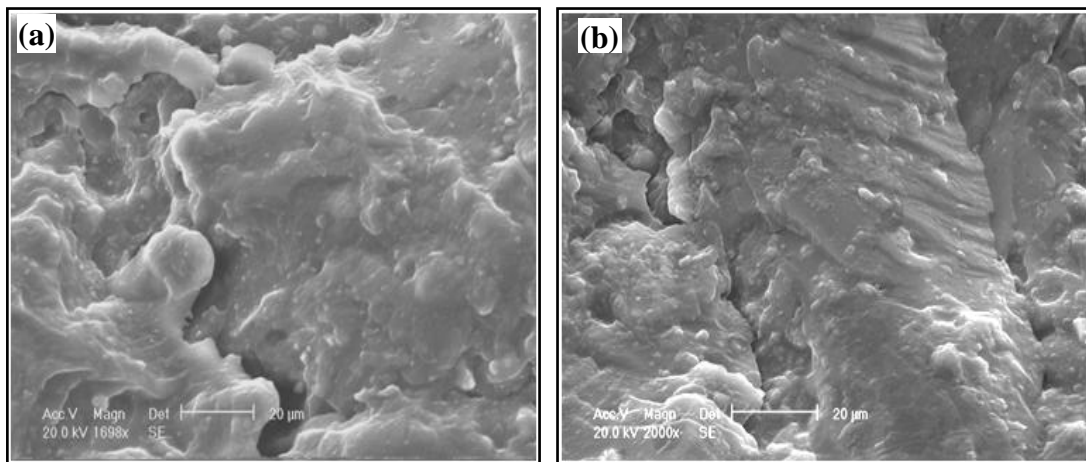


Figure 4.12: SEM Images Showing the Difference between: (a) UPE/3 Wt% Untreated HNT Surface and (b) UPE/3 Wt% S-HNT Nanocomposites Surface

The rough surface of silanised halloysite nanocomposite is likely due to the presence of multiple interfacial bonding sites on the modified surface, which induce better adhesion with the polymer chains and better load transfer across the nanotube/polymer interface (Unnikrishnan & Reddy 2012). The presence of a multilayered structure on the modified surface is probably due either to the presence of water (released by physical adsorption of inorganic substrate through direct condensation) or the presence of hydrolysable groups on the silane surface (Rothon 2003). Such groups can form a thick oxide interfacial bridge between particles-silane-polymer (Neyman, Dillard & Dillard 2006).

EDS analysis was conducted to identify the chemical composition of halloysite before and after silanisation over the neat UPE. The elemental analysis was performed on tensile-fractured surface of UPE/5% HNT and UPE/5% s-HNT nanocomposites using SEM coupled with an EDS x-ray system. Figure 4.13 illustrates the quantity of the elements presented on the HNT. Figure 4.13a shows the SEM image of a tensile-fractured surface for the UPE/5% HNT nanocomposite.

Figure 4.13b shows the element analysis of the major phase in the SEM image, showing the UPE resin. Figure 4.13c shows the chemical composition of the HNT particles.

Based on the scanning electron image and the elemental analysis results, the interaction (affinity) of HNT nanoparticles to the UPE resin seems to be relatively reasonable. In the major phase, there was a characteristic peak of C, corresponding to the polymer matrix, associated with a short fluctuation of Al and Si, corresponding to the presence of halloysite in the matrix. However, several elements—Ca, Na and O—besides Al and Si appeared in the HNT composition, but disappeared in the major phase. The sharp peaks of Pt represent the sputter coating of surface with platinum before completing the SEM analysis.

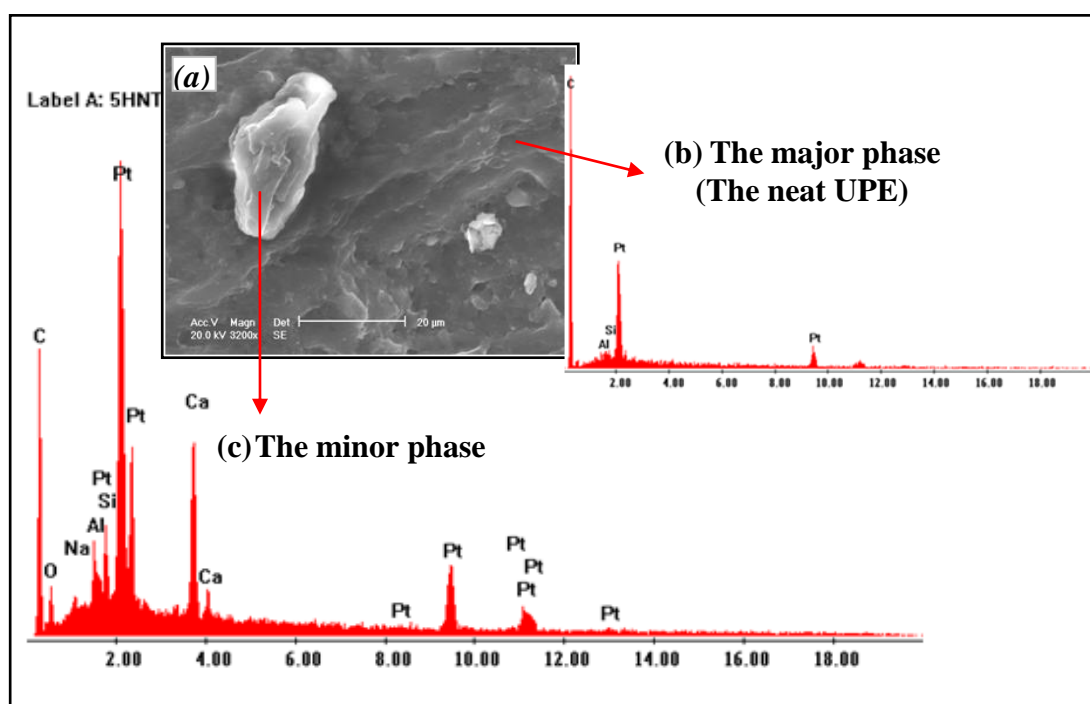


Figure 4.13: SEM Image of UPE/5% HNT Nanocomposites Showing: (a) Large Halloysite Clusters and (b) the EDX Elemental Analysis Data for Different Spots in the Nanocomposites

The EDS analysis of UPE/s-HNT nanocomposite (Figure 4.14) almost demonstrated the same fluctuations of elements as per the HNT particles. The indistinctive difference between the EDS analysis for HNT and s-HNT particles is, in the latter particles, that the fluctuations of Na, Al, Si, and Ca seem to be a little shorter and the

fluctuations of C higher than in the former particles. This phenomenon can either indicate a better interaction between the halloysite and the UPE matrix particle, or the s-HNT surface covered by multilayer silane structure, which may shorten the fluctuations of the elements.

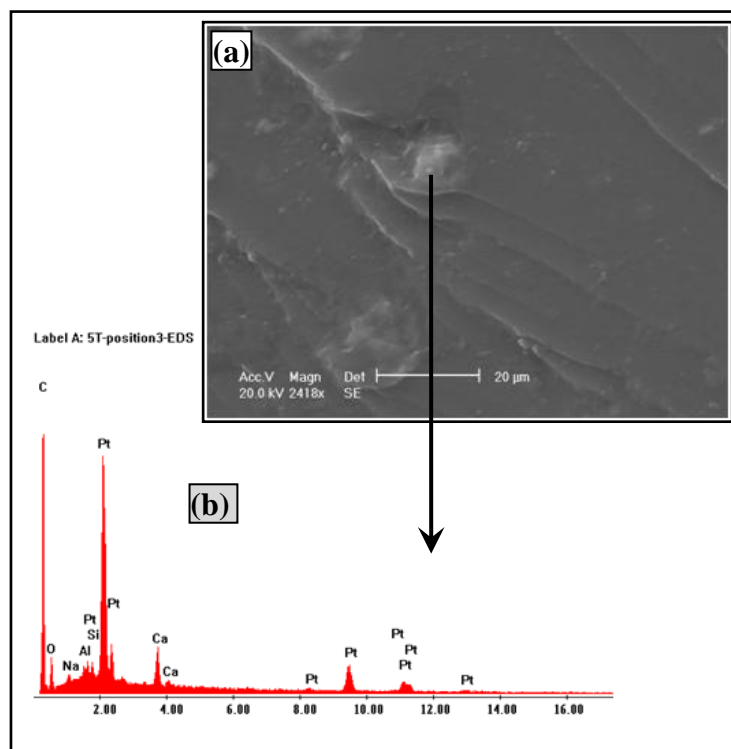


Figure 4.14: (a) SEM Image of UPE/5 wt% s-HNT Nanocomposite and (b) its EDX Elemental Analysis

4.3 FT-IR Spectra

FT-IR spectroscopy defined by its wavelength is normally used to characterise the molecular structures of polymers, and indicate the vibrational states of chemical bonds obtained after the curing process (Young & Lovell 2011). The FT-IR spectra of neat UPE, HNT and s-HNT powders, plus different UPE/HNT nanocomposites, are shown in Figure 4.15, and the assignment of IR wavenumbers is listed in Table 4.1.

The neat UPE spectrum (Figure 4.15a) shows the aromatic O-H stretching band of UPE chains at $3,457.7 \text{ cm}^{-1}$ and the carbonyl C=O stretching vibration at $1,729 \text{ cm}^{-1}$. The characteristic peaks of the C-O carboxylic acids stretch also appeared within the

UPE spectrum (Lu, Xu & Liu 2011). In the spectrum of HNT powder (Figure 4.15a), the stretch vibration of -OH groups appeared at $3,533\text{ cm}^{-1}$ and the Si-O-Si asymmetric stretching appeared at $1,085\text{ cm}^{-1}$. This conforms with the findings of Pasbakhsh et al. (2010) and Garea et al. (2011). The Si-O-Si asymmetric deformation occurred at $1,030\text{ cm}^{-1}$, while the Si-O-Si skeletal stretching and Si $(\text{CH}_3)_2$ groups occurred around 913 and 744 cm^{-1} , respectively. The Si CH_3 group appeared at $1,284\text{ cm}^{-1}$ and the Si-H group stretching appeared as a small peak around $2,052\text{ cm}^{-1}$ (Mark, Allcock & West 2005).

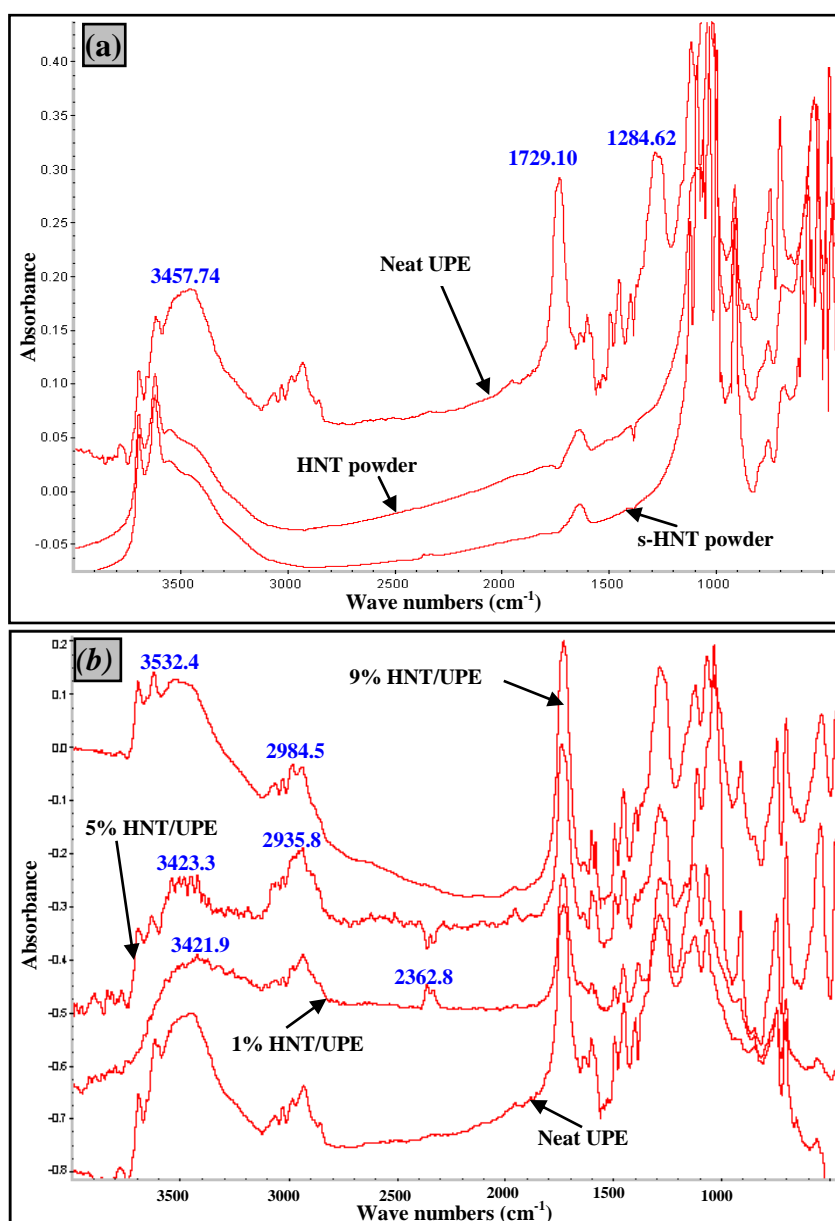


Figure 4.15: FT-IR Spectra of: (a) Neat UPE, HNT and s-HNT Powders and (b) Different UPE/Untreated HNT Nanocomposites

Table 4.1: Assignment of FT-IR Absorption Bands of UPE/HNT and UPE/s-HNT Nanocomposites

Assignments	Absorption band (cm ⁻¹)		
	Neat UPE	UPE/HNT	UPE/s-HNT
O-H absorption stretch	3,704	3,698	3,698
C=C absorption aromatic rings	3,615	3,624	3,626
Aromatic C-H band stretching	3,458	3,532	3,535
Aliphatic C-H bend	2,962	2,984	2,983
C triple bond absorption	-	2,120	2,120
Si-H stretching	-	2,051	2,052
Carbonyl C=O stretching vibration	1,729	1,729	1,731
C-H bending vibration	1,439	1,453	1,453
C-H absorption (methyl group)	-	1,395	1,396
C-O carboxylic acids stretch peaks	1,284	1,285	1,286
C-H out-of-plane bending	700	743	744
Si-O-Si asymmetric stretching	-	1,066	1,085
Si-O-Si asymmetric deformation	-	1,030	1,031
Si-O-Si skeletal stretching	912	913	913
Si (CH ₃) ₂	-	743	744

The IR spectrum of s-HNT powder (Figure 4.15a) shows that the characteristic Si-O-Si absorption band occurred over a wide range of wave numbers in the region of 701 to 1,085 cm⁻¹. Within the silanisation process, hydrolysis and condensation reactions occur on bifunctional silane molecules ((RO)₃SiCH₂CH₂CH₂-X), leading to the generation of siloxane (-Si-O-Si-), which creates a bridge bond between the hydroxyl (OH) group on the silanised surface. The silanol groups change the hydrophilic nature of these surfaces to a hydrophobic nature (Mittal 2009). The intensity of absorption in the IR spectrum is related to the change in dipole that occurs during the vibration. The vibrations lead to significant change in dipole (for example, C=O stretch) and cause more intense absorption than the vibrations causing a modest or no change in dipole (for example, C=C symmetric).

The aromatic rings characteristic of C=C absorption appeared at 3,625 cm⁻¹, and this was confirmed by the existing peak at 1,600 cm⁻¹. The rounded peaks of hydrogen bond stretches (O-H absorption) appeared in the region of 3,200 to 3,600 cm⁻¹. The characteristic absorption bands of the C-H group occurred at 2,937.9 cm⁻¹, and the symmetric band at 2,983.5 cm⁻¹ was due to aliphatic hydrogen stretching. Figure 4.16 shows the characteristic peaks that appeared in different UPE/HNT and UPE/s-HNT nanocomposites. They were as follows: the carbonyl absorption (C=O) ester peaked at 1,729 cm⁻¹; the C-H bending at 1,453 cm⁻¹; the rounded peaks (such as O-H peaks for the C-O ester) were in the range of 1,000 to 1,280 cm⁻¹; and the C-H out of plane

and the asymmetric C-H stretch were at 744 and 701 cm^{-1} , respectively. The C-H absorption of the methyl group (CH_3 symmetric deformation) appeared at 1,396.8 cm^{-1} (Roy & Bhowmick 2010; Zhou et al. 2010). Velasco-Santos et al. (2002) found that different organo-functional groups formed and attached to the silanised halloysite, such as the Si-O-C bonds. These bonds enhanced the compatibility between the chemically modified surface and the polymer matrix.

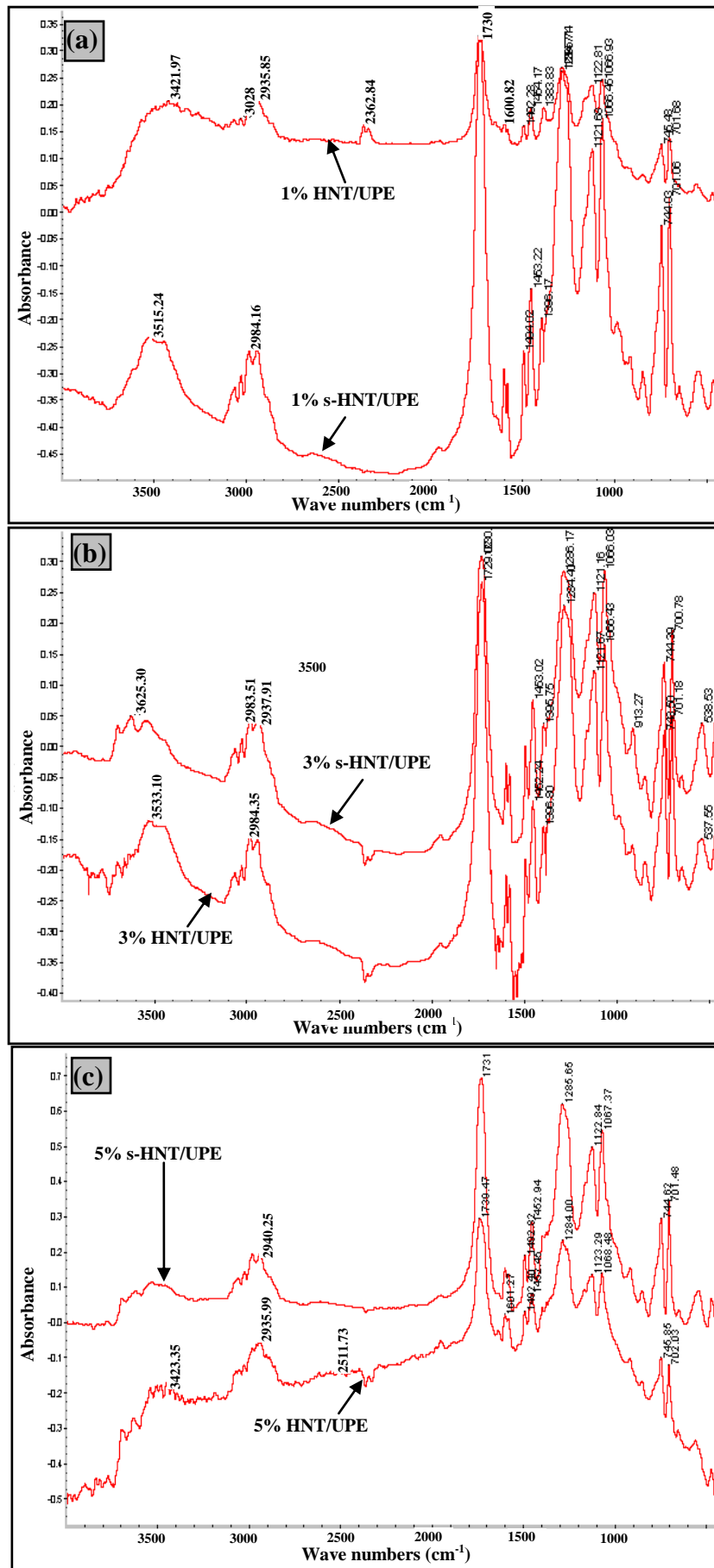


Figure 4.16: Comparison of FT-IR Spectres between Different UPE/HNT and UPE/s-HNT Nanocomposites

4.4 Summary

1. Large tactoids of HNT particles formed in the cured UPE nanocomposites, indicating poor dispersion, particularly at higher incorporation (> 5 wt%) of HNT into the UPE matrix. The s-HNT particles demonstrated a decreased tactoid size with an increased density of material randomly dispersed in the structure. However, the lengths of s-HNT particles seemed to be shorter and their aspect ratios lower than that of their HNT counterparts, due to further preparation processes.
2. The structure of cured UPE/HNT nanocomposites was characterised by a variation of rich and poor regions—some regions were crowded with halloysite, while some regions did not have any, and there were more such poor regions with a further increase of HNT content in the UPE matrix. The role of grafting HNT with silane on the structural characteristics of UPE/s-HNT composites was obvious where particles were intercalated and well dispersed without entanglement through the UPE matrix, regardless of the halloysite content.
3. The silane treatment on halloysite induced lower attractive potential among the particles and higher repulsive potential between the particle/polymer. This resulted in better particle/polymer interaction. The nature and interactions of the components and affinity between the particles and the polymer were also responsible for determining a good particle distribution.
4. Inserting HNT or s-HNT particles into the UPE matrix changed its crystalline structure. Short reflections presented in the XRD patterns of all UPE/HNT composites, corresponding to the interlayer spacing of un-intercalated halloysite ($d_{001} = 14.7\text{\AA}$). The d_{001} peak intensity increased with increasing HNT content, which may reflect the presence of large halloysite tactoids in the morphology of the UPE nanocomposites. Regardless, the additional percentages of s-HNT particles in the neat UPE matrix and the diffraction peaks in the XRD patterns of UPE/s-HNT showed nearly the same as those for the UPE/HNT nanocomposites, indicating a high degree of nanotube orientation.

5. The spectra of FT-IR for neat UPE, different UPE/HNT and UPE/s-HNT nanocomposites exhibited that the addition of HNT or s-HNT noticeably changed the molecular structures of the cured nanocomposites. The role of functionalising halloysite with silane on the vibrational states of chemical bonds was insignificant, with most assignments of the absorption bands in the UPE/s-HNT nanocomposites occurring at closer wave numbers to those for the UPE/HNT nanocomposites.

Chapter 5: Role of Silanised Halloysite on Thermo, Thermodynamic and Mechanical Properties

5.1 Background

PNCs have become one of the most interesting areas in the field of nanotechnology due to their better mechanical and thermal properties with the incorporation of a small amount of nanoparticles into the polymer matrix, compared to neat polymers or conventional particulate/composites. The main reason for this feature is the smaller dimension sizes of nanoparticles, which leads to smaller sized flaws, higher surface-to-volume ratios and a large area of interface between reinforcements and the matrix, which induces good stress transfer from the polymer to the particles (Bhattacharya, Kamal & Gupta et al. 2008; Young & Lovell 2011).

UPE resins are one of the most commonly used thermosets in different industrial applications due to their good mechanical properties, low density and easy processing (Pascault et al. 2002; Barbero 2011). However, a high crosslink density of the UPE resins and their long-chain molecules formed by copolymerisation of a monomer with a prepolymer that has several C=C bonds during the curing process, makes them stiff and brittle (Osswald & Hernández-Ortiz 2006; Young & Lovell 2011). Inserting nanosized fillers as a second phase into single-phase thermosets yields crosslink density and improves mechanical properties without compromising toughness or increasing brittleness. Improvement in strength, stiffness and yielding density was thought to be due either to the confinement effects of interrupting the high crosslink density of thermosets, or to the preferential interaction of the crosslinking agent with the particle surface (Paul & Robeson 2008; Srivastava & Koratkar 2010).

Different nanosized particles were used to modify thermosetting UPE matrices, such as nanoclay (Beheshty, Vafayan & Poorabdollah 2009; Chieruzzi, Miliozzi & Kenny 2013), TiO₂ (Omriani, Afsar & Safarpour 2010; Evora & Shukla 2003), SWCNT and MWCNT (Vera-Agullo et al. 2009; Seyhan et al. 2007; Monti et al. 2011), silica

(Zhang & Xie 2011), alumina (Baskaran, Sarojadevi & Vijayakumar 2011) and HNTs (Deng et al. 2008; Ye et al. 2011). As a result, Beheshty, Vafayan and Poorabdollah (2009) found that inserting 3 wt% of organically modified clay into the UPE nanocomposites improved their flexural and storage modulus by 31.5% and 30.2%, respectively. In addition, Chieruzzi, Miliozzi and Kenny (2013) revealed that inserting 5 wt% MMT improved the Young's modulus of the UPE/clay nanocomposite by 25% due to the disorderly exfoliated structure of nanoparticles and good adhesion between the nanoclay surfaces and UPE matrix.

Further, silanisation chemical treatment was implemented on different inorganic particles' surface to improve their interfacial adhesion (bonding) with polymer molecules and obtain better alignment and distribution of particles (Guo et al. 2009; Spencer et al. 2011; Deng, Zhang & Ye 2009). With the use of silanised halloysite particles, Deng, Zhang and Ye (2009) revealed that a uniform dispersion structure with enhanced mechanical properties of epoxy nanocomposites can be obtained. Similarly, Guo et al. (2009) obtained a homogenous nanostructure with higher mechanical properties of polyamide-6 composite filled by silanised halloysite particles.

This chapter presents the effects of HNT and s-HNT on the thermo, thermodynamic and mechanical properties of UPE-based HNT, or s-HNT nanocomposites. The elastic modulus was predicted using different mathematical models to further understand the correlation between the structure and mechanical performance. The role of s-HNT on the morphology of tensile-fractured surfaces of the UPE nanocomposites was identified using SEM examination. The related experimental procedure was described in detail in Chapter 3.

5.2 Results and Discussion

5.2.1 TGA

TGA of neat UPE and its different nanocomposites as a function of changes in temperatures (25 to 600°C at 10°C/min) was conducted to detect the thermal stability and assess the amount of organic matter exchanged on the halloysite surface during

silane treatment. Figure 5.1 shows the TGA curves for unfilled UPE and UPE nanocomposites, filled individually with 3% HNT and 3% s-HNT. Compared to unfilled UPE, no significant change in the thermal stability of UPE nanocomposites occurred after introducing HNT or s-HNT particles (see Figure 5.1). However, the s-HNT particles delayed the thermal degradation of nanocomposites by 3°C, where the temperature of 5% weight loss ($T_{5wt\%}$) of UPE/3% s-HNT was higher by 3°C than that of UPE/3% HNT (see Figure 5.1b). The occurrence of $T_{5wt\%}$ at 438°C for UPE/3% s-HNT and 435°C for UPE/3% HNT was due either to loss of adsorbed water on the halloysite’s surface or structural dehydroxylation and formation of new phases. Similarly, the decomposition temperatures at maximum weight loss rate ($T_{85wt\%}$) for neat UPE, UPE/3% HNT and UPE/3% s-HNT nanocomposites occurred at 413°C, 419°C and 422°C, respectively.

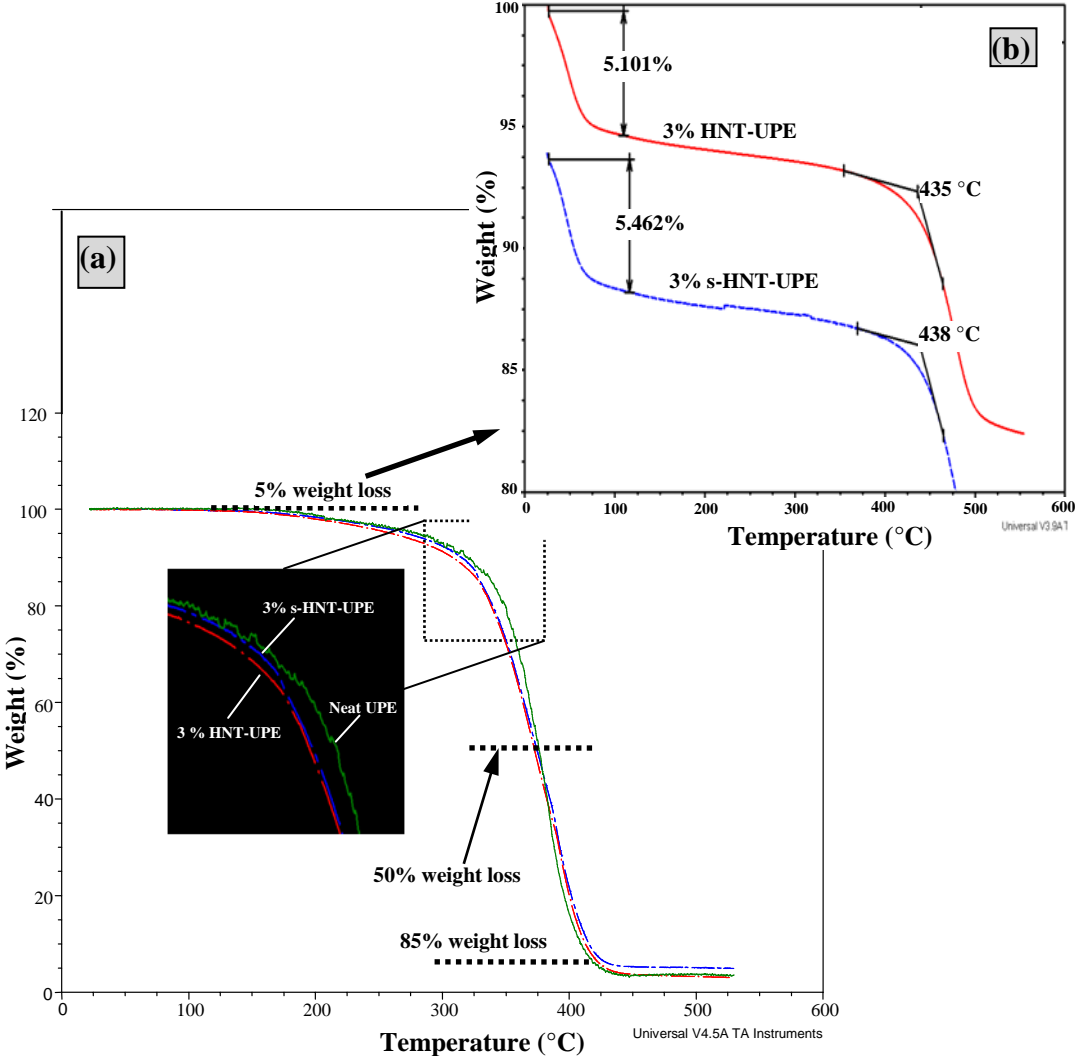


Figure 5.1: (a) TGA of Neat UPE, UPE/3% HNT and UPE/3% s-HNT Nanocomposites and (b) Close-up Image Showing 5% Weight Loss

5.2.2 Thermodynamic Properties

5.2.2.1 Glass Transition Temperature

The role of untreated and silane-treated halloysite nanoparticles on the wettability and glass transition of nanocomposites was investigated by measuring the glass transition temperature (T_g) by using DSC spectra in the heating mode. The incorporation of HNT or s-HNT nanoparticles in the crosslinked UPE resulted in a marginal reduction in T_g values, with a slight shifting in the initial formulation of a giant molecule network of the UPE matrix, as shown in Figures 5.2 and 5.3, respectively. The T_g values of neat UPE and its HNT and s-HNT nanocomposites are given in Table 5.2.

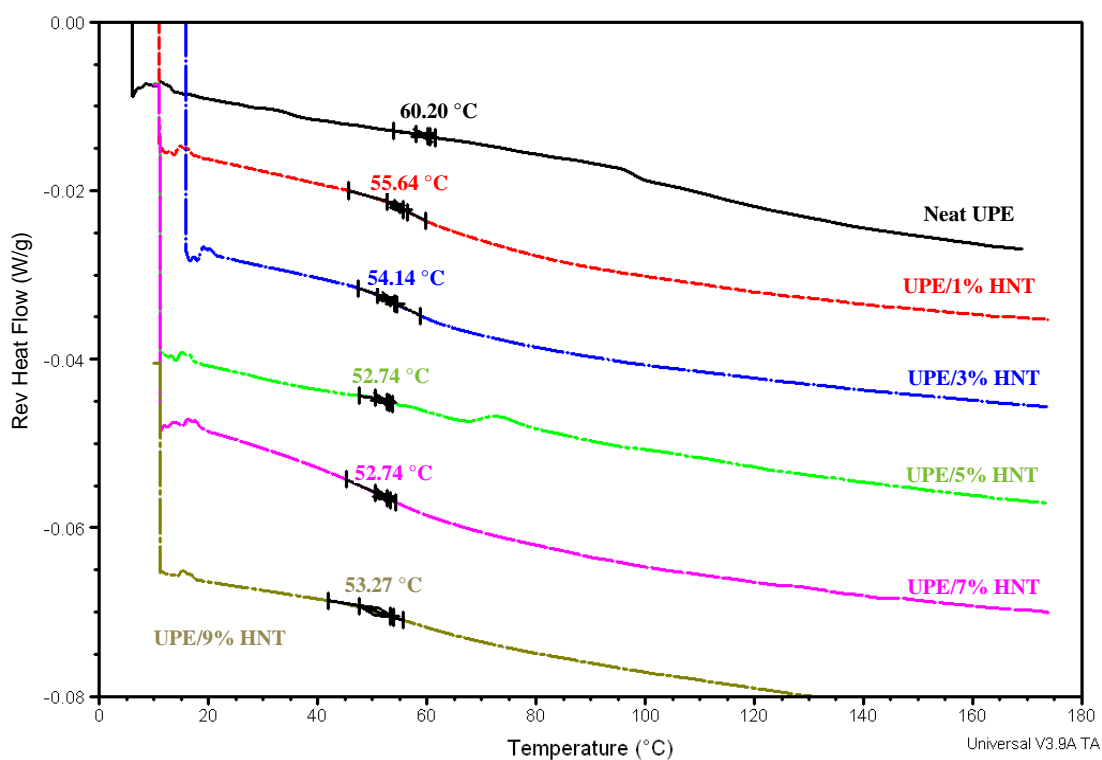


Figure 5.2: DSC Thermograms of Neat UPE and its Untreated HNT Composites

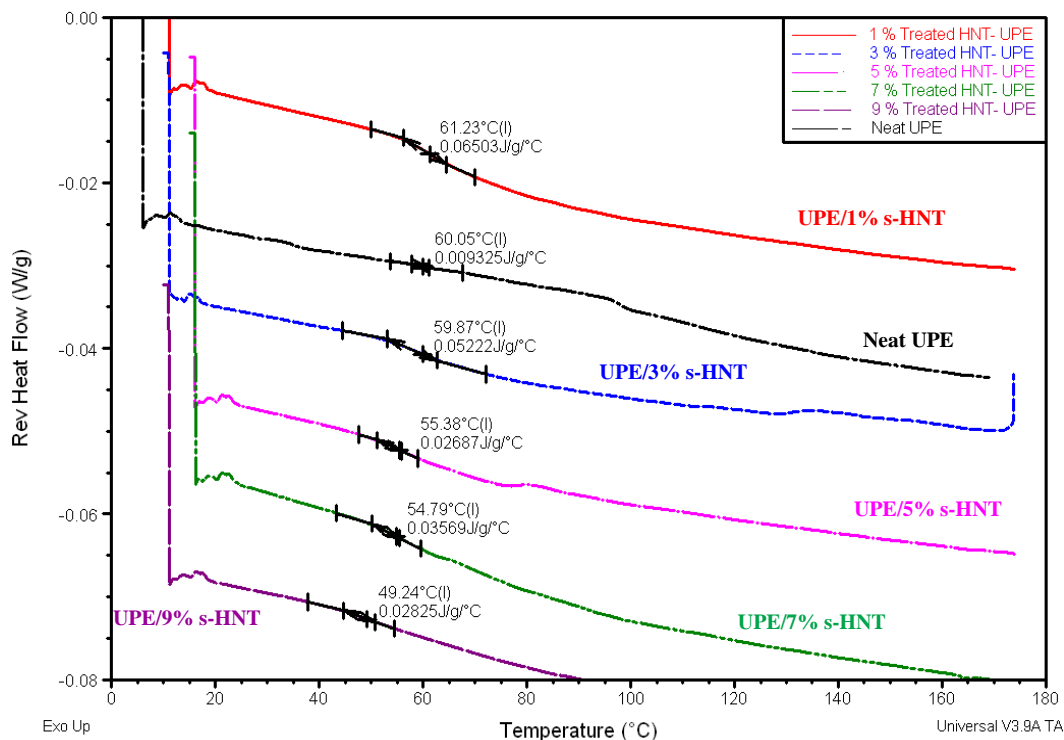


Figure 5.3: DSC Thermograms of Neat UPE and its Silanised HNT Composites

Table 5.1: Values of T_g and Viscosity of Neat UPE and UPE/HNT

Nanocomposite	T _g (°C)	Viscosity (cp)#
Neat UPE	60.2	288
UPE/1% HNT	55.6 (61.2)	380
UPE/3% HNT	54.1 (59.9)	410
UPE/5% HNT	52.7 (55.4)	414
UPE/7% HNT	52.7 (54.8)	460
UPE/9% HNT	53.3 (49.2)	490

Note: The results of UPE/s-HNT nanocomposites are given in parentheses.

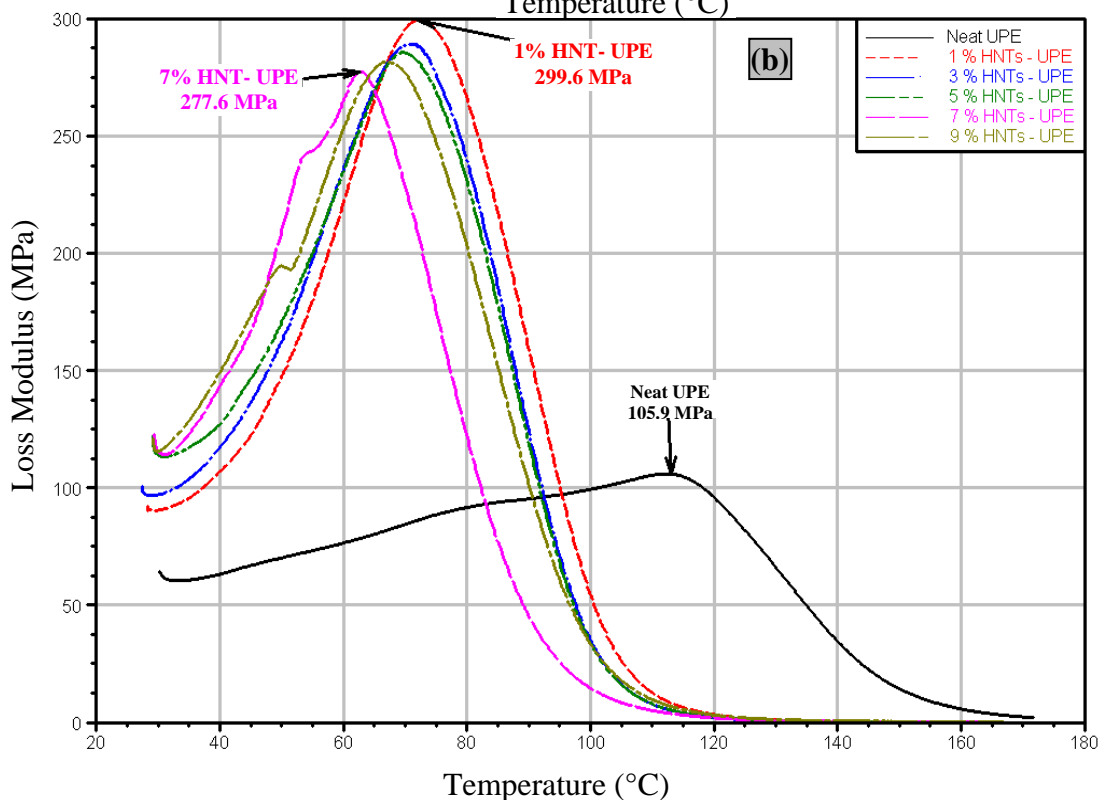
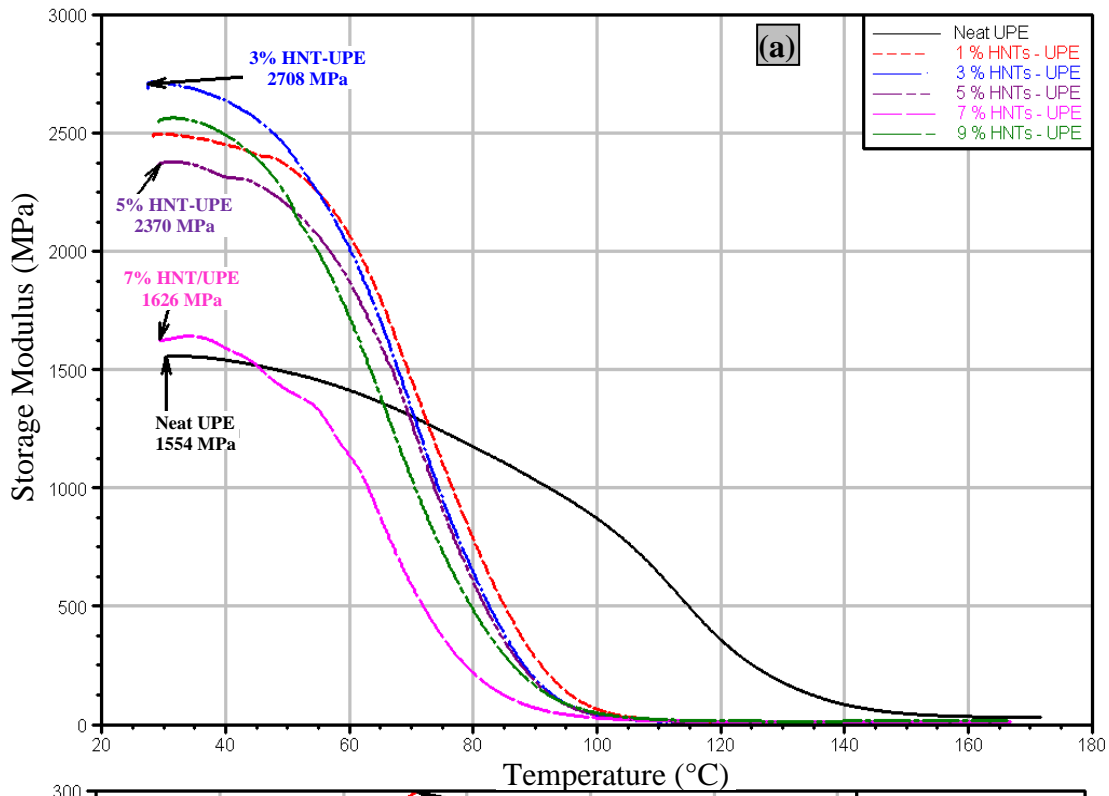
The small drops ($\leq 10^{\circ}\text{C}$) in the T_{gs} values of the UPE nanocomposites with increasing halloysite loading can be attributed to the interfacial plasticisation and preferential interactions between particle and UPE crosslinking agent. These findings of the T_{gs} values are quite consistent with previous reports, where T_{gs} was found to be lower by 6°C or less than the neat polymer matrix (Lin et al. 2011; Deng et al.

2008; Deng, Zhang & Ye 2009; John et al. 2010). Inserting a second phase into thermosetting resins yields high crosslink density and creates more rapid chain dynamics. This is as a result of generating nonreactive surfaces and local free volume in the matrix and at the particle/polymer interface, thereby reducing the T_{gs} (Koerner et al. 2006; Mittal 2012). Further, it is believed that the decrease in the T_{gs} was due to the presence of nanoparticles in the polymer matrix that caused various changes in the crosslink density (Paul & Robeson 2008).

The role of s-HNT particles on the T_{gs} of the UPE nanocomposites was relatively insignificant at all loading rates. This was likely because coupling silanised halloysite with polymer chains through adsorption and hydrogen bonding can contribute to strengthening the interface between s-HNT particles and the UPE matrix and consequently also diminish the T_g values (Zhang & Loo 2009).

5.2.2.2 DMA

The DMA analysis was undertaken at 1 Hz to evaluate the influence of HNT and s-HNT particles and their state of dispersion on the viscoelastic properties of the UPE nanocomposites. The viscoelastic properties (storage modulus E' , loss modulus E'' and $\tan \delta$) of neat UPE and its nanocomposites were investigated, as shown in Figure 5.4 (a to c). In general, all viscoelastic properties of the UPE nanocomposites demonstrated a significant increase over the neat UPE matrix. The results of these properties with the use of s-HNT nanoparticles were even higher (see Table 5.2). For instance, the storage modulus (see Figure 5.4a and Table 5.2) increased from 1,554 MPa for neat UPE; to 2,708 MPa (74% improvement) for UPE/3% HNT; and 2,772 MPa (78% improvement) for UPE/3% s-HNT. These increases likely occurred due to the restriction of the segmented motion of the UPE resin by uniformly dispersed halloysite particles.



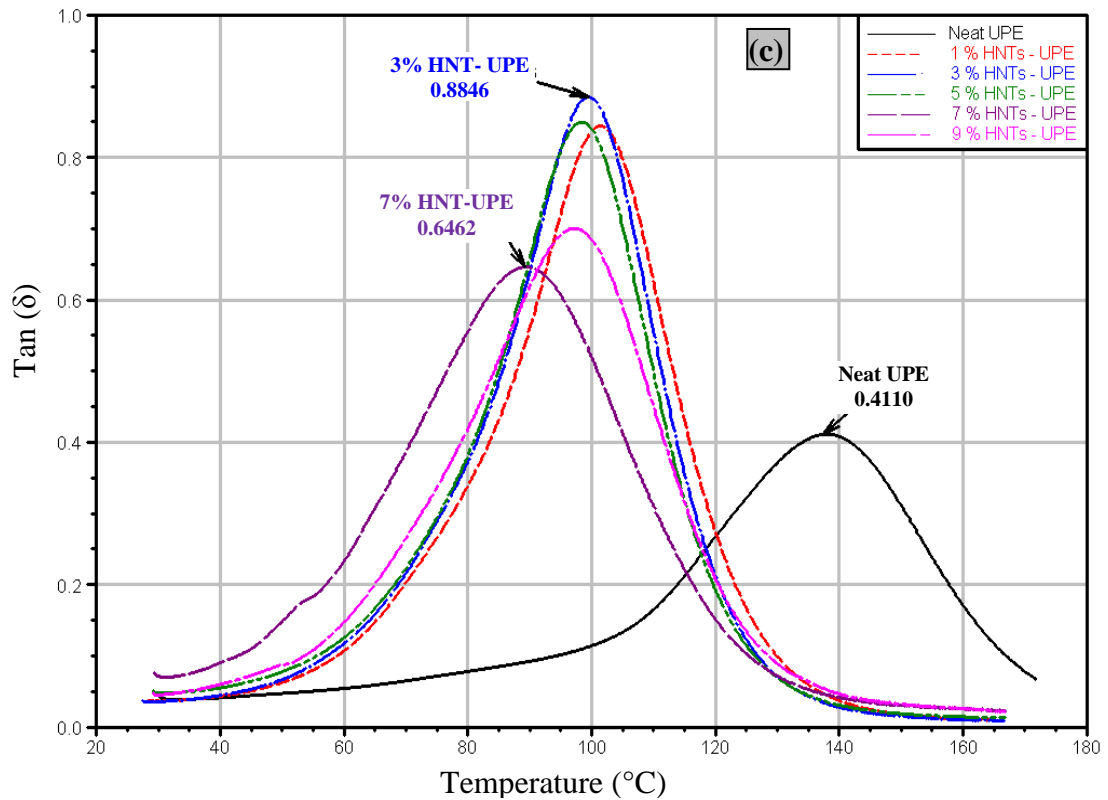


Figure 5.4: Variation of Dynamic Mechanical Properties of Neat UPE and its Untreated HNT Nanocomposites as Functions of Temperature: (a) Storage Modulus, (b) Loss Modulus and (c) Tan δ .

Table 5.2: Comparison of Viscoelastic Results (DMA) between UPE/HNT and UPE/s-HNT Nanocomposites

Nanocomposites	Storage modulus (E', MPa)	Loss modulus (E'', MPa)	tan δ
Neat UPE	1,554	105.9	0.411
UPE/1% HNT	2,494	299.6	0.855
UPE/1% s-HNT	2,612	293.6	0.88
UPE/3% HNT	2,708	288	0.8846
UPE/3% s-HNT	2,772	297	0.9408
UPE/5% HNT	2,370	280	0.862
UPE/5% s-HNT	2,155	285	0.87
UPE/7% HNT	1,626	277	0.6462
UPE/7% s-HNT	1,750	275	0.76
UPE/9% HNT	2,565	279	0.685
UPE/9% s-HNT	-	-	-

Further, in the case of using silanised halloysite nanocomposite, their better dispersion status and strong interfacial adhesion with polymer chains were other reasons that the storage modulus increased. The plasticising effect of dangling chains between the silanised halloysite and the UPE molecules further restricted the

segmented motion of the branched UPE macromolecules. The segmental motion in the polymers indicated the movement of small chain segments that occurred above the glass transition temperature (Sen 2010). Further increase of halloysite content in the UPE matrix exhibited a relative increase trend in the values of storage modulus, but the highest values were observed with the addition of 3% halloysite.

The results of loss modulus, E'' —or the ratio of energy lost to energy stored per cycle of deformation—during the friction associated with the motion of polymer chains showed a similar trend with that of storage modulus (see Figure 5.4b). The E'' values increased from 106 MPa for neat UPE to 288 MPa (172% improvement) and 297 MPa (180% improvement) for nanocomposites including 3% HNT and s-HNT, respectively.

The $\tan \delta$ measurement is an indication of a material's energy dissipation in a macromolecular network and an indication of transitions that occur in the glassy or rubbery state. The $\tan \delta$ is also an indication of the damping behaviour of materials. The damping behaviour of the nanocomposite has been frequently used to measure the interfacial adhesion of fillers (Ma et al. 2008). The $\tan \delta$ peaks of UPE nanocomposites (see Figure 5.4c) showed noticeable shifts to the left or to lower temperatures with an increase of halloysite content. These shifts have been reported before, and were ascribed to a restricted chain mobility caused by the nanoparticle effect. In Table 5.2, the magnitudes of $\tan \delta$ damping curves of halloysite nanocomposites were significantly reduced throughout the temperature range investigated upon compounding with untreated and silane-treated halloysite nanoparticles. This suggests that the nanoparticles hindered the energy dissipation process of thermosetting unsaturated polyester molecules.

5.2.3 Mechanical Tests

The typical stress-strain curves of neat UPE and different UPE/HNT and UPE/s-HNT nanocomposites are illustrated in Figure 5.5a and b, respectively. Interestingly, there was large concurrence between the stress-strain curves for the neat UPE and the UPE nanocomposite filled with 1% HNT. In terms of nanocomposites, it was evident that, after compounding HNT or s-HNT particles, they acquired an increase in tensile strength compared to the cured UPE matrix, with the nanocomposites with 3 wt% of HNT or s-HNT showing the highest tensile strength.

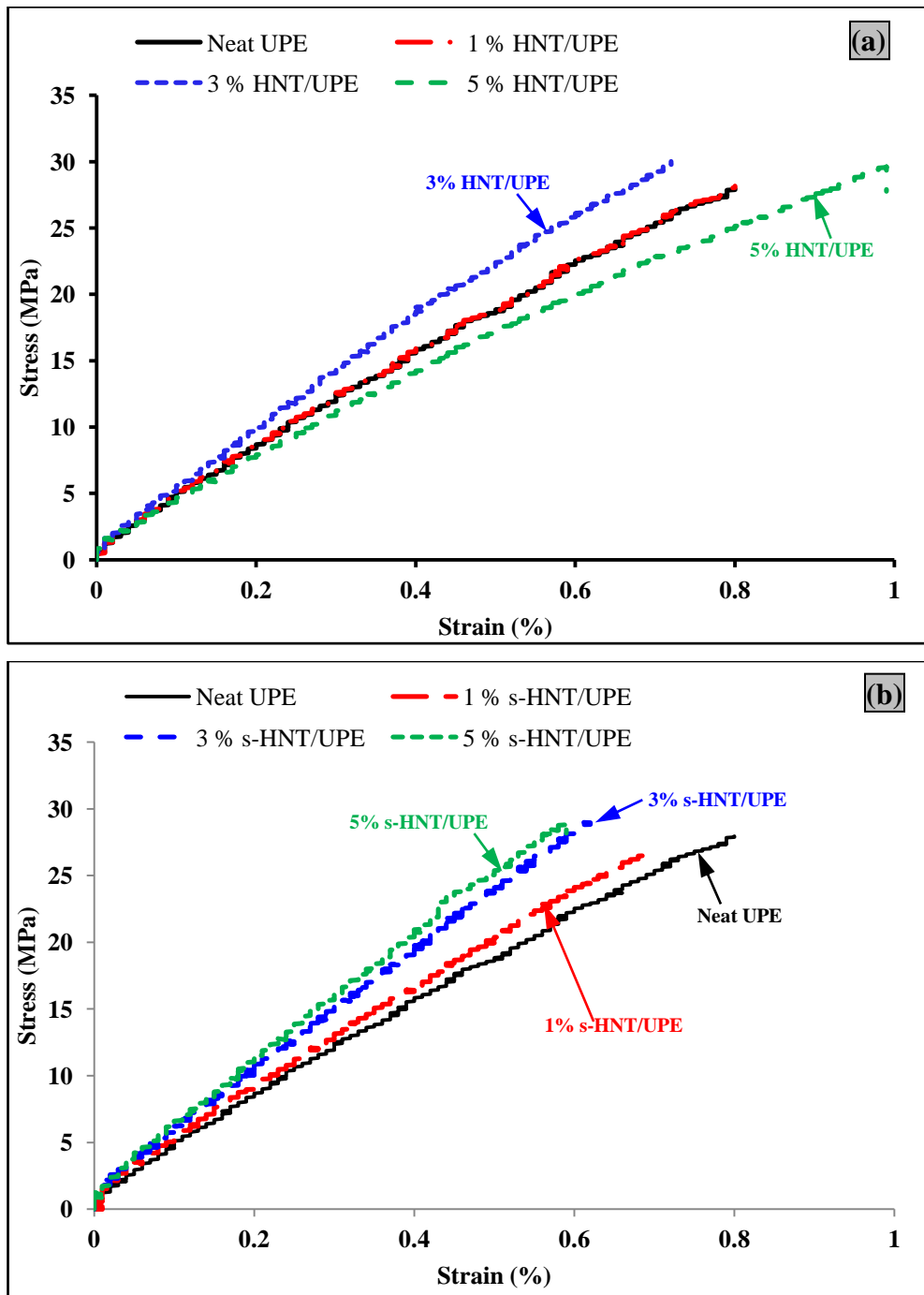


Figure 5.5: Representative Stress–strain Curves for Neat UPE and: (A) Different HNT and (B) S-HNT Nanocomposites

The tensile strengths, Young’s moduli and elongations at break of the neat UPE and its HNT or s-HNT nanocomposites are shown in Figure 5.6 (a to c). The flexural strengths and flexural moduli of neat UPE and its nanocomposites are described in

Figure 5.7. The introduction of HNT and s-HNT nanoparticles into the crosslinked UPE matrix resulted in higher tensile properties of UPE nanocomposites over the neat UPE. These increases were ascribed to the role of rigid inorganic nanoparticles in the UPE matrix.

The addition of up to 5 wt% of HNT or s-HNT into the UPE matrix showed an approximately similar increasing trend for both tensile and flexural strengths and moduli for the nanocomposites. In Figure 5.6a, the tensile strength of the 3% HNT or 3% s-HNT nanocomposites showed a higher improvement by 7% and 10%, respectively, compared to the neat UPE. Similarly, the Young's modulus (Figure 5.6b) increased from 3.78 GPa for neat UPE to the highest magnitudes of 4.08 GPa (8% improvement) and 4.25 (12% improvement) for the nanocomposite counterpart. In terms of the elongation (or strain) at break (Figure 5.6c), it was obvious that the nanocomposites with the highest tensile properties showed the lowest elongation at maximum stress or the lowest elongation at break due to the reduction of the material's ductility. However, it has been reported in different literature that both an increasing and decreasing trend in elongation at break of polymer nanocomposites occurs after introducing nanoparticles (John et al. 2010; Sen 2010).

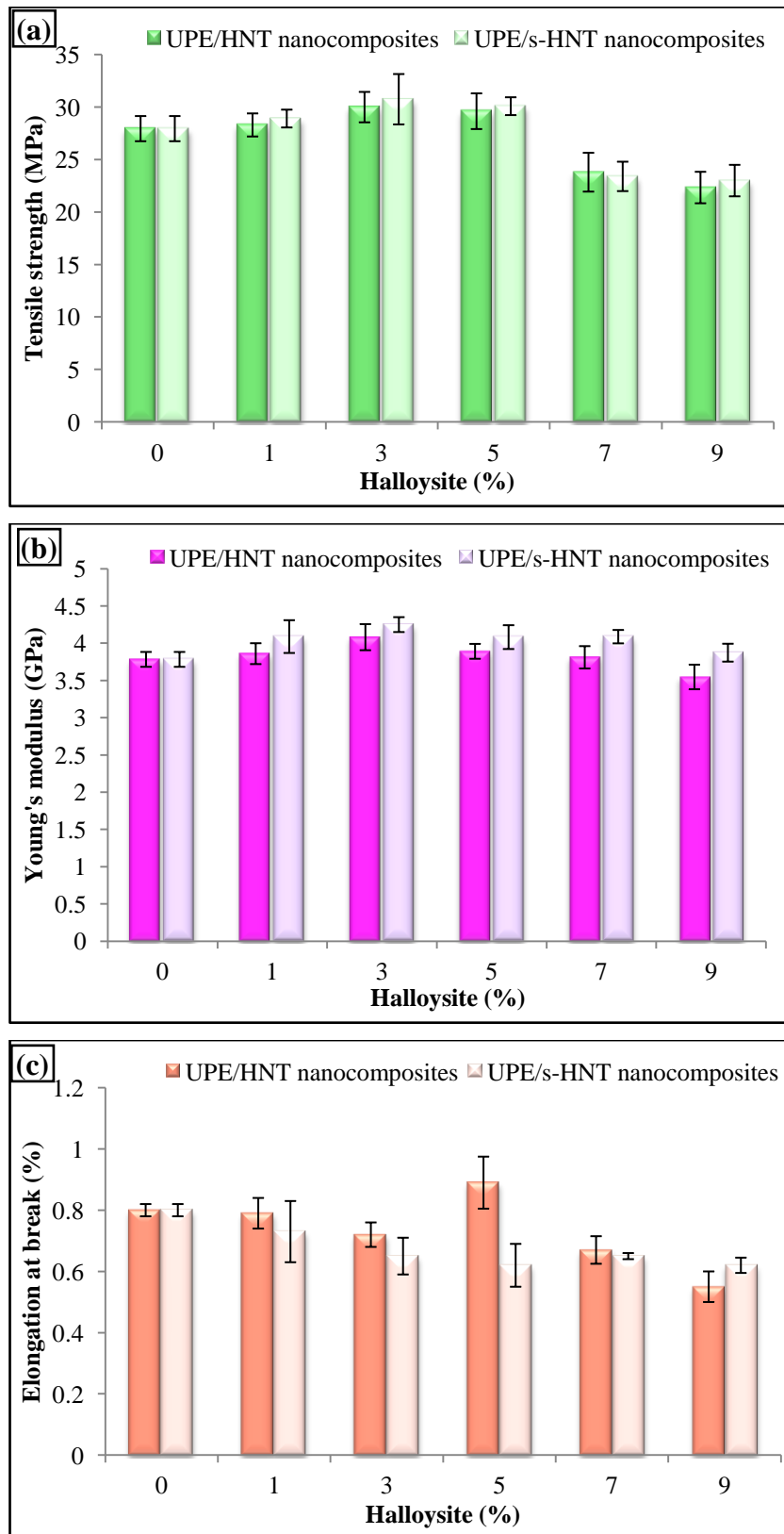


Figure 5.6: Tensile Properties of Neat UPE and UPE-based Different HNT and s-HNT Nanocomposites

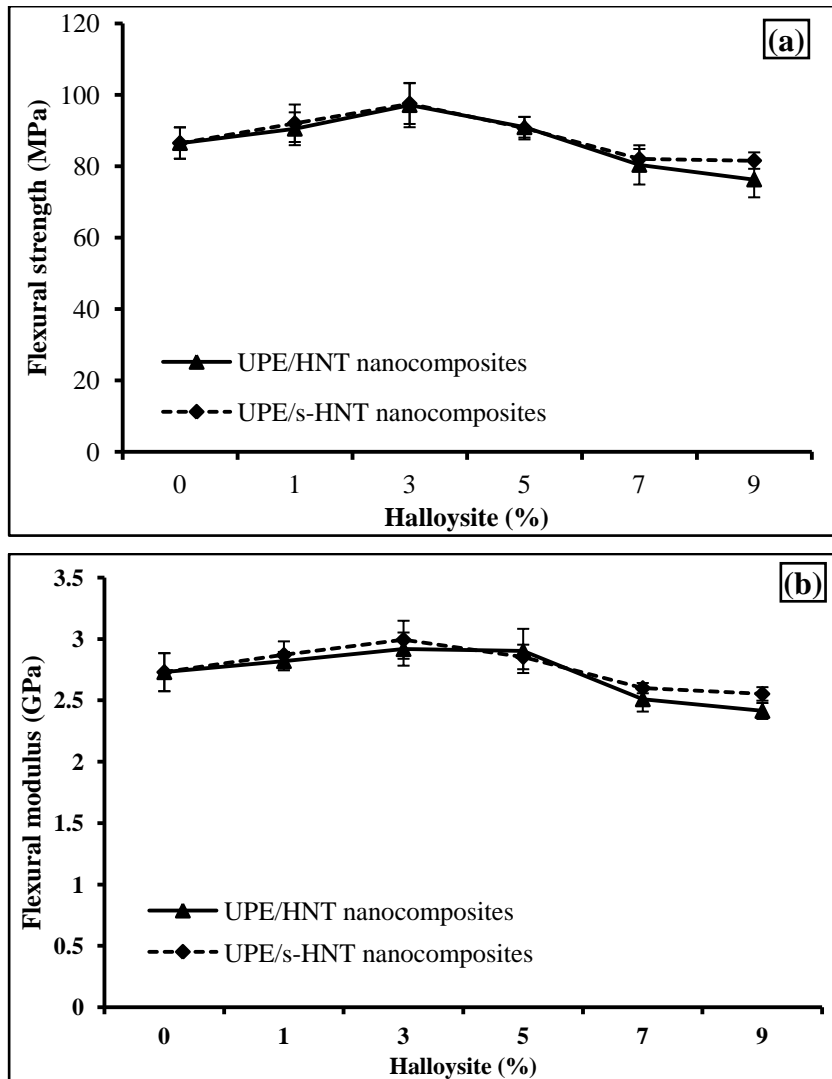


Figure 5.7: Flexural Properties of Neat UPE and UPE-based: (a) Different HNT and (b) s-HNT Nanocomposites

The flexural strength and flexural modulus of the cured UPE nanocomposites measured using 3PB fixture showed a similar maximum increase with the incorporation of 3% of HNT or 3% s-HNT nanoparticles (see Figure 5.7), since they were interfacial interaction-dependent. However, a further increase of halloysite content induced a gradual decrease in mechanical properties due to the presence of aggregates in the microstructure—that is, the presence of an immobilised or partially immobilised nanocomposite structure. As aforementioned, the presence of large agglomerates in the polymer matrix caused poor interfacial adhesion and poor stress transfer between the reinforcements and polymer chains. In addition, the presence of rich/poor particles regions with the higher addition of halloysite acted as constrained regions, restricting the full polymerisation of thermosetting UPE and subsequently

varying the crosslinking density and reducing the strength of nanocomposites (Seyhan et al. 2009).

Generally speaking, the mechanical properties of nanocomposites were directly affected by their dispersion status, which was related to material characteristics (such as nanofiller type and concentrations; compatibiliser content, if any; matrix viscosity; filler/filler interaction; and filler/polymer interaction). They were also dependent on the elastic modulus of polymer and nanofiller, the nanofiller orientation and the orientation of the polymer crystallites, as well as the interfacial stress transfer mechanisms and degree of crystallinity in the polymer matrix (Bhattacharya, Kamal & Guptaet 2008). Meanwhile, the interface reaction between functionalised HNT and the UPE matrix occurred through either molecular entanglement, hydrogen bonding, van der Waals's interactions or covalent chemical bonding (MacMillan 1997).

To further understand the effect of halloysite nanoparticles on the tensile properties of nanocomposites, impressive results showing tensile strengths and Young's moduli of different polymers-based nanocomposites were cited from numerous literature, and listed in Table 5.3. The current findings of mechanical properties revealed a similar increasing trend with those of other thermosetting polymers-based halloysite nanocomposites. However, in the case of inserting halloysite into thermoplastics, such as the polyamide-6 matrix, these properties demonstrated much higher values compared to thermosets, due to the nature of the chemical bonds, with irreversible intermolecular interactions in thermoplastics and covalently bonded giant macromolecular in thermosetts (Pascault et al. 2002).

Table 5.3: Summary of Mechanical Properties for Different Polymers-based HNTs

Materials	Tensile strength (MPa)	Improvement (%)	Young's modulus (GPa)	Improvement (%)	Processing and reference
Epoxy—5 HNTs	69.4	4 (66.7-matrix)	2.93	2 (2.87-matrix)	Mechanical mixing (Deng, Zhang & Ye 2009)
Epoxy—5 HNTs	67.3	7 (62.6-matrix)	2.93	1 (2.9-matrix)	Mechanical mixer (Deng et al. 2008)
Polyamide—6-4 HNTs	70.5	28 (55.1-matrix)	2.59	29 (2-matrix)	screw extrusion (Prashantha et al. 2011)
EPDM—5 HNTs	1.94	46 (1.32-matrix)	1.16	10 (1.05-matrix)	HAAKE mixer (Pasbakhsh et al. 2009)
Polypropylene—4 HNTs	34.5	28 (27-matrix)	1.62	26 (1.28-matrix)	Screw extrusion (Prashantha, Lacrampe & Krawczak 2011)
PVC/PMMA ¹ —3 HNTs	61	10 (55.5-matrix)	-	-	Two-roll mill (Liu et al. 2011)
UPE/3% HNT UPE/3% s-HNT	30 30.75	7 (27.95-matrix) 12 (27.95-matrix)	4.08 4.249	8 (3.78-matrix) 12 (3.78-matrix)	The present study

Note: ¹PVC/PMMA = 10 wt% poly (vinyl chloride)-grafted polymethyl methacrylate.

5.2.4 Morphology of Tensile-fractured Surface

It is essential to understand the role of HNT and s-HNT particles on the morphology of tensile-fractured surfaces of neat UPE and its nanocomposites at the microscopic level. For this purpose, SEM microscopy was used to examine the fracture modes of the nanocomposites under tensile test, and the SEM images are depicted in Figure 5.8. In Figures 5.8a and A, a highly smooth brittle fast fracture (wallner lines) was observed on the surface of the crosslinked UPE matrix.

The wallner lines occur on the fracture surface of a very brittle material and are the result of a propagating crack. They appear as parallel cleavage steps, creating a rippled pattern (Brooks & Choudhury 2002; Shukla 2005). The presence of cleavage

planes in different orientations and the formation of river patterns were observed in the fractured-surface morphology of the UPE nanocomposites after inserting untreated HNT nanoparticles, as shown in Figure 5.8 (b to d).

The morphology of the tensile-fractured surfaces for nanocomposites with different s-HNT particles (Figures 5.8B to D) showed a hackle region with river markings and evenly distributed preferential sites of phase separation. The formation of cleavage planes and their fronts connecting to the adjacent planes at plastic deformation zones are shown in Figure 5.8C. Further, the presence of rigid halloysite clusters with further increase of halloysite content led to increase in the roughness of the fracture surface (see Figures 5.8d and D) due to the deflection of the cracking path, which can tend to make crack propagation more difficult (Tang et al. 2011). To indicate the distinct difference in the crack growth under tensile load between the nanocomposites with HNT and those with s-HNT particles, Figures 5.8e and E show fast crack growth within a poorly bonded structure for the former nanocomposite, and slow crack growth within a better bonded structure for the latter nanocomposite.

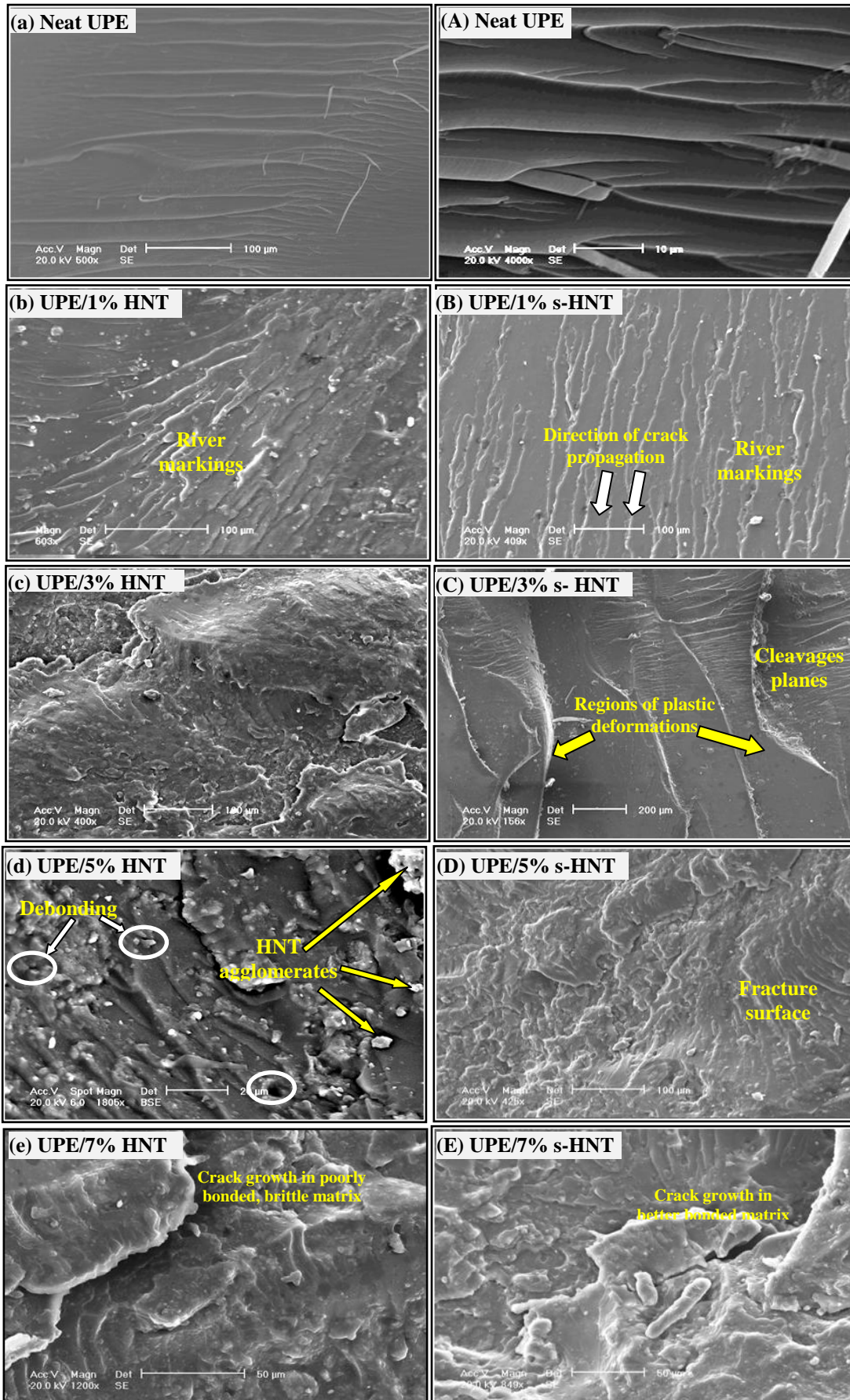


Figure 5.8: SEM Images of the Fractured Surfaces of Neat UPE and UPE-based Different HNT and s-HNT Nanocomposites

5.2.5 Mathematical Models for Modulus Predictions

Several mathematical models have been implemented to predict the elastic modulus in order to further understand the elasticity in nanocomposites in relation to their structures. Most traditional mathematical models assume ideal conditions for polymer nanocomposites that contribute to obtaining accurate results regarding the properties. For instance, the material is presumed to be isotropic, with uniform dimension nanofillers, evenly aligned orientations and good bonding between fillers, while the matrix is assumed to have no particle–particle interaction or agglomerations (Spencer et al. 2010).

In the present nanocomposite, the Halpin-Tsai model (Halpin & Kardos 1976), based on Mori-Tanaka, was used to estimate the elastic modulus of the nanocomposite as follows:

$$\frac{E}{E_m} = \frac{1 + \zeta \eta \phi_f}{1 - \eta \phi_f} \quad (5.1)$$

where E and E_m are the Young's moduli of the nanocomposite and the matrix, respectively; ϕ_f is the volume fraction of filler; and η is expressed as:

$$\eta = \frac{E_f/E_m - 1}{E_f/E_m + \zeta} \quad (5.2)$$

where E_f represents the Young's modulus of the filler, and ζ is a shape parameter that depends on nanofiller geometry and orientation. For the discontinuous oriented fillers, $\zeta = 2\alpha$ where $\alpha = L/t$, and L and t are the filler's length and thickness, respectively, which can be obtained from the TEM micrographs.

The Smallwood-Einstein equation in its simplified term (Roy & Bhowmick 2010) was applied to predict the elastic modulus of the nanocomposites. This equation was developed to consider the particle–particle interaction as follows:

$$\frac{E}{E_m} = 1 + 2.5\phi_f + 14.1\phi_f^2 \quad (5.3)$$

The Kerner model (Dong et al. 2011) was used to evaluate the elastic modulus of the composites:

$$\frac{E}{E_m} = 1 + \left(\frac{\phi_f}{1 - \phi_f} \right) \left[\frac{15(1 - \nu_m)}{8 - 10\nu_m} \right] \quad (5.4)$$

where ν_m is Poisson's ratio of the polymer matrix (unsaturated polyester) = 0.38 (Pascault et al. 2002).

The Guth and Gold (1938) model was also used to predict the elastic modulus of the nanocomposite:

$$\frac{E}{E_m} = 1 + 0.67\phi_f + 1.62\phi_f^2 \quad (5.5)$$

Figure 5.9 shows a comparison of the experimental results and predicted results obtained from different mathematical models of Young's modulus. The predicted Young's modulus values of nanocomposites containing up to 5 wt% (0.3 vol. %) of HNT loading, to some extent, appeared to be in good agreement with those of the experimental ones. However, they rather overestimated the experimental results when the HNT loading exceeded 5 wt%. The Smallwood-Einstein and Kerner models also exhibited similar trend lines of overestimation at higher HNT loadings.

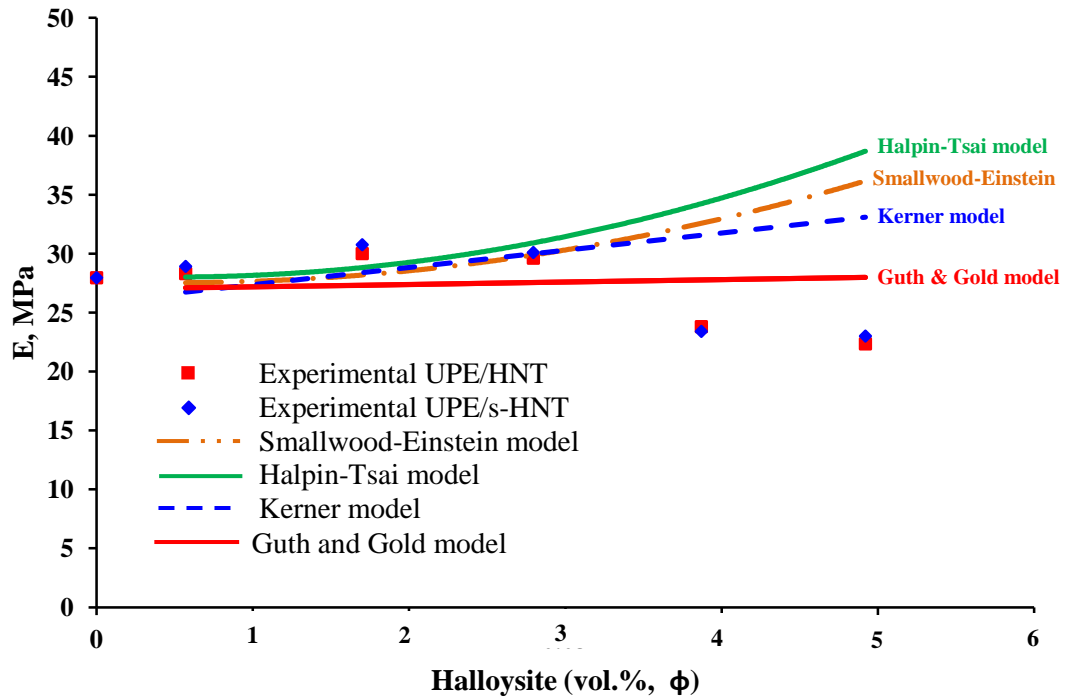


Figure 5.9: Comparison of Experimental and Mathematical Results of Young's Modulus for UPE-based Different HNT and s-HNT Nanocomposites

The deviation between the numerical and experimental results was likely due to the assumptions of a strong adhesion and well-bonded particles with the matrix within the mathematical models. However, the fact is, at higher nanoparticle contents, the nanoparticles debond and initiate void growth at certain volume fraction. Confirming that, Dittanet and Pearson (2012) suggested that 15 vol. % of nanoparticles in the epoxy matrix has the ability to debond and create void growth, and this should be considered within the numerical prediction of the mechanical properties for the composites. They also considered the energy contribution from a shear banding mechanism. However, the mathematical models used here to predict the elastic modulus did not consider the volume fraction of debonding particles, nor the energy contribution from a shear banding. The Guth and Gold model shows a levelling off trend of Young's modulus values, regardless of HNT loadings, because it considers only one term—volume fraction of particles (ϕ_f)—in the prediction.

5.3 Summary of the Results

In this chapter, the effects of untreated HNT and s-HNT nanoparticles on the thermo, thermodynamic and mechanical properties of UPE-based HNT, or s-HNT nanocomposites, were examined. The Young's modulus was predicted using different mathematical models, and the morphology of tensile-fractured surfaces for different nanocomposites was identified by the SEM examination. The findings of this chapter can be concluded as follows:

1. No significant change in the thermal stability of the UPE nanocomposites occurred with the introduction of HNT or s-HNT into the UPE matrix. The presence of 3 wt% s-HNT in the UPE nanocomposites delayed their thermal degradation by 3°C only—that is, the decomposition temperatures at 5% weight loss rate (T_{5wt%}) were 438°C for the UPE/3% s-HNT and 435°C for the UPE/3% HNT nanocomposites. Similarly, with T_{85wt%}, it occurred at 413°C for the neat UPE and at 419°C and 422°C for the UPE/3% HNT and UPE/3% s-HNT nanocomposites, respectively.
2. The incorporation of HNT or s-HNT nanoparticles into the UPE nanocomposites caused a modest decrease in the T_g values, associated with a shifting in the initial formulation of a giant molecule network of the UPE matrix. The small drop in the T_{gs} was attributed to the interfacial plasticisation and preferential interactions between the nanoparticle and thermosetting UPE crosslinking agent.
3. Inserting HNT or s-HNT particles into the UPE nanocomposites revealed a significant increase in all of their viscoelastic properties (storage modulus and loss modulus) compared to the neat UPE matrix. These increases were attributed to the uniformly dispersed halloysite particles caused by restricting the segmented motion of the UPE network. The strong interfacial adhesion of the silanised halloysite with the polymer matrix was another reason that the thermodynamic properties increased.

4. The addition of HNT and s-HNT particles with loading up to 5 wt% into the UPE nanocomposites exhibited a similar increasing trend for both tensile and flexural strengths and their moduli. The 3 wt% of HNT or s-HNT showed the maximum increase of mechanical properties, compared to the neat UPE matrix. However, further increase of halloysite contents (> 5 wt%) resulted in lower mechanical properties, due to the existence of halloysite agglomerations in the microstructure.
5. The morphology of the tensile-fractured surface showed a smooth brittle fracture with wallner lines for crosslinked UPE resin. It showed the presence of cleavage planes in different orientations with formation of river patterns for the UPE/HNT nanocomposites, and a hackle region with river markings and evenly distributed preferential sites of phase separation for the UPE/s-HNT nanocomposites.
6. The mathematical results of Young's modulus for the UPE nanocomposites containing different HNT and s-HNT particles apparently showed good agreement with those experimentally obtained for the nanocomposites filled with up to 5 wt% HNT loading. However, the results overestimated the experimental ones with increasing halloysite content over 5 wt% (0.3 vol. %).

Chapter 6: Role of Silanised Halloysite on Tribological Characteristics and Impact Fracture Behaviour

6.1 Role of Silanised Halloysite on Tribological Performance

6.1.1 Introduction

It is well known that thermosetting UPE resins are commonly used in automobile components manufacturing for their high performance-to-cost ratio (Barbero 2011). However, this efficiency is limited because all polymers generally, and unsaturated polyester particularly, are sensitive to wear damage and exhibit different modes of deformation (such as ductile ploughing, ironing, ductile or brittle machining, and so forth) (Dasari et al. 2007). Hence, various attempts have been widely devoted to enhance the material properties of UPE resins, and to reduce their wear or materials loss to a minimum, in order to attain a precise engineering design of parts.

This was first undertaken via reinforcing them with different traditional fibres, such as glass fibres (Yousif & El-Tayeb 2010; El-Tayeb & Yousif 2007), hybrid composites (Patnaik et al. 2009; Mahapatra & Patnaik 2009; Hashmi, Dwivedi & Chand 2007) and different treated and untreated natural fibres (El-Tayeb 2009; Yousif & Ku 2012). These studies' results clearly indicated that the wear-reducing and anti-friction abilities in the composite materials were better than those for the neat polymer matrix. This was due either to an energy transfer concept and the strong interfacial adhesion between the fibre and polymer matrix, or to the adherence of some fine fibres on the surface, which assisted in reducing material removal in the composite.

The recent emergence of nanotechnology and the availability of different nanosized fillers with good performance, low cost and ease in manufacturing have been invariably used with polymers to improve their tribological properties against the severe effects of environment, temperature, relative speed of interacting surfaces, and applied normal loads (Friedrich & Schlarb 2008). Therefore, various nanofillers—such as CNTs, nanoclay, nanosilica, nano-TiO₂, nano-ZnO and others (Dasari, Yu &

Mai 2009)—have been widely used with thermoset and thermoplastic polymers to examine the wear damage in relation to the structure of the polymer nanocomposite.

For instance, Jawahar, Gnanamoorthy and Balasubramanian (2006) revealed that the CoF and wear loss of thermosetting polyester/clay nanocomposites reduced with the presence of organoclay, due to the good dispersion of organoclay in the polymer matrix. This decrease in wear loss was also attributed to the combined effect of the three-body roller-bearing action of both nanoclay and nanoclay-reinforced wear debris, and the formation of transfer film on the steel counterface. However, the CoF and wear loss increased with increasing inorganic conventional clay-filled composites, where no transfer film occurred on the steel counterface. Similarly, Rashmi et al. (2011) attributed the enhanced dry sliding wear resistance in epoxy/5 wt% organoclay nanocomposites to the uniformly distributed particles and the subsequent improved hardness of the nanocomposites.

Further, HNTs have been widely implemented in the most recent studies on polymer/nanocomposites for their feature that combines the geometry of nanotubes with the chemistry of kaolinite. However, due to the hydrophilic nature of inorganic particles, different chemical treatments using different functional coupling agents, such as silane, have been commonly used (Rothon 2003; Mittal 2009). It has been reported that the silanised process of particles leads to improving their compatibility with polymer molecules and lowering the friction coefficient and specific wear rate in nanocomposites (Ha & Rhee 2008).

However, no study in the literature has investigated the effects of either HNT or s-HNT particles on the tribological performance of UPE-based nanocomposite. The current study thoroughly investigates the effective role of as-received untreated HNT and silane-treated HNT particles on the tribological characterisation of UPE nanocomposites. The CoF and specific wear rate (w_s) for neat UPE and its different nanocomposites using BOR under certain sliding conditions were measured as wear resistance parameters. The wear mechanisms and morphology of the worn surfaces were examined as wear mechanisms by SEM observations.

The materials used for the experiments, the preparation of nanocomposites, and the silane treatment of halloysite were discussed in Chapter 3, as was a detailed description of the measurements of the wear rate and the CoF.

6.1.2 Results and Discussion

This section is classified into three sub-sections: weight loss, friction coefficient and specific wear rate.

6.1.2.1 Weight Loss

Figures 6.1a and b show the variation in weight loss as a function of HNT contents at various sliding times for both untreated HNT and s-HNT nanoparticles. The most intriguing observation from the figures was that the effective role of HNT and s-HNT particles on the diminishing material removal of UPE-based nanocomposites was apparently unremarkable, especially with the use of treated silane particles. In the case of untreated HNT/UPE nanocomposites (Figure 6.1a), the lower addition of HNT revealed poor tribological performance compared to that for neat UPE. The nanocomposite containing 1 wt% HNT showed the highest weight loss, which may be due to the absence of nanoparticles at the rubbing surface and/or the modification on the wear track of the counterface with low particle contents. However, the intermediate additions of HNT (between 3 wt% and 7 wt%) revealed a good enhancement in wear properties, where the weight loss reduced by about 55% with a 7 wt% of HNT particles.

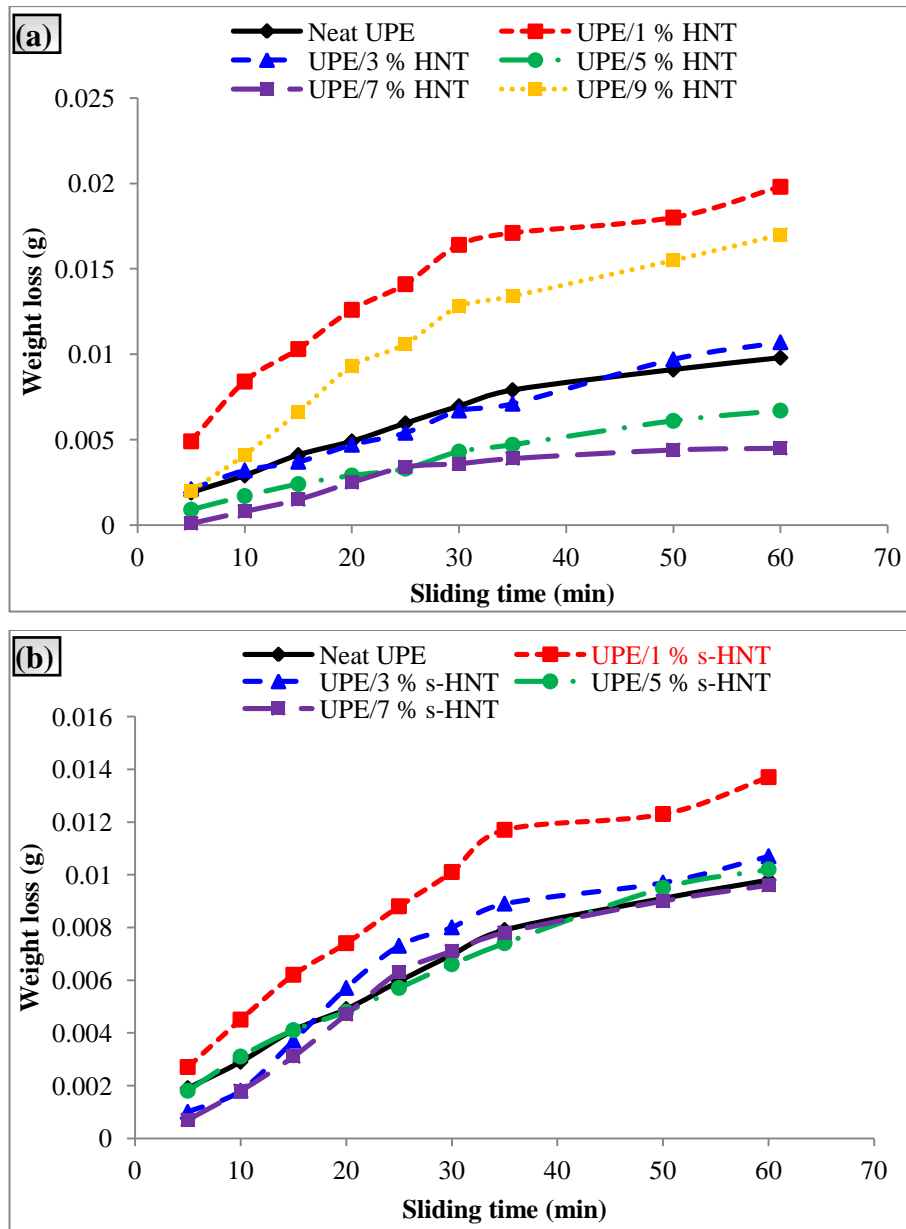


Figure 6.1: Variation of Weight Loss as a Function of HNT Contents with Various Sliding Times: (a) UPE/HNT and (b) UPE/s-HNT Nanocomposites

It was revealed by Jawahar, Gnanamoorthy and Balasubramanian (2006) that, with a higher particle content in the polymer matrix, higher material removal can be easily completed by the cutting action of the asperities in the counterface due to the lack of resinous regions and the reduced load transferred from the polymer to the particles. Zhang et al. (2013) claimed that, with high nanoparticle contents, a continuous transfer film can be formed on the counterface, which may contribute to determining the wear performance of nanocomposites at steady-state period.

In the case of using s-HNT particles, silane treatment showed a negative effect on the wear performance of the UPE-based nanocomposites (see Figure 6.1b). This was believed to be because the presence of silane molecules on the halloysite surface may act as barriers between the resinous regions and the halloysite, leading to detachment of the particles during sliding. This phenomenon was observed by the naked eye during the test. In contrast, Ha and Rhee (2008) reported that a decrease in material loss of epoxy filled by silanised clay nanocomposite took place due to the improved dispersion of clay particles in the epoxy matrix, and their good adhesion with the polymer matrix.

To overcome this discrepancy (contradiction) about the role of inserting silanised particles into thermosetting polymers, many researchers have written in different literature—regarding the effect of the modifying particle surface on the tribological performance—that uniform dispersion of particles in the polymer matrix alone could not be sufficient to enhance the tribological performance of the composite. This is because the interfacial adhesion between the nanofillers and the matrix, along with the morphology, is critical (Jawahar, Gnanamoorthy and Balasubramanian 2006; Chang et al. 2007; Ha & Rhee 2008). In terms of the neat UPE blocks, the weight losses were relatively reasonable due to high-crosslinked density in their hyperbranched architecture (Pascault et al. 2002).

To better understanding the relationship between the morphological structures and the tribological performance, and to clarify the critical roles of HNT, s-HNT on the deformation in the UPE nanocomposites, Shore D hardness for neat UPE and its HNT and s-HNT nanocomposites was measured. The values are shown in Figure 6.2.

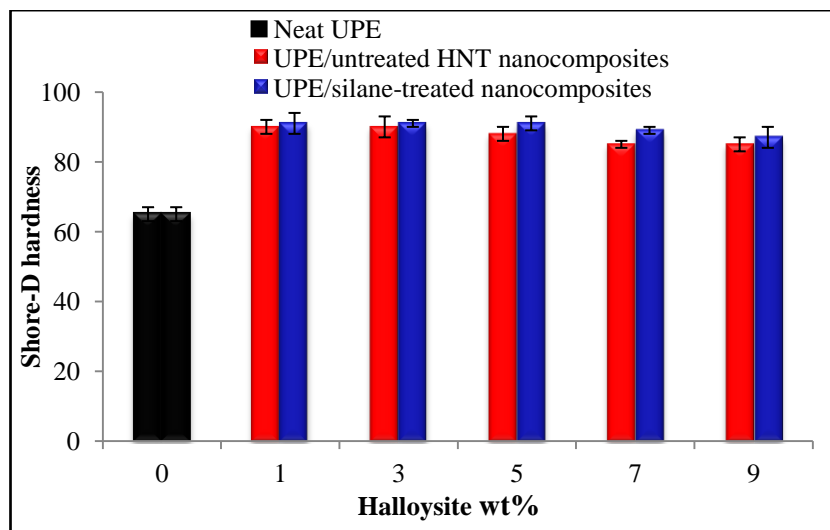


Figure 6.2: Hardness Results of Neat UPE and its HNT and s-HNT Nanocomposites

The testing of hardness was undertaken in several positions of material blocks, covering different areas along their surfaces. An average of five readings was considered. It is clear from Figure 6.2 that a significant increase in the Shore D hardness from 65 to 91 (40% improvement) occurred in the cured UPE nanocomposites with the presence of halloysite in the UPE matrix. This was obvious because the intrinsic hardness of the uniformly dispersed rigid halloysite in the polymer matrix tended to hinder the indentation. Interestingly, the hardness of UPE/s-HNT nanocomposite levelled off, even with further additions of s-HNT. This meant that the manufacturing process used in the preparation of materials did not cause any porosity in the final structure of the nanocomposites. Conversely, it was reported that a further increase of clay nanoplatelets in the polymer raised aggregate population and presented porosity. As a result, the contact between clay and the polymer was much more restricted, and the expected reinforcement effect was no longer observed (Arranz-Andrés, Pérez & Cerrada 2012).

6.1.2.2 The CoF (μ)

The CoF of UPE/HNT and UPE/s-HNT nanocomposites as a function of halloysite content is presented in Figure 6.3. A steady-state trend experiencing a noticeable drop at an early stage (or a running-in stage) of the CoF could be observed with the use of different halloysite contents. The CoF values of UPE/s-HNT showed lower

trends than the UPE/HNT nanocomposites due to a uniform dispersion of silanised halloysite in the UPE matrix.

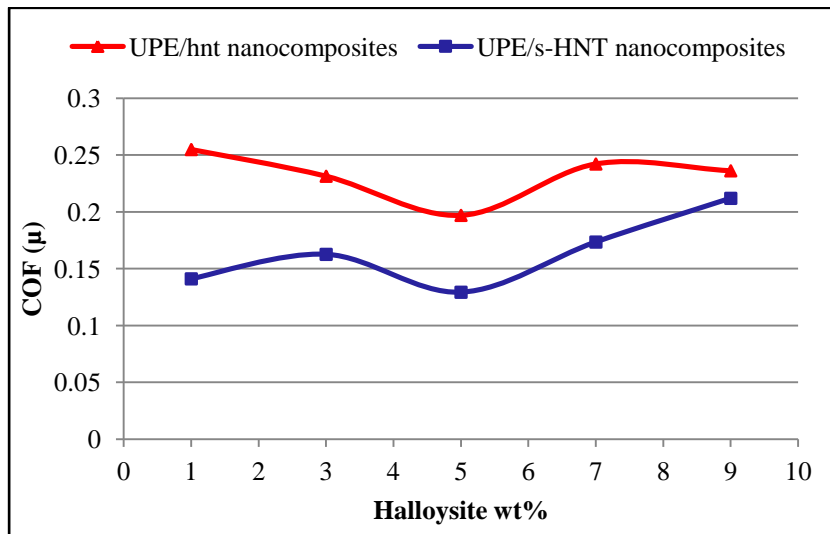


Figure 6.3: The CoF of UPE/HNT and UPE/s-HNT Nanocomposites

Additionally, it has been reported that the released nanoparticles, as wear debris during sliding of the contact surface at high rotation speed, act as three-body roller bearings, so they help reduce the dynamic effect of the moving indenter, reduce contact stresses and strains between the indenter and the surface, and consequently lower the CoF (Jawahar, Gnanamoorthy & Balasubramanian 2006; Dasari et al. 2007). It is also worth mentioning here that the dense structure of crosslinked UPE resin, along with large arrays of multiple bonds, occur between hydroxyl groups on the silanised halloysite surface. In addition, the polymer molecules, the covalent link between the constituents, the intermolecular hydrogen bonding and the strong van der Waals's interactions can also affect the CoF and enhance tribological performance (Friedrich & Schlarb 2008).

The changes in the CoF of the chosen nanocomposite samples versus the sliding distances at a constant applied load of 20 N and sliding speed of 2.8 m/s are shown in Figure 6.4. An obvious considerable oscillation with almost similar trend can be observed for all the materials within a running-in period. The trend of CoF for neat UPE was the highest, while the lowest was for the UPE/5% s-HNT nanocomposite. This could be due to a uniform transfer film formed on the SS counterface through a

sliding contact between blocks of the silanised halloysite nanocomposite and counterpart.

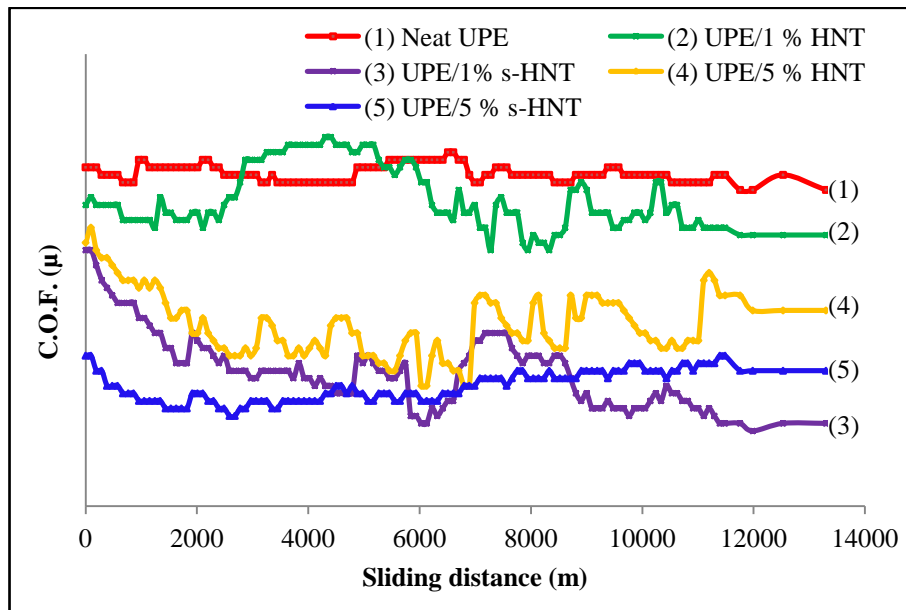


Figure 6.4: Friction Coefficient of Neat UPE and its Nanocomposites as a Function of Sliding Distance

Further, after reaching a steady-state process and completing the wear experiments, the surface roughness of wear tracks was measured in different spots to identify the correlation between material properties and subsurface deformation. The average values of roughness in the wear tracks for various nanocomposites are presented in Figure 6.5.

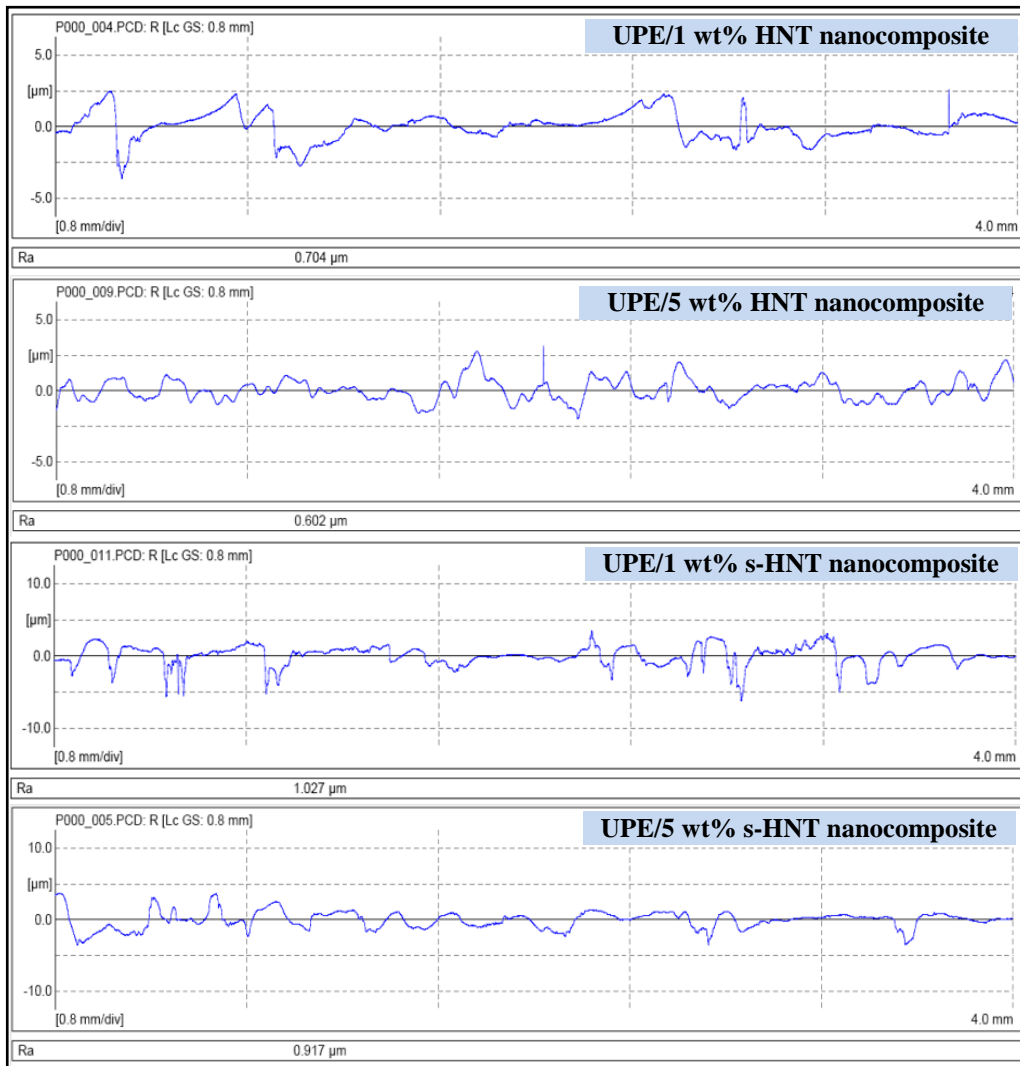


Figure 6.5: Roughness Profile of the Counterface After Testing Different Nanocomposite Samples

The average values of the surface roughness of UPE/1% HNT, UPE/1% s-HNT, UPE/5% HNT and UPE/5% s-HNT were 0.704 μm Ra, 0.602 μm Ra, 1.027 μm Ra and 0.917 μm Ra, respectively. Relatively, the s-HNT nanocomposites showed lower surface roughness since the well-adhered modified particles with the polymer chains caused better delamination strength of the particles and smoother worn surfaces, compared to the neat UPE or unmodified composites. Better surface roughness also resulted from the role of two-body abrasion wear and three-body abrasion wear that resulted from the use of the silanised particles (Dasari, Yu & Mai 2009).

6.1.2.3 The Specific Wear Rate (W_s)

The variation of specific wear rate (W_s) of unfilled UPE and UPE/HNT and UPE/s-HNT nanocomposites versus sliding distance is presented in Figures 6.6 and 6.7, respectively. All the specific wear rates of neat UPE and its nanocomposites were measured using Equation (3.2), Section 3.4.8. The conditions of the wear testing were as follows: sliding distance: 11.5 km, applied load: 20 N and sliding speed: 2.8 m/s.

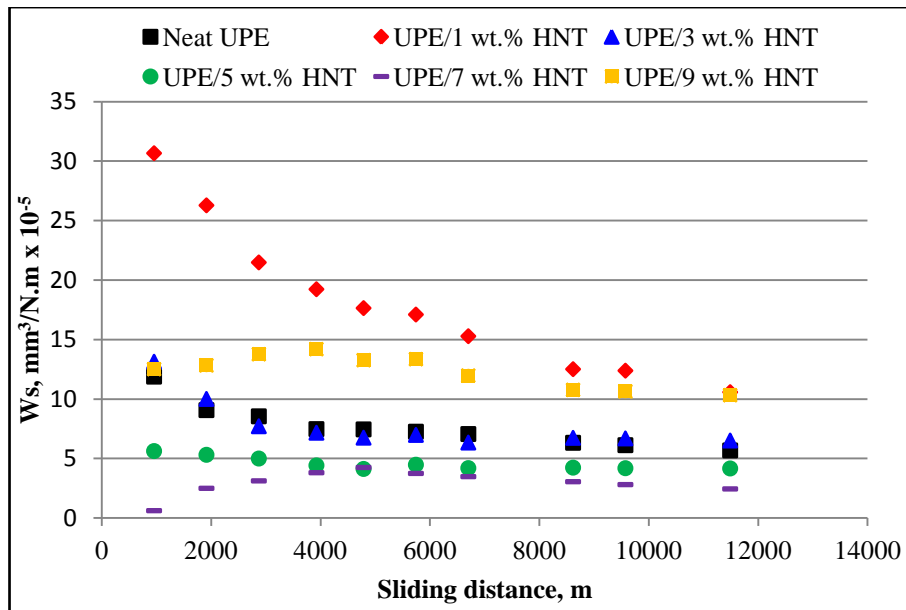


Figure 6.6: Specific Wear Rate of Neat UPE and UPE/HNT Nanocomposites Tested at Sliding Distance of 11.5 Km, Normal Load of 20 N and Sliding Speed of 2.8 m/s

The trend of the wear rate for all materials showed immense fluctuation within the running-in stage, while it stabilised beyond this stage, specifically at a sliding distance of around 8,000 m. However, incorporation of unmodified or surface-modified halloysite into thermosetting UPE matrix had an insignificant effect on the W_s values of the UPE nanocomposites. The W_s values, as shown in Figure 6.8, increased considerably from $6.13 \text{ mm}^3/\text{N.m} \times 10^{-5}$ for unfilled UPE to $8.53 \text{ mm}^3/\text{N.m} \times 10^{-5}$ and $8.12 \text{ mm}^3/\text{N.m} \times 10^{-5}$ for filled UPE with 1% HNT and 1% s-HNT nanocomposites, respectively.

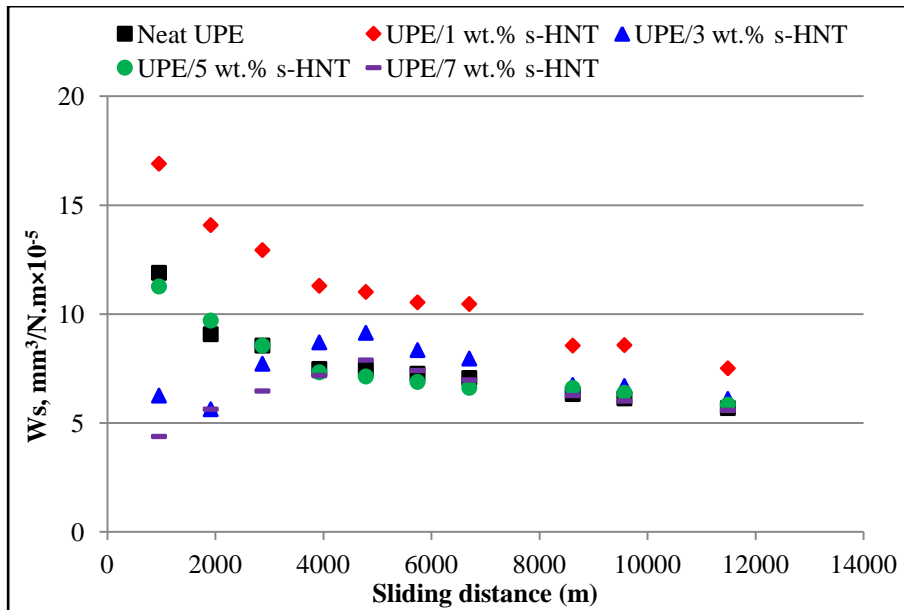


Figure 6.7: Specific Wear Rate of Neat UPE and UPE/s-HNT Nanocomposites Tested at Sliding Distance of 11.5 Km, Normal Load of 20 N and Sliding Speed of 2.8 m/s

Nevertheless, further additions of nanoparticles to the UPE resin demonstrated better wear resistance, where a 7 wt% HNT or s-HNT incorporation had the lowest values of the specific wear rates. This finding is in accordance with the study conducted by Zhang et al. (2013), where they claimed that a continuous transfer film could be formed on the counterface only with higher nanoparticle contents (≥ 10 wt%). However, these results would contrast with those mentioned in Sections 5.2.2 and 5.2.3 regarding the mechanical and thermodynamic properties, which showed that further increase of halloysite induced lower properties. On the other hand, Jia et al. (2008) and Siddhartha, Patnaik and Bhatt (2011) revealed that the 3-D network structure of thermoset polymers prevent them being an ideal material for sliding wear applications, compared to thermoplastics. Hence, one should say that there is no simple correlation between mechanical properties (strength, Young's modulus and fracture toughness) and the wear properties of thermosets-based nanocomposites.

To reiterate again, despite the improvement of the mechanical properties of polymer-based nanocomposites due to the incorporation of surface-modified nanoparticles, no qualitative evidence shows a positive role of these particles in terms of improving the tribological performance of the nanocomposites. However, there is concurrence

regarding the improved particle dispersion in the polymer matrix due to the surface modification. However, in this study, it was noted that the well-dispersed particles in the nanocomposites irrevocably were not associated with any improvement in the friction and scratch-wear resistance.

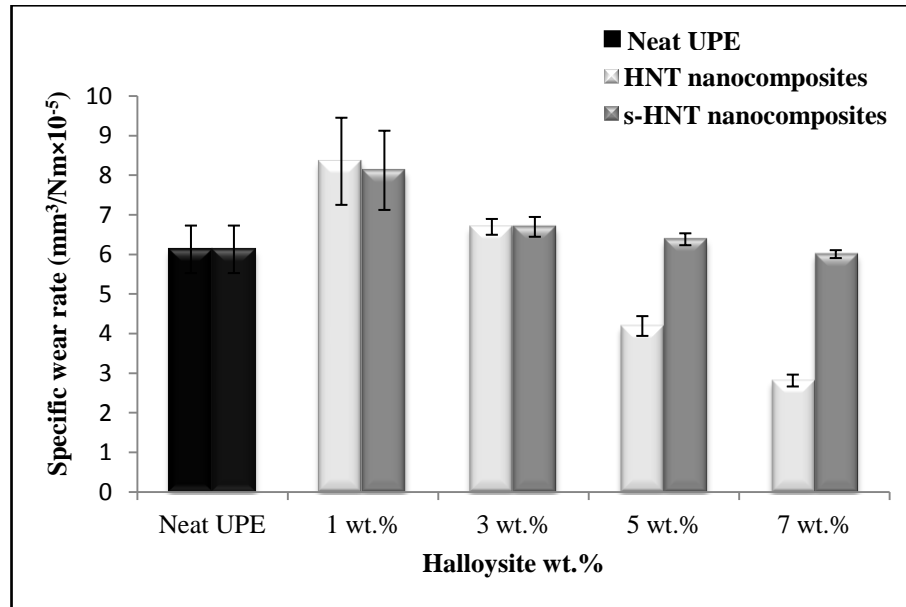


Figure 6.8: Specific Wear Rate of Neat UPE and its Nanocomposites Under Wearing Conditions of Sliding Distance: 11.5 Km, Load: 20 N and Sliding Speed: 2.8 m/s

Figure 6.9 shows the typical curves of contact temperatures as a function of sliding time for neat UPE and its nanocomposites. It seemed that the longer the sliding time, the higher the contact temperatures for all materials. This was an obvious phenomenon since the energy dissipated by friction generates heat, which then flows into the rubbing bodies, thereby causing an increase in the ring's temperature. Both untreated and silane-treated halloysite nanocomposites achieved the lowest peak values of contact temperature. These reduced contact temperatures could be ascribed to the thicker transfer film that formed on the counterface when the role of nanoparticles acted as a thermal barrier (Friedrich, Zhang & Schlarb 2005; Chang et al. 2007).

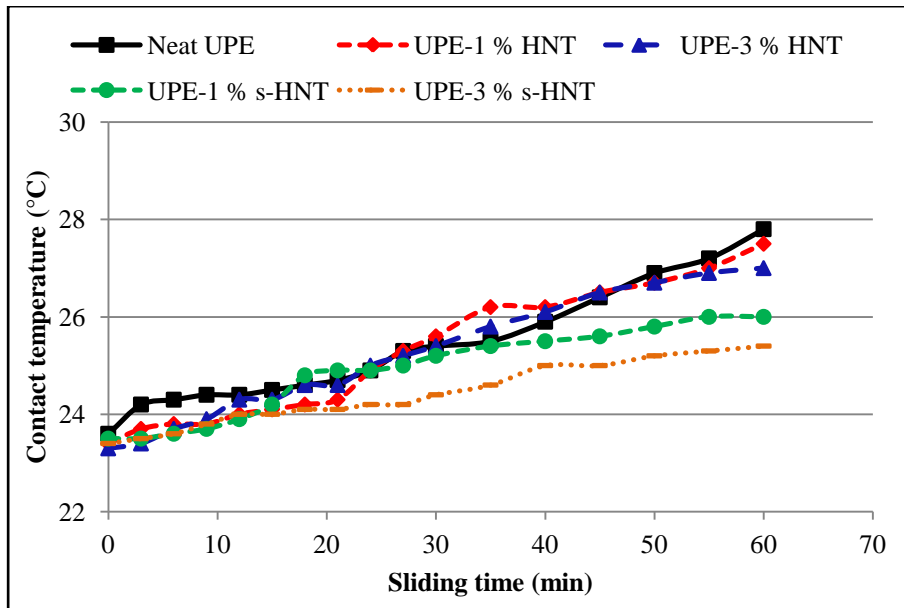


Figure 6.9: Typical Curves of Contact Temperatures as Functions of Sliding Time for Neat UPE and its Nanocomposites

As the wear processing continues, the temperature of the counterface track rises due to a relatively lower thermal conductivity of polymers, leading to softening, melting and pyrolysis on the surface of the polymer, and thereby forming a continuous film that obliterates the original machining marks on the surface. In general, there are several parameters affecting the formation of the transfer film and its role on the subsequent wear processes (such as the thickness of transfer film, cohesion between the transfer layers, adhesion between the transfer film and the slider, sliding conditions, and energy consumed in the processes of friction and wear). The kinematics of the contact configuration also affect the formation of transfer film and thus the overall wear response.

To obtain more information about the wear mechanism, the worn surfaces and the transfer film on the wear tracks for pure UPE and UPE filled with different halloysite, the nanocomposites were examined by SEM, as shown in Figures 6.10 and 6.11. At the low-magnification observations, the morphology of the worn surface for different nanocomposite systems appeared similar, with all involving microgrooves formed parallel to the sliding direction. These microgrooves were formed due to the ploughing actions of rigid metal counterface asperities on the soft polymer/composite surfaces.

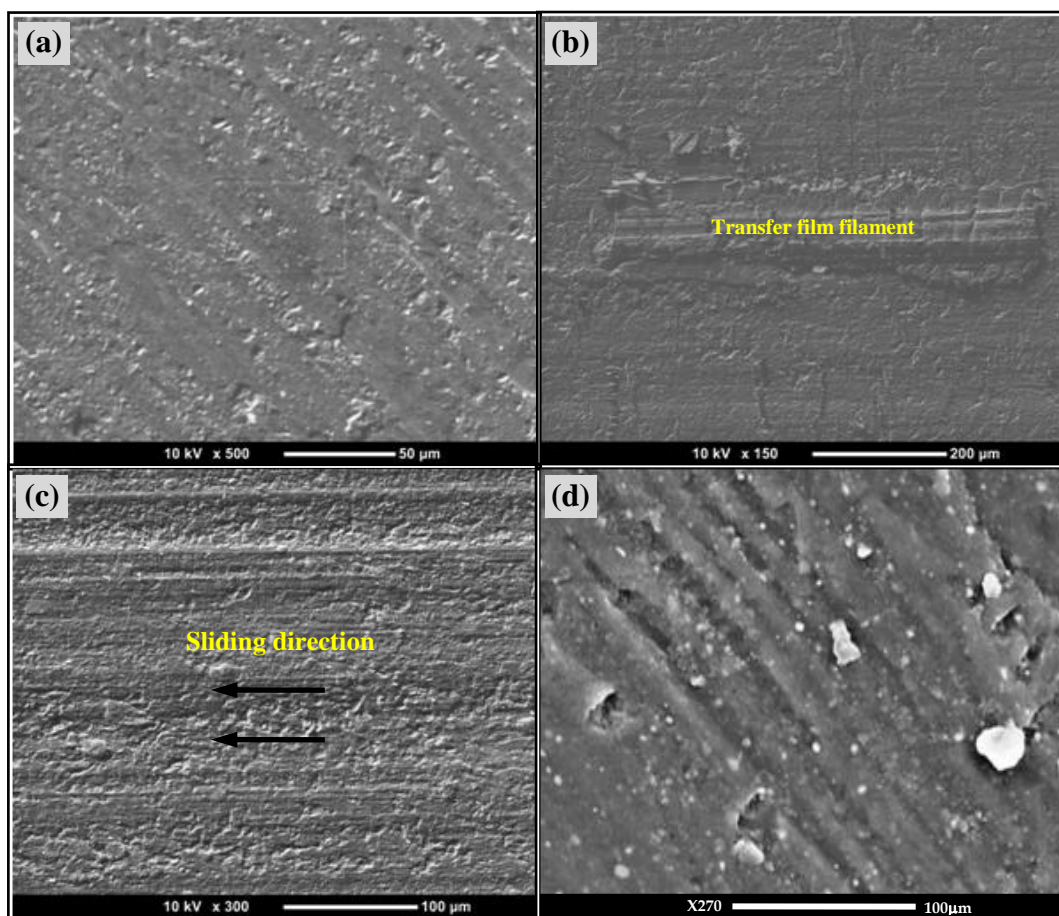


Figure 6.10: SEM Micrographs of the Worn Surfaces for: (a) UPE/1% HNT, (b) UPE/3% HNT, (c) UPE/5% HNT and (d) UPE/7% HNT Nanocomposites

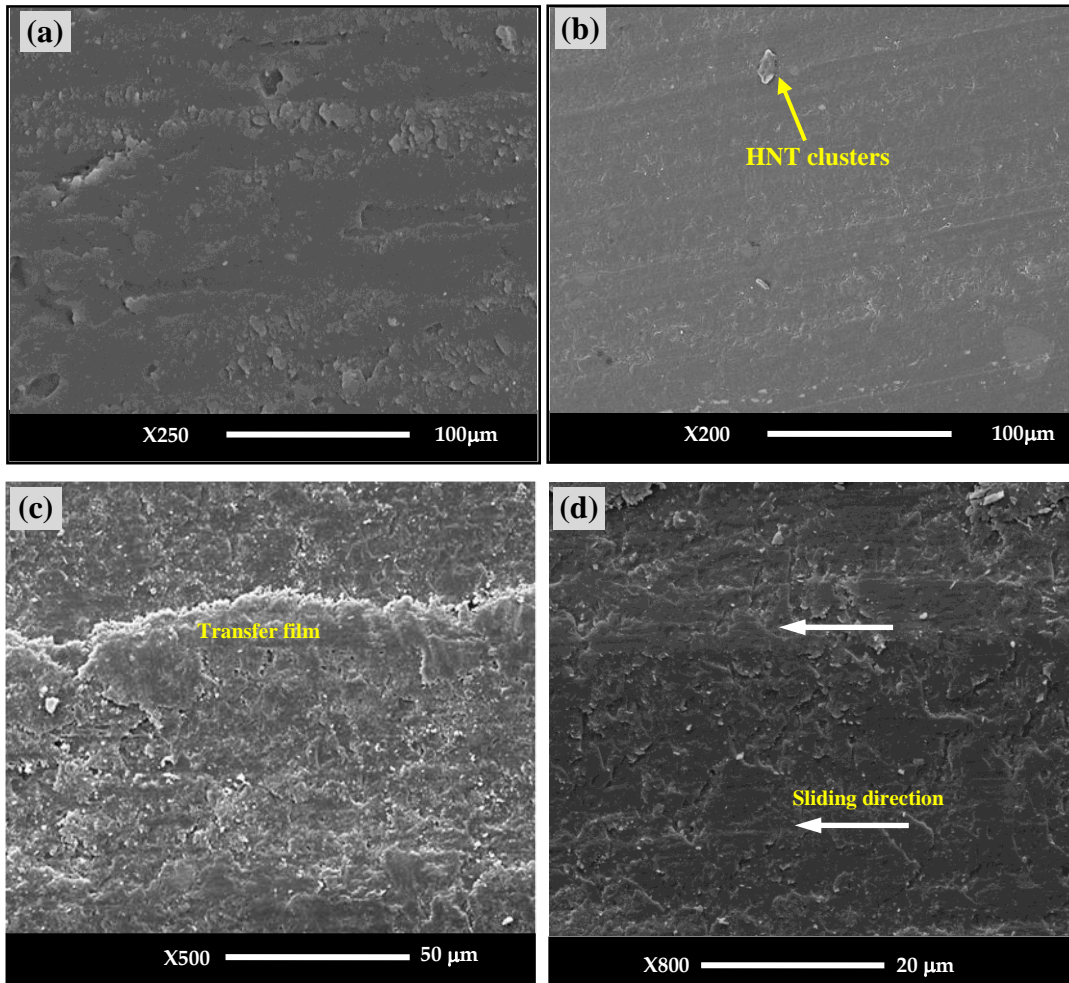
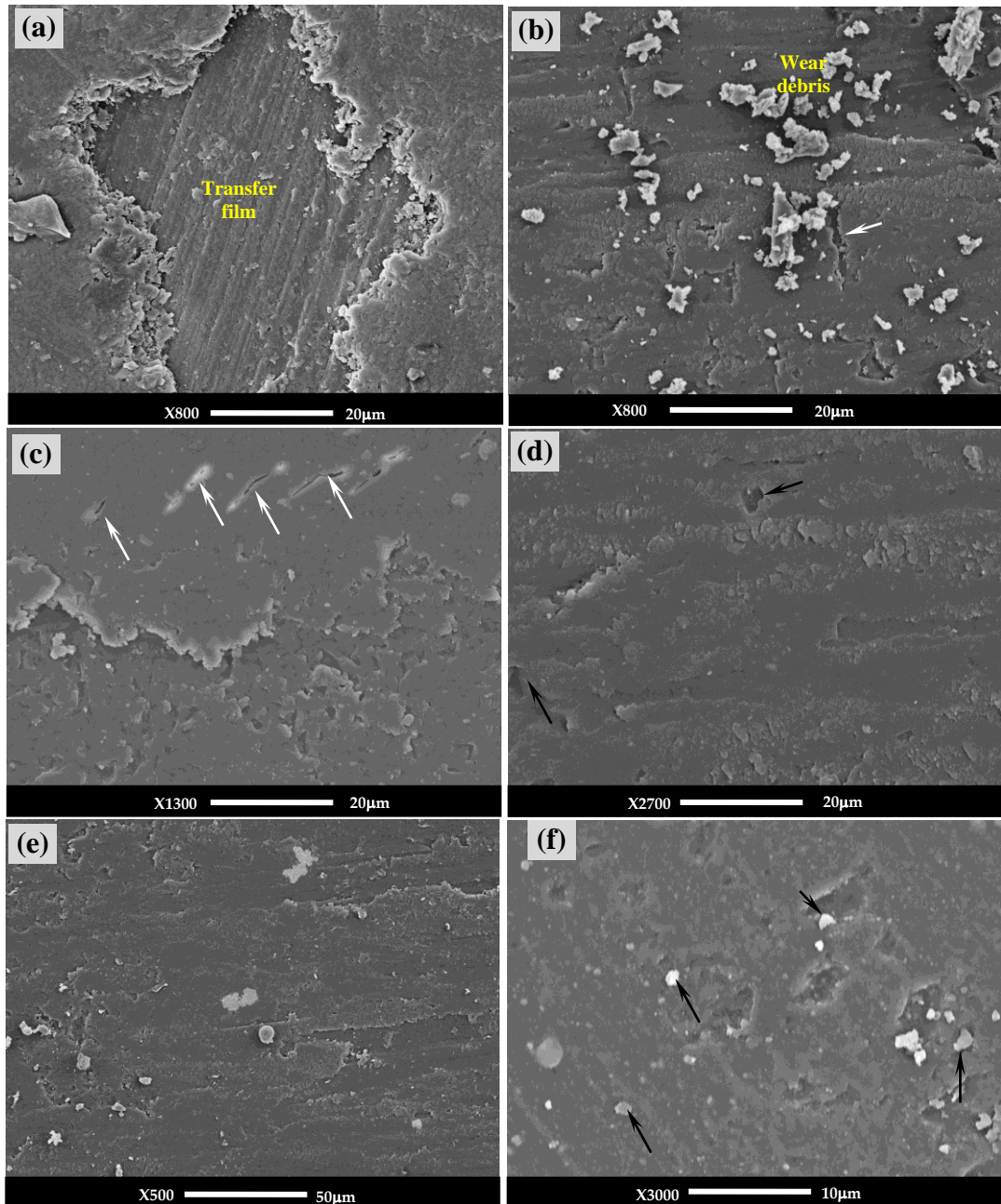


Figure 6.11: SEM Micrographs of the Worn Surfaces for: (a) UPE/1% s-HNT, (b) UPE/3% s-HNT, (c) and (d) UPE/5% s-HNT Nanocomposites

Figure 6.12a shows a large flake-like segment that has broken (detached) and peeled off from the UPE nanocomposite filled with 3% HNT due to the applied load and slider velocity as polymer film transfer. It is believed that subsurface damage and extensive material loss occurred due to the repeated sliding of the hard counterface asperities on the soft surface of the nanocomposite, which consequently extended, detached and pulled out the particles as wear debris. These broken and released particles could result in the initiation of the debonding first and the elongated cracks later, resulting in a large amount of debris (ploughing and furrowing) and a high abrading wear rate (Dasari et al. 2007; Dasari, Yu & Mai 2009). See Figure 6.13 for further understanding of this phenomenon. The mechanism of wear debris forming on the worn surfaces seemed to be an abrasive wear (see Figure 6.12b). The mechanism of the abrasive wear is generally associated with micro ploughing, micro

cutting and micro cracking wear due to hard asperities of the counterface slider. It can also occur by material transfer from one surface to the another (Cenna et al. 2001).



Note: The white arrows show debonding initiation and formation of the cracks beneath the wear track, while the black arrows indicate the voids due to the particles pulling out.

Figure 6.12: SEM Micrographs of the Worn Surfaces for: (a) UPE/3% HNT, (b) UPE/5% HNT, (c) UPE/7% HNT, (d) UPE/3% s-HNT, (e) UPE/5% s-HNT and (f) UPE/7% s-HNT at a Sliding Speed of 2.8 m/s and Applied Load of 20 N

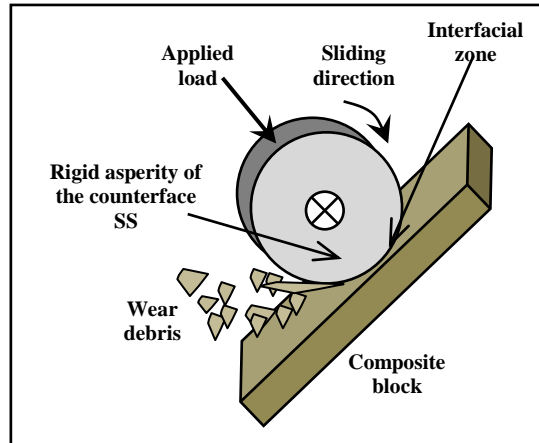


Figure 6.13: Schematic Represents a Dry Interfacial Wear Mechanism

At higher concentrations of halloysite content, the surface exhibited a relatively lower density than the UPE resin, hence a surface pitting occurred, leading to initiate debonding, delamination, and subsequently forming cracks beneath the wear track, as illustrated by the white arrows in Figure 6.12c. This was perhaps due to the weak interfacial adhesion between the particles and matrix. To conclude, based on the microscopic observations, the dominant wear damage in UPE/HNT nanocomposites was mainly caused by two-body abrasion wear and three-body abrasion wear. The two-body abrasion occurred when hard counterface asperities ploughed and caused plastic deformation or fracture of the softer composites; while the three-body abrasion occurred when hard abrasive particles or wear debris were introduced to the sliding contact, either as products of two-body abrasion or as environmental contaminants.

In contrast, upon the incorporation of s-HNT, a transition in the wear mechanism from three-body abrasive to two-body abrasive wear was noticed. This was likely due to the decrease in surface friction, leading to a transition from particles rolling over the surface to sliding across the surface. However, during the prolonged sliding, the adhesive wear mechanism of UPE/s-HNT nanocomposites was the dominant theory, accompanied with a series of microvoids formed from the particles pulling out. Junctions or fragments from a relative motion and the contact between hard asperities and the polymer/composites surface were formed due to the heating generated from the physical and chemical interactions. On further sliding, these fragments ruptured under shear and detached on the slider contact surface, resulting

in an adhesive wear (Wan et al. 2006; Dasari, Yu & Mai 2009). Interestingly, the interfacial debonding and subsurface cracks that appeared through the untreated particles nanocomposites completely disappeared in the UPE/treated particles nanocomposites, disregarding particle content. This was because no delamination in silanised particles had taken place because the bifunctional silane coupling agent resulted in a good interface between the hydroxyl groups on the halloysite surface and the UPE network.

6.1.3 Summary of the Results

In this study, the critical role of incorporating untreated HNT and s-HNT on the tribological performance of a UPE-based nanocomposite was investigated. The following points were the main findings:

1. The role of HNT or s-HNT on the friction coefficient and specific wear rates of the UPE nanocomposites showed a negative effect at low particle contents, and better friction and wear resistance at higher particle contents in the UPE matrix. The 1 wt% HNT, s-HNT particles-filled UPE nanocomposite showed the worst wear resistance—that is, higher material loss and higher specific wear rates—while the 7 wt% HNT, s-HNT nanocomposites showed the best wear resistance.
2. The role of silanised halloysite particles on the tribological performance manifested an insignificant effect or even a negative role in some cases, despite the improved particle dispersion in the polymer matrix and the good interfacial adhesion between the modified surface particles and the polymer matrix thereof.
3. Based on the microscopic observations, the dominant damage mechanism of the worn surfaces was two-body abrasion wear and three-body abrasion wear for the UPE/HNT nanocomposites, and was adhesive associated with pitting and particles pulling out for the UPE/s-HNT nanocomposites. Microgrooves parallel to the sliding direction, formed due to the ploughing actions of the rigid counterface asperities on the soft polymer/nanocomposite surface, were observed in the morphology of the worn surface for neat UPE and its nanocomposites systems.

6.2 Role of Silanised Halloysite on Impact Fracture Behaviour

6.2.1 Background

The generation of a 3-D network structure with crosslinking chains in thermoset polymers—from a free-radical copolymerisation between a low molar mass (prepolymer) that possessed several covalent C=C bonds and a monomer (solvent), typically styrene—induces localised plastic deformation in front of the crack tip, with a little absorption of energy, leading to catastrophic brittle failure (Young & Lovell 2011). Therefore, much effort has been devoted to reducing the brittleness and damage severity of the thermosets, without sacrificing their strength and stiffness.

For this purpose, various synthetic strong fibres (glass, carbon, Kevlar and so forth) have been initially and continuously used in producing composites with good mechanical properties, low cost and low weight. However, several drawbacks can accompany the manufacturing processes of fabric composites because they need to be laid up one-by-one and being isolated by a layer of matrix thereby long and well-bonded fibres have to be guaranteed. Otherwise, the weak adhesion at the interface induces poor reinforcement and properties due to the reduction of the stress transfer between the fibres and the polymer matrix (Banea & Silva 2009). Moreover, other issues associated with polymer fibre composites include the weakness in out-of-plane direction, when compared with in-plane direction, and the anisotropic behaviour of the laminate composites (Gibson 2007).

The recent emergence of nanotechnology and newly developed nano-reinforcements (such as CNTs, nano-SiO₂, nano-Al₂O₃, nano-TiO₂, nanoclay and HNTs) have led the literature of polymer nanocomposites to become one of the most popular areas for current research and development (Paul & Robeson 2008). Thus, many diverse investigations have been conducted to examine a broad range of topics, including structure-property relationship, composite reinforcement, non-reinforcement (flame resistance, barrier properties) and so forth. Among these, some preliminary studies have been conducted on the impact resistance of polymer nanocomposites.

For example, Yuan and Misra (2006a) examined the micromechanism of plastic deformation under impact loading of PP/clay nanocomposites in the temperature range from -40 to +70°C. They found that the impact strength in the range of 0 to +70°C increased with the addition of clay into the PP. The enhancement of the nanocomposite's toughness on reinforcement of PP with nanoclay was explained by the change in the primary mechanism of plastic deformation from crazing and vein-type in neat PP to microvoid-coalescence-fibrillation in the nanocomposites.

Lin (2008) characterised the fracture behaviour under impact loading of three different polymer matrices (polyacrylate, polyimide and PP) reinforced by silicate layers. The results showed that the interfacial crack area in low-energy impact was reduced for all silica-filled composites due to the interfacial reaction providing an effective barrier for advancing cracks. The polyacrylate/30 wt% silica had the best structural stiffness of the specimens tested. Moreover, using multi-walled carbon nanotubes enhanced the load-carrying capability and toughness of the PP composites. It was found that the impact resistance was highly temperature-dependent, since it notably improved at a temperature above the glass transition temperature (T_g) of the polymer. It was also observed that the impact behaviour varied with the length of the nanotubes—the longer nanotubes exhibited higher toughening efficiency than did the shorter ones at temperatures above T_g (Zhang & Zhang 2007).

Nevertheless, there has thus far been no qualitative study describing the effective role of nanoparticles on the energy dissipation and material resistance in thermosetting polymers under impact loading. This experimental investigation investigates the role of pristine untreated HNT and s-HNT on the impact fracture behaviour of UPE-based HNT, or s-HNT nanocomposites. It also considers the relationship between morphological structures and total energy absorption under impact loading in a range of temperature from -20 to +60°C. Chapter 3 detailed the procedure, materials used for the impact experiments, and preparation of nanocomposites based on HNT or s-HNT particles. The implementation of the impact strength and total energy, as well as the SEM examination of the fractured-surface morphology, were also given.

6.2.2 Results and Discussion

6.2.2.1 Impact Testing

The impact strength and total energy of unfilled UPE and its nanocomposites as a function of different HNT loadings and testing temperatures (-20°C, +20°C and +60°C) are shown in Figures 6.14 and 6.15, respectively. It can be observed from the figures that both impact strength and the amount of energy absorbed by specimens during the entire impact test (total energy) modestly increased with the addition of halloysite of up to 5 wt% in all testing temperatures.

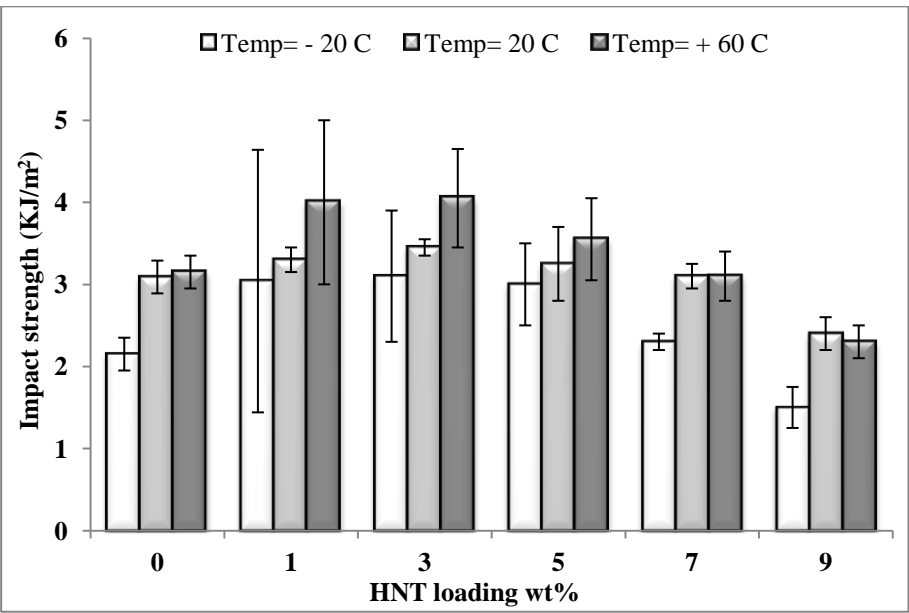


Figure 6.14: Comparison of the Impact Strength for Neat UPE and its Nanocomposites as a Function of Untreated Halloysite (HNT) and Temperature

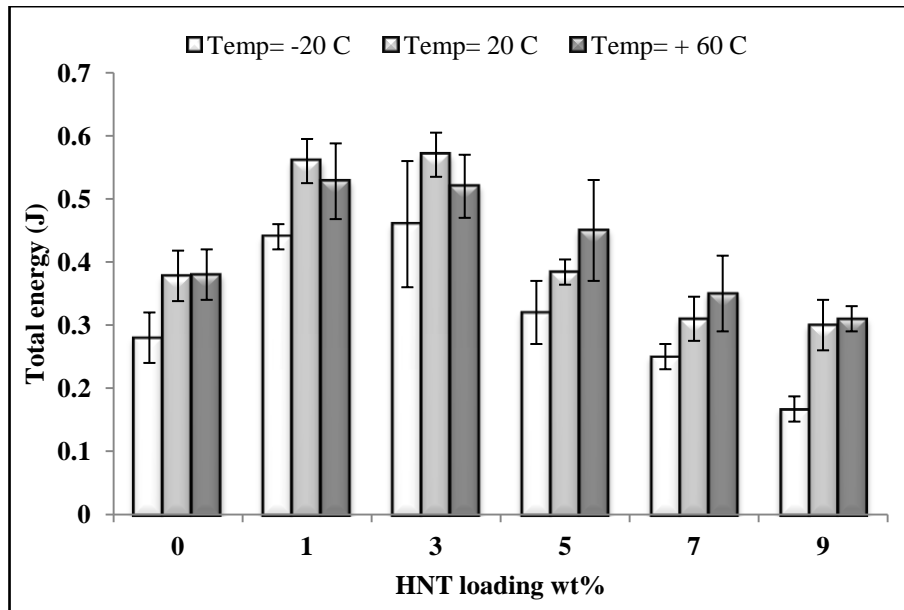


Figure 6.15: Variation of the Total Energy for Neat UPE and its Nanocomposites as a Function of Untreated Halloysite (HNT) and Temperature

However, further addition above this content caused decreasing impact strength due to particle clustering and the poor interactions between the HNT particles and polymer. This agrees with the findings of Lin et al. (2011), which reported a tremendous improvement in impact strength obtained after reinforcing PS with up to 5 wt% HNT nanocomposites, but further addition (> 5 wt%) of HNT significantly reduced the impact strength of the PS/HNT nanocomposite.

Along with the role of nanoparticles on the impact parameters (impact strength and total energy) of the nanocomposites, it was observed that these parameters were temperature-dependent, with a moderate increase following an increase in the testing temperature, regardless of the halloysite content (see Figures 6.14 and 6.15). Indeed, the manner behind which is upon increasing HNT content, the ductile-brittle transition temperature (DBTT) increased and made the composite more brittle below this transition. When the testing temperature increased, the interfacial strength that affects the DBTT improved, thereby inducing an important toughening criterion and interparticle ligament thickness (Yuan & Misra 2006b).

From the results obtained, at sub-zero temperature (-20°C) and room temperature (+20°C), all nanocomposite systems broke in a brittle manner because they could not

absorb much energy before failing. This phenomenon was characterised with an abrupt breakage after reaching the peak values of impact load. Comparatively, obvious crack propagation took place for samples impacted at higher temperatures (+60°C), which approximated to the glass transition temperature (T_g) of the UPE, so that the test time (or fracture deflection) was dramatically prolonged (Friedrich, Fakirov & Zhang 2005).

In terms of using s-HNT on the impact parameters, it was found that the impact strength and total energy of the nanocomposites slightly improved with the incorporation of s-HNT into the UPE matrix, as shown in Figures 6.16 and 6.17, respectively. This increase may be attributed to the good interfacial adhesion between the s-HNT and UPE matrix due to being chemically treated with silane. This could assist to prevent the cracks propagation generated through the impact test. Better interfacial bonded materials require more energy-absorbing capacity, which subsequently leads to higher impact strength (Deng, Zhang & Ye 2009).

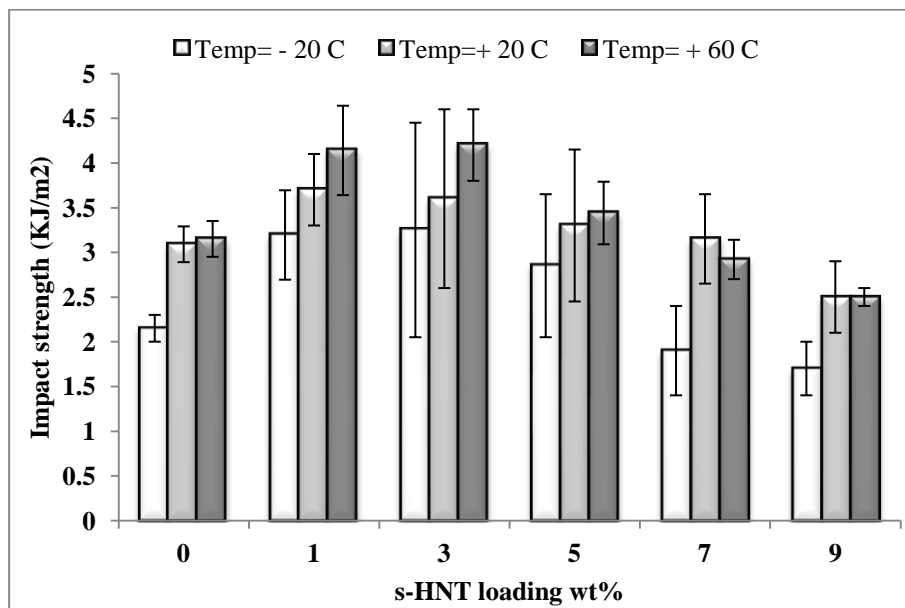


Figure 6.16: Impact Strength of Neat UPE and its Nanocomposites as a Function of s-HNT Content and Temperature

At room temperature (20°C), the impact strength of the UPE nanocomposites improved by 12% upon reinforcement of the UPE matrix with 3 wt% HNT, and by 17% after introducing the same amount of s-HNT particles. That is, it increased from

3.09 KJ/m² for unfilled UPE to 3.45 KJ/m² and 3.6 KJ/m² for UPE filled with 3 wt% HNT and 3 wt% s-HNT composites, respectively. At higher temperatures and upon using the same quantities of 3% HNT or 3% s-HNT particles, the impact strength of the nanocomposites further improved by 28% and 33%, respectively. Morote-Martinez, Pascual-Sanchez and Martin-Martinez (2008) revealed that the addition of nanosilica to the UPE resin imparted a higher shear thinning index value, which subsequently resulted in higher pseudoplasticity and better impact strengths.

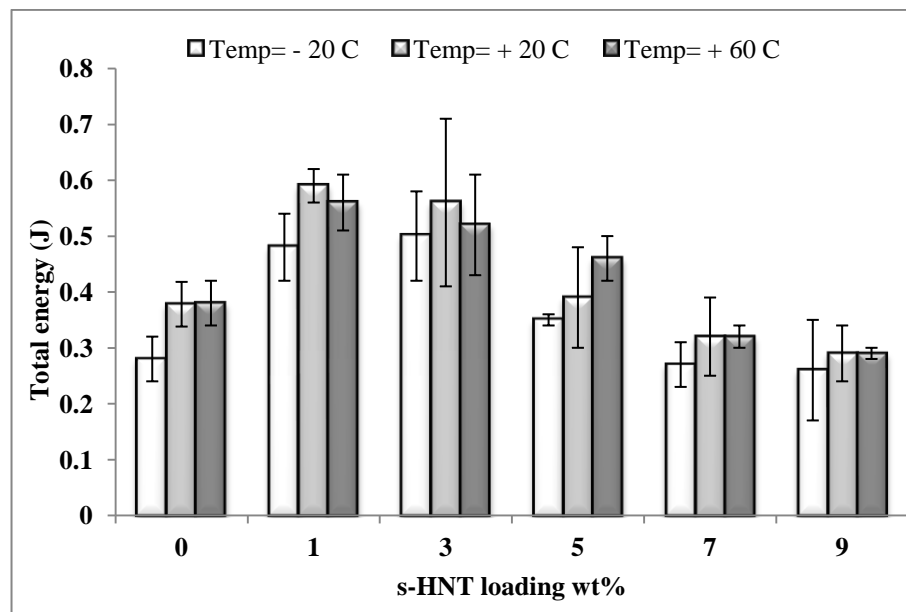


Figure 6.17: Variation of the Total Energy for Neat UPE and its Nanocomposites as a Function of S-HNT Loading and Temperature

Further, it was revealed that the addition of silane-treated nanosilica gives thixotropy to the UPE resin, resulting in higher impact energy values and improved rheological properties. All of these were attributed to the low primary particle size of nanosilica, which contains siloxane and silanols groups on its surface. Moreover, the uniform distribution of HNT particles in the UPE matrix, as shown in the TEM micrographs in Figure 6.18, was found to affect the deformation behaviour towards a higher energy absorption by activating localised cavitation craze-like and shear yielding mechanisms.

However, further increase of halloysite in the thermosetting UPE matrix tended to increase the tendency of particle agglomerations in the nanocomposite. These may

have acted as stress concentrators, increased the surface reactivity, increased the brittleness and reduced the absorbed impact energy and the impact strength, since a highly crosslinked network of thermoset is very sensitive to notches and local inhomogeneities. The impact strength decreased from 3.09 KJ/m² for neat UPE to 2.4 KJ/m² and 2.5 KJ/m² for UPE filled with 9 wt% HNT and s-HNT nanocomposites, respectively.

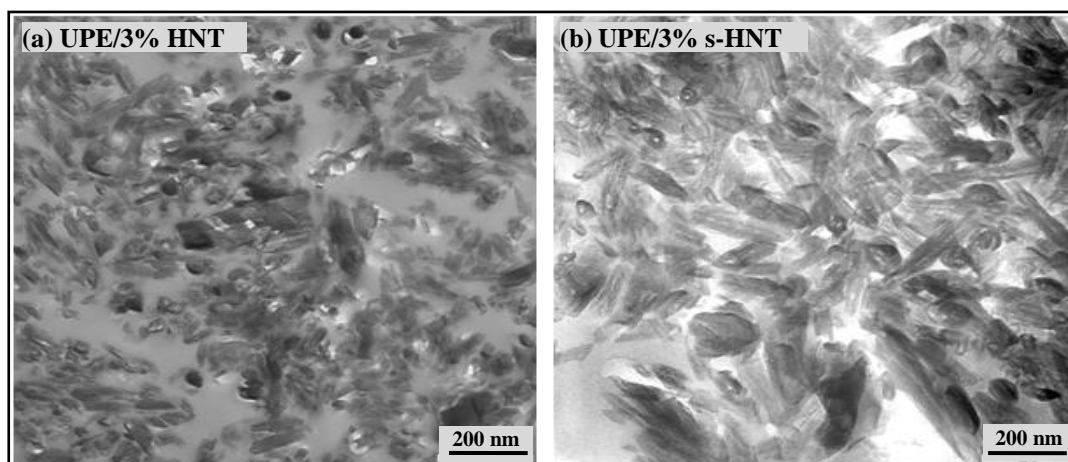


Figure 6.18: TEM Micrographs of UPE Filled with: (a) 3 wt% HNT Nanocomposite and (b) UPE with 3 wt% s-HNT Nanocomposite

6.2.2.2 Impact-fracture Morphology

To identify the fracture mode at a microscopic level, as well as the role of halloysite on toughening mechanisms in the nanocomposites under impact load, the morphology of impacted fracture surfaces deformed by weight drop at room temperature for neat UPE and UPE/3% HNT and UPE/3% s-HNT nanocomposites were examined using SEM, as shown in Figure 6.19. As expected, it was revealed that the fracture surface of the unfilled UPE (Figure 6.19a) was smooth (fast brittle fracture mode)—that is, no absorbed energy occurred in the polymer resin.

In contrast, the morphology of the impacted-surface for the HNT nanocomposites (Figure 6.19b) exhibited plastic deformation with the presence of halloysite in the polymer matrix, which could contribute to hindering the crack propagation in the composite nanostructure. Nevertheless, high halloysite contents, a high strain rate of dropped tip of the tup in the impact machine, and a dense network of the crosslinked

UPE led to restrict the extent of plastic deformation and subsequently reduced the impact strength.

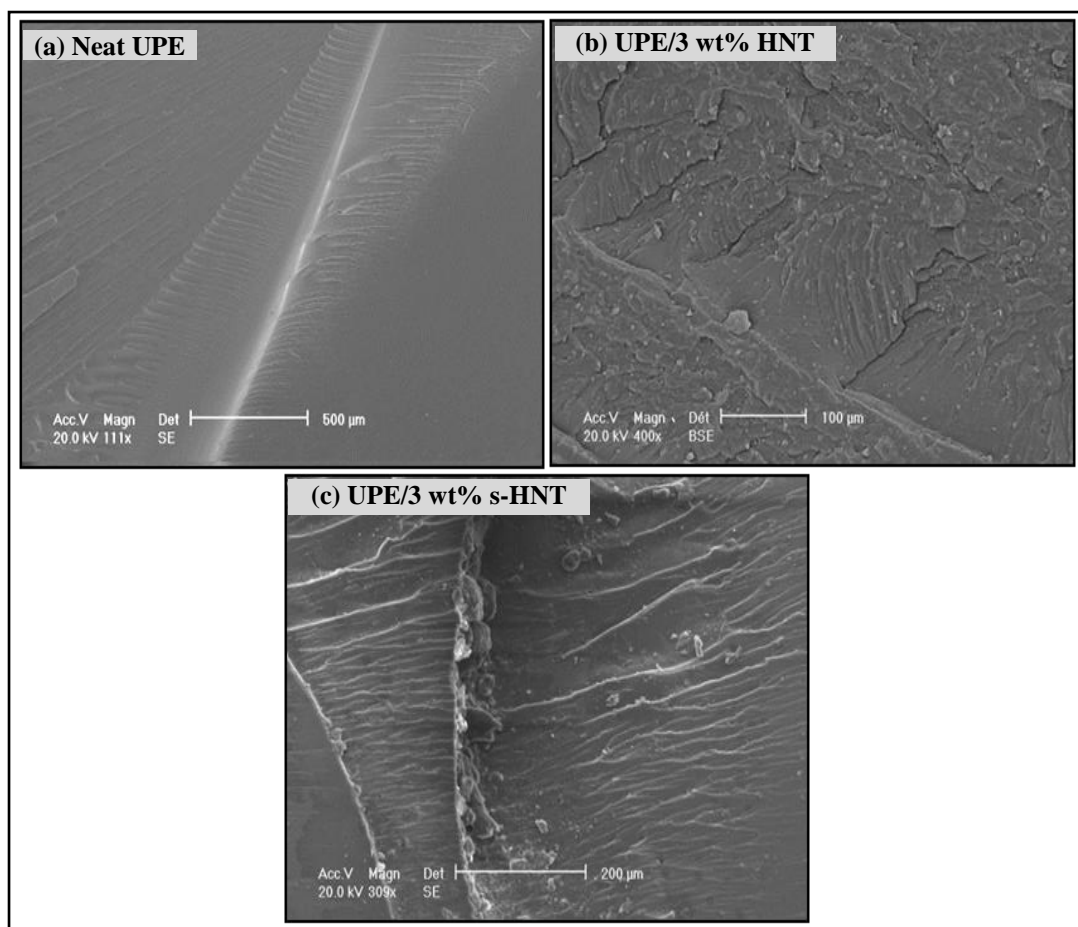


Figure 6.19: SEM Micrographs of Fractured Surfaces for: (a) Neat UPE, (b) UPE/3 wt% HNT and (c) UPE/3 wt% s-HNT Nanocomposites Impacted at Room Temperature

The incorporation of s-HNT into the UPE matrix (Figure 6.19c) led to the creation of plastic deformation, while the dominant mechanism of the energy absorption was the shear yielding mechanism. Such plastic flow might spread shear bands in the whole sample, absorbing a significant quantity of energy, or might tend to localised yielding, resulting in isolated shear bands. The manner of such phenomenon is again due to the functionalising of the surface of halloysite with the silane coupling agent inducing good interfacial adhesion and uniform morphological structures. The impact resistance of particulate-filled polymer composites largely depends on these parameters and is highly dependent on the presence and shape of stress concentrators and molecular properties (Nelson 2010).

Generally speaking, in unfilled thermosetting polymers, the impact toughness and molecular aspects of craze/yield behaviour are controlled by two parameters—the entanglement density and characteristic ratio of the chain (Pascault et al. 2002; Srivastava & Koratkar 2010). The higher the crosslink density, the lower the impact fracture toughness at any given temperature, where the glass transition temperature will be shifted upwards and the total crack-tip strain will be limited. The impact toughness and brittle-ductile transition are related to the filler shape and content, particle size and distribution in the polymer nanocomposites.

To conclude, the critical role of untreated and silane-treated halloysite on the impact fracture behaviour of UPE nanocomposites, variations of impact strength and total energies for neat UPE and its nanocomposites are given in Figures 6.20 and 6.21, respectively. The incorporation of up to 5 wt% of halloysite into the UPE matrix demonstrated relatively higher impact parameters over the neat UPE. The effect of silane-modified halloysite on these parameters was even higher due to the improved dispersion of particles in the polymer and improved interfacial adhesion between the silanised particles and the polymer. However, higher halloysite loadings showed a gradual reduction in impact toughness. Further, the impact properties of crosslinked thermosets nanocomposites seemed to be temperature-dependent, with the impact strength of nanocomposites tested at higher temperature (60°C) exhibiting significant enhancement compared to those tested at sub-zero temperatures or even at room temperature. Nevertheless, several studies have been devoted to impart the ductility and increase the impact strength by blending them with impact modifications, such as reactive (flexibilisers or elastomers) or nonreactive (plasticisers) (Huang et al. 1993; Srivastava & Koratkar 2010).

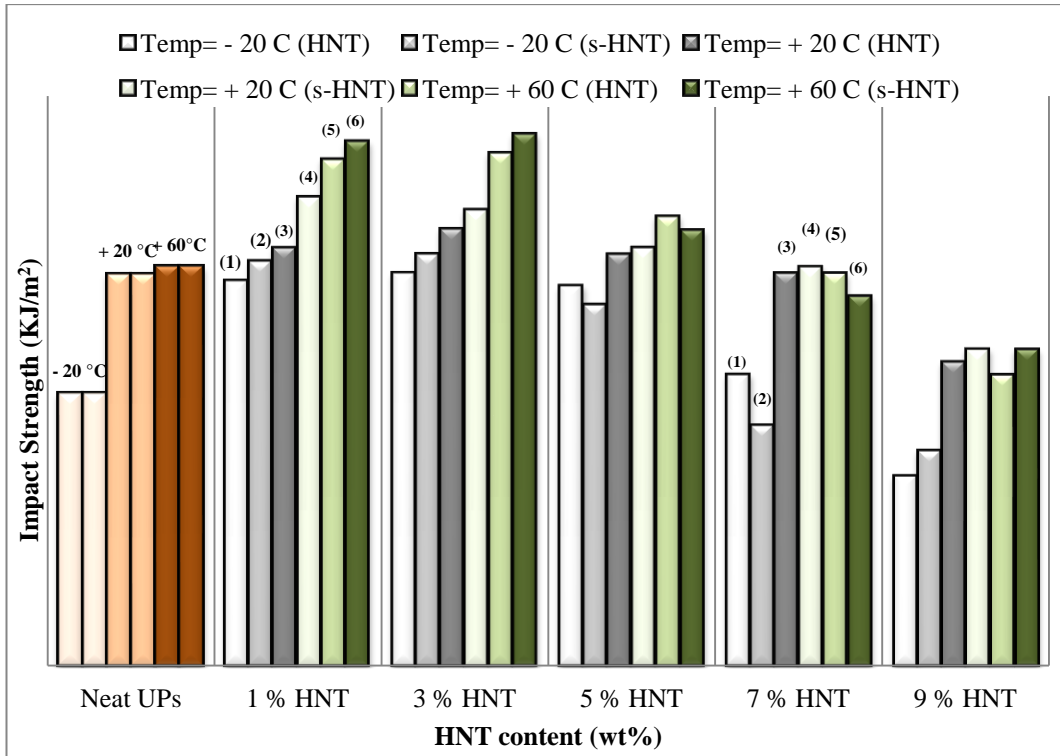


Figure 6.20: Variations of the Impact Strengths for Neat UPE and its Nanocomposites as a Function of Different Halloysite (HNT and s-HNT) Contents and Testing Temperatures (-20°C, +20°C and +60°C)

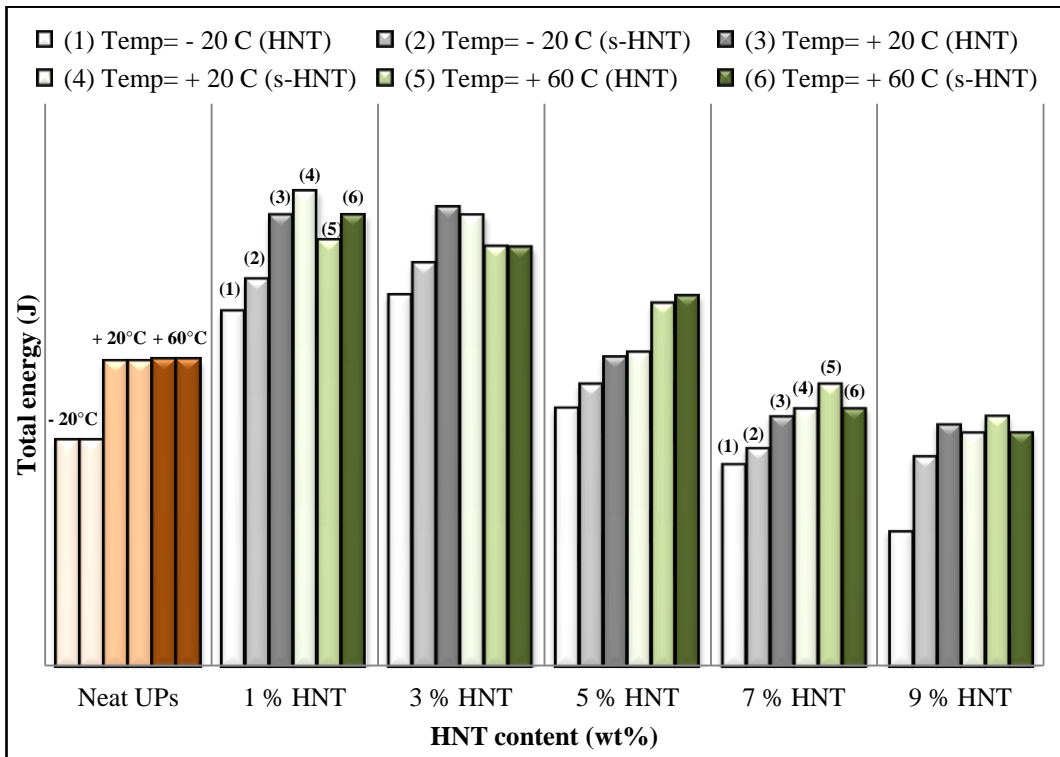


Figure 6.21: Variations of Total Energies for Neat UPE and its Nanocomposites as a Function of Different Halloysite (HNT and s-HNT) Contents and Testing Temperatures (-20°C, +20°C and +60°C)

6.2.3 Summary

This experimental study was performed to identify the role of unmodified HNT and s-HNT on the impact performance for neat UPE and its nanocomposites, using a falling-weight tester. The correlation between the morphological and impact strength under different particle loadings was also determined. The impact test was conducted in a temperature range from -20°C to +60°C, and the following points describe the main results:

1. The impact strength and total energy slightly increased with the addition of HNT or s-HNT up to 5 wt% for all testing temperatures. However, further increase in the halloysite content induced lower impact strength, owing to the presence of halloysite clusters and the poor interactions between the halloysite and the polymer.
2. All materials had fast shatter when impacted at sub-zero temperatures. However, increasing the testing temperature to be closer to the T_g value of the polymer tended to improve the impact parameters, with an acceptable toughening criterion due to the improved interfacial strength and the shifted DBTT thereof.
3. Considering the SEM observations, the presence of halloysite in the UPE resin caused change in the fracture mode from cleavage and fast brittle fracture in the neat UPE to microvoid-coalescence with minor plastic deformation in the nanocomposites.

Chapter 7: Role of Silanised Halloysite on Failure and Toughening Mechanisms of Thermoset Nanocomposites

7.1 Background

Measuring fracture toughness and materials' resistance to crack growth in thermosetting polymers-based nanocomposites has become a prominent area in current research and development. This is considered important because thermosets have a giant macromolecule covalently bonded network structure, with high crosslink density and little dissipated energy—that is, plastic deformation in front of the crack tip is localised, leading to a catastrophic brittle failure (Pascault et al. 2002; Srivastava & Koratkar 2010). Hence, much effort has been devoted to initiate a localised energy-absorbing mechanism in the fracture process zone of such a material to reduce plastic resistance and delay reaching brittle strength (Wetzel et al. 2006; Chen et al. 2008; Liang & Pearson 2010; Gubeljak et al. 2011; Kumar, Chitsiriphanit & Sun 2011; Quaresimin, Salviato & Zappalorto 2012; Zamanian et al. 2013).

For example, Wetzel et al. (2006) experimentally studied the fracture and toughening mechanisms of epoxy/alumina nanocomposites using the LEFM approach. They found that the presence of alumina particles in the epoxy matrix improved the fracture toughness of the nanocomposites and the plastic deformation process and crack pinning occurred thereof, blunting the crack tip. Similarly, the fracture toughness of epoxy/nanosilica (NS) composites increased with increasing NS content due to a zone shielding mechanism that involves plastic deformation. No significant change in the toughness was noticed with changing particle sizes of NS (Liang & Pearson 2010). Four toughening mechanisms were observed in the epoxy/NS composites: particle debonding, matrix ligament bridging, matrix dilation bands and matrix shear banding.

In general, the resistance of a material to crack propagation is represented by the fracture toughness—either the critical stress intensity factor (K_{Ic}) or the critical strain energy release rate (G_{Ic}) values. The K_{Ic} or G_{Ic} values at which crack propagation

occurs depend on many factors, such as loading conditions, temperature, the material and geometry of the specimen, and the crack length and stress concentration (Brooks & Choudhury 2002). Different experimental and numerical investigations reported in the literature have been performed to measure the crack propagation resistance in thermoset polymers/nanocomposites. The fracture behaviour obtained is a reflection of deformation processes taking place at the crack tip.

For example, Giner et al. (2009) and Silani et al. (2012) implemented the XFEM to investigate crack propagation under mixed-mode conditions and to simulate crack initiation and propagation in epoxy/clay nanocomposites, respectively. In the latter study, a cohesive segments method, based on linear elastic traction-separation behaviour and phantom nodes, was considered to numerically simulate the crack growth using the ABAQUS package. Compared to the experimental data, it was proven that this method can successfully predict the crack initiation and propagation path in the epoxy/nanoclay composites. Sun, Gibson and Gordaninejad (2011) predicted the fracture toughness of a CT sample of epoxy/nanosilica composites using a 3-D micromechanics global-local multiscale FE model based on VCCT. The results of the 3-D model, based on a representative volume element, showed good agreement with previously published experimental results that could be applied to study toughness mechanisms at both macro- and nanoscale. Nevertheless, the mechanisms of crack propagation in thermosets-based nanocomposites have not yet been well addressed because it is not simple to analyse shear yielding, and multiple crazing often takes place at the vicinity of the crack tip. The unstable crack propagation in the thermosets further complicates the analysis.

This investigation was aimed at experimentally and theoretically investigating the role of pristine HNT and s-HNT nanoparticles on the failure behaviour of UPE/HNT, or UPE/s-HNT nanocomposites. Thus, a three-fold analysis was considered. First, the toughness of the nanocomposites was characterised in terms of K_{Ic} and G_{Ic} , using two different specimen geometries (SENB and CT) and applying two different loading conditions. Second, the crack initiation and propagation in the nanocomposites was simulated by applying an FE calculation with the ABAQUS software and cohesive element method. Finally, the toughening mechanisms

occurring in the UPE nanocomposites were identified after halloysite nanoparticle incorporation.

The novelty of this study lies in understanding whether the improved wettability and better adhesion between the silanised particles and UPE matrix changed the fracture modes. That is, determining whether the well-embedded rough surface nanoparticles pulled out or immediately broke, deflected the crack path or transferred the stresses between two crack faces as bridging elements. All the experimental materials and methods used to complete this investigation were described in Chapter 3.

7.2 Cohesive Element Model

The cohesive element model was first introduced by Barenblatt (1962) as a mathematical theory based on traction-separation law to explain the decohesion in atomic lattices and cracks formed in brittle fracture. It has been widely used to simulate damage process—that is, crack initiation, propagation and coalescence (Cornec, Scheider & Schwalbe 2003). In simulating crack propagation in a discrete crack along an arbitrary, the cohesive zone model treats each potential crack path as two internal surfaces connected by cohesive tractions (see Figure 7.1). It uses a traction-separation law to describe the damage process between these two surfaces. The crack surfaces resist normal separation (T_n) and tangential sliding (T_t) before covalent bonds break by the cohesive tractions, where they are a function of the respective normal and tangential displacements.

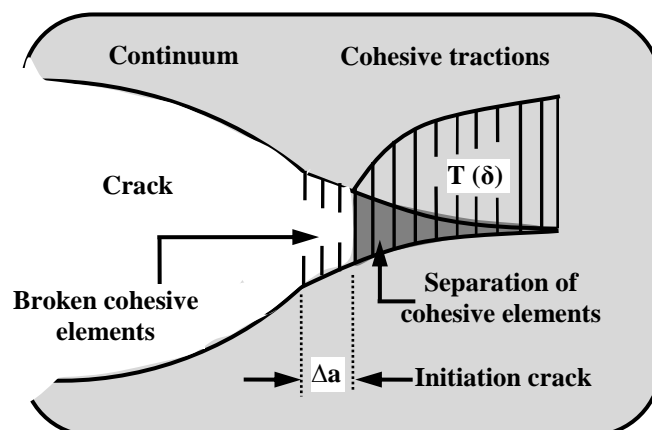


Figure 7.1: Schematic of Fracture Process by the Cohesive Zone Model

7.3 Computational Simulations

This section discusses an FE model used to simulate crack growth along an arbitrary, based on linear traction-separation laws and damage evolution. It also discusses the methods and techniques of computational simulations employed to do this.

7.3.1 FE Model

The simulation of the crack growth through polymer nanocomposites was undertaken using ABAQUS/standard commercial FE software (version 6.11-2). A 3-D eight-node linear brick FE C3D8R model, with reduced integration and hourglass control, was built using cohesive element method and damage for traction-separation laws.

7.3.2 Initiation and Evolution of Damage

In the present analysis, the linear traction-separation model was used, as illustrated in Figure 7.2a. This model assumes initially linear elastic behaviour followed by the initiation and evolution of damage. The linear elastic behaviour is expressed in terms of an elastic constitutive matrix that relates the normal and shear stresses to the normal and shear separations of cracked elements. In 3-D problems, as used here, the nominal traction stress vector, t , consists of normal traction, t_n , and two shear tractions, t_s and t_t . The corresponding separations of these tractions are denoted by δ_n , δ_s and δ_t , respectively, and the elastic behaviour can be written as:

$$t = \begin{Bmatrix} t_n \\ t_s \\ t_t \end{Bmatrix} = \begin{bmatrix} K_{nn} & 0 & 0 \\ 0 & K_{ss} & 0 \\ 0 & 0 & K_{tt} \end{bmatrix} \begin{Bmatrix} \delta_n \\ \delta_s \\ \delta_t \end{Bmatrix} = K\delta \quad (7.1)$$

In Equation 7.1, the off-diagonal components in the stiffness matrix are zero; hence, the normal stiffness K_{nn} and tangential stiffness K_{ss} and K_{tt} will not be coupled. The components K_{nn} , K_{ss} and K_{tt} are calculated based on the elastic properties for an enriched element. Specifying the elastic properties for an enriched element is sufficient to define both the elastic stiffness and the traction-separation behaviour.

Pure normal separation by itself does not give rise to cohesive forces in the shear directions, and pure shear slip with zero normal separation does not give rise to any cohesive forces in the normal direction. The definition of linear evolution of damage model (Figure 7.2b) involves the effective displacement at the initiation of damage, δ_m^0 ; the effective displacement at complete failure, δ_m^f ; and the energy dissipated due to failure, G^C . This model describes the rate at which the cohesive stiffness is degraded once the corresponding initiation criterion is reached.

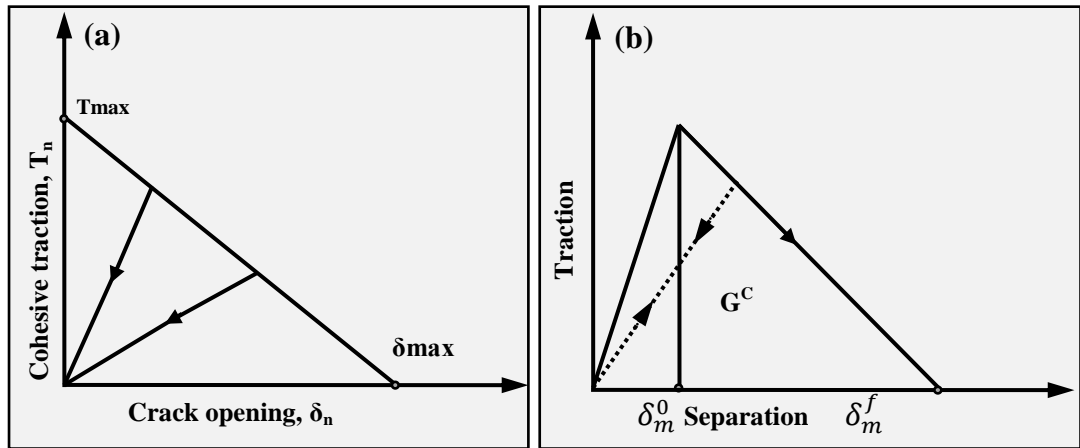


Figure 7.2: (a) Typical Linear Traction-separation Law and (b) Linear Damage Evolution

To simulate the crack growth characterisation in the nanocomposite based on the cohesive element and damage for traction-separation laws, the maximum principal stress (σ_{max}) was extracted from the experimental results, and the damage evolution criterion was built based on 3-D fracture power law. The maximum principal stress criterion is defined in Dai and Jr. (2013) as:

$$f = \left\{ \frac{\langle \sigma_{max} \rangle}{\sigma_{max}^0} \right\} \quad (7.2)$$

where f is the maximum principal stress ratio and σ_{max}^0 is the maximum allowable principle stress. The symbol $\langle \rangle$ represents the Macaulay brackets, which let $\langle \sigma_{max} \rangle$

$$\text{have the alternative value of: } \langle \sigma_{max} \rangle = \begin{cases} 0, & \text{when } \sigma_{max} < 0 \\ \sigma_{max} & \text{when } \sigma_{max} \geq 0 \end{cases}$$

The Macaulay brackets are used to identify that damage does not initiate at a purely stress state, but the damage is assumed to initiate when $f = 1$.

7.3.3 The Geometry of Model, Mesh Module and Boundary Conditions

The CT specimen geometry used for the experimental study was also used for the FE analysis. In order to meet the requirements of the surface-to-surface contact interaction used in this FE model, the CT geometry was partitioned into two faces—master and slave surfaces—using datum plane. See Figures 7.3a and b, respectively.

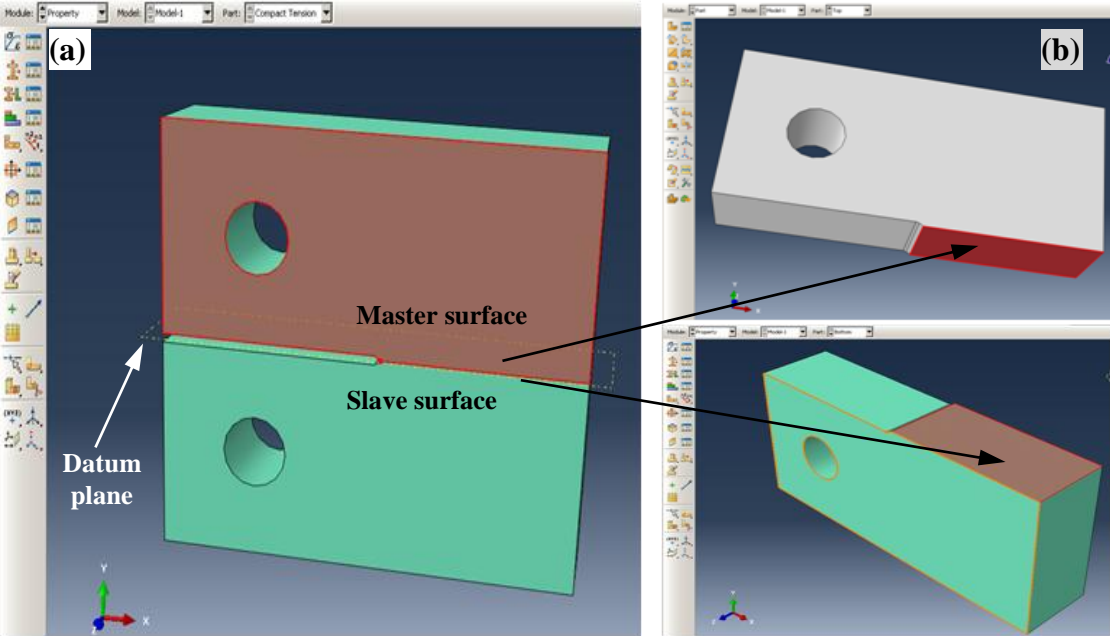


Figure 7.3: (a) Partitioning the CT Geometry Using Datum Plane and (b) Master and Slave Surfaces

The applied displacement and symmetric boundary conditions required to input the data within the analysis step are described in Figure 7.4a. The FE mesh of 5,640 3-D solid elements and 7,047 nodes was generated and the mesh density around local interaction cohesive zone was refined to improve the quality of mesh and obtain more convergent results, as shown in Figure 7.4b.

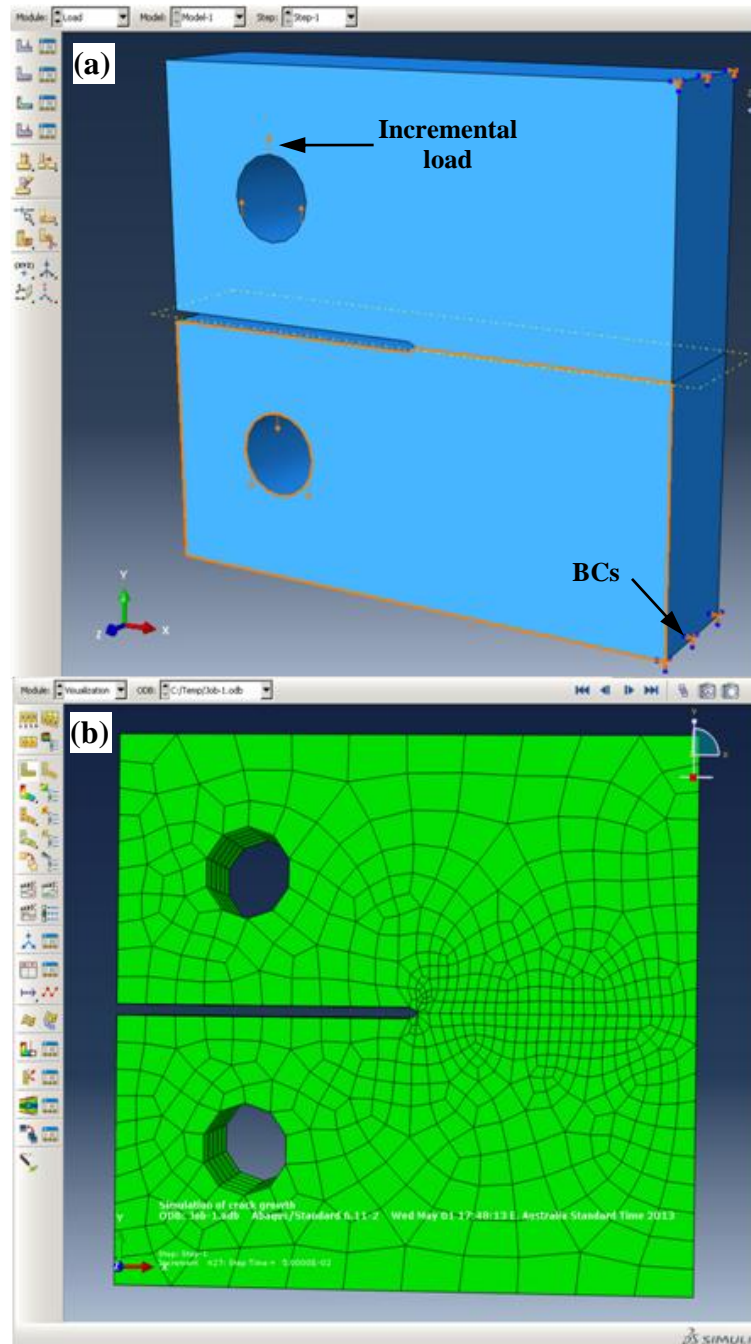


Figure 7.4: (a) Applied Load and Boundary Conditions and (b) FE Mesh of the Part Used in the Analysis

7.4 Results and Discussion

7.4.1 Fracture Toughness Test

The representative load-displacement curves for neat UPE and its nanocomposites are shown in Figure 7.5. In general, all composites tested in the opening deformation

mode (Mode I), using CT specimen geometry, showed unstable crack propagation under a continuous tension loading condition. The load dropped down to zero after reaching the maximum, indicating a linear elastic and brittle behaviour. It also implies that most energy is consumed in the initiation stage, while little energy is dissipated in the rapid crack-propagation stage.

The 3% HNT nanocomposites (see Figure 7.5a) or the 3% s-HNT nanocomposites (Figure 7.5b) showed their ability to carry higher loads of 972 N and 1,000 N, respectively, compared to 862 N for the neat UPE. This indicated that the presence of plastic deformation in the nanocomposites, imparted by the incorporation of HNT particles, blunted the crack tip and reduced the local stress concentration. As a result, this allowed composites to carry higher loads before failure occurred. Figure 7.5b also clearly shows that the displacement of the 3% s-HNT nanocomposites was larger than that of the 3% HNT nanocomposites. This was clearly due to the improved wettability and adhesion between the s-HNT particles and the polymer matrix that resulted in higher fracture forces and higher crack opening displacements (COD) than in the untreated HNT ones.

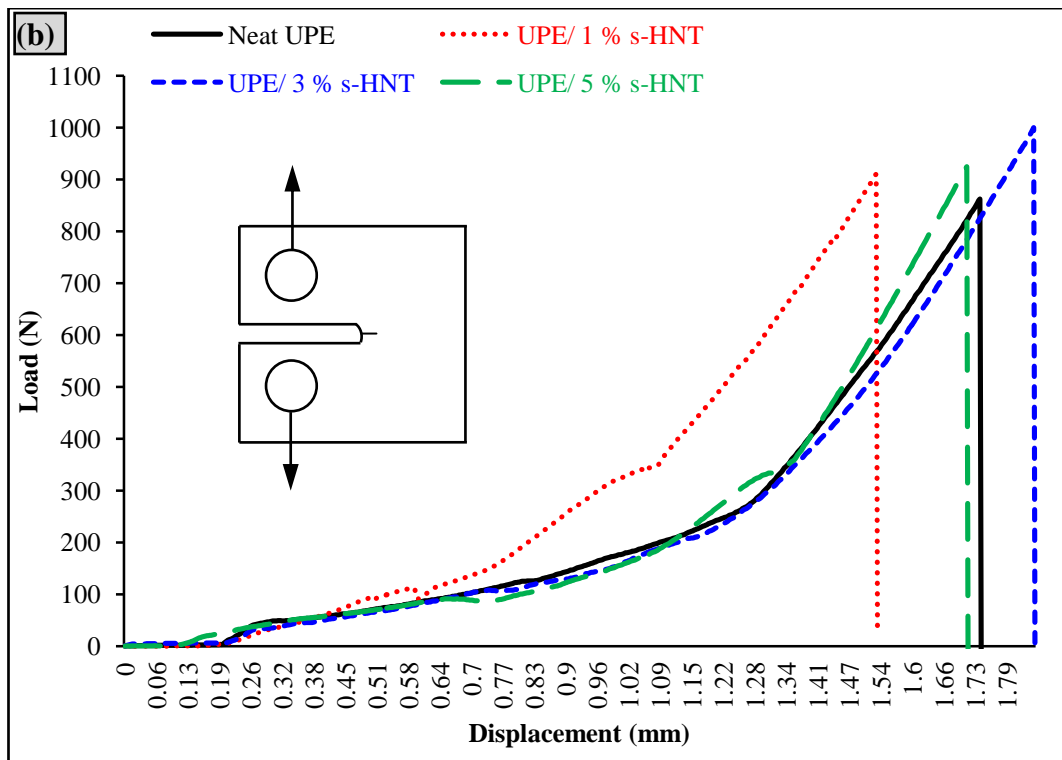
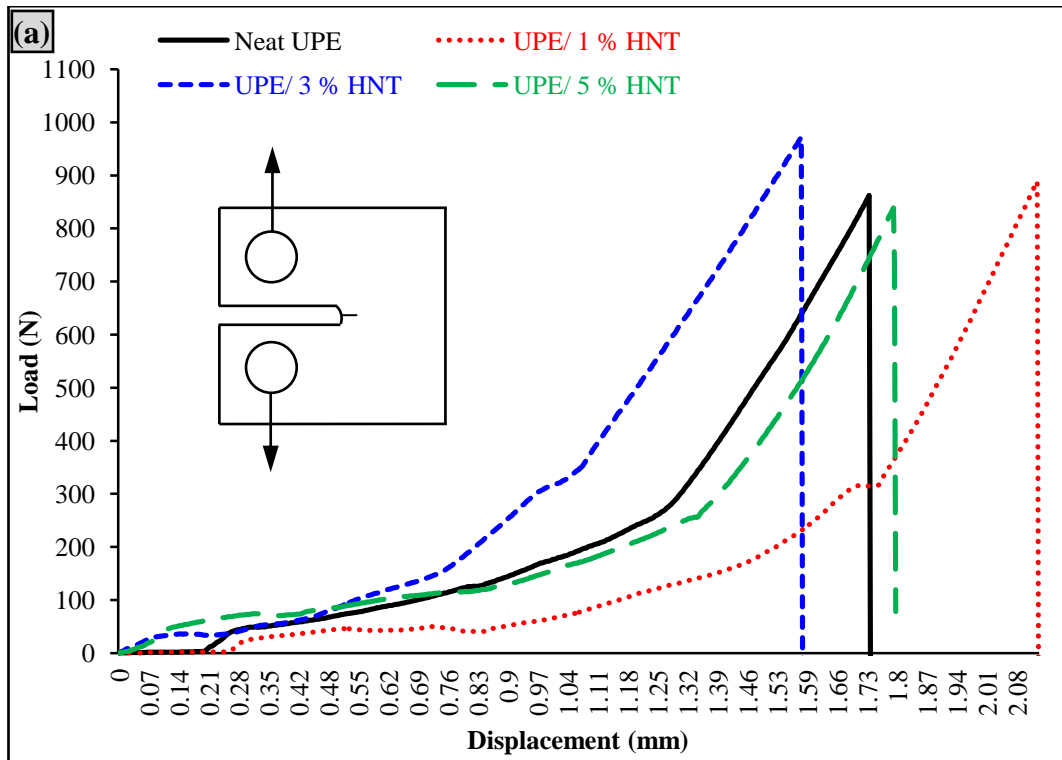


Figure 7.5: Load-displacement Curves of CT Samples for: (a) Neat UPE and Different UPE/HNT Nanocomposites and (b) Neat UPE and Different UPE/s-HNT Nanocomposites Fractured Under Tensile Loads

The load-displacement curves of neat UPE and its different nanocomposites using SEN geometry fractured during the SEN-3PB technique are shown in Figure 7.6. Unlike the crack propagation in the UPE composites with CT specimens, it was observed that the crack propagation in the composites fractured at SEN-3PB technique was unstable and showed saw tooth-shaped curves. However, they exhibited the same as the CT samples—an abrupt drop of load to zero at the instant of crack growth initiation when reaching the maximum loads, thereby indicating brittle fracture behaviour. However, with the SENB samples, the nanocomposite systems carried lower loads, lower displacements and subsequently lesser areas under the curves compared to those of the CT samples.

Interestingly, the 3% HNT nanocomposite (Figure 7.6a) and 3% s-HNT nanocomposite (Figure 7.6b) again showed their ability to carry higher forces to propagate the crack. The former nanocomposite presented a maximum load of 141 N and maximum displacement of 0.25 mm, while the latter presented a 1,000 N and 1.85 mm, versus 101 N and 0.19 mm for the neat UPE counterparts. The other system of the s-HNT nanocomposites tested indicated a similar trend, as shown in Figure 7.6b.

The experimental values of the critical Mode I stress intensity factor (K_c) and critical strain energy release rate or fracture energy (G_c), as often used in brittle or quasi-brittle materials, were determined using two kinds of specimen geometries (CT and SENB). These are listed in Table 7.1.

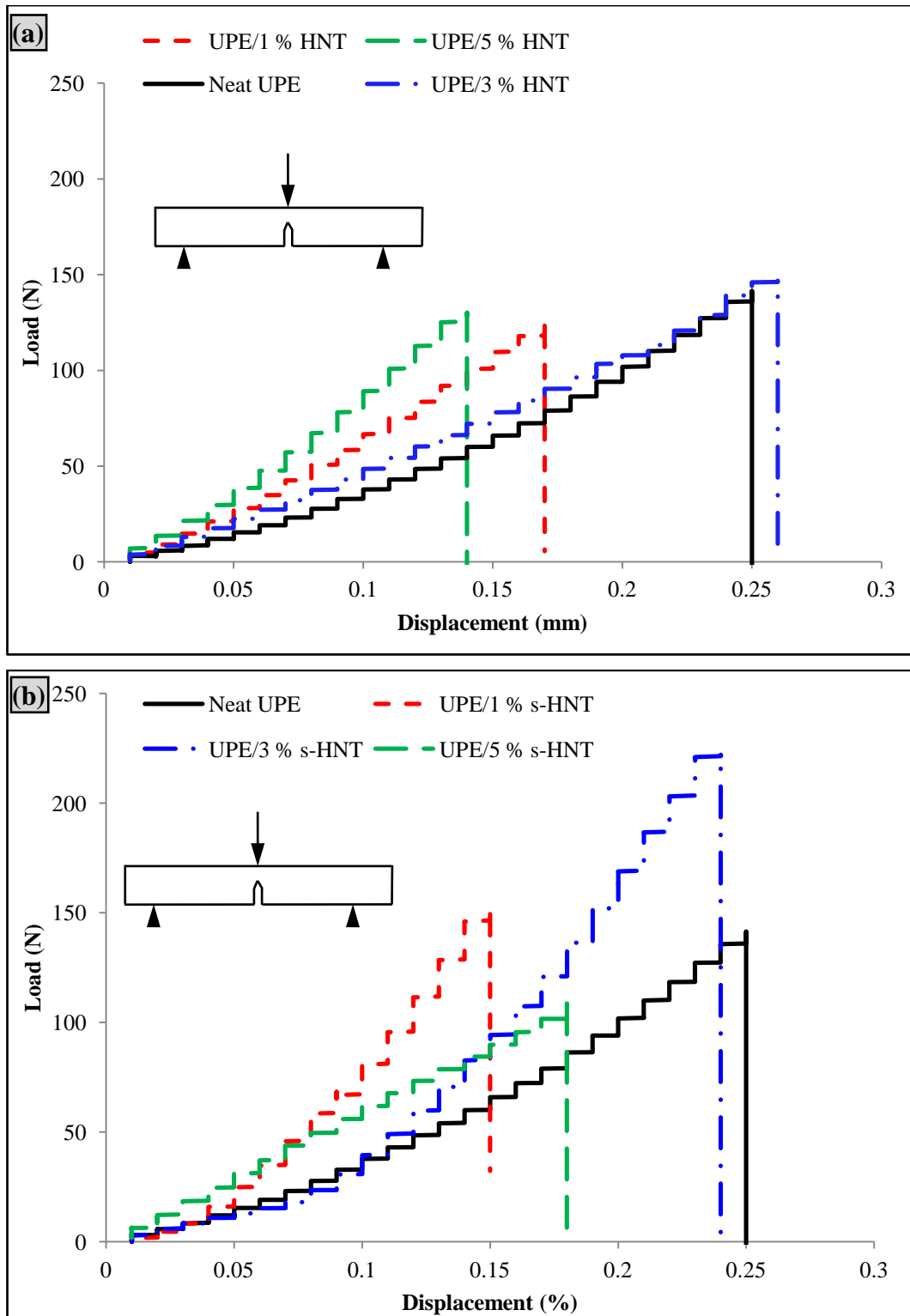


Figure 7.6: Load-displacement Curves of SENB Samples for: (a) Neat UPE and Different UPE/HNT Nanocomposites and (b) Neat UPE and Different UPE/s-HNT Nanocomposites Fractured Under 3PB Technique

The averaged values of all fracture properties were obtained from testing at least five specimens exhibiting a deviation in the range of 0.04 to 0.4 for the K_c values, and 0.05 to 0.45 for the G_c values. Regardless of the specimen geometry, the incorporation of HNT and s-HNT into the UPE resin showed a significant improvement in the fracture toughness, with the addition of 3 wt% HNT or 3 wt% s-HNT presenting the highest values for K_c and G_c (see Table 7.1). For example, with the use of the SEN-3PB technique, the K_c increased from 2.04 MPa.m^{0.5} for neat UPE to 2.28 MPa.m^{0.5} (11% improvement) and 3.33 MPa.m^{0.5} (63% improvement) for UPE/3% HNT and UPE/3% s-HNT nanocomposites, respectively. The values of G_c also improved by 16% for UPE/3% HNT and 137% for UPE/3% s-HNT nanocomposites. However, further addition of more than 5 wt% HNT or s-HNT particles reduced the toughness of the UPE nanocomposites.

Table 7.1: Fracture Properties of Neat UPE and UPE/HNT Nanocomposites

Nanocomposites	K_c (MPa. \sqrt{m})		G_c (J/m ²)	
	CT	SENB	CT	SENB
Neat UPE	1.2 ± 0.1	2.04 ± 0.13	0.32 ± 0.05	0.94 ± 0.09
UPE/1% HNT (UPE/1% s-HNT)	1.24 ± 0.16 (1.28 ± 0.13)	2.1 ± 0.2 (2.44 ± 0.18)	0.33 ± 0.06 (0.33 ± 0.08)	0.97 ± 0.09 (1.24 ± 0.1)
UPE/3% HNT (UPE/3% s-HNT)	1.4 ± 0.4 (1.36 ± 0.25)	2.28 ± 0.33 (3.33 ± 0.41)	0.39 ± 0.12 (0.35 ± 0.08)	1.09 ± 0.2 (2.23 ± 0.32)
UPE/5% HNT (UPE/5% s-HNT)	1.17 ± 0.09 (1.3 ± 0.1)	2.28 ± 0.45 (2.56 ± 0.35)	0.29 ± 0.05 (0.335 ± 0.07)	1.14 ± 0.09 (1.37 ± 0.11)
UPE/7% HNT (UPE/7% s-HNT)	1.09 ± 0.12 (1.26 ± 0.15)	1.65 ± 0.4 (2.4 ± 0.25)	0.26 ± 0.04 (0.315 ± 0.06)	0.61 ± 0.11 (1.2 ± 0.12)
UPE/9% HNT (UPE/9% s-HNT)	1.05 ± 0.1 (1.16 ± 0.2)	1.42 ± 0.15 (1.65 ± 0.22)	0.26 ± 0.06 (0.29 ± 0.05)	0.48 ± 0.05 (0.61 ± 0.07)

Note: The values of the UPE/s-HNT nanocomposites are shown in parentheses.

Additionally, the measurements of Mode I plane-strain fracture toughness parameters (K_{Ic} and G_{Ic}), based on CT specimen configuration and tensile load, were conducted in accordance with ASTM D 5045 (as described in Section 3.4.9). The purpose of this measurement was to determine the effect of using different sizes of fracture specimens on the fracture results, and elucidate the sequence of events that occurred during the fracture process—that is, to understand the mechanisms that contribute to the observed differences in toughness. As can be seen in Table 7.1, with increasing

weight fraction of halloysite particles, the values of both K_{Ic} and G_{Ic} steadily increased.

From the results obtained, it was observed that the UPE nanocomposites filled with silane-modified halloysite particles induced higher values of fracture toughness and fracture energy compared to neat UPE or UPE/HNT nanocomposites. These increases in toughness with the incorporation of up to 5 wt% HNT or s-HNT nanoparticles were attributed to the ability of particles to induce an increased extent of plastic deformation in front of the cracking path in the nanocomposite. The initiation of plastic deformation with the presence of halloysite nanoparticles is one of the most dominant toughening mechanisms noticed when toughening thermosetting polymers with nanoparticles. This hypothesis was further supported by the SEM images, and will be discussed in detail later in the section on toughening mechanisms. Further, it was also believed that the presence of halloysite particles in the thermosetting UPE matrix—which generated nonreactive surfaces and local free volume in the structure and then reduced the glass transition temperature (T_g) (see Section 5.2.2.1)—usually increased toughness and damage tolerance.

Nevertheless, further increase of halloysite content (> 5 wt%) induced lower values of both K_{Ic} and G_{Ic} , which is related to the structure/property considerations. This meant that the presence of higher contents of halloysite particles in the crosslinked UPE extremely toughened the UPE structure, caused the structure to become inhomogeneous, increased its ability to undergo strain-softening and led to the localised nature of the plastic deformation (Hsieh et al. 2010b).

It is essential here to further discuss the difference in toughness due to using different thicknesses of specimen geometry (CT and SENB). According to the ASTM standard test method for plain-strain fracture toughness and strain energy release rate of plastic materials, D 5045 (ASTM 2007), the validity of calculated K_{Ic} and the size criteria must be satisfied to:

$$B, a, (W - a) \succ 2.5(K_{Ic} / \sigma_y)^2 \quad (7.3)$$

where σ_y is the yield strength (MPa). Hence, the magnitude of K_{Ic} measured with the use of the configuration of CT geometry was a valid test, and the criterion was

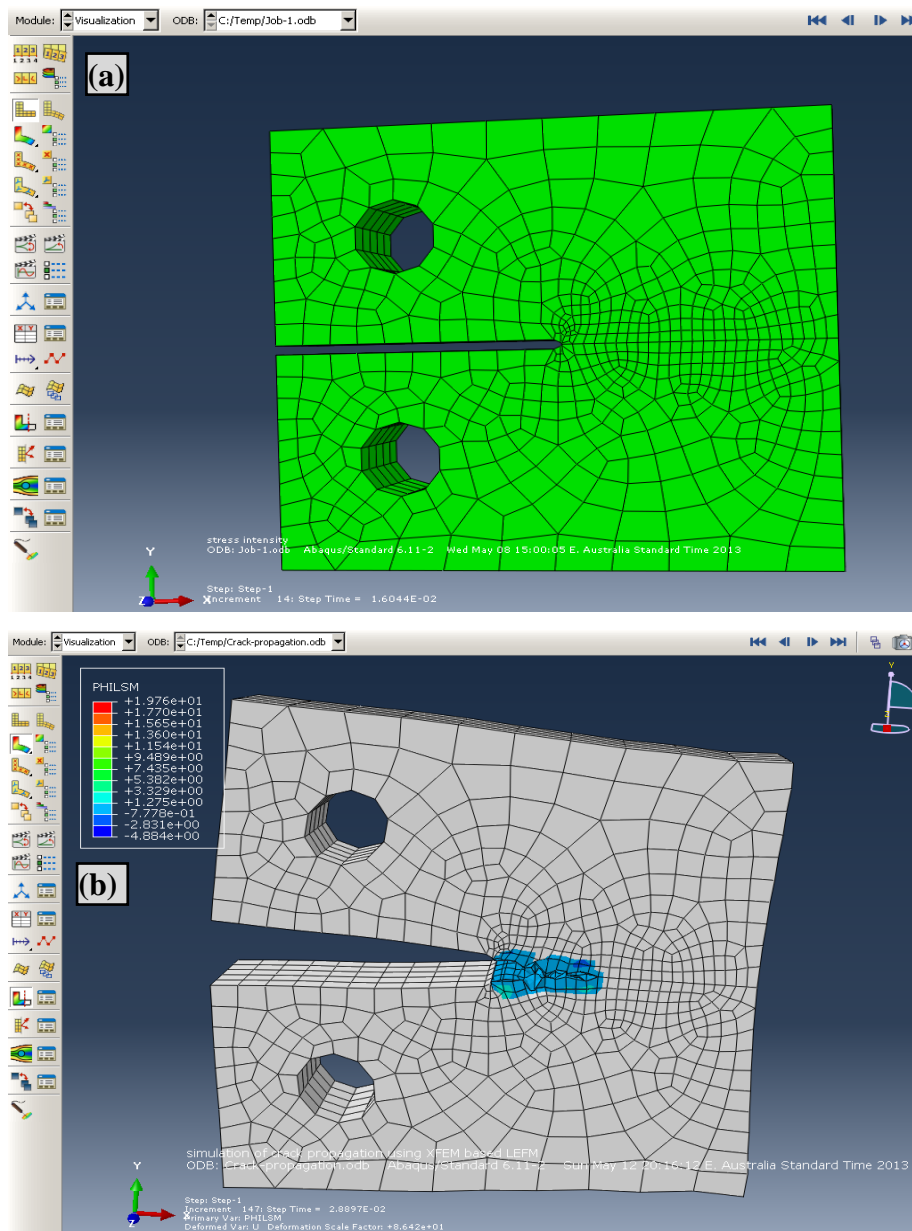
sufficient to ensure plain strain, since the quantity of $2.5(K_{Ic}/\sigma_y)^2$ was less than the specimen thickness (B), the crack length (a) or the ligament ($W - a$). On the other hand, in the case of using the configuration SENB geometry, the quantity was not satisfied with the size criteria required by the ASTM standard test method. As a result, it is obvious that the values of stress intensity factors (K_c) calculated with the SENB-3PB under plain stress conditions were higher than those calculated with the use of CT specimens under plain-strain conditions (Ruiz-Perez et al. 2008).

7.4.2 Cohesive Model Versus Experimental Results

The 3-D FEM model was carried out on the CT specimen geometry using the ABAQUS software to simulate the crack propagation characterisation based on power law fracture criteria. The maximum principal stress of 30 MPa and Young's modulus of 30 GPa used in the crack onset criterion were obtained from the experimental results. The simulation results of the crack initiation and propagation process in nanocomposites filled with halloysite are given in Figure 7.7. Before crack initiation, there was no cohesive segment and only the bulk damage mechanism was active in the model (see Figure 7.7a). This agreed with the previous numerical investigation of the damage parameters in clay/epoxy nanocomposites using the XFEM (Silani et al. 2012). Figure 7.7b shows the location of crack initiation, while the final failure of the sample is illustrated in Figure 7.7c. These simulations were carried out for UPE 1%, 3% and 5% HNT/UPE nanocomposite samples. The location of crack initiation did not relate to halloysite percentage, and the simulation of the crack evolution was almost similar for all samples. Meanwhile, please note that the effects of nanotube aspect ratio, nanotube size and silane-treated surface on the damage of nanocomposites were not considered within the current simulation analysis.

As shown in Figure 7.7c, upon loading, the crack first initiated horizontally fast, following an unstable crack growth, and then deflected when the crack tip moved into the interface between different phases of materials. Figure 7.8 shows the comparison between the simulation results and experimental results of the stress-strain curves for neat UPE and 3% HNT nanocomposites. With respect to the simulation curves in the figure, they are directly drawn by ABAQUS based on the

given dimensions in Fig. 3.12 (b) for the CT specimen. Fairly good agreement was seen between the simulation and experimental results of 3% HNT-UPE nanocomposites. However, the experimental results of the nanocomposite systems reached the peak stress first, and relatively had the highest peak stress. The sawtooth-shaped stress-strain curve of the simulation results indicated unstable crack propagation. This also implied that the halloysite clusters acted as stress concentrators and promoted the formation of a large number of microcracks when the sample was loaded. Further understanding of this phenomenon will be obtained from the discussion of toughening mechanisms in the next section.



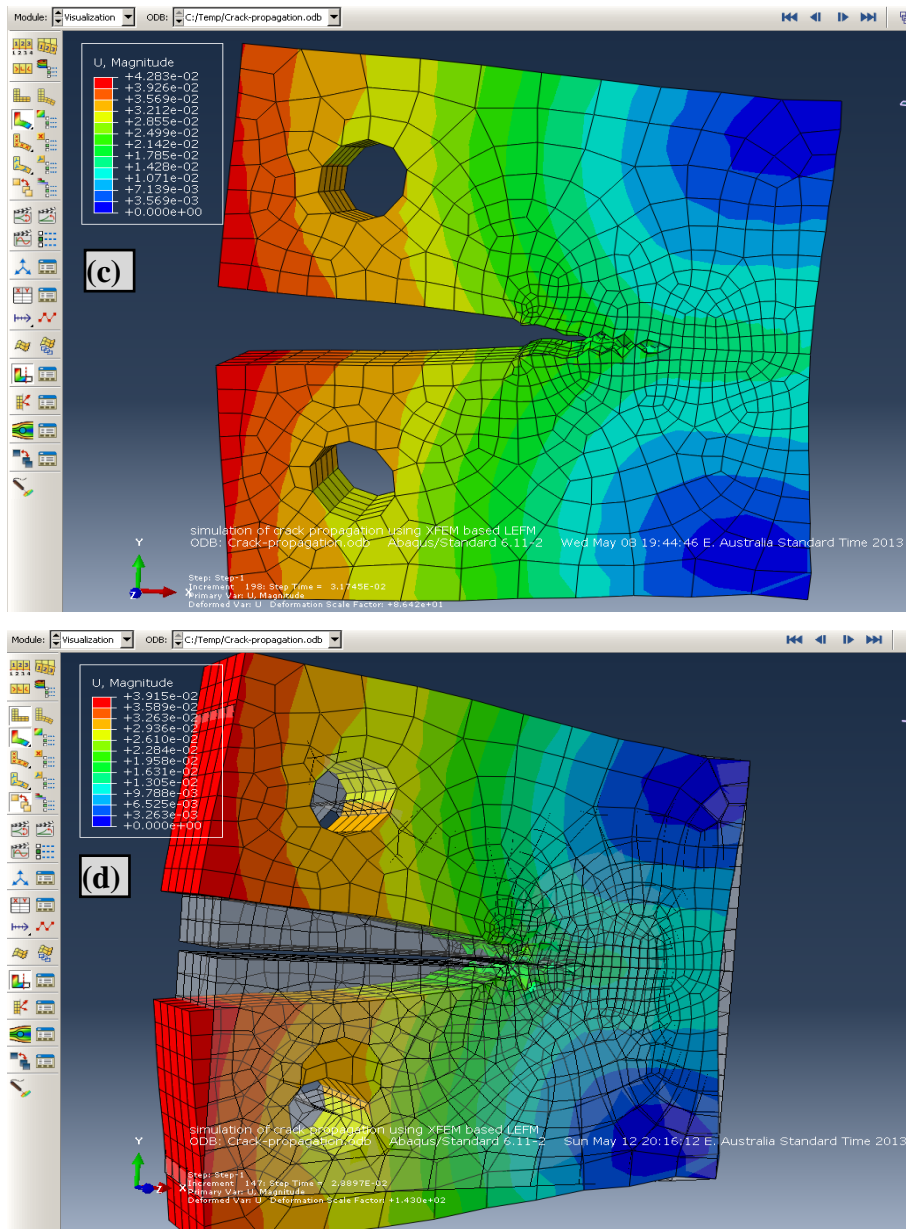


Figure 7.7: Propagation of the Crack of CT Sample for 3% HNT Nanocomposite: (a) Specimen Before Crack Initiation, (b) Crack Path, (c) Final Failure of the Sample and (d) Comparison of the Real and Final Failure Situation, Demonstrating the COD

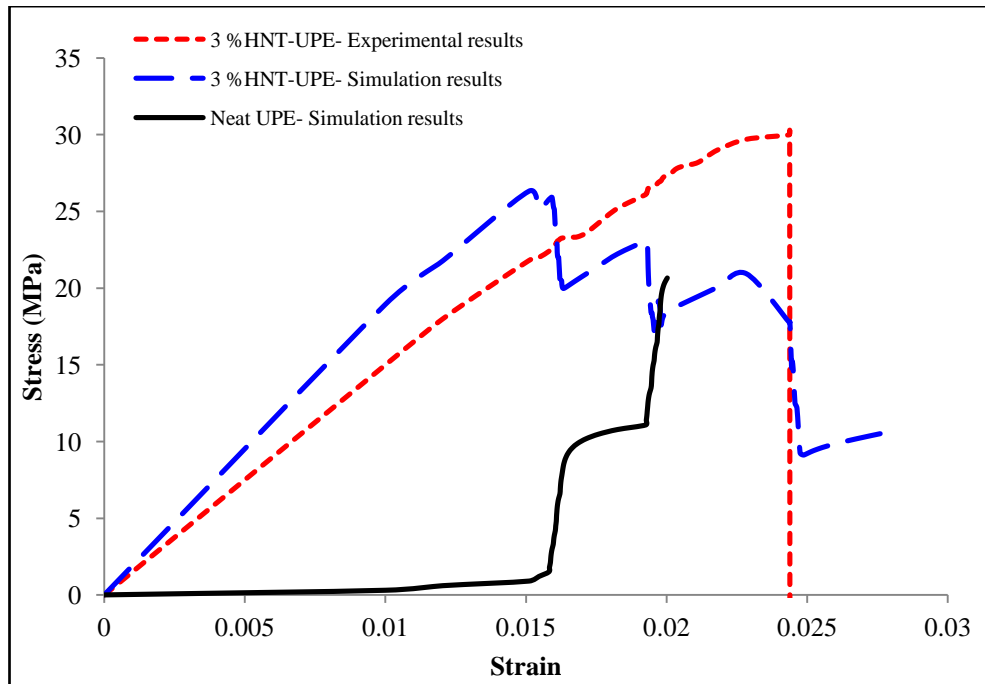


Figure 7.8: Stress-strain Curves for Neat UPE and 3% HNT-UPE Nanocomposite Based on FEM and Experimental results

7.4.3 Toughening Mechanisms

The SEM examination was conducted on the morphology of different fracture surfaces taken from different locations in the SENB and CT specimens in order to quantitatively understand the toughening mechanisms occurring in the nanocomposites filled with untreated and silane-treated halloysite particles. In general, under triaxial stress and plane-strain conditions, thermosetting polymers exhibit inherent brittle fracture mode with low toughness and poor crack growth due to their tight 3-D molecular network structure and because they do not have a constraint-releasing mechanism resistance (Pascault et al. 2002). The experimental observations of previous studies (Kim, Park & Lee 2008; Deng, Zhang & Ye 2009; Hsieh et al. 2010b; Ayatollahi, Shadlou & Shokrieh 2011; Zappalorto, Salviato & Quaresiminet 2012; Zamanian et al. 2013) have revealed that improvements in both the fracture toughness and fracture energy shown by nano-filled polymers are strictly related to the large amount of energy dissipated by the initiation of different plastic deformation mechanisms and different damaging mechanisms occurring at the nanoscale.

Supported by the SEM images, the fractographic analysis of the fractured surface for the unfilled UPE matrix tested with both the CT geometry under tension and the SENB under bending showed a highly brittle fracture, as depicted in Figure 7.9. The surface topography of the unfilled UPE matrix exhibited both smooth and rough surface features. The smooth surfaces were represented by mist regions, while the rough surfaces were represented by hackle regions (see Figure 7.9b). Hackle regions frequently appear in areas where the stress field (direction or magnitude) is changing rapidly, or the stress state changes from plain strain to plain stress (Lampman 2003). In the current case, hackle regions appeared in the region of a specimen subjected to bending on the compression side of the specimen, but there were changes to tension as the crack approached from the tension side. Further, different directions of crack propagation were observed in the morphology of the unmodified brittle UPE matrix, irrespective of the applied loads or specimen geometries.

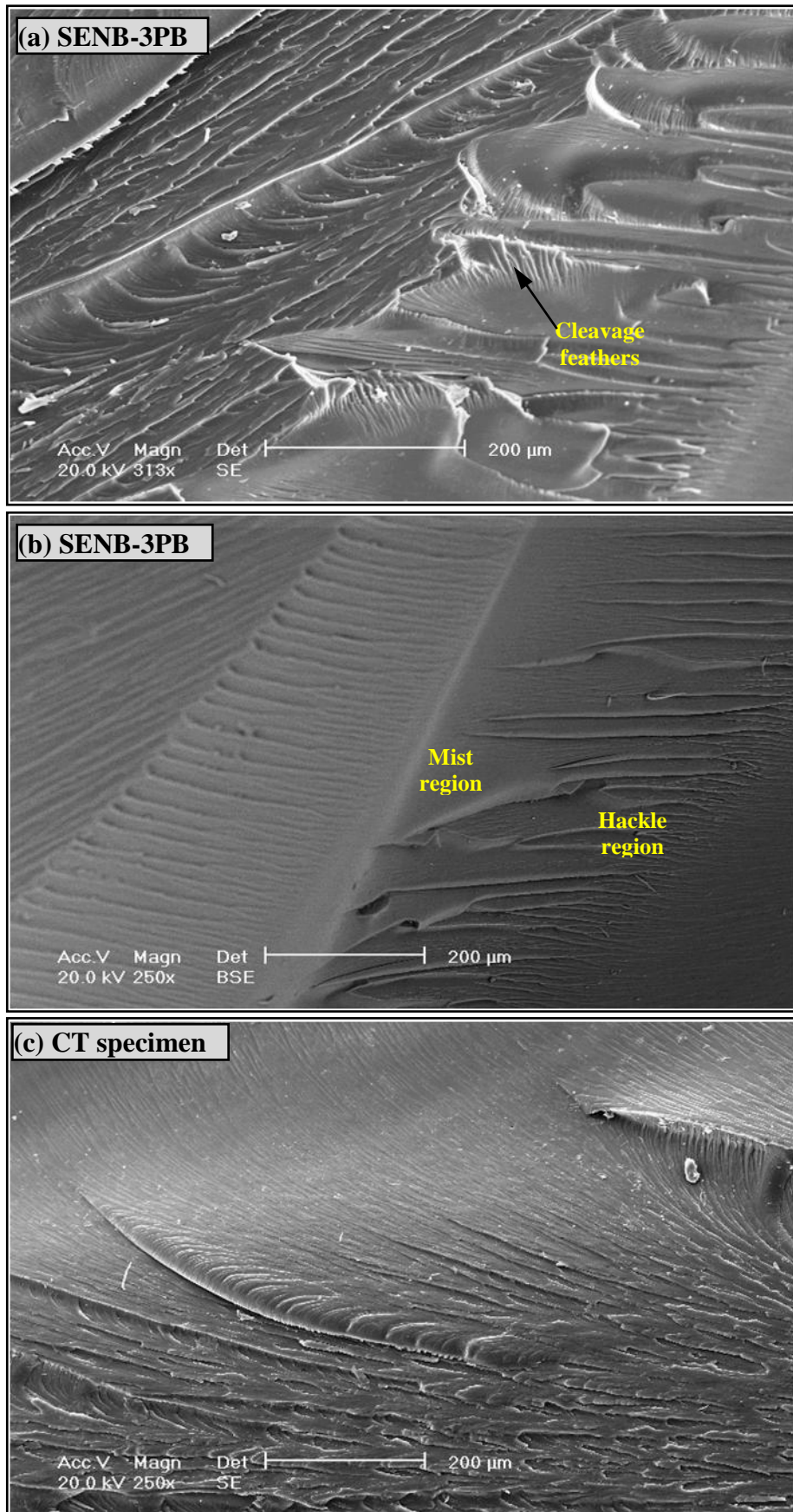


Figure 7.9: SEM Images of Different Fractured Surfaces for Unfilled Brittle UPE Matrix Fractured Under Different Loads and Specimen Geometries

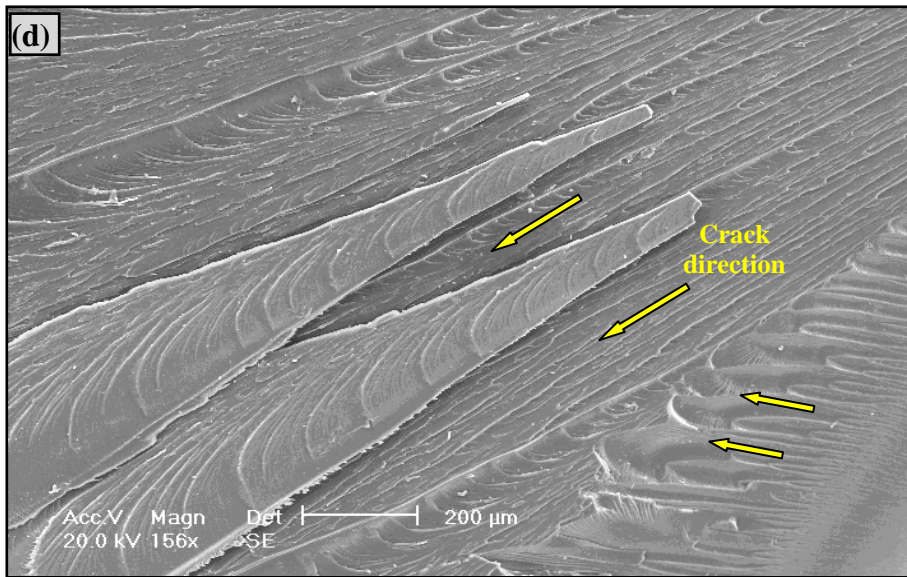
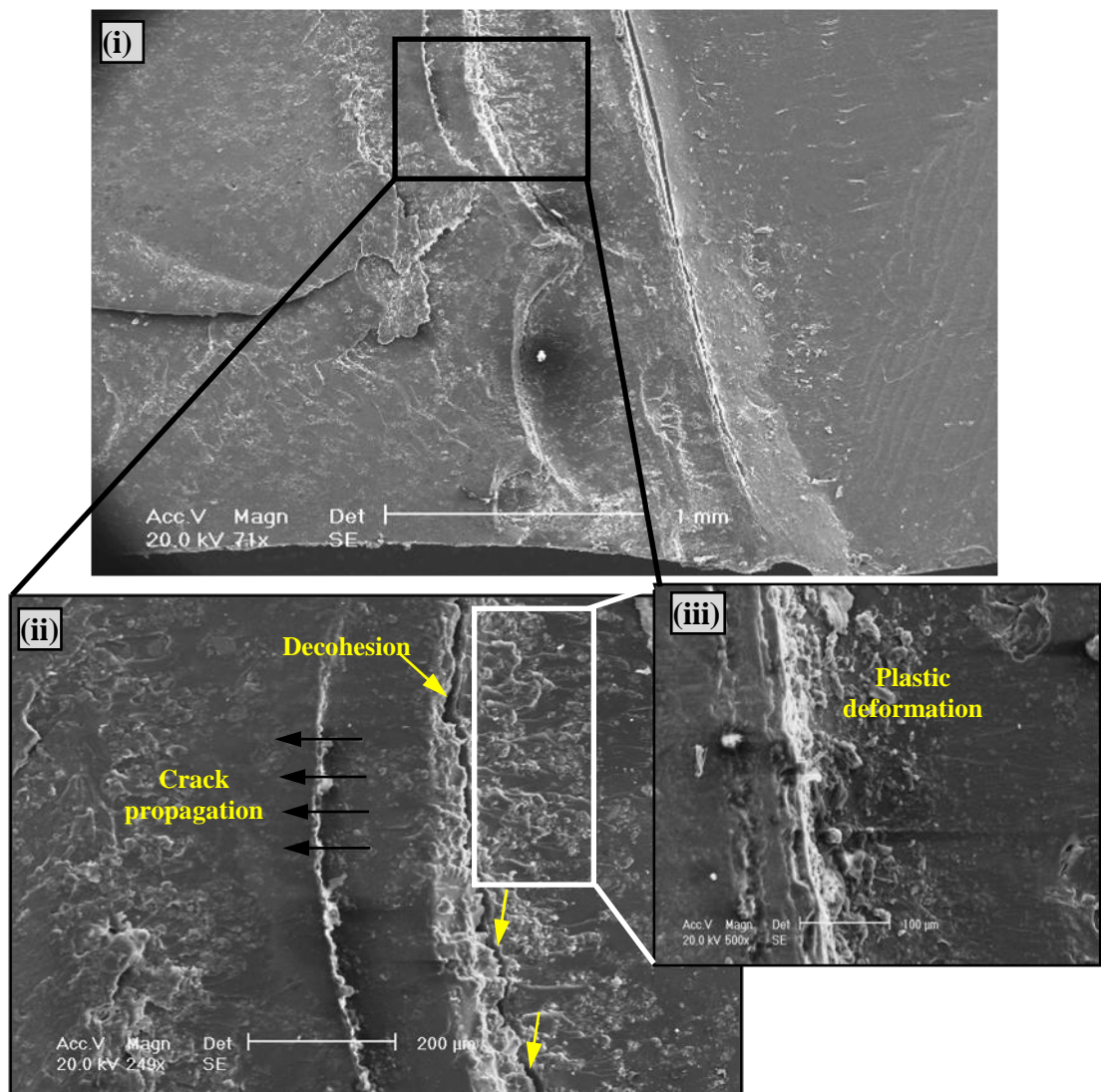


Figure 7.9 (Continued): Fracture Surface of Unfilled UPE Matrix Fractured Under Tension Load and CT Geometry

The presence of rigid particles in the thermosetting polymer matrix undoubtedly contributed to the initiation of various mechanisms of energy absorption before the appearance of the first crack (Anderson 2005). These fracture energy dissipation mechanisms observed in the fractured surfaces for different cured UPE/HNT nanocomposites were characterised as follows.

The addition of HNT particles into the UPE matrix introduced more local plastic deformations near the crack tip (Figure 7.10) and was important for toughening behaviour and improving fracture energy. This meant higher G_{Ic} values, since the energy absorbed by the creation of additional fracture surface area necessitates additional energy input to the system to continually drive crack growth (Dittanet & Pearson 2012). The 5% HNT/UPE fracture surfaces near the pre-crack front region were examined under SEM. The black arrows at the bottom left image of Figure 7.10(ii) indicate the crack growth direction, while the yellow arrows in the same image refer to the decohesion (intergranular fracture) that probably occurred along the weakened hydrophilic particle and polymer interface. Liang and Pearson (2010) revealed that the plastic deformation verified in a lightly crosslinked epoxy matrix included shear yielding and matrix dilation. This finding agrees well with those of Ma et al. (2008), in which a small birefringent zone was found to be associated with

the creation of an obvious dilatation zone under loading, thus indicating local matrix deformation. Dilatation refers to an expansion in volume of a material under stress.



Note: The yellow arrows represent the decohesion and the black arrows indicate the direction of the crack propagation.

Figure 7.10: Fractography of Mode I Fracture Toughness Using CT Geometry for 5% HNT/UPE Nanocomposite Showing the Process Zone

The zone shielding toughening mechanism represented by the formation of microvoids around the crack tip was observed, as shown in Figure 7.11.

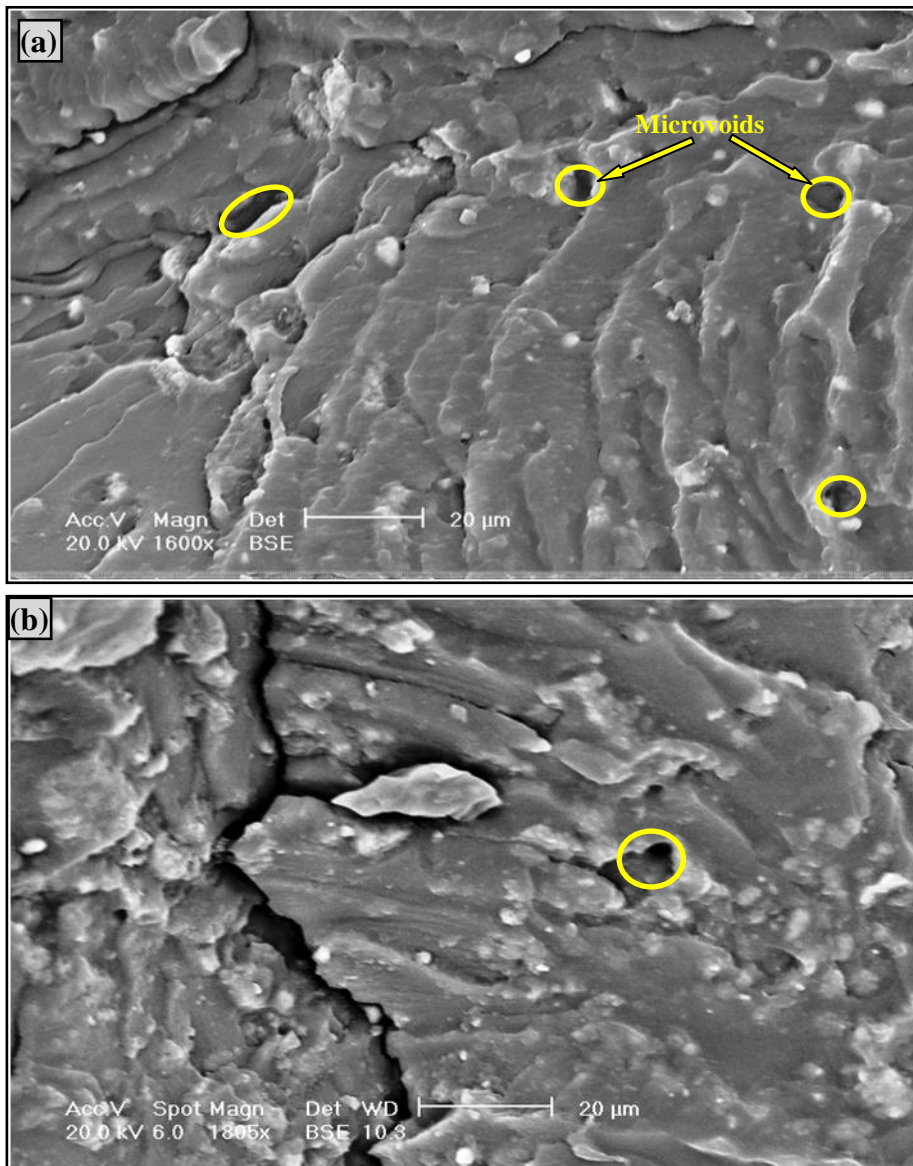


Figure 7.11: Fracture Surface for UPE/3% HNT Nanocomposite Showing the Microvoids that Occurred due to the Particle-polymer Interface Debonding

In general, there are three different mechanisms categorised under zone shielding mechanisms. The first is the transformation toughening that occurs when the crack actually changes the crystalline structure of the surrounding material to inhibit crack growth. The second is microcrack formation, and the third is crack field void formation (Liang & Pearson 2010). Numerous microcracks or microvoids form simultaneously in a brittle material when the applied loads reach a certain level. The distribution of these microcracks depends essentially on the local stress concentration and the material heterogeneity, where the formation of either microcracks or microvoids around the crack tip reduces stress concentration and interferes with

crack propagation. In contrast, the presence of stress concentration can lead to shear yielding around every particle and hence throughout a large volume of material, rather than just at the crack tip (Young & Lovell 2011). Thus, the polymer matrix absorbs a large amount of energy during deformation and is toughened due to the initiation of matrix shear yielding mechanism.

The matrix shear yielding mechanism was observed in the fracture surface of the untreated halloysite nanocomposite, as depicted in Figure 7.12. This mechanism is also thought to be initiated by the stress concentrations around the periphery of the nanoparticles (Hsieh et al. 2010b). Further, clear evidence of halloysite particle debonding could be found in the untreated system (Figures 7.13a and b), but not in the silanised system. On the fracture surface of the silanised nanocomposite, partially debonded or even fully debonded halloysite particles were found (Figures 7.14a and b), but much less commonly than in the case of the untreated nanocomposite.

Interestingly, contributing the total fracture energy, the presence of particle debonding is considered one of the prerequisites to activate void expansion and matrix shear deformation energy dissipation mechanisms (Srivastava & Koratkar 2010). Nevertheless, discussion of these energy dissipation mechanisms has been mainly qualitative; hence, the qualitative observation of increased toughness and the quantitative increase in the fracture energy in this study appear to agree with interface debonding, shear yielding, and the theory that states the initiation of stress concentration in the surrounding area of halloysite particles. To this end, stress fields are formed due to the difference in strength modulus and Poisson's ratio between halloysite and unsaturated polyester.

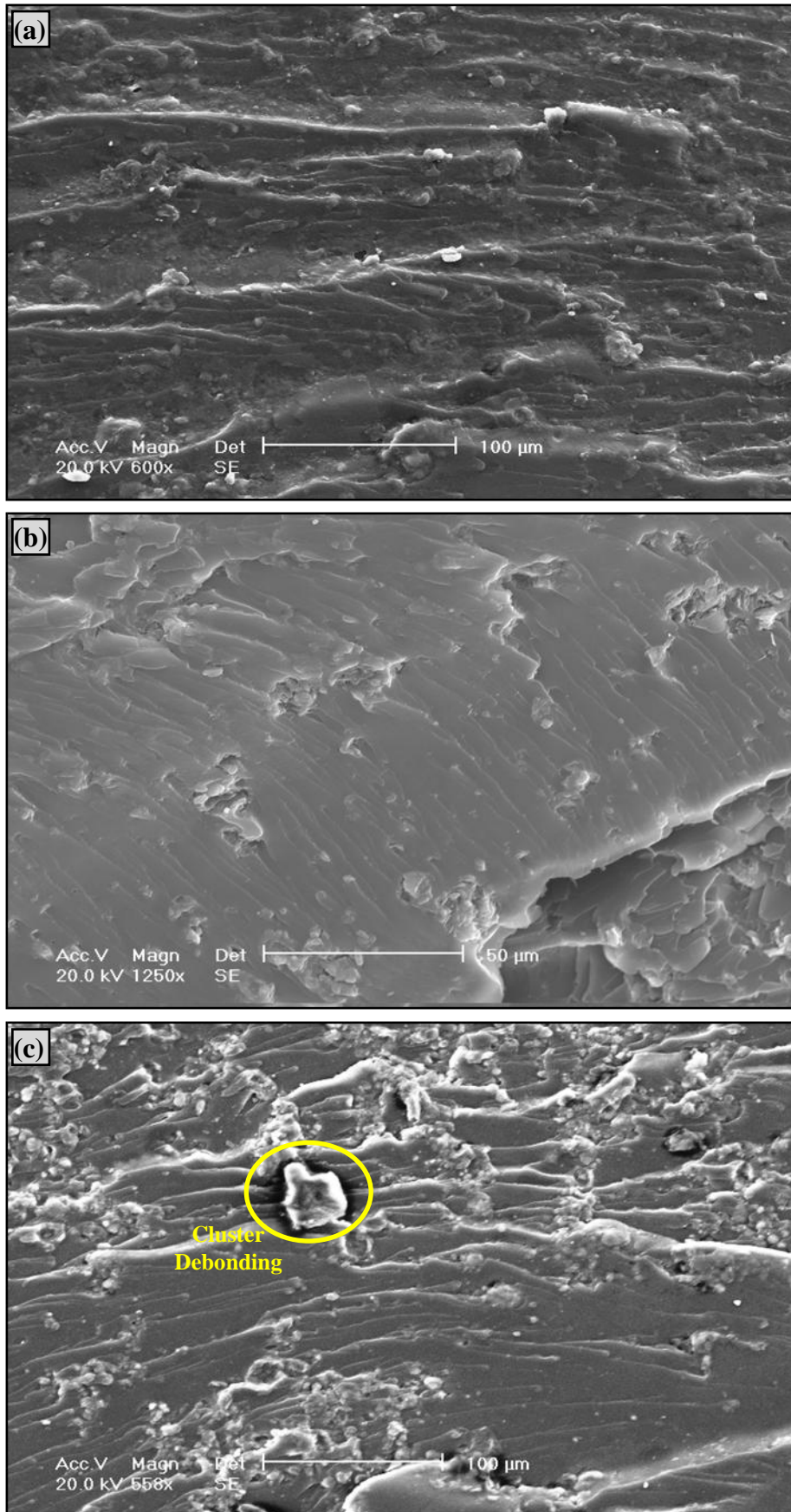


Figure 7.12: Fracture Surface of: (a) 1% HNT/UPE Nanocomposite, (b) 3% HNT/UPE and (c) 5% HNT/UPE Tested with the SENB Geometry Under Bending, Showing Shear Yielding Mechanism

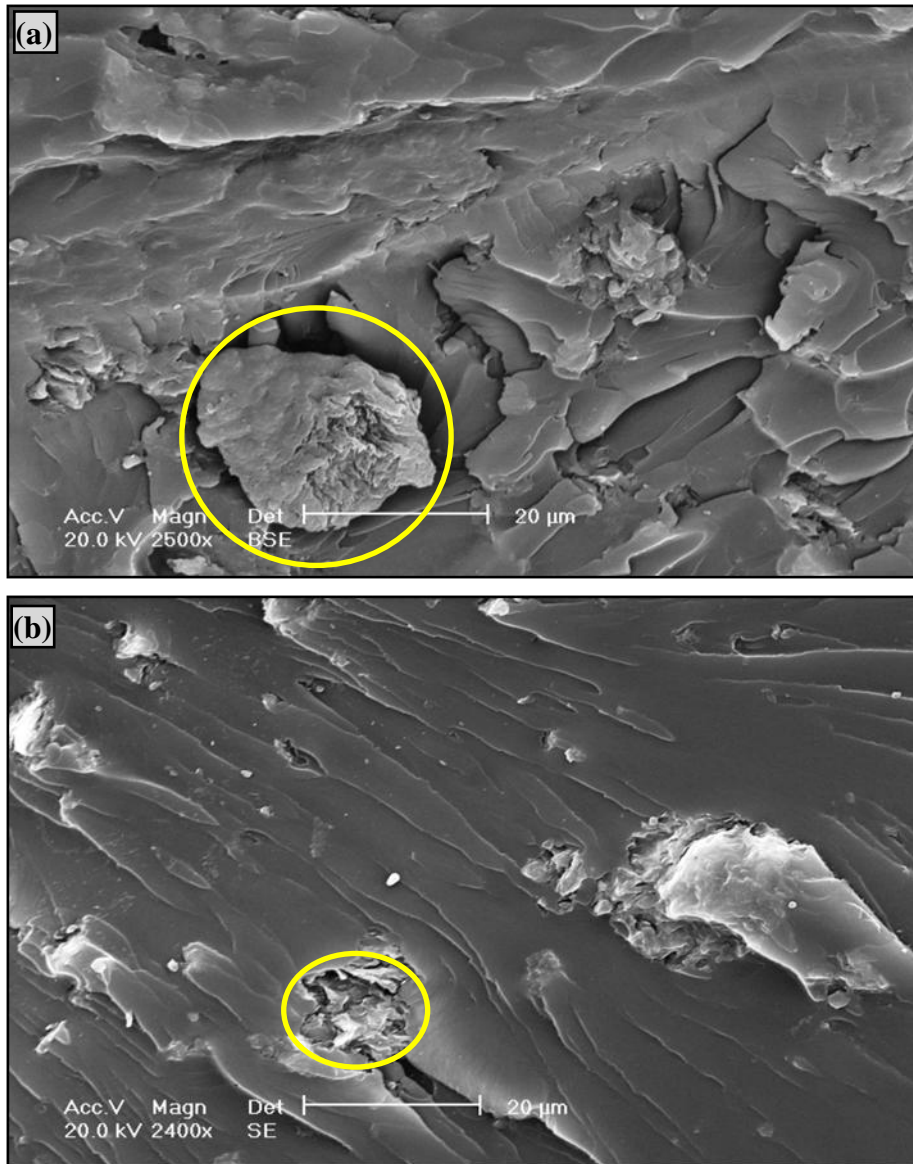


Figure 7.13: SEM Images Illustrating the Fracture Surface of: (a) 3% HNT/UPE Nanocomposite and (b) 5% HNT/UPE After Debonding

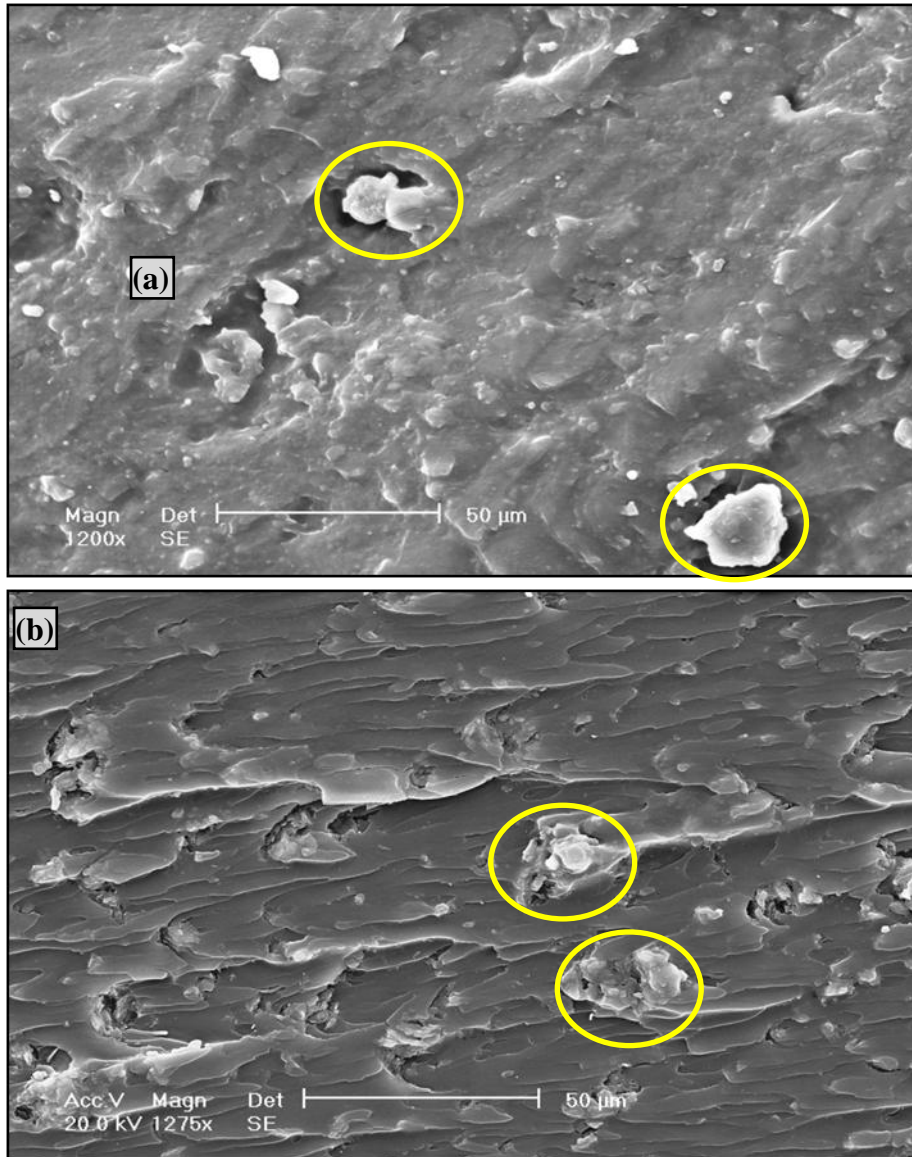


Figure 7.14: SEM Images Illustrating the Fracture Surface of: (a) 1% S-HNT/UPE Nanocomposite and (b) 3% S-HNT/UPE Nanocomposite After Debonding

In contrast, the topography analysis of fracture surfaces of the silanised halloysite nanocomposites—although they appeared similar to those of the untreated halloysite systems—appeared relatively finer with complex features. This was perhaps due to the formation of multiple interfacial bonding sites on the surface of the silanised halloysite. Such multiple sites normally form during the hydrolysis process, and can act as a thick interfacial bridge between particles-silane-polymer. Before identifying the toughening mechanisms in the s-HNT nanocomposites, it is necessary to clarify the fracture behaviour that can be expected to occur in such composites. As the

silanised halloysite nanoparticles are much stronger than and have a strong interface with the UPE matrix, particle deformation, internal cavitation and particle–polymer interface debonding would unlikely occur under loading. However, as discussed before, partial particle debonding was observed in the silanised halloysite nanocomposites versus full debonding in the un-silanised halloysite composites (see Figures 7.13 and 7.14). This meant that the particle debonding and subsequent void growth, as well as the matrix shear band, also played roles in the toughening of the silanised halloysite nanocomposites. Hsieh et al. (2010b) and Liang and Pearson (2010) reported that the matrix shear band contributed more to the fracture toughness than the plastic void growth effect.

The matrix shear yielding (or matrix shear banding) was also observed in the topography analysis of the silanised halloysite nanocomposite. This is an energy absorption mechanism associated with polymer failure. It occurs when localised plastic flow starts in response to an applied stress at approximately 45° to the applied load (Figure 7.15). Such plastic flow can spread shear bands in the whole sample, absorbing a significant quantity of energy, or can lead to localised yielding. Localised shear yielding is a narrow zone of intense shearing strain forming due to a material instability, corresponding to an abrupt loss of homogeneity of deformation. Increase in the tendency to shear yield in nanocomposites results in isolated shear bands and increases energy absorption prior to fracture (Srivastava & Koratkar 2010). Usually, spread shear yielding is initiated by debonding of inorganic nanoparticles, whereas debonding of particles triggers spread shear yielding around the cavity of the matrix left by the debonded particles (Dittanet & Pearson 2012). The size of both dilational bands and shear bands increases with increasing halloysite content.

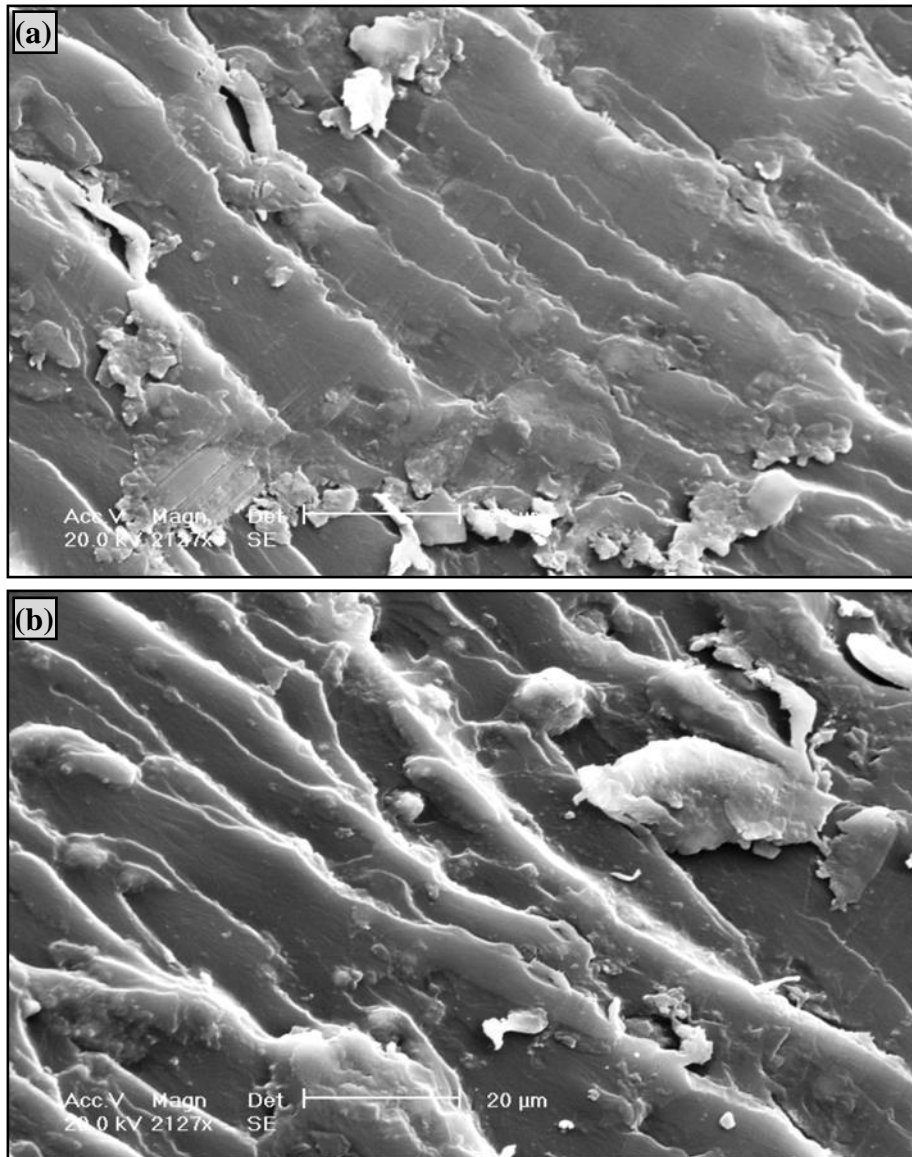


Figure 7.15: Fracture Surfaces from SENB Geometries of: (a) 3% s-HNT/UPE and (b) 5% s-HNT/UPE Nanocomposite, Showing Matrix Shear Band Mechanism

Regarding the role of s-HNT particles in the initiation of shear yielding, the higher contents of s-HNT caused the initiation of the massive shear banding, as can be observed in the fracture surface of 7 wt% s-HNT nanocomposites in Figure 7.16. The massive shear banding mechanism is a crack-tip shielding that occurs due to the reduction in yield stress by the stress concentration of the compliant nanoscale particles that facilitate shear yielding. Similar observations of micro-shear banding, shear yielding and massive shear yielding mechanisms have been reported in the literature (Zhao & Hoa 2007; Ma et al. 2008; Hsieh et al. 2010a). Dittanet and

Pearson (2012) reported that the size of shear bands increases with increasing filler content, whereas size does not significantly affect the use of different particle sizes.

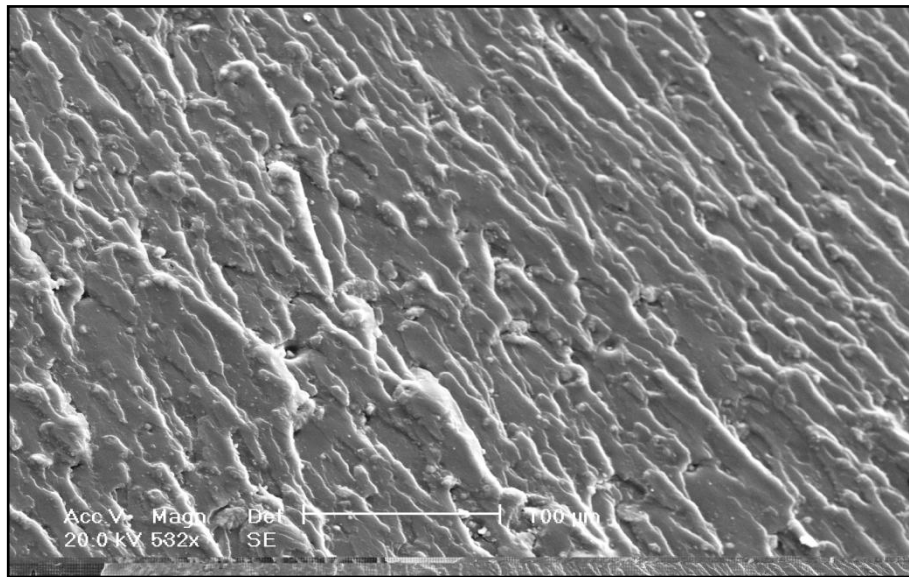


Figure 7.16: Fracture Surfaces from SENB Geometry of 7% s-HNT/UPE Nanocomposite Showing the Massive Shear Yielding Mechanism

Despite the inherent interdependence of the shear yielding toughening mechanisms described above, the energy dissipation through this mechanism was thought to be insufficient to be responsible for the overall increased toughness in the thermosetting polymers nanocomposites. Other energy dissipation mechanisms—such as crack pinning, crack deflection/bifurcation effects, twisting, and immobilised polymer around the particles, as well as river patterns and matrix ligament bridging—were thought to be equally dominant mechanisms contributing to overall toughness in the UPE nanocomposites.

To this end, in the current investigation, it was found that the well-dispersed s-HNT particles in the polymer matrix associated with their high aspect ratios helped promote crack bridging, deflected the advancing crack, and forced growth to deviate from the existing fracture plane during the crack propagation. However, the better dispersion of the s-HNT particles and the further preparation processes to functionalise them tended towards a reduction in their aspect ratio, which obviously reduced the possible effect of crack bridging and crack path deflection. Generally speaking, in the particle bridging toughening mechanism, the additive rigid particles

act as bridging particles granting compressive grip in the crack path. The additive soft or flexible particles, such as rubber deforming plastically in the material surrounding the crack tip, provide additional crack shielding (Gupta et al. 2010).

To further understand the bridging mechanism in this study, Figure 7.17 depicts the bridging mechanism of particles in the UPE thermosetting composite. Figure 7.17b shows that a large cluster of silanised halloysite particles appeared with further addition of filler content, bridging the crack when it passed through and resisting the advanced of the crack. However, such large clusters may also reduce the threshold of carrying loads and thus cause premature failure (see Table 7.1). This finding was supported by Varela-Rizo et al. (2010) and Tang et al. (2012b), with the former authors reporting that functionalised CNTs were a good additive for fracture toughness enhancement of polymethylmethacrylate nanocomposites. The CNTs play a key role in dissipating the energy associated with the crack growth, via promoting crack bridging and crack deflection mechanisms; however, this is only observed with a high CNT content and at high aspect ratio.

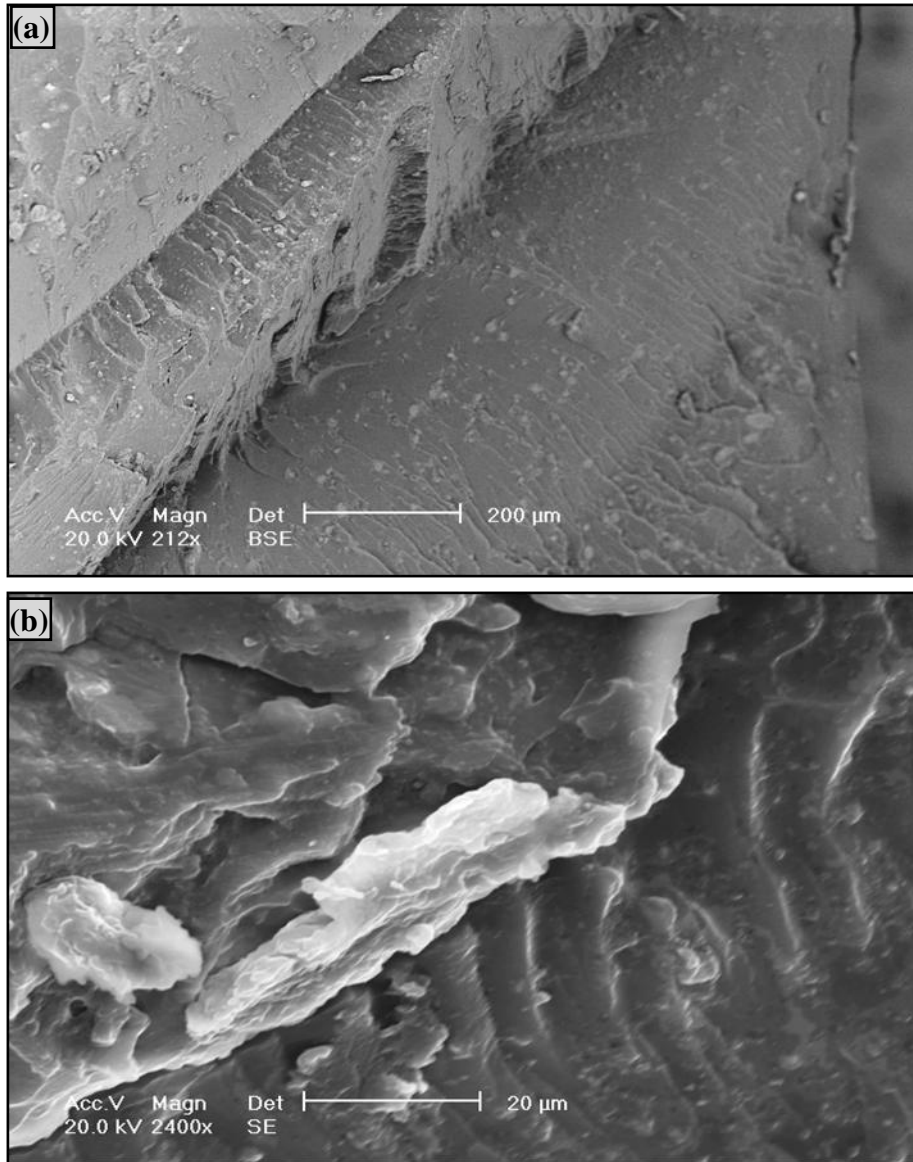
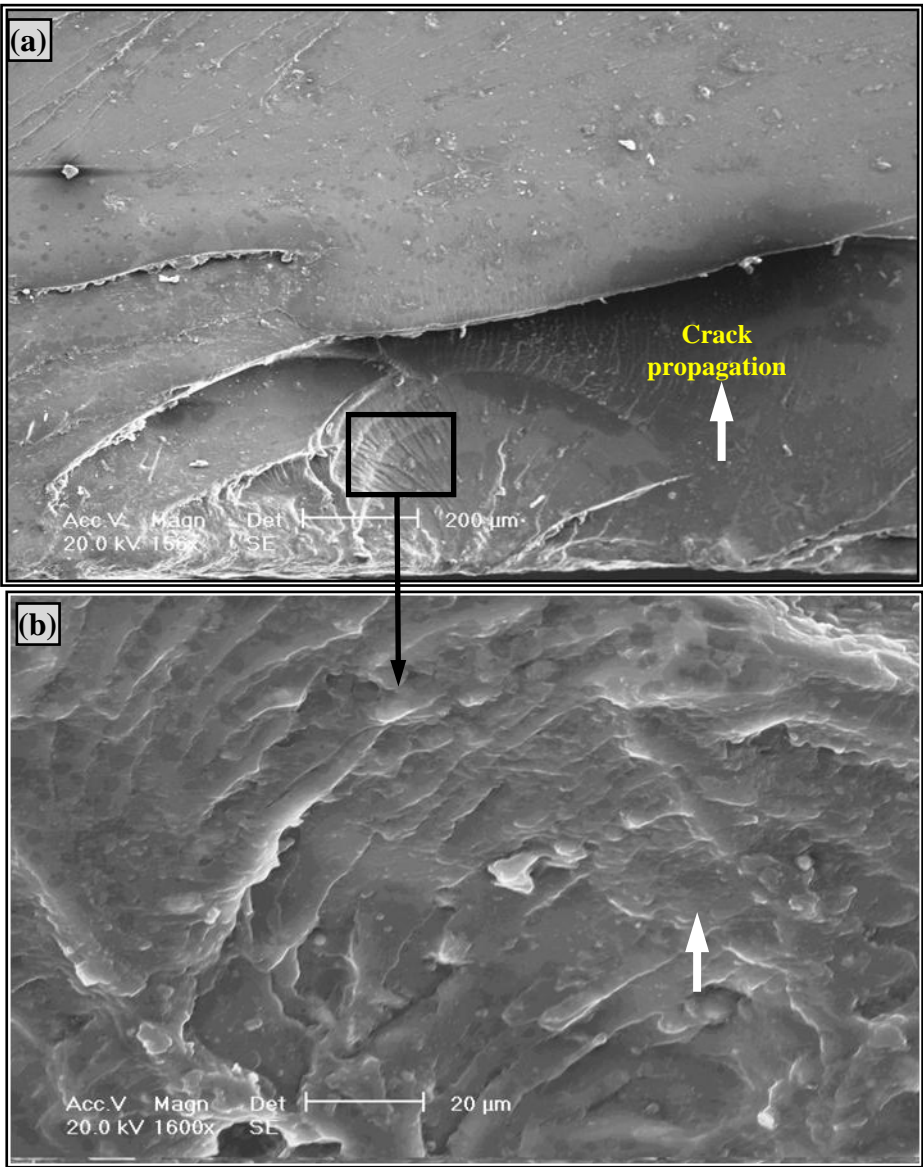


Figure 7.17: SEM Images of Fracture Surfaces near Crack Tip of: (a) 5% s-HNT/UPE and (b) 7% s-HNT/UPE Nanocomposites, Showing Crack Bridging Mechanism

In light of the above findings and discussion, the fracture surface of 3% s-HNT/UPE nanocomposite after SEN-3PB testing showed a semicircular region of well-defined local plastic deformation process around the crack initiation zone, as shown in Figure 7.18. This deformation process involved some toughness enhancement via blunting the crack tip and increasing the size of the plastic zone. With further increase of silanised halloysite, instead of the occurrence of local deformation process in the crack initiation zone and crack propagation zone, river liner markings (Figure 7.19) leading to the initial site of crack growth were detected in the topography of 5% s-

HNT nanocomposite, but substantial indications of plastic deformation in the control group were not noted. Hence, the lack of observed plastic deformation process and a smooth fracture surface agree well with the relatively low measured toughness of the nanocomposite. River pattern is a mechanism in which a pattern similar to a river and its branches are generated on the new cleavage plane at slightly different elevations. As the crack propagates, these levels combine to form a crack that advances on fewer parallel planes (Brooks & Choudhury 2002).



Note: White arrows indicate the direction of crack propagation.

Figure 7.18: SEM Micrographs of the Fracture Surfaces Near Crack Tip After SEN-3PB Testing of 3% S-HNT/UPE Nanocomposite, Showing the Crack Initiation Zone at Different Magnifications with a Local Deformation Process

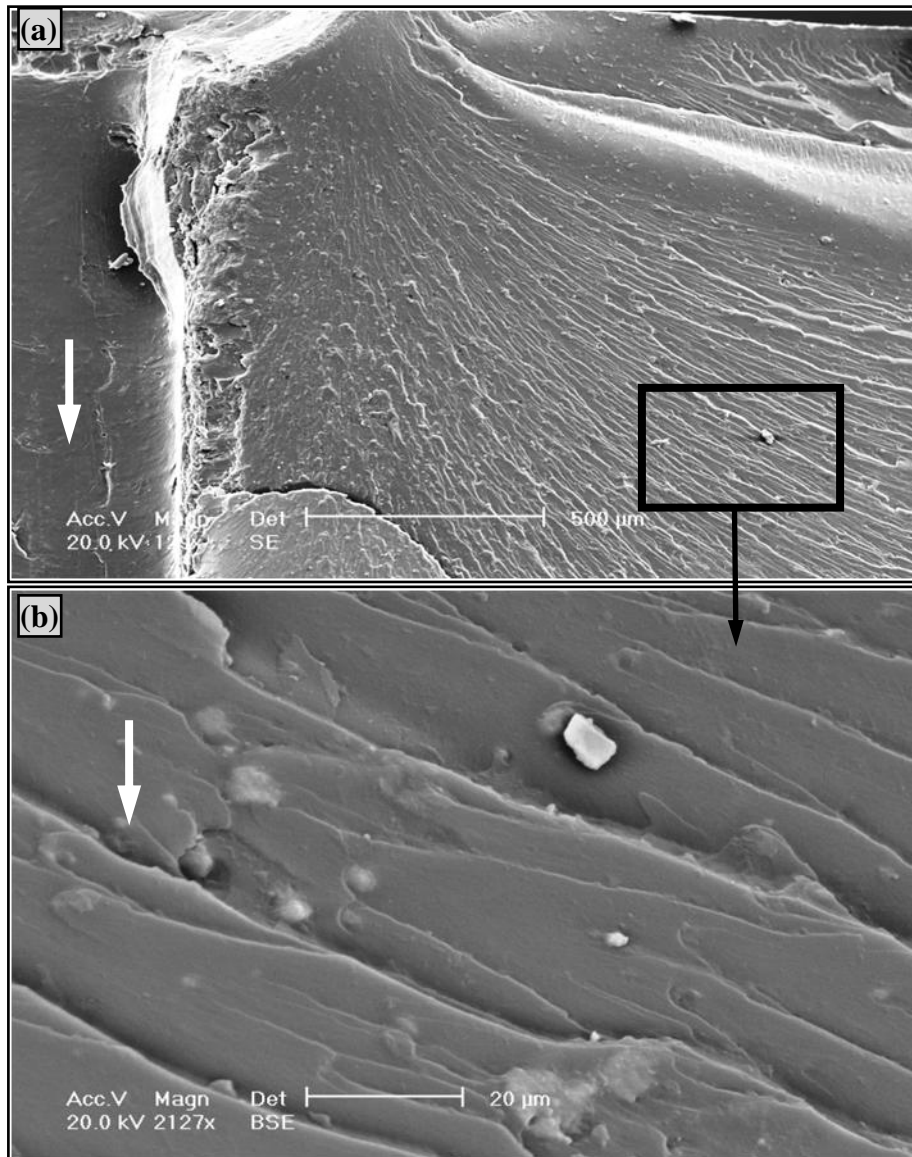


Figure 7.19: Scanning Electron Micrographs of Fracture Surface for 5% S-HNT/UPE Nanocomposite After SEN-3PB Testing, Showing Crack Initiation Zone at Different Magnifications with River Liners

Further, characteristic tail-like structures formed behind halloysite aggregates in the process zone on the fracture surface, as can be observed in Figure 7.20, which are often observed in nanoparticle-filled epoxy systems (Wang et al. 2005). The tail-like structures are actually steps that are formed when two secondary crack fronts, divided by aggregates, meet with each other. With an increase of halloysite content, the aerial density of these steps increased (see Figure 7.20b), the fracture surface became rougher, and more characteristic tails appeared and interconnected with each other (Figure 7.21). Wang, Zhang and Ye (2011) suggested that tail structure usually

forms when the two secondary crack fronts separated by a particle meet with each other after crack front bowing.

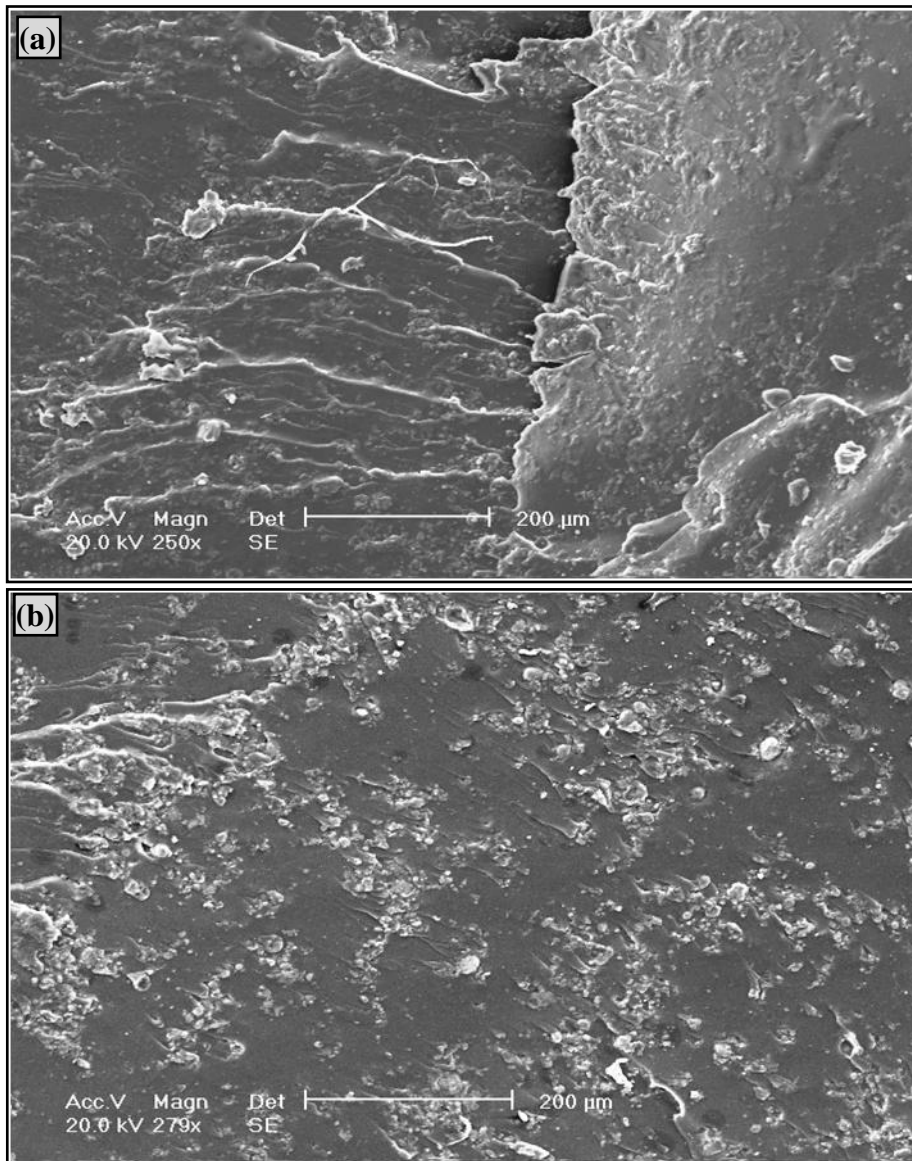


Figure 7.20: SEM Micrographs Illustrating the Fracture Surface of UPE Reinforced with: (a) 3 wt% s-HNT and (b) 5 wt% s-HNT Nanocomposites, Demonstrating the Tail-like Structures

Nevertheless, no qualitative interpretation of Figure 7.21 was found in the literature. Seyhan et al. (2009) claimed that a combination of well-dispersed nanotubes with well-impregnated smaller agglomerates leads to trigger void nucleation and/or microcrack coalescences at the interface between nanotubes and the surrounding matrix resin. Later, Tang et al. (2011) reported that treated halloysite particles in the

epoxy nanocomposite manifest small crack trajectories that are deflected and meander through the matrix, giving rise to increased resistance to crack propagation. However, the particle agglomerates may also promote premature failure ahead of crack. The current researcher's perspective actually aligns with both observations, with micro- and macrocracks found in the treated halloysite-unsaturated polyester composites, formed along the matrix-halloysite interfaces (see Figure 7.22).

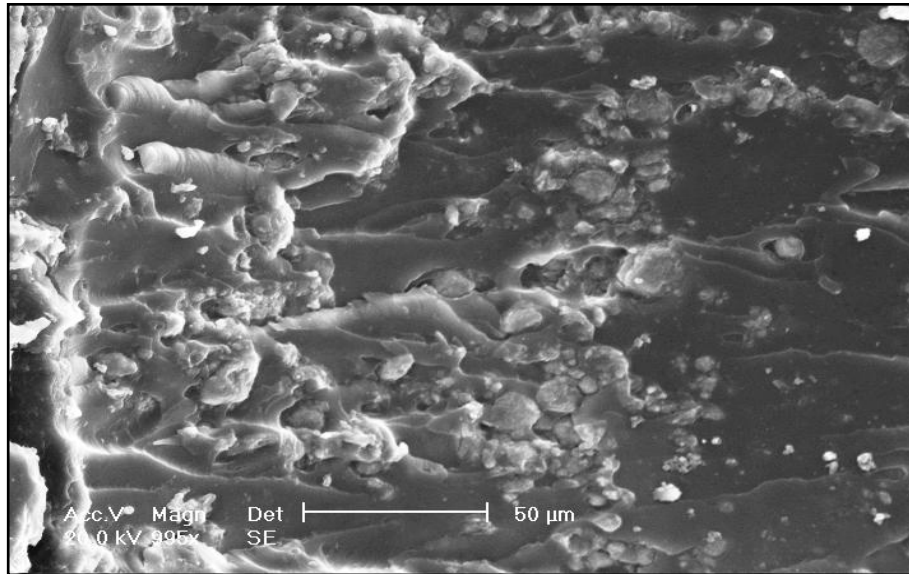


Figure 7.21: Fracture Surface Morphology After SEN-3PB Test of 5% S-HNT/UPE Nanocomposite

The formation of a large number of microcracks and the increase in the fracture surface area were due to crack deflection. This is a suitable answer to the earlier question regarding whether the nanoparticles in the thermosetting polymers deflected or bridged the crack. The formation of microcracks caused tensile yielding, and then a large tensile deformation aided to deflect the crack path. However, when these microcracks open, voids result and permit large strains. Consequently, the microcracks effectively lower the modulus in the frontal zone around the crack tip, and thus effectively reduce the stress intensity factor.

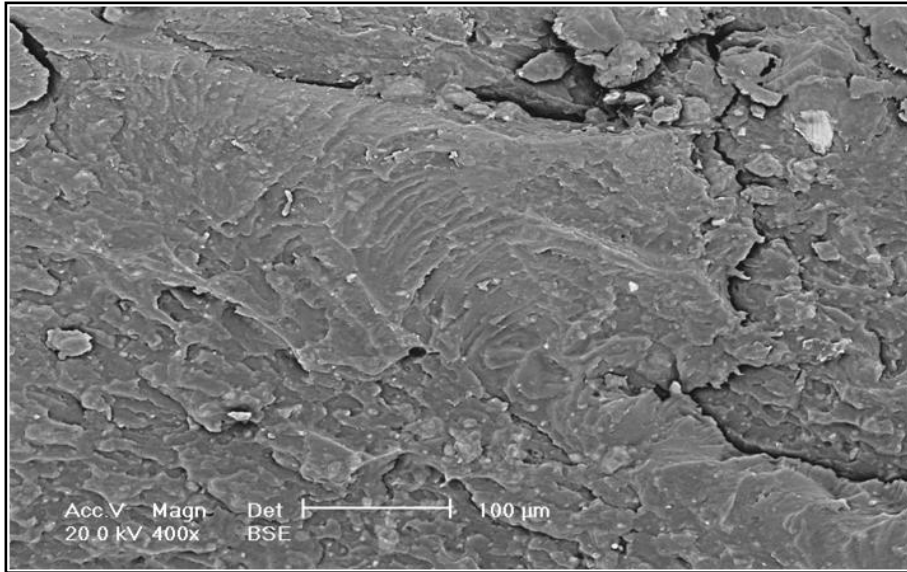


Figure 7.22: Fracture Surface Morphology After SEN-3PB Test of 5% S-HNT/UPE Nanocomposite, Showing Macrocracks

The situation of topography analysis (Figure 7.23) is very complicated for nanocomposites containing higher halloysite contents, with the fracture surface being very rough and filled with scale-like steps, indicating that the presence of halloysite layers forced the crack to propagate along a very tortuous path (see Figure 7.23a). This observation is supported by Ayatollahi, Shadlou and Shokrieh (2011), who found that the curved path of crack growth can be because the maximum tangential stress direction changes as the crack advances. At each step of crack propagation, the crack plane rotates and grows in a new direction, which has the maximum tangential stress.

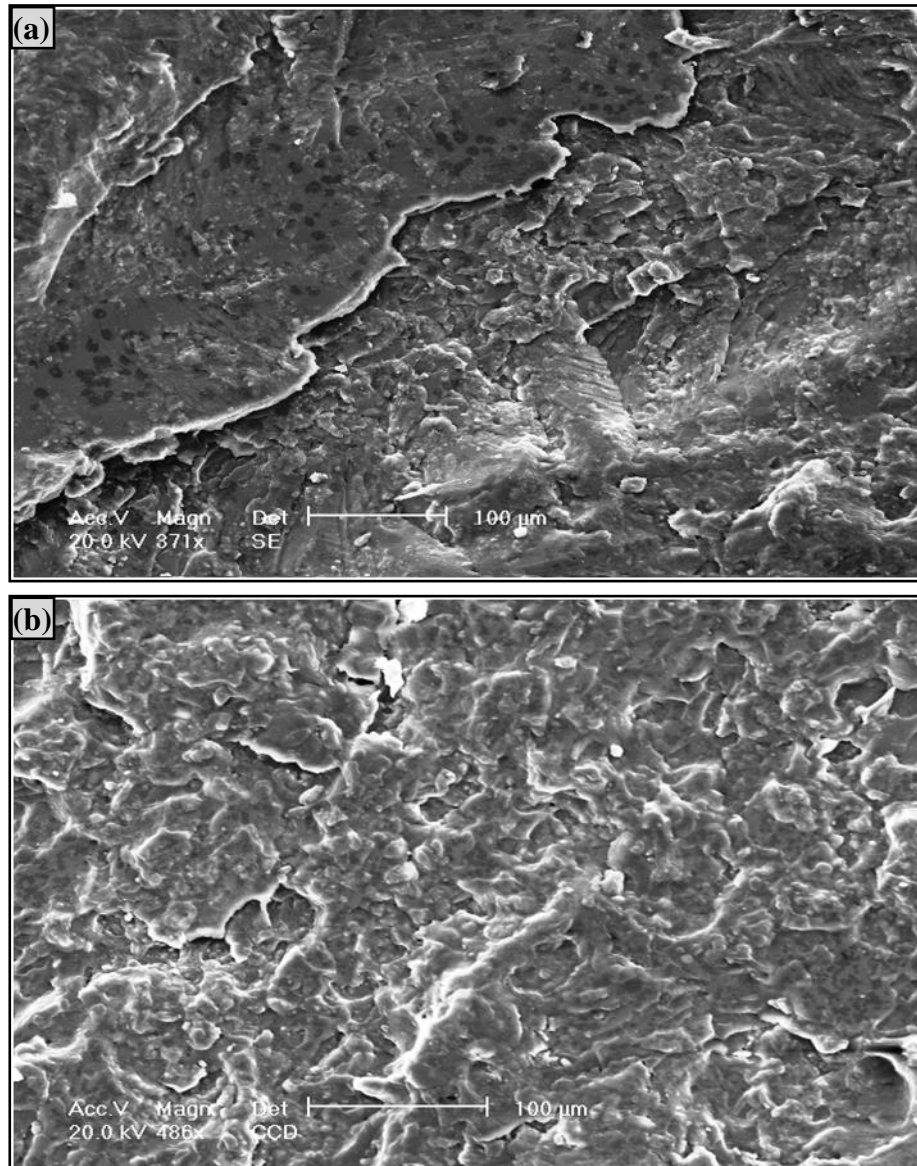


Figure 7.23: SEM Micrographs of the Fracture Surface for: (a) 7% s-HNT/UPE and (b) 9% s-HNT/UPE Nanocomposites

7.5 Summary

In this chapter, theoretical and experimental investigations were conducted to examine the role of untreated and silane-treated halloysite particles on the crack propagation and the quasi-static fracture toughness of thermosetting UPE nanocomposites. Two different fracture specimen geometries with two different loading conditions were analysed via ASTM D5045 standard to measure the fracture parameters of the UPE nanocomposites. The 3-D FE model based on cohesive

element method was undertaken using the ABAQUS software to simulate the crack growth through thermosetting polymer composite. Toughening mechanisms were identified using the SEM examination.

The incorporation of 3 wt% HNT or 3 wt% s-HNT particles into the UPE matrix exhibited their ability to carry the highest loads, over the neat UPE and the other nanocomposite systems. However, further studies would be required to figure out the optimization of the best weight percentage of HNT or s-HNT particles. Regardless of the specimen geometry and loading conditions, compounding halloysite particles into the UPE matrix showed significant improvements in toughness and fracture energy. The chemical silane treatment on the halloysite surface played a key role in improving the interfacial adhesion between the particles and the polymer matrix, and then in further enhancing toughness.

The toughness improvement was attributed to the presence of plastic deformation that blunts the crack tip, reduces the local stress concentration, and consequently allows composites to carry higher loads before failure occurs. The crack initiation and propagation in the halloysite/UPE nanocomposite was successfully simulated using the cohesive element method. Compared to the experimental observation, this method can accurately predict the crack propagation path in the composite, with the stress-strain curves obtained experimentally and theoretically being well convergent.

The fractographic analysis of the fracture surface for the unfilled UPE matrix tested using either CT specimen under tension or SEN under bending showed a highly smooth brittle fracture. The addition of rigid halloysite particles into the UPE matrix contributed to the initiation of various mechanisms of energy absorption before the appearance of the first crack, with different major and minor toughening mechanisms generated. With the use of untreated halloysite, several main toughening mechanisms were observed and believed to be responsible for the toughness improvement in the nanocomposites. These were zone shielding and shear yielding with the presence of fully particles debonding, which activates the void expansion and matrix shear deformation energy dissipation mechanisms.

The matrix shear yielding was also noted as a toughening mechanism in the fracture surface of silanised halloysite nanocomposite. However, it was thought that the energy dissipation through this mechanism was insufficient to be responsible for the overall increased toughness in such nanocomposites. Other major mechanisms—such as massive shear banding, crack deflection and local plastic deformation occurring around the crack initiation zone, as well as river line patterns, tail-like structure and the formation of microcrack mechanisms—played key roles in blunting crack tip, increasing the size of the plastic zone and subsequently improving the toughness.

Chapter 8: Conclusion and Future Works

8.1 Conclusion

This thesis experimentally investigated the effects of untreated HNT and VTMS-treated HNT (s-HNT) on the structural and material properties of UPE-based HNT or s-HNT nanocomposites, prepared by mechanical mixing and ultrasonic process. The crack initiation and growth in the nanocomposites was numerically simulated using ABAQUS FE software. To summarise the main findings of the thesis, the following sections individually discuss the roles of HNT and s-HNT particles on the structural characteristics and material performance of the developed composites.

8.1.1 Morphological Characteristics

1. The incorporation of untreated halloysite (HNT) in the thermosetting UPE matrix showed large tactoids of HNT, especially at higher loadings (> 5 wt %) in the cured UPE/HNT nanocomposites, indicating poor dispersion of HNT particles. The morphology was characterised by a variation of rich and poor regions. Some regions were crowded with halloysite, while other regions did not have any, and there were more such regions with a further increase of halloysite content in the UPE matrix. In contrast, the addition of silanised halloysite (s-HNT) showed a decreased tactoid size with an increased density of material randomly dispersed in the structure.
2. The compatibility between the particles and polymer chains was one of the most important factors influencing the state of dispersion in the nanocomposites. The nature and interactions of the components and affinity between the particles and polymer were also responsible for determining good particle distribution. The effect of grafting HNT with silane on the structural characteristics of UPE/s-HNT nanocomposites was obvious, with the particles intercalated and well dispersed without entanglement through the UPE matrix, regardless of the halloysite content.

3. The addition of HNT or s-HNT to the UPE matrix changed its crystalline structure—the degree of exfoliation was less and the peaks were more frequent with high loadings of HNT or s-HNT particles. Short reflections presented at $2\theta \approx 2.78^\circ$ in the XRD patterns of all UPE/HNT nanocomposites corresponded to the interlayer spacing of un-intercalated halloysite ($d_{001} = 14.7\text{\AA}$). The d_{001} peak intensity increased with increasing halloysite content, which may reflect the presence of large halloysite tactoids in the morphology of the nanocomposites.

8.1.2 Thermo, Thermodynamic and Mechanical Properties

1. The effect of HNT and s-HNT particles on the thermo, thermodynamic and mechanical properties of UPE/HNT and UPE/s-HNT nanocomposites showed unremarkable changes in the thermal stability of the UPE matrix. The presence of 3% s-HNT in the nanocomposites delayed their thermal degradation by only 3°C . The decomposition temperatures at 5% weight loss rate ($T_{5\text{wt}\%}$) reduced from 438°C for the UPE/3% s-HNT to 435°C for the UPE/3% HNT nanocomposites.
2. The role of HNT or s-HNT particles in the UPE nanocomposites caused a modest decrease in the T_g values, associated with a shift in the initial formulation of a giant molecule network of the UPE matrix. The small drop in T_{gs} was attributed to the interfacial plasticisation and preferential interactions between the particle and thermosetting UPE crosslinking agent. However, it caused significant increase in all viscoelastic properties (the storage modulus and loss modulus) of the nanocomposites, compared to the neat UPE matrix. This increase was because of strong interfacial adhesion and the uniformly dispersed halloysites that restricted the segmented motion of the UPE network.
3. The role of HNT and s-HNT in the UPE matrix also caused a similar increasing trend for both tensile and flexural strengths and their moduli with loading up to 5%, and the 3% HNT or s-HNT showed the greatest increase of mechanical properties, compared to the unfilled UPE. However, further increase of halloysite contents resulted in lower properties, due to the existence of HNT agglomerations in the microstructure.

4. The mathematical results of Young's modulus of the composites with various HNT loadings apparently showed good agreement with the experimentally obtained results of nanocomposites, including up to 5 wt% HNT content. However, the results overestimated the experimental results with increasing HNT content over 5 wt% (3 vol. %).

8.1.3 Tribological Behaviour

1. The effect of the incorporation of HNT and s-HNT nanoparticles on the CoF and specific wear rates of the cured UPE nanocomposites exhibited a negative effect at low particle contents, and better performance with high particle contents. That is, the 7% HNT and 7% s-HNT nanocomposites showed better wear resistance than the others.
2. Based on the microscopic observations, the dominant wear mechanisms of the UPE/HNT nanocomposites were two-body abrasion wear and three-body abrasion wear. In some conditions, adhesive was associated with pitting and particles pulling out for the UPE/s-HNT nanocomposites.

8.1.4 Impact Toughness

1. The additions of HNT and s-HNT particles into the UPE nanocomposite contributed to slightly increasing the impact strength and total energy with increasing HNT or s-HNT loadings up to 5 wt% for all testing temperatures (-20°C, 20°C and 60°C). Further increase of halloysite loading induced lower impact strength due to the presence of halloysite clusters and the poor interactions between halloysite and the UPE polymer matrix.
2. All the materials had fast shatter when impacted at sub-zero temperatures. However, increasing the testing temperature closer to the T_g tended to improve the impact resistance with an acceptable toughening criterion due to the shifted DBTT. The SEM observations showed that, with the presence of halloysite in the UPE resin, there was a change in fracture mode from cleavage and fast brittle

fracture in the neat UPE to microvoid-coalescence with a minor plastic deformation in the nanocomposites.

8.1.5 Failure Analysis and Toughening Mechanisms

1. The 3 wt% HNT and 3 wt% s-HNT nanocomposites demonstrated their ability to carry the highest loads, compared to the neat UPE. However, further studies would be required to figure out the optimization of the best weight percentage of HNT or s-HNT particles. Regardless of the specimen geometry and loading conditions, compounding HNT particles into the UPE matrix showed significant improvements in toughness and fracture energy.
2. Silane treatment on the halloysite surface played a key role in improving the dispersion of particles and interfacial adhesion between the particles and the polymer matrix, and consequently in further enhancing toughness. This enhancement was attributed to the presence of plastic deformation due to the particles' role, which blunts the crack tip, reduces the local stress concentration, and consequently allows composites to carry higher loads before failure occurs.
3. The simulation of crack initiation and propagation in the UPE/HNT nanocomposite using the cohesive element method exhibited well convergent results compared to the experimental ones. Hence, this method can accurately be used to predict the crack propagation path in the composite.
4. The fractographic analysis of the fracture surface for the unfilled UPE matrix tested using either CT specimen under tension or SEN under bending showed a highly smooth brittle fracture. The addition of rigid halloysites into the UPE matrix contributed to the initiation of various mechanisms of energy absorption before the appearance of the first crack, and different major and minor toughening mechanisms were generated. With the use of HNT particles, several major toughening mechanisms were observed and believed to be responsible for the toughness improvement in the composites.

8.2 Future Works

This study examined the roles of HNT and s-HNT particles on the structure/property relationship in UPE/HNT and UPE/s-HNT nanocomposites. Different properties were considered in this research, including the dispersion status of HNT in the UPE matrix and UPE/HNT interaction, composite reinforcement, wear resistance and impact strength, as well as fracture toughness and toughening mechanisms. Nevertheless, other important properties of crosslinked UPE filled by HNT nanocomposites can be considered for future research. The following suggestions are given, based on the findings of the current study:

1. Investigate the role of HNT and s-HNT particles on the fire retardancy and reduced heat release rate, barrier properties or thermal insulation/mass barrier, membrane separation and ultraviolet resistance.
2. Study the effect of using different silane coupling agents and different silane treatment times on the interfacial adhesion (or affinity) of HNT particles with the UPE matrix, and then on mechanical performance, fracture toughness and toughening mechanisms.
3. Examine the synergistic effect of using different commercial fillers (such as polytetrafluorethylen and graphite) with higher HNT loadings on the frictional coefficient and wear rate in the UPE nanocomposites. Graphene oxide is also potential filler that could be used to enhance the tribological performance.
4. Study the effects of HNT aspect ratio, orientation and different particle sizes on the crack initiation and growth, and then on fracture toughness.
5. Investigate the role of HNT or s-HNT on the fracture behaviour of UPE/HNT and UPE/s-HNT nanocomposites under mixed-mode I/II brittle fracture test and under shear loading conditions.

6. Study the effects of a combination of different impact modifiers, such as micro-sized rubber particles or block copolymer (nonreactive or reactive modifiers) with the UPE resin on the fracture properties of UPE/HNT nanocomposites.
7. Seek to understand the interface behaviour in UPE/HNT nanocomposites by using Materials Studio 4.3 or the molecular dynamic simulator, LAMMPS, in order to study the ultra high interface/volume ratio.
8. Perform a crack propagation simulation by considering particle size and particle boundary strength on the cracking patterns and fracture toughness. Discontinuous crack bridging or the crack bridge model could be applied to analyse fracture toughness in brittle materials (or thermosetting polymers-based nanocomposites).

References

Alamri, H & LOW, IM 2012, 'Effect of water absorption on the mechanical properties of nano-filler reinforced epoxy nanocomposites', *Materials and Design*, vol. 42, pp. 214–222.

Anderson, BJ & Zukoski, CF 2010, 'Rheology and microstructure of polymer nanocomposite melts: variation of polymer segment-surface interaction', *Langmuir*, vol. 26, pp. 8709–8720.

Anderson, TL 2005, *Fracture mechanics: fundamentals and applications*, Taylor and Francis Group, Florida.

Arora, A, Choudhary, V & Sharma, DK 2010, 'Effect of clay content and clay/surfactant on the mechanical, thermal and barrier properties of polystyrene/organoclay nanocomposites', *Journal of Polymer Research*.

Arranz-Andrés, J, Pérez, E & Cerrada, ML 2012, 'Smectic polyester/layered silicate nanostructured hybrids: effect of modified nanoclay in the phase transitions', *Polymer*, vol. 53, pp. 386–394.

ASTM 2007, *Standard test method for plain-strain fracture toughness and strain energy release rate of plastic materials. D 5045-99*, Author, Philadelphia, US.

ASTM 2010a, *Standard test method for ranking resistance of materials to sliding wear using block-on-ring wear test. G77-10*, Author, Philadelphia, US.

ASTM 2010b, *Standard test method for rubber property—durometer hardness. D2240-10*, Author, Philadelphia, US.

Ayatollahi, MR, Shadlou, S & Shokrieh, MM 2011, 'Mixed mode brittle fracture in epoxy/multi-walled carbon nanotube nanocomposites', *Engineering Fracture Mechanics*, vol. 78, pp. 2620–2632.

Banea, MD & Silva, LFMD 2009, 'Adhesively bonded joints in composite materials: an overview', *Proceedings of the Institution of Mechanical Engineers, Part L: Journal of Materials Design and Applications*, p. 223.

Barbero, EJ 2011, *Introduction to composite materials design*, Taylor and Francis Group, Florida.

Barenblatt, GI 1962, 'The mathematical theory of equilibrium cracks in brittle fracture', *Advances in Applied Mechanics*, vol. 7, pp. 55–129.

Barick, AK & Tripathy, DK 2010, 'Effect of organoclay on the morphology, mechanical, thermal, and rheological properties of organophilic montmorillonite

nanoclay based thermoplastic polyurethane nanocomposites prepared by melt blending', *Polymer Engineering and Science*, pp. 484–498.

Barrientos-Ramirez, S, Oca-Ramirez, GMD, Ramos-Fernandez, EV, Sepulveda-Escribano, A, Pastor-Blas, MM & Gonzalez-Montiel, A 2011, 'Surface modification of natural halloysite clay nanotubes with aminosilanes. Application as catalyst supports in the atom transfer radical polymerization of methyl methacrylate', *Applied Catalysis A: General*, vol. 406, pp. 22–33.

Barus, S, Zanetti, M, Lazzari, M & Costa, L 2009, 'Preparation of polymeric hybrid nanocomposites based on PE and nanosilica', *Polymer*, vol. 50, pp. 2595–2600.

Bashar, M, Sundararaj, U & Mertiny, P 2012, 'Microstructure and mechanical properties of epoxy hybrid nanocomposites modified with acrylic tri-block-copolymer and layered-silicate nanoclay', *Composites: Part A*, vol. 43, pp. 945–954.

Baskaran, R, Sarojadevi, M & Vijayakumar, CT 2011, 'Unsaturated polyester nanocomposites filled with nano alumina', *Journal of Materials Science*, vol. 46, pp. 4864–4871.

Beheshty, MH, Vafayan, M & Poorabdollah, M 2009, 'Low profile unsaturated polyester resin—clay nanocomposite properties', *Polymer Composites*, pp. 629–638.

Behradfar, A, Shojaei, A & Nasrin S 2010, 'Rheological and mechanical characteristics of low density polyethylene/ethylene-vinyl acetate/organoclay nanocomposites', *Polymer Engineering and Science*, pp. 1315–1325.

Bhattacharya, SN, Kamal, MR & Gupta, RK 2008, *Polymeric nanocomposites: theory and practice*, Carl Hanser Verlag, Munich.

Brooks, CR & Choudhury, A 2002, *Failure analysis engineering materials*, McGraw-Hill Companies Inc., New York.

Cenna, AA, Dastoor, P, Beehag, A & Page, NW 2001, 'Effects of graphite particle addition upon the abrasive wear of polymer surfaces', *Journal of Materials Science*, vol. 36, pp. 891–900.

Chabert, E, Bornert, M, Bourgeat-Lami, E, Cavallé, J-Y, Dendievel, R, Gauthier, C, Putaux, JL & Zaoui, A 2004, 'Filler–filler interactions and viscoelastic behavior of polymer nanocomposites', *Materials Science and Engineering A*, vol. 381, pp. 320–330.

Chacko, A, Sadiku, ER & Vorster, OC 2010, 'The rheological and mechanical properties of ethylene-vinyl acetate (EVA) copolymer and organoclay nanocomposites', *Journal of Reinforced Plastics and Composites*, 29.

Chang, L, Zhang, Z, Ye, L & Friedrich, K 2007, 'Tribological properties of epoxy nanocomposites III: characteristics of transfer films', *Wear*, vol. 262, pp. 699–706.

Chen, B & Evans, J 2008, 'Impact and tensile energies of fracture in polymer-clay nanocomposites', *Polymer*, vol. 49, pp. 5113–5118.

Chen, Q, Chasiotis, I, Chen, C & Roy, A 2008, 'Nanoscale and effective mechanical behavior and fracture of silica nanocomposites', *Composites Science and Technology*, vol. 68, pp. 3137–3144.

Chieruzzi, M, Miliozzi, A & Kenny, JM 2013, 'Effects of the nanoparticles on the thermal expansion and mechanical properties of unsaturated polyester/clay nanocomposites', *Composites: Part A*, vol. 45, pp. 44–48.

Chinellato, AC, Vidotti, SE, Hu, G-H & Pessan, LA 2010, 'Compatibilizing effect of acrylic acid modified polypropylene on the morphology and permeability properties of polypropylene/organoclay nanocomposites', *Composites Science and Technology*, vol. 70, pp. 458–465.

Cornec, A, Scheider, I & Schwalbe, K-H 2003, 'On the practical application of the cohesive model', *Engineering Fracture Mechanics*, vol. 70, pp. 1963–1987.

Dai, G & Jr, LM 2013, 'Damage evolution in nanoclay-reinforced polymers: a three-dimensional computational study', *Composites Science and Technology*, vol. 74, pp. 67–77.

Dasari, A, Lim, S-H, Yu, Z-Z & Mai, Y-W 2007, 'Toughening, thermal stability, flame retardancy, and scratch-wear resistance of polymer-clay nanocomposites', *Australian Journal of Chemistry*, vol. 60, pp. 496–518.

Dasari, A, Yu, Z-Z & Mai, Y-W 2009, 'Fundamental aspects and recent progress on wear/scratch damage in polymer nanocomposites', *Materials Science and Engineering R*, vol. 63, pp. 31–80.

Dayma, N & Satapathy, BK 2012, 'Microstructural correlations to micromechanical properties of polyamide-6/low density polyethylene-grafted-maleic anhydride/nanoclay ternary nanocomposites', *Materials and Design*, vol. 33, pp. 510–522.

Deng, S, Zhang, J & Ye, L 2009, 'Halloysite–epoxy nanocomposites with improved particle dispersion through ball mill homogenisation and chemical treatments', *Composites Science and Technology*, vol. 69, pp. 2497–2505.

Deng, S, Zhang, J, Ye, L & Wu, J 2008, 'Toughening epoxies with halloysite nanotubes', *Polymer*, vol. 49, pp. 5119–5127.

Deshmane, C, Yuan, Q, Perkins, RS & Misra, RDK 2007, 'On striking variation in impact toughness of polyethylene–clay and polypropylene–clay nanocomposite systems: the effect of clay–polymer interaction', *Materials Science and Engineering A*, vol. 458, pp. 150–157.

Dittanet, P & Pearson, RA 2012, 'Effect of silica nanoparticle size on toughening mechanisms of filled epoxy', *Polymer*, vol. 53, pp. 1890–1905.

- Dong, Y, Chaudhary, D, Ploumis, C & Lau, K-T 2011, 'Correlation of mechanical performance and morphological structures of epoxy micro/nanoparticulate composites', *Composites Part A*, vol. 42, pp. 1483–1492.
- El-Tayeb, NSM 2009, 'Two-body abrasive behaviour of untreated SC and R-G fibres polyester composites', *Wear*, vol. 266, pp. 220–232.
- El-Tayeb, NSM & Yousif, BF 2007, 'Evaluation of glass fiber reinforced polyester composite for multi-pass abrasive wear applications', *Wear*, vol. 262, pp. 1140–1151.
- Esfahani, JM, Sabet, AR & Esfandeh, M 2011, 'Assessment of nanocomposites based on unsaturated polyester resin/nanoclay under impact loading', *Polymers for Advanced Technologies*.
- Evora, VMF & Shukla, A 2003, 'Fabrication, characterization, and dynamic behavior of polyester/TiO₂ nanocomposites', *Materials Science and Engineering A*, vol. 361, pp. 358–366.
- Friedrich, K, Fakirov, S & Zhang, Z 2005, *Polymer composites: from nano-to-macro-scale*, Springer Science & Business Media, Inc, US.
- Friedrich, K & Schlarb, AK (eds.) 2008, *Tribology of polymeric nanocomposites*, Elsevier, Amstrdam.
- Friedrich, K, Zhang, Z & Schlarb, AK 2005, 'Effects of various fillers on the sliding wear of polymer composites', *Composites Science and Technology*, vol. 65, pp. 2329–2343.
- Gahleitner, M, Kretzschmar, B, Vliet, GV, Devaux, J, Pospiech, D, Bernreitner, K & Ingolic, E 2006, 'Rheology/morphology interactions in polypropylene/polyamide-6 nanocomposites', *Rheologica Acta*, vol. 45, pp. 322–330.
- Garea, SA, Ghebaur, A, Constantin, F & Iovu, H 2011, 'New hybrid materials based on modified halloysite and unsaturated polyester resin', *Polymer-Plastics Technology and Engineering*, vol. 50, pp. 1096–1102.
- Gibson, RF 2007, *Principles of composite material mechanics*, CRC Press, UK.
- Giner, E, Sukumar, N, Tarancon, JE & Fuenmayor, FJ 2009, 'An Abaqus implementation of the extended finite element method', *Engineering Fracture Mechanics*, vol. 76, pp. 347–368.
- Gubeljask, N, Chapetti, MD, Predan, J & Landes, JD 2011, 'CTOD-R curve construction from surface displacement measurements', *Engineering Fracture Mechanics*, vol. 78, pp. 2286–2297.
- Guo, B, Zou, Q, Lei, Y & Jia, D 2009, 'Structure and performance of polyamide 6/halloysite nanotubes nanocomposites', *Polymer Journal*, vol. 41, pp. 835–842.

Gupta, RK, Kennel, E & Kim, K-J 2010, *Polymer nanocomposites handbook*, Taylor and Francis Group, LLC, Florida.

Guth, E & Gold, O 1938, 'Hydrodynamical theory of the viscosity of suspensions', *Physical Review*, vol. 53, p. 322.

Ha, S-R, Rhee, K-Y, Park, S-J & Lee, JH 2010, 'Temperature effects on the fracture behavior and tensile properties of silane-treated clay/epoxy nanocomposites', *Composites: Part B*, vol. 41, pp. 602–607.

Ha, SR & Rhee, KY 2008, 'Effect of surface-modification of clay using 3-aminopropyltriethoxysilane on the wear behavior of clay/epoxy nanocomposites', *Colloids and Surfaces A: Physicochemical and Engineering Aspects*, vol. 322, pp. 1–5.

Halpin, JC & Kardos, JL 1976, 'The Halpin-Tsai equations: a review', *Polymer Engineering and Science*, vol. 16, pp. 344–352.

Hashmi, SAR, Dwivedi, UK & Chand, N 2007, 'Graphite modified cotton fibre reinforced polyester composites under sliding wear conditions', *Wear*, vol. 262, pp. 1426–1432.

Hsieh, TH, Kinloch, AJ, Masania, K, Lee, JS, Taylor, AC & Sprenger, S 2010a, 'The toughness of epoxy polymers and fibre composites modified with rubber microparticles and silica nanoparticles', *Journal of Materials Science*, vol. 45, pp. 1193–1210.

Hsieh, TH, Kinloch, AJ, Masania, K, Taylor, AC & Sprenger, S 2010b, 'The mechanisms and mechanics of the toughening of epoxy polymers modified with silica nanoparticles', *Polymer*, vol. 51, pp. 6284–6294.

Huang, Y, Hunston, DL, Kinloch, AJ & Riew, CK 1993, Mechanisms of toughening thermoset resins', in CK Riew (ed.), *Toughened plastics I*, American Chemical Society, Washington, DC.

Ianchis, R, Corobea, MC, Donescu, D, Rosca, ID, Cinteza, LO, Nistor, LC, Vasile, E, Marin, A & Preda, S 2012, 'Advanced functionalization of organoclay nanoparticles by silylation and their polystyrene nanocomposites obtained by miniemulsion polymerization', *Journal of Nanoparticle Research*, vol. 14, p. 1233.

Ingram, S, Dennis, H, Hunter, I, Liggat, JJ, McAdam, C, Pethrick, RA, Schaschke, C & Thomson, D 2008, 'Influence of clay type on exfoliation, cure and physical properties of in situ polymerised poly(methyl methacrylates) nanocomposites', *Polymer International*, vol. 57, pp. 1118–1127.

Ismail, H. & Shaari, SM 2010, 'Curing characteristics, tensile properties and morphology of palm ash/halloysite nanotubes/ethylene-propylene-diene monomer (EPDM) hybrid composites', *Polymer Testing*, vol. 29, pp. 872–878.

Jancar, J, Douglas, JF, Starr, FW, Kumar, SK, Cassagnau, P, Lesser, AJ, Sternstein, SS & Buehler, MJ 2010, 'Current issues in research on structure-property relationships in polymer nanocomposites', *Polymer*, vol. 51, pp. 3321–3343.

Janssen, M, Zuidema, J & Wanhill, R 2004, *Fracture mechanics*, TJ International Ltd, Cornwall.

Jawahar, P, Gnanamoorthy, R & Balasubramanian, M 2006, 'Tribological behaviour of clay—thermoset polyester nanocomposites', *Wear*, vol. 261, pp. 835–840.

Jia, Q, Shan, S, Wang, Y, Gu, L & Li, J 2008, 'Tribological performance and thermal behavior of epoxy resin nanocomposites containing polyurethane and organoclay', *Polymers for Advanced Technologies*, vol. 19, pp. 859–864.

John, B, Nair, CPR & Ninan, KN 2010, 'Effect of nanoclay on the mechanical, dynamic mechanical and thermal properties of cyanate ester syntactic foams', *Materials Science and Engineering A*, vol. 527, pp. 5435–5443.

Joo, JH, Shim, JH, Choi, JH, Choi, C-H, Kim, D-S & Yoon, J-S 2008, 'Effect of the silane modification of an organoclay on the properties of polypropylene/clay composites', *Journal of Applied Polymer Science*, vol. 109, pp. 3645–3650.

Kango, S, Kalia, S, Celli, A, Njuguna, J, Habibi, Y & Kumar, R 2013, 'Surface modification of inorganic nanoparticles for development of organic–inorganic nanocomposites—a review', *Progress in Polymer Science*, vol. 38, pp. 1232–1261.

Kaushik, AK, Podsiadlo, P, Qin, M, Shaw, CM, Waas, AM, Kotov, NA & Arruda, EM 2009, 'The role of nanoparticle layer separation in the finite deformation response of layered polyurethane-clay nanocomposites', *Macromolecules*, vol. 42, pp. 6588–6595.

Kheng, E, Iyer, HR, Podsiadlo, P, Kaushik, AK, Kotov, NA, Arruda, EM & Waas, AM 2010, 'Fracture toughness of exponential layer-by-layer polyurethane/poly(acrylic acid) nanocomposite films', *Engineering Fracture Mechanics*, vol. 77, pp. 3227–3245.

Kim, BC, Park, SW & Lee, DG 2008, 'Fracture toughness of the nano-particle reinforced epoxy composite', *Composite Structures*, vol. 86, pp. 69–77.

Koerner, H, Misra, D, Tan, A, Drummy, L, Mirau, P & Vaia, R 2006, 'Montmorillonite-thermoset nanocomposites via cryo-compounding', *Polymer*, vol. 47, pp. 3426–3435.

Koo, JH 2006, *Polymer nanocomposites processing, characterization, and applications*, McGraw-Hill Professional Publishing, Ohio.

Kotsilkova, R & Pissis, P (eds) 2007, *Thermoset nanocomposites for engineering applications*, Smithers Rapra Technology Ltd, UK.

Krishnamoorti, R & Vaia, RA (eds) 2002, *Polymer nanocomposites synthesis, characterization, and modeling*, American Chemical Society, Washington, DC.

Krueger, R 2004, 'Virtual crack closure technique: history, approach, and applications', *Applied Mechanics Reviews*, 57.

Kumar, B, Chitsiriphanit, S & Sun, CT 2011, 'Significance of K-dominance zone size and nonsingular stress field in brittle fracture', *Engineering Fracture Mechanics*, vol. 78, pp. 2042–2051.

Lampman, S 2003, *Characterization and failure analysis of plastics*, ASM International, Ohio.

Lauke, B 2008, 'On the effect of particle size on fracture toughness of polymer composites', *Composites Science and Technology*, vol. 68, pp. 3365–3372.

Liang, YL & Pearson, RA 2009, 'Toughening mechanisms in epoxy–silica nanocomposites (ESNs)', *Polymer*, vol. 50, pp. 4895–4905.

Liang, YL & Pearson, RA 2010, 'The toughening mechanism in hybrid epoxy-silica-rubber nanocomposites (HESRNs)', *Polymer*, vol. 51, pp. 4880–4890.

Lin, J-C 2008, 'Investigation of impact behavior of various silica-reinforced polymeric matrix nanocomposites', *Composite Structures*, vol. 84, pp. 125–131.

Lin, Y, Chen, H, Chan, C-M & Wu, J 2008, 'High impact toughness polypropylene/CaCO₃ nanocomposites and the toughening mechanism', *Macromolecules*, vol. 41, pp. 9204–9213.

Lin, Y, Ng, KM, Chan, C-M, Sun, G & Wud, J 2011, 'High-impact polystyrene/halloysite nanocomposites prepared by emulsion polymerization using sodium dodecyl sulfate as surfactant', *Journal of Colloid and Interface Science*, vol. 358, pp. 423–429.

Liu, C, Luo, YF, Jia, ZX, Zhong, BC, Li, SQ, Guo, BC & Jia, DM 2011, 'Enhancement of mechanical properties of poly(vinyl chloride) with polymethyl methacrylate-grafted halloysite nanotube', *eXPRESS Polymer Letters*, vol. 5, pp. 591–603.

Lu, P, Xu, J & Liu, K 2011, 'Preparation and properties of unsaturated polyester nanocomposites based on silylated sepiolite nanofibers', *Journal of Applied Polymer Science*, vol. 119, pp. 3043–3050.

Ma, J, Mo, M-S, Du, X-S, Rosso, P, Friedrich, K & Kuan, H-C 2008, 'Effect of inorganic nanoparticles on mechanical property, fracture toughness and toughening mechanism of two epoxy systems', *Polymer*, vol. 49, pp. 3510–3523.

Macmillan, JH 1997, 'Using silanes as adhesion promoters', *American Chemical Society* [Online].

Mahapatra, SS & Patnaik, A 2009, 'Study on mechanical and erosion wear behavior of hybrid composites using Taguchi experimental design', *Materials & Design*, vol. 30, pp. 2791–2801.

Maji, PK, Guchhait, PK & Bhowmick, AK 2009, 'Effect of nanoclays on physico-mechanical properties and adhesion of polyester-based polyurethane nanocomposites: structure-property correlations', *Journal of Materials Science*, vol. 44, pp. 5861–5871.

Mark, JE, Allcock, HR & West, R 2005, *Inorganic polymers*, Oxford University Press, New York.

Merhari, L (ed.) 2009, *Hybrid nanocomposites for nanotechnology: electronic, optical, magnetic and biomedical applications*, Springer Science LLC, US.

Milne, I, Ritchie, RO & Karihaloo, B (eds) 2003, *Comprehensive structural integrity: fracture of materials from nano to macro*, Elsevier Ltd, Oxford.

Mittal, KL 2009, *Silanes and other coupling agents*, Koninklijke Brill NV, Leiden, The Netherlands.

Mittal, V (ed.) 2012, *In-situ synthesis of polymer nanocomposites: polymer-, nano-, micro- and macrocomposites*, Wiley-Vch Verlag GmbH & Co. KGaA, Weinheim, Germany.

Moczko, J & Pukanszky, B 2008, 'Polymer micro and nanocomposites: structure, interactions, properties', *Journal of Industrial and Engineering Chemistry*, vol. 14, pp. 535–563.

Monti, M, Puglia, D, Natali, M, Torre, L & Kenny, JM 2011, 'Effect of carbon nanofibers on the cure kinetics of unsaturated polyester resin: thermal and chemorheological modelling', *Composites Science and Technology*, vol. 71, pp. 1507–1516.

Morote-Martinez, V, Pascual-Sanchez, V & Martin-Martinez, JM 2008, 'Improvement in mechanical and structural integrity of natural stone by applying unsaturated polyester resin-nanosilica hybrid thin coating', *European Polymer Journal*, vol. 44, pp. 3146–3155.

Mu, B, Zhao, M & Liu, P 2008, 'Halloysite nanotubes grafted hyperbranched (co)polymers via surface-initiated self-condensing vinyl (co)polymerization', *Journal of Nanoparticle Research*, vol. 10, pp. 831–838.

Nelson, JK (ed.) 2010, *Dielectric polymer nanocomposites*, Springer Science, New York.

Neyman, E, Dillard, JG & Dillard, DA 2006, 'Plasma and silane surface modification of SiC/Si: adhesion and durability for the epoxy-SiC system', *Journal of Adhesion*, vol. 82, pp. 331–353.

- Nuhiji, B, Attard, D, Thorogood, G, Hanley, T, Magniez, K & Fox, B 2011, 'The effect of alternate heating rates during cure on the structure–property relationships of epoxy/MMT clay nanocomposites', *Composite Science and Technology*, vol. 71, pp. 1761–1768.
- Omrani, A, Afsar, S & Safarpour, MA 2010, 'Thermoset nanocomposites using hybrid nano TiO₂–SiO₂', *Materials Chemistry and Physics*, vol. 122, pp. 343–349.
- Osswald, TA & Hernández-Ortiz, JP 2006, *Polymer processing: modeling and simulation*, Carl Hanser Verlag, Munich.
- Paci, M, Filippi, S & Magagnini, P 2010, 'Nanostructure development in nylon 6-Cloisite 30B composites. Effects of the preparation conditions', *European Polymer Journal*, vol. 46, pp. 838–853.
- Park, S-J, Kim, B-J, Seo, D-I, Rhee, K-Y & Lyu, Y-Y 2009, 'Effects of a silane treatment on the mechanical interfacial properties of montmorillonite/epoxy nanocomposites', *Materials Science and Engineering A*, vol. 526, pp. 74–78.
- Pasbakhsh, P, Ismail, H, Fauzi, MNA & Bakar, AA 2009, 'Influence of maleic anhydride grafted ethylene propylene diene monomer (MAH-g-EPDM) on the properties of EPDM nanocomposites reinforced by halloysite nanotubes', *Polymer Testing*, vol. 28, pp. 548–559.
- Pasbakhsh, P, Ismail, H, Fauzi, MNA & Bakar, AA 2010, 'EPDM/modified halloysite nanocomposites', *Applied Clay Science*, vol. 48, pp. 405–413.
- Pascault, J-P, Sautereau, H, Verdu, J & Williams, RJ 2002, *Thermosetting polymer*, Marcel Dekker, Inc., New York.
- Patnaik, A, Satapathy, A, Mahapatra, SS & Dash, RR 2009, 'Tribo-performance of polyester hybrid composites: damage assessment and parameter optimization using Taguchi design', *Materials & Design*, vol. 30, pp. 57–67.
- Paul, DR & Robeson, LM 2008, 'Polymer nanotechnology: nanocomposites', *Polymer*, vol. 49, pp. 3187–3204.
- Pavlidou, S & Papaspyrides, CD 2008, 'A review on polymer-layered silicate nanocomposites', *Progress in Polymer Science*, vol. 33, pp. 1119–1198.
- Pereira, CMC, Herrero, M, Labajos, FM, Marques, AT & Rives, V 2009, 'Preparation and properties of new flame retardant unsaturated polyester nanocomposites based on layered double hydroxides', *Polymer Degradation and Stability*, vol. 94, pp. 939–946.
- Pettarin, V, Fasce, L, Pita, VR, Dias, ML & Frontini, P 2009, 'Thermal degradation behavior, permeation properties and impact response of polyethylene/organo-montmorillonite/(ethylene methacrylic acid) ternary nanocomposites', *Composite Interfaces*, vol. 16, pp. 201–218.

Phonthammachai, N, Li, X, Wong, S, Chia, H, Tjiu, WW & He, C 2011, 'Fabrication of CFRP from high performance clay/epoxy nanocomposite: preparation conditions, thermal–mechanical properties and interlaminar fracture characteristics', *Composites: Part A*, vol. 42, pp. 881–887.

Plueddemann, EP 1991, *Silane coupling agent*, Plenum Press, New York.

Pluta, M, Jeszka, JK & Boiteux, G 2007, 'Polylactide/montmorillonite nanocomposites: structure, dielectric, viscoelastic and thermal properties', *European Polymer Journal*, vol. 43, pp. 2819–2835.

Prashantha, K, Lacrampe, MF & Krawczak, P 2011, 'Processing and characterization of halloysite nanotubes filled polypropylene nanocomposites based on a masterbatch route: effect of halloysites treatment on structural and mechanical properties', *eXPRESS Polymer Letters*, vol. 5, pp. 295–307.

Prashantha, K, Schmitt, H, Lacrampe, MF & Krawczak, P 2011, 'Mechanical behaviour and essential work of fracture of halloysite nanotubes filled polyamide 6 nanocomposites', *Composites Science and Technology*, vol. 71, pp. 1859–1866.

Quaresimin, M, Salviato, M & Zappalorto, M 2012, 'Fracture and interlaminar properties of clay-modified epoxies and their glass reinforced laminates', *Engineering Fracture Mechanics*, vol. 81, pp. 80–93.

Rashmi, Renukappa, NM, Suresha, B, Devarajaiah, RM & Shivakumar, KN 2011, 'Dry sliding wear behaviour of organo-modified montmorillonite filled epoxy nanocomposites using Taguchi's techniques', *Materials and Design*, vol. 32, pp. 4528–4536.

Richardson, MOW & Wisheart, MJ 1996, 'Review of low-velocity impact properties of composite materials', *Composites: Part A*, vol. 27, pp. 1123–1131.

Rothon, RN (ed.) 2003, *Particulate-filled polymer composites*, Smithers Rapra Technology, Shrewsbury.

Roy, N & Bhowmick, AK 2010, 'Novel in situ polydimethylsiloxane-sepiolite nanocomposites: structure-property relationship', *Polymer*, vol. 51, pp. 5172–5185.

Ruiz-Perez, L, Royston, GJ, Fairclough, PA & Ryan, AJ 2008, 'Toughening by nanostructure', *Polymer*, vol. 49, pp. 4475–4488.

Samadi, A & Kashani, MR 2010, 'Effects of organo-clay modifier on physical–mechanical properties of butyl-based rubber nano-composites', *Journal of Applied Polymer Science*, vol. 116, pp. 2101–2109.

Santos, KS, Liberman, SA, Oviedo, MAS & Mauler, RS 2009, 'Optimization of the mechanical properties of polypropylene-based nanocomposite via the addition of a combination of organoclays', *Composites: Part A*, vol. 40, pp. 1199–1209.

Sawyer, LC, Grubb, DT & Meyers, GF 2008, *Polymer microscopy*, Springer, New York.

Schwartz, MM 1997, *Composite materials processing, fabrication, and applications: volume II (polymers, ceramics, metal matrices)*, Prentice Hall PRT, New Jersey.

Sen, S 2010, 'Effect of both silane-grafted and ion-exchanged organophilic clay in structural, thermal, and mechanical properties of unsaturated polyester nanocomposites', *Polymer Composites*, pp. 482–490.

Seyhan, AT, Gojny, FH, Tanoglu, M & Schulte, K 2007, 'Critical aspects related to processing of carbon nanotube/unsaturated thermoset polyester nanocomposites', *European Polymer Journal*, vol. 43, pp. 374–379.

Seyhan, AT, Tanoglu, M & Schulte, K 2009, 'Tensile mechanical behavior and fracture toughness of MWCNT and DWCNT modified vinyl-ester/polyester hybrid nanocomposites produced by 3-roll milling', *Materials Science and Engineering A*, vol. 523, pp. 85–92.

Shukla, A 2005, *Practical fracture mechanics in design*, Marcel Dekker, New York.

Siddhartha, Patnaik, A & Bhatt, AD 2011, 'Mechanical and dry sliding wear characterization of epoxy–TiO₂ particulate filled functionally graded composites materials using Taguchi design of experiment', *Materials and Design*, vol. 32, pp. 615–627.

Silani, M, Ziaei-Rad, S, Esfahanian, M & Tan, VBC 2012, 'On the experimental and numerical investigation of clay/epoxy nanocomposites', *Composite Structures*, vol. 94, pp. 3142–3148.

Spencer, MW, Cui, L, Yoo, Y & Paul, DR 2010, 'Morphology and properties of nanocomposites based on HDPE/HDPE-g-MA blends', *Polymer*, vol. 51, pp. 1056–1070.

Spencer, MW, Hunter, DL, Knesek, BW & Paul, DR 2011, 'Morphology and properties of polypropylene nanocomposites based on a silanized organoclay', *Polymer*, vol. 52, pp. 5369–5377.

Srivastava, I & Koratkar, N 2010, 'Fatigue and fracture toughness of epoxy nanocomposites', *JOM*, vol. 62, pp. 50–57.

Sun, L, Gibson, RF & Gordaninejad, F 2011, 'Multiscale analysis of stiffness and fracture of nanoparticle-reinforced composites using micromechanics and global-local finite element models', *Engineering Fracture Mechanics*, vol. 78, pp. 2645–2662.

Tang, L-C, Zhang, H, Sprenger, S, Ye, L & Zhang, Z 2012a, 'Fracture mechanisms of epoxy-based ternary composites filled with rigid-soft particles', *Composites Science and Technology*, vol. 72, pp. 558–565.

Tang, Y, Deng, S, Ye, L, Yang, C, Yuan, Q, Zhang, J & Zhao, C 2011, 'Effects of unfolded and intercalated halloysites on mechanical properties of halloysite–epoxy nanocomposites', *Composites Part A: Applied Science and Manufacturing*, vol. 42, pp. 345–354.

Tang, Y, Ye, L, Deng, S, Yang, C & Yuan, W 2012b, 'Influences of processing methods and chemical treatments on fracture toughness of halloysite–epoxy composites', *Materials and Design*, vol. 42, pp. 471–477.

Uddin, MF & Sun, CT 2010, 'Improved dispersion and mechanical properties of hybrid nanocomposites', *Composites Science and Technology*, vol. 70, pp. 223–230.

Unnikrishnan, V & Reddy, JN 2012, 'Multiscale analysis of the core nanotube in a nanocomposite system', *Finite Elements in Analysis and Design*, vol. 49, pp. 13–18.

Valles-Lluch, A, Ferrer, GG & Pradas, MM 2010, 'Effect of the silica content on the physico-chemical and relaxation properties of hybrid polymer/silica nanocomposites of P(EMA-co-HEA)', *European Polymer Journal*, vol. 46, pp. 910–917.

Varela-Rizo, H, Weisenberger, M, Bortz, DR & Martin-Gullon, I 2010, 'Fracture toughness and creep performance of PMMA composites containing micro and nanosized carbon filaments', *Composites Science and Technology*, vol. 70, pp. 1189–1195.

Velasco-Santos, C, Martinez-Hernandez, AL, Lozada-Cassou, M, Alvarez-Castillo, A & Castano, VM 2002, 'Chemical functionalization of carbon nanotubes through an organosilane', *Nanotechnology*, vol. 13, pp. 495–498.

Vera-Agullo, J, Glória-Pereira, A, Varela-Rizo, H, Gonzalez, JL & Martin-Gullon, I 2009, 'Comparative study of the dispersion and functional properties of multiwall carbon nanotubes and helical-ribbon carbon nanofibers in polyester nanocomposites', *Composites Science and Technology*, vol. 69, pp. 1521–1532.

Wan, YZ, Chen, GC, Raman, S, Xin, JY, Li, QY, Huang, Y, Wang, YL & Luo, HL 2006, 'Friction and wear behavior of three-dimensional braided carbon fiber/epoxy composites under dry sliding conditions', *Wear*, vol. 260, pp. 933–941.

Wang, H, Hoa, SV & Wood-Adams, PM 2006, 'New method for the synthesis of clay/epoxy nanocomposites', *Journal of Applied Polymer Science*, vol. 100, pp. 4286–4296.

Wang, K, Chen, L, Wu, J, Toh, ML, He, C & Yee, AF 2005, 'Epoxy nanocomposites with highly exfoliated clay: mechanical properties and fracture mechanisms', *Macromolecules*, vol. 38, pp. 788–800.

Wang, Q & Pei, X 2013, 'Chapter 4: the influence of nanoparticle fillers on the friction and wear behavior of polymer matrices' in *Tribology of polymeric nanocomposites*, 2nd edn, Butterworth-Heinemann, Oxford.

Wang, Y, Zhang, B & Ye, J 2011, 'Microstructures and toughening mechanisms of organoclay/polyethersulphone/epoxy hybrid nanocomposites', *Materials Science and Engineering: A*, vol. 528, pp. 7999–8005.

Weon, J-I 2009, 'Mechanical and thermal behavior of polyamide-6/clay nanocomposite using continuum-based micromechanical modeling', *Macromolecular Research*, vol. 17, pp. 797–806.

Wetzel, B, Rosso, P, Hauptert, F & Friedrich, K 2006, 'Epoxy nanocomposites—fracture and toughening mechanisms', *Engineering Fracture Mechanics*, vol. 73, pp. 2375–2398.

Wong, KJ, Zahi, S, Low, KO & Lim, CC 2010, 'Fracture characterisation of short bamboo fibre reinforced polyester composites', *Materials and Design*, vol. 31, pp. 4147–4154.

Xanthos, M (ed.) 2010, *Functional fillers for plastics*, Wiley-VCH GmbH & Co. KGaA, Weinheim, Germany.

Xie, D & Waas, AM 2006, 'Discrete cohesive zone model for mixed-mode fracture using finite element analysis', *Engineering Fracture Mechanics*, vol. 73, pp. 1783–1796.

Xu, L & Lee, J 2004, 'Effect of nanoclay on shrinkage control of low profile unsaturated polyester (UP) resin cured at room temperature', *Polymer*, vol. 45, pp. 7325–7334.

Ye, Y, Chen, H, Wu, J & Ye, L 2007, 'High impact strength epoxy nanocomposites with natural nanotubes', *Polymer*, vol. 48, pp. 6426–6433.

Ye, Y, Chen, H, Wua, J & Chan, CM 2011, 'Interlaminar properties of carbon fiber composites with halloysite nanotube-toughened epoxy matrix', *Composites Science and Technology*, vol. 71, pp. 717–723.

Yilmaz, O, Cheaburu, CN, Durraccio, D, Gulumser, G & Vasile, C 2010, 'Preparation of stable acrylate/montmorillonite nanocomposite latex via in situ batch emulsion polymerization: effect of clay types' *Applied Clay Science*, vol. 49, pp. 288–297.

Young, RJ & Lovell, PA 2011, *Introduction to polymers*, Taylor and Francis Group, Florida.

Yousif, BF & El-Tayeb, NSM 2010, 'Wear characteristics of thermoset composite under high stress three-body abrasive', *Tribology International*, vol. 43, pp. 2365–2371.

Yousif, BF & Ku, H 2012, 'Suitability of using coir fiber/polymeric composite for the design of liquid storage tanks', *Materials & Design*, vol. 36, pp. 847–853.

Yuan, Q, Chen, J, Yang, Y & Misra, RDK 2010, 'Nanoparticle interface driven microstructural evolution and crystalline phases of polypropylene: the effect of nanoclay content on structure and physical properties', *Materials Science and Engineering A*, vol. 527, pp. 6002–6011.

Yuan, Q & Misra, RDK 2006a, 'Impact fracture behavior of clay–reinforced polypropylene nanocomposites', *Polymer*, vol. 47, pp. 4421–4433.

Yuan, Q & Misra, RDK 2006b, 'Polymer nanocomposites: current understanding and issues', *Materials Science and Technology*, vol. 22, pp. 742–755.

Yudin, VE, Otaigbe, JU, Svetlichnyi, VM, Korytkova, EN, Almjasheva, OV & Gusarov, VV 2008, 'Effects of nanofiller morphology and aspect ratio on the rheo-mechanical properties of polyimide nanocomposites', *eXPRESS Polymer Letters*, vol. 2, pp. 485–493.

Zamanian, M, Mortezaei, M, Salehnia, B & Jam, JE 2013, 'Fracture toughness of epoxy polymer modified with nanosilica particles: particle size effect', *Engineering Fracture Mechanics*, vol. 97, pp. 193–206.

Zappalorto, M, Salviato, M & Quaresimin, M 2012, 'A multiscale model to describe nanocomposite fracture toughness enhancement by the plastic yielding of nanovoids', *Composites Science and Technology*, vol. 72, pp. 1683–1691.

Zeng, QH, Yu, AB & Lu, GQ 2008, 'Multiscale modeling and simulation of polymer nanocomposites', *Progress in Polymer Science*, vol. 33, pp. 191–269.

Zhang, A-B, Pan, L, Zhang, H-Y, Liu, S-T, Ye, Y, Xia, M-S & Chen, X-G 2012a, 'Effects of acid treatment on the physico-chemical and pore characteristics of halloysite', *Colloids and Surfaces A: Physicochemical and Engineering Aspects*, vol. 396, pp. 182–188.

Zhang, G, Sebastian, R, Burkhart, T & Friedrich, K 2012b, 'Role of monodispersed nanoparticles on the tribological behavior of conventional epoxy composites filled with carbon fibers and graphite lubricants', *Wear*, vol. 292–293, pp. 176–187.

Zhang, H & Zhang, Z 2007, 'Impact behaviour of polypropylene filled with multi-walled carbon nanotubes', *European Polymer Journal*, vol. 43, pp. 3197–3207.

Zhang, J, Chang, L, Deng, S, Ye, L & Zhang, Z 2013, 'Some insights into effects of nanoparticles on sliding wear performance of epoxy nanocomposites', *Wear*, vol. 304, pp. 138–143.

Zhang, J & Xie, X 2011, 'Influence of addition of silica particles on reaction-induced phase separation and properties of epoxy/PEI blends', *Composites Part B: Engineering*, vol. 42, pp. 2163–2169.

Zhang, M & Singh, RP 2004, 'Mechanical reinforcement of unsaturated polyester by AL₂O₃ nanoparticles', *Materials Letters*, vol. 58, pp. 408–412.

Zhang, X & Loo, LS 2009, 'Study of glass transition and reinforcement mechanism in polymer/layered silicate nanocomposites', *Macromolecules*, vol. 42, pp. 5196–5207.

Zhao, Q & Hoa, SV 2007, 'Toughening mechanism of epoxy resins with micro/nano particles', *Journal of Composite Materials*, vol. 41, pp. 201–219.

Zhou, H, Su, Y, Chen, X, Yi, S & Wan, Y 2010, 'Modification of silicalite-1 by vinyltrimethoxysilane (VTMS) and preparation of silicalite-1 filled polydimethylsiloxane (PDMS) hybrid pervaporation membranes', *Separation and Purification Technology*, vol. 75, pp. 286–294.

Zhou, Y, Yang, X & Jia, D 2007, 'Cure behavior of unsaturated polyester/modified montmorillonite nanocomposites', *Polymer International*, vol. 56, pp. 267–274.

Appendix A: Preliminary Study

Morphological, Mechanical and Fracture Toughness Characteristics of Unsaturated Polyester-based Clay Nanocomposite

Abstract

In this study, the role of nanoclay platelets on the micro- and nanoscale deformation and fracture behaviour of a highly crosslink unsaturated polyester (UPE)–based nanocomposite was investigated. Nanocomposites from different well-dispersed nanoclay contents (1 to 9 wt%) and UPE were prepared by a combination of mechanical stirrer and ultrasonication processes. Morphological structures for all nanocomposite systems were examined via transmission electron microscopy (TEM). Tensile testing and critical stress intensity factor (K_{Ic}) based on LEFM and CT specimen geometry were evaluated. The morphology of fracture surface was examined by scanning electron microscopy (SEM) to identify the toughening mechanisms of the nanocomposites. The intercalation/partially exfoliation structure of the UPE/clay nanocomposite with a significant enhancement in the mechanical and fracture characteristics were observed. Thought to be responsible for the toughness improvement were two main toughening mechanisms—shear bands and particles' debonding followed by subsequent plastic void growth of the polymer resin, achieved by the ordered nanoclay layers with different orientations.

Introduction

In general, the properties of polymer-clay nanocomposites are directly dependent on the state of particle dispersion—whether it is immiscible, intercalated or exfoliated nanocomposites (Utracki 2004; Koo 2006; Chinellato et al. 2010). The exfoliated/intercalated nanostructure and strong interaction between the clay nanolayers and the polymer chains play an emerging role in constraining the mobility of the polymer matrix and delaying the crack initiation and propagation, which consequently induces reasonable mechanical strength and toughness (Okamoto 2003). Fracture toughness is a critical mechanical property that characterises the

resistance of a material to crack propagation or fracture. The toughness of materials is directly dependent on the energy dissipation—that is, the energy absorbed in the fracturing of the part.

UPE resins are one of the most commonly used thermosetting polymers in different industrial applications due to their good mechanical properties and low cost and density (Pascault et al. 2002). However, the brittleness of such materials—due to their radical polymerisation between an unsaturated prepolymer and styrene—is one of their major drawbacks (Arends 1996). Hence, numerous experimental studies have been devoted to investigating the role of inserting second-phase fillers into thermosetting polymers in order to control their toughness.

For example, Evora and Shukla (2003) embedded a small content of TiO₂ nanoparticles in the UPE resin. They found that the presence of TiO₂ contributed to improving the tensile strength and fracture toughness. Baskaran, Sarojadevi and Vijayakumar (2011) revealed that the fracture energy of unfilled UPE resin improved by 60% with the addition of 5% alumina (Al₂O₃) nanoparticles. Further, the role of multi-walled carbon nanotubes (MWCNTs) on the fracture behaviour and toughening mechanisms of the UPE nanocomposite was investigated by Vera-Agullo et al. (2009) and Seyhan et al. (2009). The use of MWCNTs effectively increased the fracture toughness and energy without sacrificing other properties, such as strength, modulus and glass transition temperature.

As a result of the aforementioned investigations, several toughening mechanisms have been noted in polymers filled by micro- and nanoparticles, such as microcracking (Liang & Pearson 2009) and multiple craze-like banding with dilatation (Ma et al. 2008). Crack-pinning is another mechanism in which the crack front bows out between the filler particles and remains pinned at the particles (Srivastava & Koratkar 2010). Localised shear yielding (or shear banding) mechanism is a narrow zone of intense shearing strain forming due to material instability, corresponding to an abrupt loss of homogeneity of deformation. Massive shear-banding is another mechanism that occurs due to the reduction in yield stress by the stress concentration of the compliant nanoscale or rubber particles that facilitate shear yielding (Ma et al. 2008). The particle bridging mechanism involves a

rigid or ductile particle acting as a bridging particle. The present study was undertaken to investigate the mechanical and fracture characteristics of UPE/nanoclay composites in order to understand the structure/property relationship and to determine to what extent clay layers contribute to inhabiting the crack propagation and improve the toughness of these nanocomposites.

Experimental Setup

Materials and Nanocomposites Preparation

In this study, organoclay platelets with a brand of Cloisite[®] 30B—provided by Southern Clay Products, Inc., via Jim Chambers & Associates, Australia—were used as reinforcements. The alkyl ammonium surfactant used in the organoclay was methyl, tallow, bis-2-hydroxyethyl quaternary ammonium chloride as an organic modifier having a cation exchange capacity of 90 meq/100 g, as shown in Figure A.1.

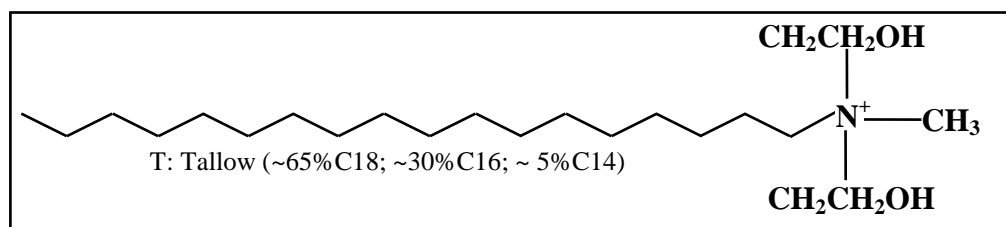


Figure A.1: Structures of Organoclay (Cloisite[®] 30B)

Thermosetting UPE resin from AROPOL[®]-1472PLSE, Nupol, Australia, and 45% styrene was used as polymer matrix. Different amounts (1, 3, 5, 7, and 9 wt%) of nanoclay were used to prepare UP/clay nanocomposites by means of high shear mixing followed by an ultrasonication process. To achieve full polymerisation, after mixing, the catalyst MEKP (MEKP/Butanox-M50) with 33% peroxide content was added to the mixture at 2% of the UP weight percentage, and stirred manually for one minute, as per the instructions of the supply company. Later, the mixture was poured into special plastic moulds with the designated fracture specimen's geometry,

then cured at room temperature for 24 hours, post-cured at 60°C for two hours, and then at 90°C for two hours, following an increment rate of 10°C/30 minutes.

Morphological Characterisation

A transmission electron microscope was used to observe the dispersion of clay layers in the UPE resin. Ultrathin sections of approximately 70 nm in thickness were cut by diamond knife from the nanocomposites at room temperature and examined using a JEOL (JEM-1010) TEM instrument at an acceleration voltage of 100 KV. A scanning electron microscope (Philip XL-30) was used to identify the failure modes and toughening mechanism in the clay nanocomposites. The SEM observations were carried out after sputter coating with a thin layer of platinum to increase the electric conductivity.

Tensile and Fracture Tests

Tensile mechanical tests were performed according to ASTM D 638, using an Instron model (Alliance RT/10) machine to measure the basic material properties of the neat UPE and UPE filled with different nanoclay particles. A laser extensometer was used to determine the axial strain for each nanocomposite system. A crosshead loading rate of 1 mm/minute was adapted for all tensile tests. The strength of each nanocomposite system was evaluated from the testing and averaging of at least five samples at 24°C.

The elongation at break was taken as the averaged value of at least three specimens. The stress intensity factor (K_{Ic}) of the cured UP and UP/clay nanocomposites was evaluated using the CT configurations applying the tensile load. The CT samples were prepared according to ASTM D5045 (Figure A.2). A pre-crack was generated by tapping a fresh razor blade into the notch tip with a drop weight to ensure an accurate K_{Ic} value. A loading rate of 5 mm/min was adapted to measure the K_{Ic} using the following relationships:

$$K_{Ic} = \frac{P_Q}{BW^{1/2}} \cdot f\left(\frac{a}{W}\right) \quad (\text{A.1})$$

$$f\left(\frac{a}{W}\right) = \frac{\left(2 + \frac{a}{W}\right) \left\{0.886 + 4.64\left(\frac{a}{W}\right) - 13.32\left(\frac{a}{W}\right)^2 + 14.72\left(\frac{a}{W}\right)^3 - 5.6\left(\frac{a}{W}\right)^4\right\}}{\left(1 - \frac{a}{W}\right)^{3/2}} \quad (\text{A.2})$$

where P_Q is the load determined from the load-displacement curve and B is the specimen thickness. The K_{Ic} values were checked against the following:

$$B, a, (W-a) > 2.5 (K_{Ic}/\sigma_y)^2 \quad (\text{A.3})$$

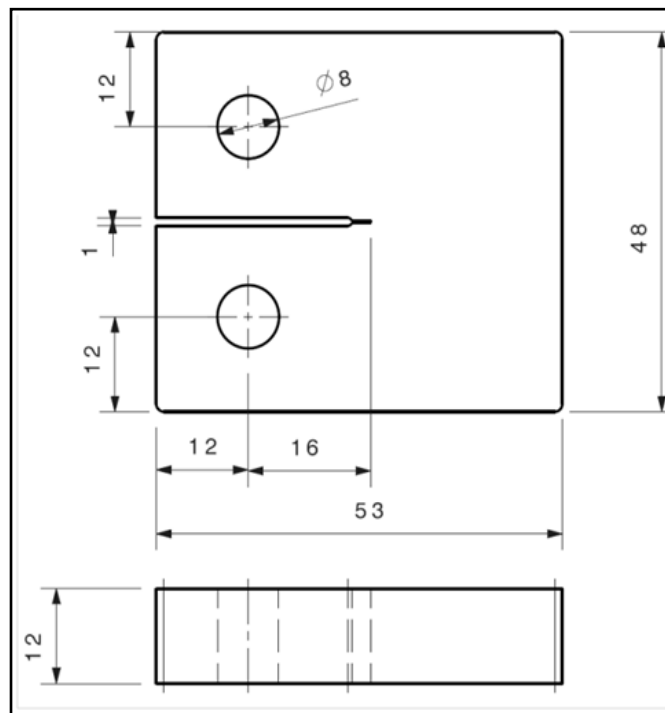


Figure A.2: Dimension of the CT Configuration Used in this Study

Results and Discussion

Morphology

Figure A.3 (a to e) shows the representative TEM micrographs of the cured UPE filled with different nanoclay percentages. It can be noted that a good dispersion of clay layers in the polymeric matrix with a plausible intercalation between nanoclay and the polymer chains was achieved with the use of direct high shear mixing and ultrasonication process. However, several agglomerates of microparticles with a thickness of 100 nm or greater created at the higher nanoclay loadings can also be noted in Figure A.3 (c to e). The appearance of these particle clusters was attributed to the structure of the clay, which comprised of platelets with an inner octahedral layer surrounded by two silicate tetrahedral layers. The natural state of clay—which exists as stacks of many platelets at several hundred nanometres long and wide, separated by an interlayer distance of ~1 to 3 nm—may also tend to create clay clusters (Boukerrou et al. 2007; Park, Davis & Sullivan 2010).

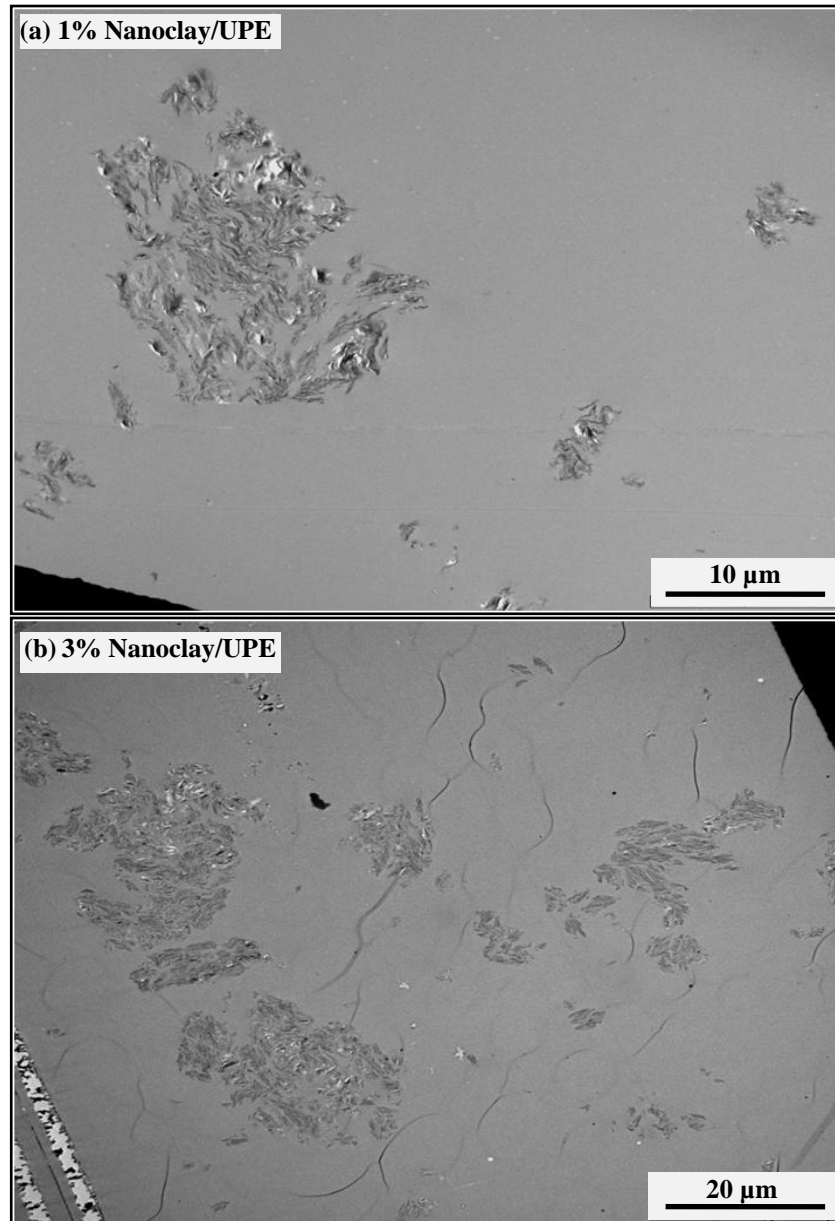


Figure A.3: TEM Photomicrographs of UPE Filled by Different Clay Nanocomposites

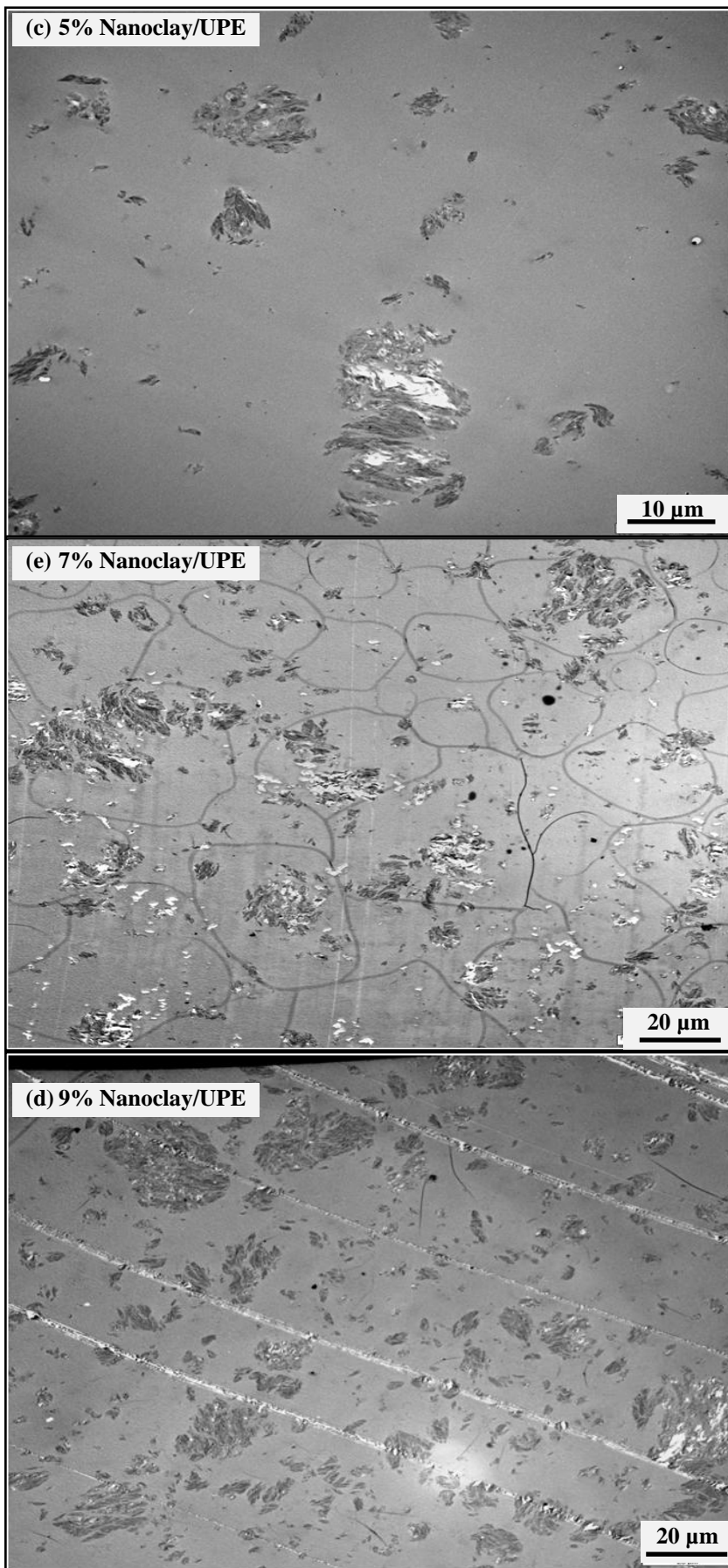


Figure A.3 (Continued)

Tensile Properties

The tensile properties of the cured UP matrix and its different clay nanocomposites are summarised in Table A.1. The tensile strength and modulus of the composites significantly increased with increasing nanoclay content over the neat UPE matrix. The 3% clay nanocomposite exhibited the highest values of tensile strength and modulus, and the 9% clay showed the lowest values compared to the neat UPE resin. These property enhancements were ascribed to the reinforcing effect of the clay nanoplatelets. This postulation has supported by the TEM images those shown the uniform dispersion of the nanoclay layers throughout the nanocomposites.

Table A.1: Tensile Properties of Nanoclay Modified UPE

Materials	Tensile properties		
	Strength (MPa)	Modulus (GPa)	Elongation at break (%)
Neat UPE	19.8 ± 2	34.41 ± 2	0.63 ± 0.03
UP/1% Nanoclay	20.8 ± 4	37.8 ± 4	0.53 ± 0.04
UP/3% Nanoclay	32.2 ± 2	40.05 ± 1	0.43 ± 0.02
UP/5% Nanoclay	25.9 ± 3	38.2 ± 3	0.44 ± 0.03
UP/7% Nanoclay	22.2 ± 4	36.35 ± 3	0.49 ± 0.02
UP/9% Nanoclay	18.9 ± 2	34.85 ± 2	0.58 ± 0.05

Fracture Toughness Test

Figure A.4 shows a set of typical load of COD curves obtained after Mode I fracture toughness testing using the CT geometry for the neat UPE and its different clay nanocomposites. Upon loading, all systems had undergone an unstable crack growth with a straight line dropped to zero when the maximum loads were reached. This was because of the highly crosslinked density of the thermosetting UPE resin and its inclination to fast fracture. Meanwhile, the 3 wt% clay/UPE nanocomposite system manifested its ability to carry higher loads with lesser displacements (COD). The 5 wt% clay nanocomposite showed lower loads with higher displacements, and the unfilled UPE resin exhibited the lowest load before failure occurred.

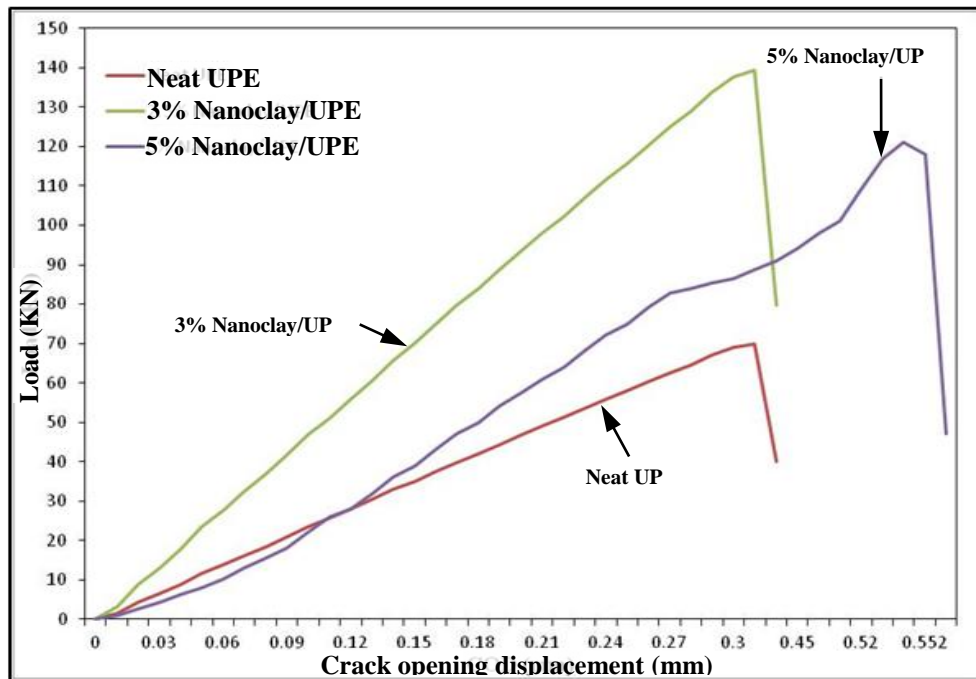


Figure A.4: Typical Load Versus COD Curves for UPE Matrix and its Different Clay Nanocomposites

The values of fracture toughness (K_{Ic}) versus different clay loadings (1–9 wt%) are illustrated in Figure A.5. The K_{Ic} magnitudes of the modified UP modestly improved with nanoclay platelets incorporation. The introduction of 3 wt% clay into the UPE matrix showed the highest K_{Ic} with a 61% improvement (from 1.51 MPa.m^{0.5} for neat UP to 2.435 MPa.m^{0.5} for the nanocomposite). However, further increase of nanoclay content demonstrated a gradual decrease in the toughness due to the presence of clay aggregates and the weak interaction between the clay layers and the polymer resin. These findings conform with those reported by Quaresimin, Salviato and Zappalorto (2012).

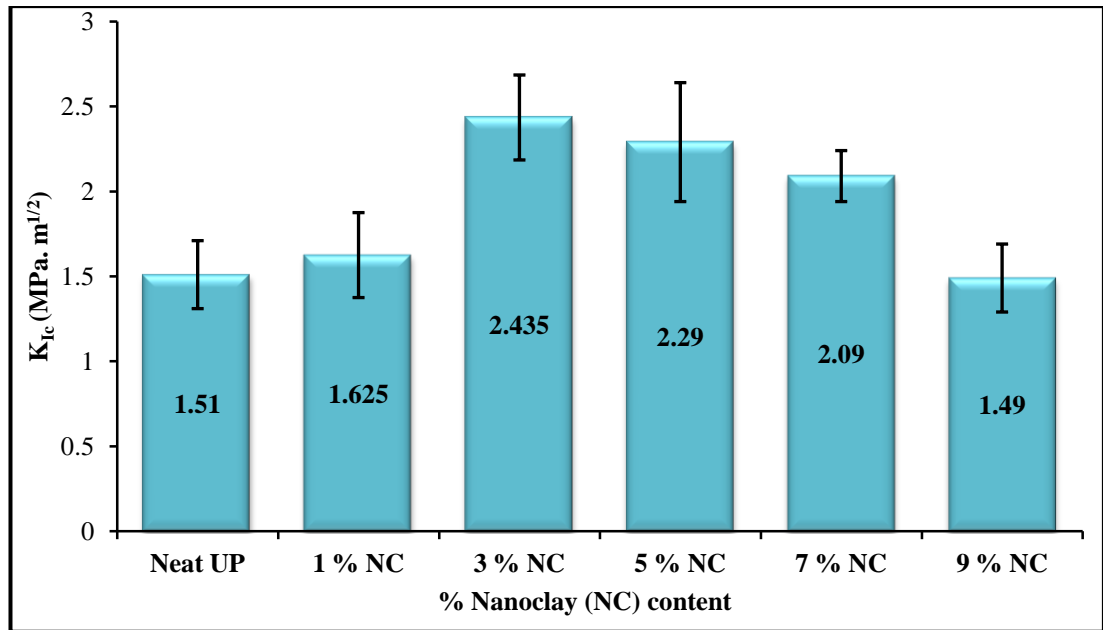


Figure A.5: Fracture Toughness of the Neat UPE and UPE/MMT Nanocomposites

To further understanding the role of nanoclay on the fracture toughness of the UPE nanocomposites, different K_{Ic} values obtained from different published studies are compared in Table A.2. From this table it can be seen that the incorporation of even low levels of nanoparticle into the neat UPE resin resulted in significant changes in the fracture toughness of the produced nanocomposites, compared to the neat UPE matrix. This observation was attributed to the fact that the initiation of plastic deformation due to the nanoparticle role helps restrict the crack propagation under continuous load. Further discussion on toughening mechanisms to support this claim is provided in the next section.

Table A.2: Fracture Toughness (K_{Ic}) of Different Particle-filled UPE

Materials	K _{Ic} (MPa.m ^{1/2}) {Specimen geometry used}	Preparation method and reference
UPE/3 wt% MMT	2.435 [1.51: Neat UP] {CT}	The present study
UPE/1 wt% TiO ₂	0.85 [0.5: Neat UP] {SENB}	Direct ultrasonification and Evora and Shukla (2003)
UPE/1 wt% Alumina	1.42 [1: Neat UP] {SENB}	Direct mixing approach and Zhang and Singh (2004)
UPE/40% bamboo fibre (10 mm length)	1.2 [0.5: Neat UP] {CT}	Laminating lay-up process and Wong et al. (2010)

Note: SENB = single-edge notched bending.

Toughening Mechanisms

The SEM examination was used to identify the toughening mechanisms that occurred in the neat UP and its different clay nanocomposites fractured under Mode I fracture toughness at ambient temperature. The fracture surface of the neat UPE (Figure A.6a) exhibited a very smooth, highly brittle fracture mode, except for the initiation of some feather-like structure. This indicated that the resistance to crack propagation was very low, and consequently the fracture toughness was low. The introduction of clay particles into the UPE resin was associated with better absorbing of energy, leading to localised shear yielding.

Supporting that finding, Srivastava and Koratkar (2010) revealed that inserting nanoclay particles as a second phase into a single-phase thermosetting polymer contributed to the presence of isolated shear bands associated with local plastic deformation, as the energy absorption mechanism was responsible for improving the toughness. Further, inserting nanoclay particles into the UPE resin induced a particle-pinning mechanism in front of the crack (Figure A.6c), leaving behind a tail-like structure. An SEM image of the fracture surface of UP/5 wt% clay nanocomposite (Figure A.6d) indicated that the crack propagation travelled in different directions on the cleavage surface. The directions of crack advancement were from top to bottom, with an irregular curved path. Further clay incorporation (> 5 wt%) into the crosslink UPE resin, accompanied with mixed toughening mechanisms (Figure A.6e and f), was represented by matrix-particle debonding, followed by a matrix plastic void growth mechanism, which is a significant part of matrix plastic deformation in clay nanocomposites (Liang & Pearson 2009).

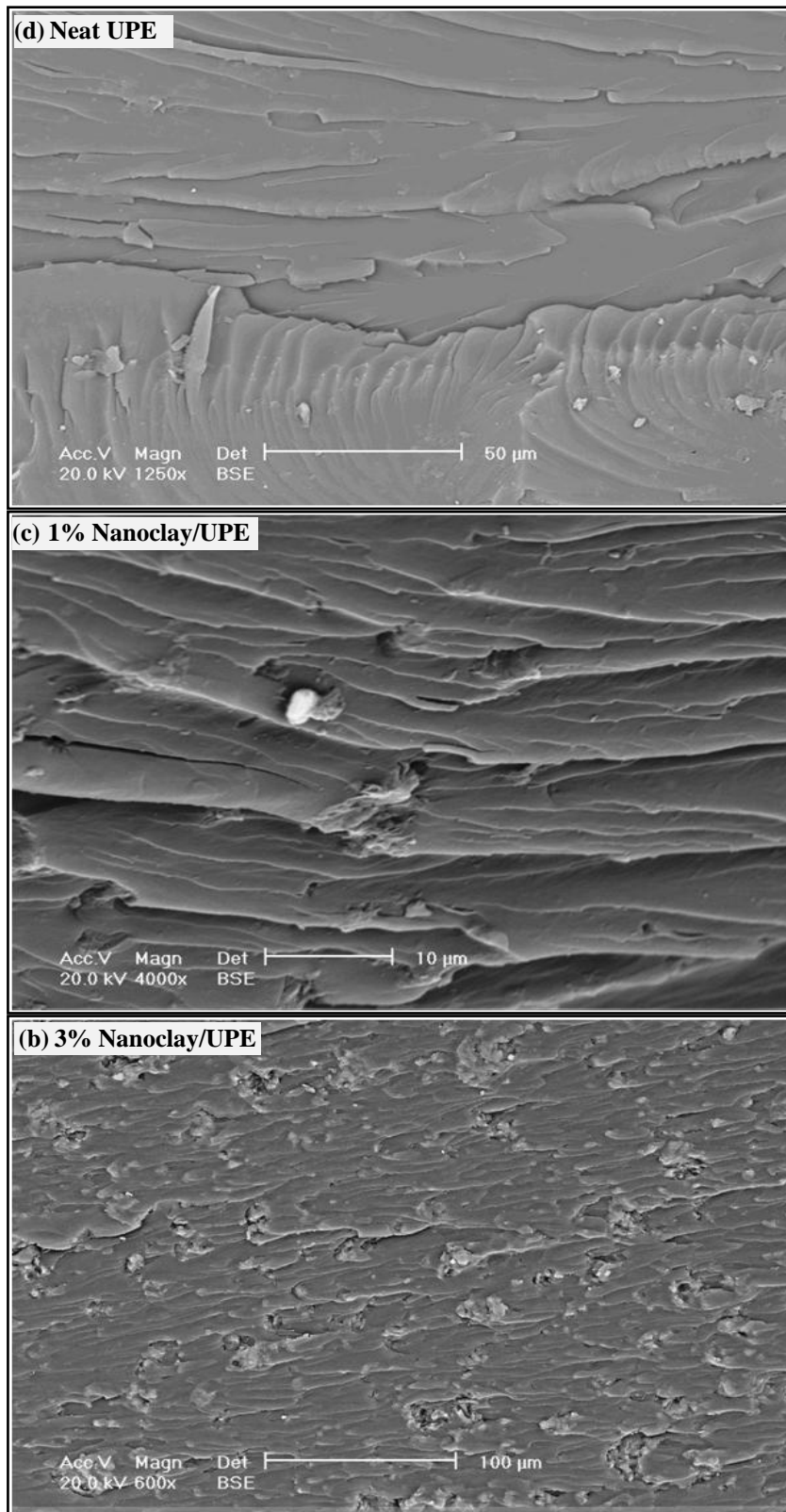


Figure A.6: Fracture Surface of the Neat UP and its Different Clay Nanocomposites After Testing the CT Samples Under Mode I Fracture Toughness

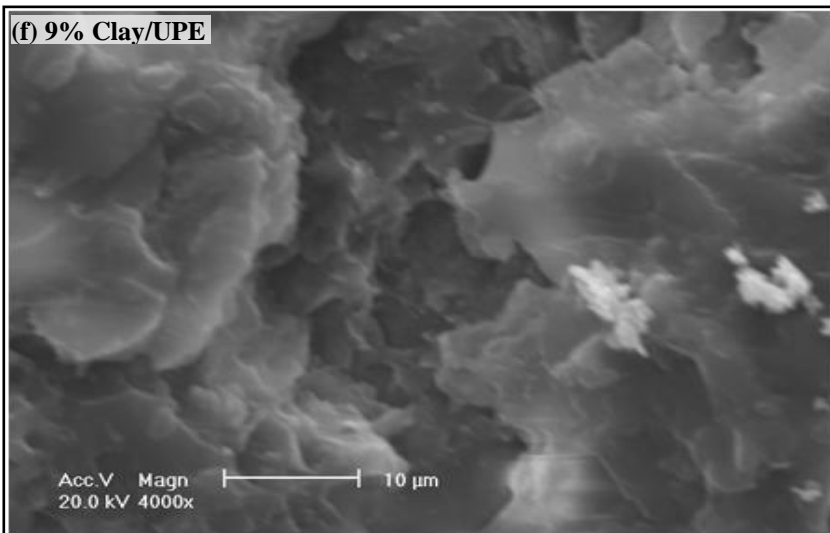
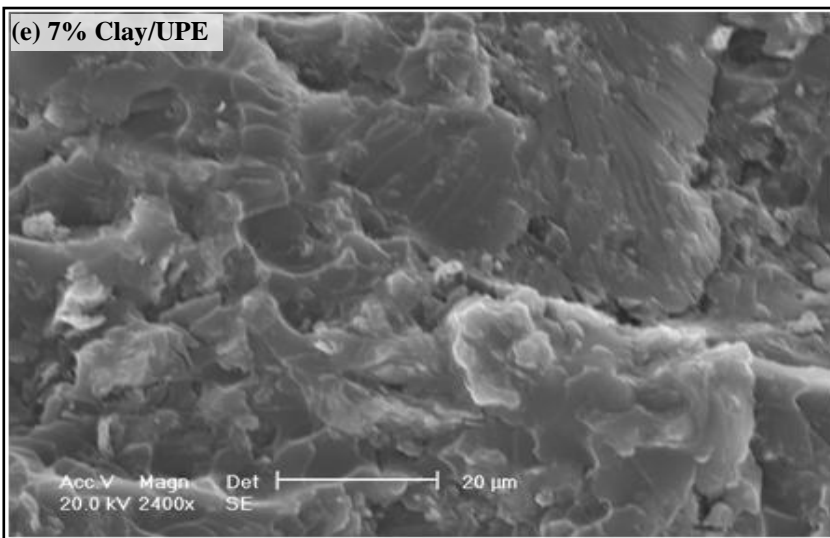
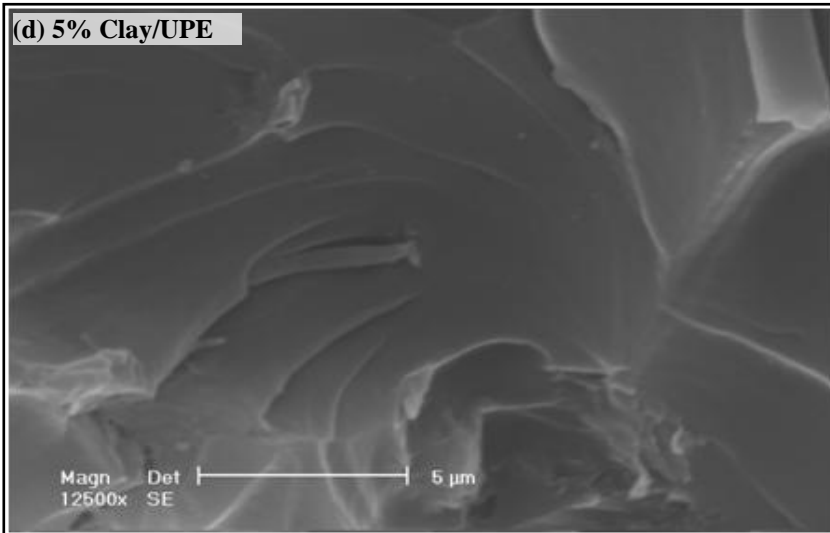


Figure A.6 (Continued)

This study sought to provide further insight into the nano-effect of clay particles on the fracture surface of the UPE/clay nanocomposite. Thus, different fracture surfaces of the UP/3 wt% clay nanocomposite were examined with different magnifications using the SEM, as shown in Figure A.7. The topography view of the surface at low magnification, indicating different zones of the crack initiation and propagation, is presented in Figure A.7a. Compared with that of the other zones, Zone 1 near the crack tip seemed to be smooth, without any qualitative evidence of the initiation of plastic deformation. This was probably related to the preparation of pre-cracks—that is, the pre-cracks made with a razor blade may have a near fully developed damage zone caused by the razor insertion. This observation was also noted by Wang et al. (2005).

Another SEM observation at low magnification (Zone 2A in Figure A.7b) indicates crack initiation and growth, in which the formation of microcracks can be noted. At higher magnification of the same zone (Figure A.7c), it is shown that tearing of the connected materials—the particle-matrix interface—and decohesion occurred at the weakest locations. Additionally, with the zone that is further from the crack tip (Zone 2B—see images d and e), the matrix plastic deformation was found to play an essential role in the zone shielding mechanism, which is definitely credited for the toughening mechanism in the UPE/clay nanocomposite. Considering the furthest zones from the crack tip (Zones 2C and 2D), the fracture surface is very rough and filled with scale-like steps, revealing the presence of nanoclay platelets that forced the crack to grow along a very tortuous path. In addition, many micro- and macrocracks are observed between the scale-like steps, indicated by yellow arrows. The same observation was noted and discussed in the section on toughening mechanisms in the UPE/HNT nanocomposites in Chapter 7.

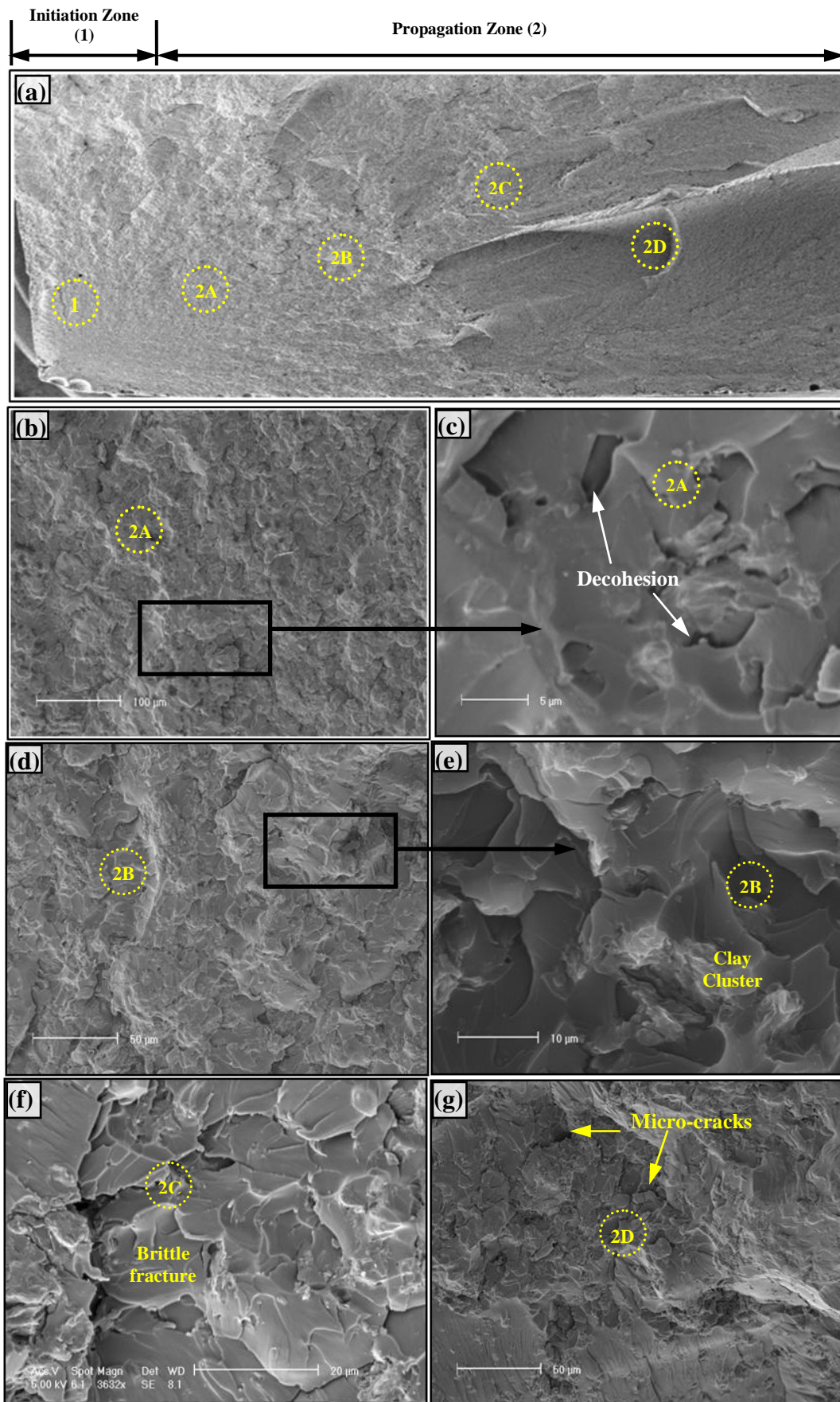


Figure A.7: SEM Images with Different Magnifications of the Fracture Surfaces of UP/3 wt% Clay Nanocomposites Ruptured at Room Temperature, Showing Different Zones of the Initiation and Crack Propagation

Conclusion

This preliminary study investigated the nano-effect of nanoclay platelets on the morphological, mechanical and fracture toughness characteristics of the UPE nanocomposites prepared by high mechanical stirrer and ultrasonication process. The morphological characterisation showed an intercalation structure with a uniform dispersion of clay particles in the nanocomposites. The highest increase in the tensile strength and modulus was found to be with the incorporation of 3% clay into the UPE nanocomposite. These properties improved by 62% and 16%, respectively, due to the role of clay reinforcement. The introduction of clay nanoparticles induced higher fracture toughness, with the stress intensity factor (K_{Ic}) improving by 61% in the nanocomposite containing 3% clay. The presence of nanoclay in the UPE matrix contributed to a shift in the deformation mechanic. The initial state of the neat UPE was a very smooth, highly brittle fracture with some feather-like structure. This changed to a localised shear yielding with crack pinning that left behind a tail-like structure and particle debonding, followed by a matrix plastic void growth mechanism, which is a significant part of the matrix plastic deformation. This occurred in the clay nanocomposites and was responsible for the main energy absorption in the clay nanocomposites.

References

- Arends, CB (ed.) 1996, *Polymer toughening*, Marcel Dekker Inc., New York.
- Baskaran, R, Sarojadevi, M & Vijayakumar, CT 2011, 'Unsaturated polyester nanocomposites filled with nano alumina', *Journal of Materials Science*, vol. 46, pp. 4864–4871.
- Boukerrou, A, Duchet, J, Fellahi, S, Kaci, M & Sautereau, H 2007, 'Morphology and mechanical and viscoelastic properties of rubbery epoxy/organoclay montmorillonite nanocomposites', *Journal of Applied Polymer Science*, vol. 103, pp. 3547–3552.
- Chinellato, AC, Vidotti, SE, Hu, G-H & Pessan, LA 2010, 'Compatibilizing effect of acrylic acid modified polypropylene on the morphology and permeability properties of polypropylene/organoclay nanocomposites', *Composites Science and Technology*, vol. 70, pp. 458–465.

Evora, VMF & Shukla, A 2003, 'Fabrication, characterization, and dynamic behavior of polyester/TiO₂ nanocomposites', *Materials Science and Engineering A*, vol. 361, pp. 358–366.

Koo, JH 2006, *Polymer nanocomposites processing, characterization, and applications*, McGraw-Hill Professional Publishing, Ohio.

Liang, YL & Pearson, RA 2009, 'Toughening mechanisms in epoxy–silica nanocomposites (ESNs)', *Polymer*, vol. 50, pp. 4895–4905.

Ma, J, Mo, M-S, Du, X-S, Rosso, P, Friedrich, K & Kuan, H-C 2008, 'Effect of inorganic nanoparticles on mechanical property, fracture toughness and toughening mechanism of two epoxy systems', *Polymer*, vol. 49, pp. 3510–3523.

Okamoto, M 2003, *Polymer/layered silicate nanocomposites*.

Park, JY, Davis, TB & Sullivan, PL 2010, 'Parametric study on the fabrication of clay-containing thermosetting nanocomposites', *Journal of Reinforced Plastics and Composites*, 29.

Pascault, J-P, Sautereau, H, Verdu, J & Williams, RJ 2002, *Thermosetting polymer*, Marcel Dekker, Inc., New York.

Quaresimin, M, Salviato, M & Zappalorto, M 2012, 'Fracture and interlaminar properties of clay-modified epoxies and their glass reinforced laminates', *Engineering Fracture Mechanics*, vol. 81, pp. 80–93.

Seyhan, AT, Tanoglu, M & Schulte, K 2009, 'Tensile mechanical behavior and fracture toughness of MWCNT and DWCNT modified vinyl-ester/polyester hybrid nanocomposites produced by 3-roll milling', *Materials Science and Engineering A*, vol. 523, pp. 85–92.

Srivastava, I & Koratkar, N 2010, 'Fatigue and fracture toughness of epoxy nanocomposites', *JOM*, vol. 62, pp. 50–57.

Utracki, LA 2004, *Clay-containing polymeric nanocomposites*, Smithers Rapra, Shrewsbury.

Vera-Agullo, J, Glória-Pereira, A, Varela-Rizo, H, Gonzalez, JL & Martin-Gullon, I 2009, 'Comparative study of the dispersion and functional properties of multiwall carbon nanotubes and helical-ribbon carbon nanofibers in polyester nanocomposites', *Composites Science and Technology*, vol. 69, pp. 1521–1532.

Wang, K, Chen, L, Wu, J, Toh, ML, He, C & Yee, AF 2005, 'Epoxy nanocomposites with highly exfoliated clay: mechanical properties and fracture mechanisms', *Macromolecules*, vol. 38, pp. 788–800.

Wong, KJ, Zahi, S, Low, KO & Lim, CC 2010, 'Fracture characterisation of short bamboo fibre reinforced polyester composites', *Materials and Design*, vol. 31, pp. 4147–4154.

Zhang, M & Singh, RP 2004, 'Mechanical reinforcement of unsaturated polyester by AL_2O_3 nanoparticles', *Materials Letters*, vol. 58, pp. 408–412.